Universitat Autònoma de Barcelona

GRAPHENE FIELD-EFFECT TRANSISTORS AS FLEXIBLE NEURAL INTERFACES FOR INTRACORTICAL ELECTROPHYSIOLOGY

Andrea Bonaccini Calia

GRAPHENE FIELD-EFFECT TRANSISTORS AS FLEXIBLE NEURAL INTERFACES FOR INTRACORTICAL ELECTROPHYSIOLOGY

Andrea Bonaccini Calia

Doctor of Philosophy in Electrical and Telecomunication Engineering
of the
Universitat Autònoma de Barcelona

Supervisor: Prof. José A. Garrido Ariza
Thesis Tutor: Prof. David Jiménez Jiménez

Catalan Institute of Nanoscience and Nanotechnology
Barcelona, Spain, December 2020

ICN2 Institut Català de Nanociència i Nanotecnologia
EXCELENCIA SEVERO OCHOA

UAB Universitat Autònoma de Barcelona

Abstract

Recent years have witnessed novel technology developments of neural implants for medical applications which are expected to pave the way to unveil functionalities of the central nervous system. Understanding the human brain is commonly considered one of the biggest scientific challenges of our time; as a consequence we are witnessing an intensified research in the development of brain-machine-interfaces (BMIs) , which would allow us to both read and stimulate brain activity. Nevertheless, currently available neural implants offer a modest clinical efficacy, partly due to the limitations posed by the invasiveness of the implants materials and technology and by the metals used at the electrical interface with the tissue. Such materials compromise the interfacing resolution, the performance and the long term stability of neural implants. Development of flexible electronics using biocompatible materials is key for the realisation of minimally invasive neural implants, which can be chronically implanted without causing rejection from the immune system.

A relatively young yet very promising research field, that is increasingly drawing attention is the use of two dimensional materials, such as graphene, for bioelectronic applications. Graphene solution-gated field effect transistor (gSGFET) is one of several emerging new neural technologies. These devices can overcome the above-mentioned limitations thanks to the outstanding properties of graphene, such as mechanical flexibility, electrochemical inertness, biocompatibility and high sensitivity. In this PhD thesis, arrays of gSGFETs have been fabricated and iteratively optimized in terms of sensitivity and signal-to-noise ratio, adopting wafer-scale micro-fabrication methods. The 1/f noise in gSGFETs has been characterised and the optimisation of both, contact and channel noises was achieved by UVO-treatment at the metal/graphene interface, as well as by decoupling the graphene channel from the substrate, using different nanomaterials such as graphene encapsulation with hexagonal boron nitride (hBN), self assembled monolayers and double transferred graphene.

Moreover, flexible and ultra-thin epicortical and intracortical neural probes, contain-

ing arrays of gSGFETs, have been successfully fabricated and used during *in vivo* microelectrocorticography recordings in anaesthesized and awake rodents. Flexible intracortical devices were inserted into the brain using a back-coating stiffening protocol with bioresobable silk fibroin protein, developed during this PhD thesis. The results presented in this PhD demonstrate the superior spatio-temporal resolution of gSGFETs compared to standard microelectordes technology; particularly the ability to map with high fidelity, infraslow activity (ISA, < 0.1 Hz) together with signals in the typical local field potential bandwidth.

Today it is known that infraslow brain activity, including spreading depolarisations, contribute to the pathophysiology of several neurological disorders such as stroke, traumatic brain injury, migraine and epilepsy. However, this activity is seldom recorded due to intrinsic technical limitations of conventional AC-coupled electrodes. To demonstrate the usefulness of the developed flexible gSGFET arrays technology, recordings have been obtained with multichannel flexible graphene depth neural probes (gDNP) in relevant awake animal models of seizures and established epilepsy. ISA was detected and mapped through different cortical layers and subcortical regions, whilst simultaneously recording epileptiform activity in more conventional frequency bands (1-600Hz). Furthermore, the assessment of the long term recording stability and functionality, as well as biocompatibility of the gDNP has also been demonstrated as part of this thesis.

The graphene based bioelectronic technology here described has the potential to become a gold standard tool for full bandwidth electrophysiology. This technology is envisioned to have a great impact on a broad and multidisciplinary community including neurotechnology researchers, biomedical engineers, neuroscientists studying wide-band cortical dynamics associated with spontaneous behaviour and/or brain states, as well as clinical researchers interested in the role of infraslow activity in epilepsy, stroke and migraine.

Dedicated to my beloved mother and father,
and to all my Masters
in the journey of life.

Acknowledgements

I acknowledge Prof. J. A. Garrido and my colleagues, , who have worked with me during the PhD period, and have made together possible the setup, the evolution and progress of our graphene technology labs, as well as the progressive accomplishment of this work from the very beginning of the AEMD-group. A big thanks to Prof. Rosa Villa and the whole CNM-group for the opportunity to work together and to share great achievements. To Anton Guimerá for the technical support in the data analysis. To Xavi Illa for the kind and essential support in the development of the technology. To Nathan Schäfer, Damiá Viana, Clement Hébert, Eduard Masvidal, Elena Del Corro, Jessica Busquet and Jose Manuel de la Cruz, friends and colleagues, for the astonishing team work and the motivation during all these years. I thank all for the encouragement, the patience, the broad mind, the collaborative attitude, the good atmosphere, the teamwork, the joint efforts, the sharing.

I have learned, I have taken and given a lot in these years, and the success of this work is also due to the dedication, interconnections and exchanges which have happened all along.

I also would like to wholeheartedly thank Dr. R. Wykes, Dr. T. M. Smith and the whole UCL-epilepsy team for the amazing collaboration and the opportunity to participate in neuroscience research, from a very deep perspective. I would like to thank Prof. Kostas Kostarelos and colleagues, from the Nanomedicine lab in Manchester, for the rich, multidisciplinary exchange of ideas and experiments. I would also like to acknowledge my parents, Anna and Domenico, for always being by my side; Harmony Rutherford, for always showing me patience and great, heartfelt support; and my friend Lorenzo Di Santa Cristina, for the deep philosophical discussions and inspirational conversations.

Table of Contents

List of Figures

List of Tables

1

Introduction

1.1 Current technologies for neural interfaces

During the 20th century, neural interfaces have offered a powerful toolkit for novel clinical interventions, which aims at stimulating and/or recording the electrical activity of the nervous system. Historically, the discovery of electrical sensitivity in living tissue, referred to as 'bioelectricity', dates back to the 17th century [1]. Luigi Galvani and Jan Swammerdam were the first who observed that electrical current flows in the nerves of living organisms; they used frog legs to show the contraction of muscles by electrical stimulation applied via metal wires first, and later using directly the frog's sciatic nerve. Nowadays, there are multiple active implantable devices available, which interface with neural tissue. They offer a promising approach for the treatment of various chronic diseases of the central nervous (CNS) or peripheral nervous systems (PNS), by electrically stimulating different neuronal structures[2]. Examples of successfully implemented stimulation devices in the clinics include cochlear implants, which restore hearing (the devices converts sound waves into electrical impulses that goes to electrodes arrrays, which stimulates the cochlea nerve) and deep brain stimulators (DBS), applied for the symptomatic treatment of motor-related disorders, such as Parkinson's disease, dystonia and tremor [3]. Currently under clinical development are DBS to be used for other drug-resistant neurological disorders, such as depression, obsessive–compulsive disorder and others [4, 5]. Another type are the retinal implants, intended to partially restore vision in blind patients, suffering from retinal diseases leading to the loss of photoreceptors [6].

Electrical stimulation of the nervous systems has also been applied via implanted neuroprosthetic devices at the spinal cord, or at peripheral nerves and muscles to restore sensory and motor functions in a novel and promising field of therapeutic interventions, termed "bioelectronics".

By stimulating the somatosensory cortex, tactile information such as contact location, pressure, and temporal information was restored [7, 8]. These techniques can be further integrated into an external hand prosthesis for complete recovery of tactile sensing and precise motor control in future works, which could open a new era of rehabilitation [9].

Neural interfaces that only record electrical activity of the brain aim at addressing different clinical needs, with respect to those mentioned above. Recording electrodes in the context of basic electrophysiology research have been essential to our understanding on how electrical signals propagates by individual neurons producing action potentials. They provide also insight into neuron coupling phenomena as well as into the genesis of neural networks and circuitry in the brain [10]. Electrophysiological recordings of brain activity can be performed by positioning electrode arrays in different areas, such as externally onto the scalp as in electroencephalography (EEG), above or under the dura mater such as electrocorticography (ECoG) and subcortically such as in stereotactic electroencephalography (SEEG). Non-invasive electrodes located on the scalp allow recording of the global activity of different areas in the brain, hence provide useful functional information. However, intracranial electrodes are able to record electrical signals with higher spatial and temporal resolution since the signal is not attenuated by the scalp, meninges and muscles; therefore, they are the standard of choice for several clinical applications. For example, cortical neural interfaces are employed in acute clinical setting for diagnostic purposes and/or for pre-interventional brain mapping conducted prior to brain surgery. Particularly, intracranial neurophysiology is routinely applied in the clinic for surgical resection in epilepsy, brain tumors, chronic pain or even psychiatric conditions [11]. Thanks to the development of new brain interfaces, novel techniques are now available to control artificial limbs through brain–machine interfaces (BMI), which use the concept of brain-activity recording. They aim at recording the activity of a single or group of neurons using an electrode array, subsequently processing and digitizing the collected signals, sent as commands to external devices [12]. Clinically, effort is directed toward the development of motor BMIs for control of robotic upper limbs [13, 14]. In addition to restoration of motor functionality, cortical BMIs are also employed to enhance communication with patients with severe neurological disorders

(e.g., spinal cord injury, amyotrophic lateral sclerosis) using a typing interface [15] or, for development of speech neuroprosthesis [16]. Reconstructing speech from the human auditory cortex creates the possibility of a speech neuroprosthetic to establish a direct communication with the brain. It will potentially enable people affected with aphasia, a neurological disorder that results in the inability to comprehend or formulate language because of damage in specific brain regions, to restore speech [17].

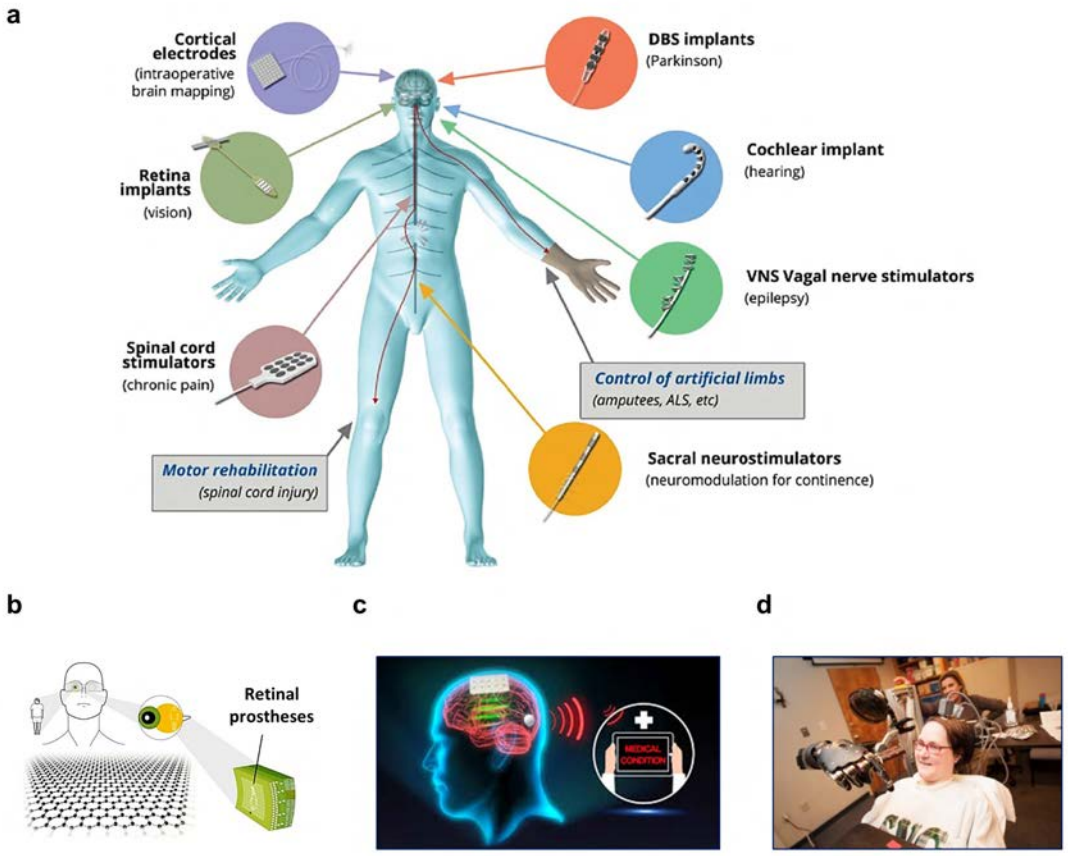

Figure 1.1: a. Clinically developed neural interfaces. Schematics of the actual devices are shown (not to scale) along with each disease indication (in parentheses) mainly used or developed for. Picture credit from [18]. **b**. Retinal prostheses using bioelectronic devices will potentially restore visual perception in blind patients affected by retinal diseases. Adapted from [19]. **c**. People suffering from chronic CNS disorders, such as epilepsy, will potentially be diagnosed and treated remotely using a chronic implanted cortical neural interface [ICN2]. **d**. A person with tetraplegia could use a brain–computer interface (BCI) to control a sophisticated anthropomorphic robotic arm with skill and speed approaching that of an able-bodied person, to do actions such as self feeding a chocolate bar [14].

Combining high precision recordings of brain activity with methods of brain stimulation, could give rise to a new spectrum of therapeutics strategies. The ideal pattern and amplitude of electric stimulation to the brain is highly dependent on the actual state of neural activity at the exact moment of stimulation [20, 21, 22]. Thus, accurate recordings of the brain activity prior to stimulation, combined with its real-time processing, would allow adjustment of the stimulation protocol to reduce side effects and improve the efficiency of brain stimulation. This procedure is known as 'closed-loop neuromodulation'[23].
All the medical technologies mentioned above have reached different stages of clinical development, but they are all based on the same concept: direct interaction with neural elements in different tissues, connected through wired means to a power source and digital processors. As can be seen from Figure 1.1, current neural interfaces applied in the clinic have rather elementary designs, mostly based on small arrays (few tens of electrodes) usually with large (mm size) metal electrodes. There is a net contrast to the potential offered by microelectronics, such as the very high integration density as well as on-site signal processing and transmission capabilities.

Every new discovery and technological development, should always be followed, ideally preceded, by ethical concerns in order to mitigate the technological transition of new human-interacting-technologies, that will inevitably affect our lives. The outcome of the use (or misuse) of emerging technologies for human life quality, can have a positive or negative impact depending on the ethical and moral choices. The famous physicist *Richard Feynman*, which during II world war was involved in helping build the first atomic bomb, said: "Scientific knowledge enables us to do all kinds of things and to make all kind of things. Of course if we make good things, it is not only to the credit of science; it is also the credit of moral choices, which led us to good work. Scientific knowledge is an enabling power to do either good or bad- but it does not carry instructions on how to use it" - *The Value of science* (1955)

1.1.1 Non-invasive and invasive recording methods

While there are different ways to record brain neural activity, the focus in this work is placed on electrophysiological extracellular recordings in vivo. Below, we briefly describe various methods being currently used.
Commonly used tools to monitor brain activity are imaging technologies that indirectly correlate anatomical and functional variations in the brain with neural activity, such as blood flow and cerebral perfusion in functional magnetic resonance

imaging (fMRI) [24] and in functional ultrasound imaging (fUS) [25]; as well as the detection of radio labelled tracers in the blood stream to trace cerebral glucose utilization, as in positron emission tomography (PET) [26] and single-photon emission tomography (SPET) [27].

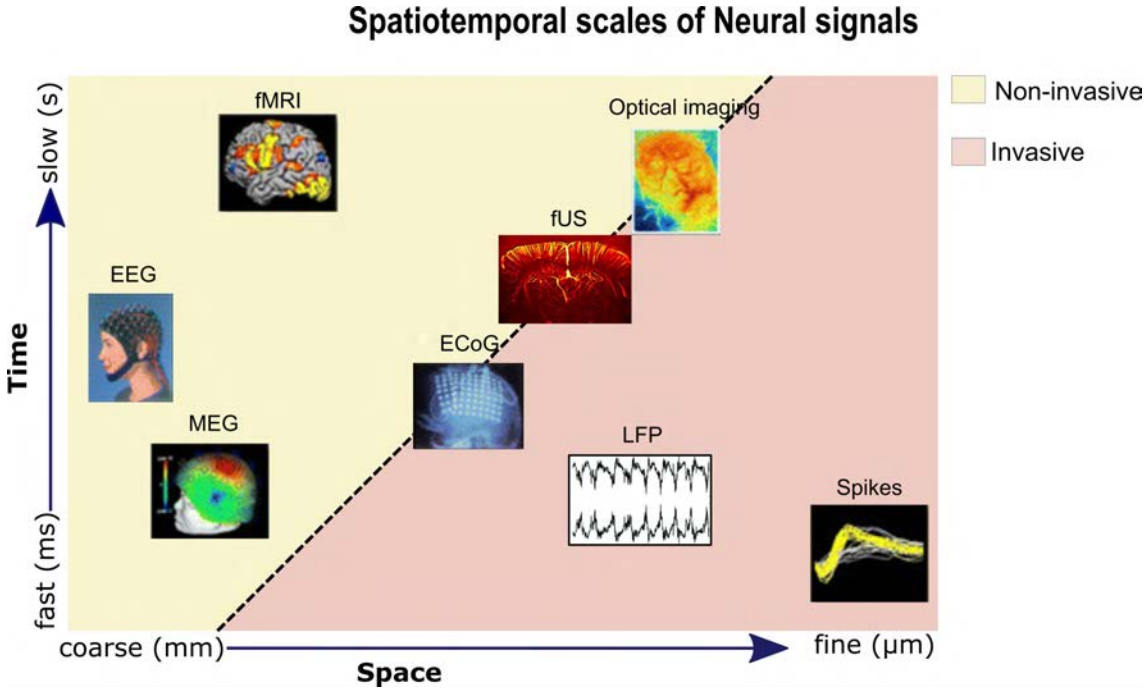

Figure 1.2: Spatiotemporal scales of neural signals that can potentially be used for brain–machine interfaces. Invasive neural signals can provide a fine spatial resolution, whereas non-invasive neural signals such as EEG and MEG have a coarse spatial resolution. Adapted from [28]

Electrophysiology is one of the most commonly used techniques by neurologists; it is applied in the clinic to investigate and identify large-scale brain dynamics by analyzing the spatiotemporal signals generated by populations of neurons, that take the form of field potentials [29, 30]. Field potentials can be recorded with good temporal precision (in the millisecond range) with non-invasive techniques such as skull electroencephalography (EEG) [31] and magnetoencephalography (MEG) [32] or with more invasive techniques, such as electrocorticography (ECoG) and intracranial stereotactic electroencephalography (SEEG), in which metal electrodes are in direct contact with the surgically exposed neural tissue [33]. These techniques vary primarily in their spatial resolution, their degree of invasiveness and their brain coverage [29] (Figure 1.2). The highest spatiotemporal resolution can be achieved through SEEG by using intracortical microelectrodes, which are inserted deep inside the brain, reaching targeted brain regions [33].

Examples of intracortical microelectrodes include a platform array which is placed on the cortical surface (like the Utah array), depth probes which goes multiple centimetres deep into the brain, assemblies of microwires and cone electrodes, which is a microwire placed in a glass micro-pipette that is open at the end (Figure 1.3) [34]. In general, the platform arrays and microwires have conductive tips, through which the electrical brain rhythms are recorded; depth probes on the other hand, have multiple recording sites along the length of the shank, enabling brain network and signal propagation studies between brain regions. Glass-filled (cone) microelectrodes, despite being extremely invasive and difficult to translate into clinics, provide the closest distance to the neurons, giving the highest signal resolution, with capabilities to record LFPs rhythms and spikes of cluster or single neurons (see section 1.2.1).

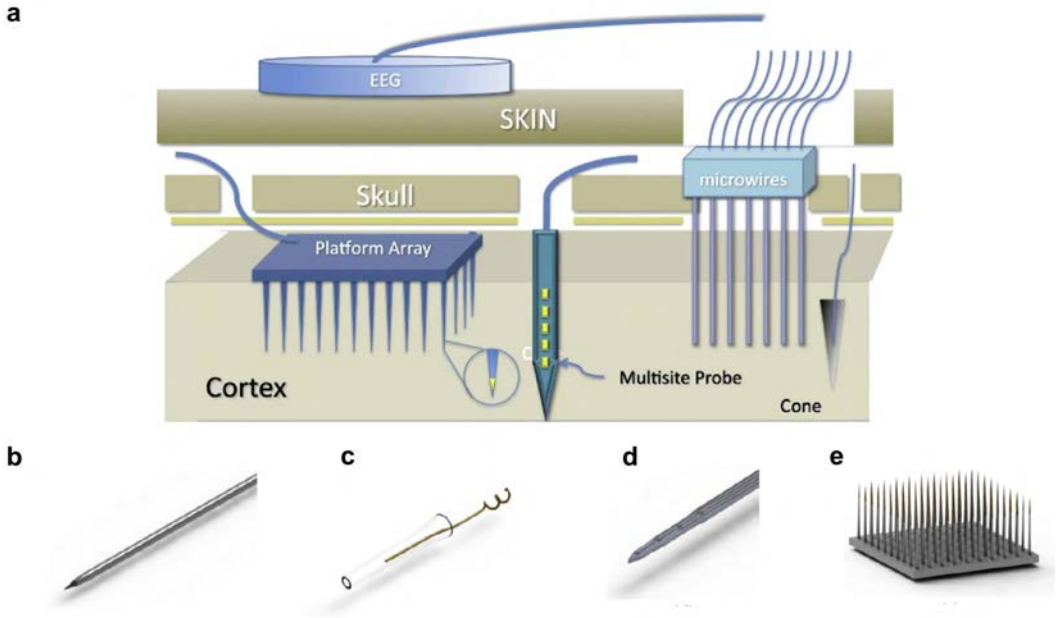

Figure 1.3: **a**, Illustration of the three main types of intraparenchymal (intracortical) sensors now in use. Platform arrays and microwires, in their present form, record from an exposed conductive tip (enlargement, yellow), while multisite probes record from many conductive stripes along their length. **b**, Microwire assemblies, consisting of fine wires; **c**, Cone electrodes are a form of microwire placed within a glass cone that is open at its end. Cellular elements can grow into the cone to establish contact with the wire. **d**, Multisite probe, with contacts along a flattened shank; **e**, Platform array, i.e. an array of electrodes emanating from a substrate that rests on the cortical surface. Adapted from [34]

Cone electrodes allow only single - or a few-points - measurement and therefore have serious mapping limitations in neuroelectrophysiology. They are typically implemented in ex-vivo experiments within a patch clamp set-up, in which the electrode is placed inside the cell membrane to measure the action potential of single

neurons [34]. Commonly used metal microelectrodes can measure frequencies down to 0.1 Hz (see Section 1.1.3), ideal for electrophysiological research, for the mapping of connectivity and for brain machine interfaces [34].

Shortcomings of invasive neural interfaces.
In the late 1980's, silicon-based microelectrodes were developed with the advances made in semiconductor microfabrication, in order to decrease the size of neural devices and increase their spatio temporal resolution [35, 36]. Well-known examples are the Michigan probes and the Utah array, which are both metallic-based electrodes produced on silicon substrates by means of lithography, to interface the brain at deep regions or at its surface, respectively (Figure 1.3). Around the same time, stereotrodes and tetrodes were developed, which are two or four polymer insulated micro-wires, electrochemically coated with gold. Bundles of multiple microwires allowed for a more precise study of individual neural communication in large groups of neurons [37].

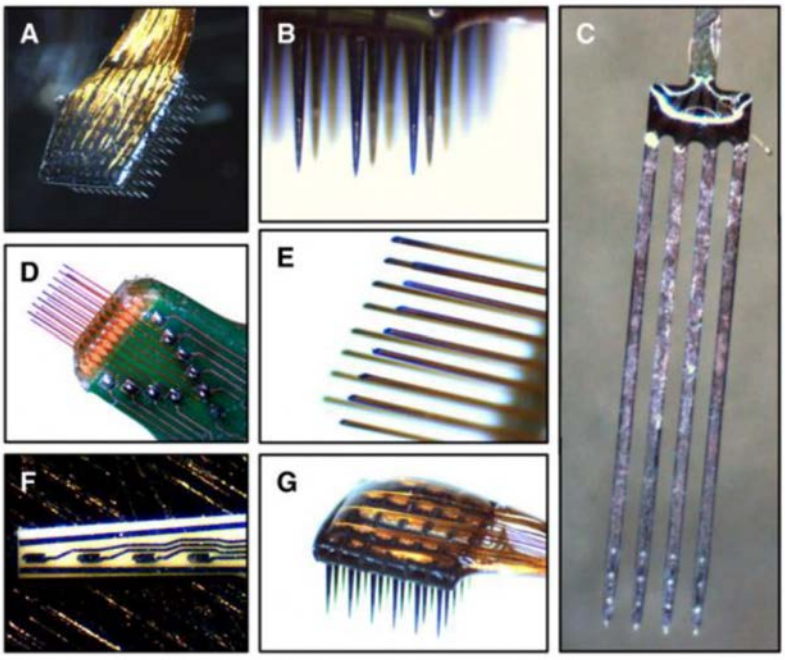

Figure 1.4: Examples of invasive neural probes. **A**, Cyberkinetics Silicon-based 100-channel MEA. **B**, View of recordings sites on the Cyberkinetics arrays (metallic portion on tip of each shank). **C**, View of NeuroNexus Silicon-based MEA shanks (4 recording per shank). **D**, Tucker-Davis Technologies Microwire MEA. **E**, View of recording sites on the TDT microwire array. **F**, Moxon Thin-Film Ceramic-based MEA. **G**, View of bond pads on a 36-channel Cyberkinetics array. Adapted from [38]

Currently, platinum-iridium microelectrodes are used for DBS treatment and platform arrays (Utah array), which are being evaluated in human clinical trials [34]. The DBS system and the Utah array have been FDA approved and received the CE mark in Europe [35]. Other devices have not reached that stage yet or have been refused due to device failure and short-term clinical viability, with potential health consequences. The main issue with these interfaces is the rigid nature of the devices, which excessively damage brain tissue and lose their function months after the surgery, due to the foreign body response. Examples of commercially available silicon-based probes are shown in Figure 1.4.

Generally, these rigid devices are prone to failure just a few weeks after implantation. There are many interplaying issues at the probe-brain interface [35, 36]. The origin of the failure can have either an engineering (i.e.device failure) or biological (i.e. gliosis) cause and include problems such as direct mechanical damage, degradation of device layers, corrosion of electrical contacts, and the foreign-body response, resulting in electrical isolation of the probes (see Figure 1.5).

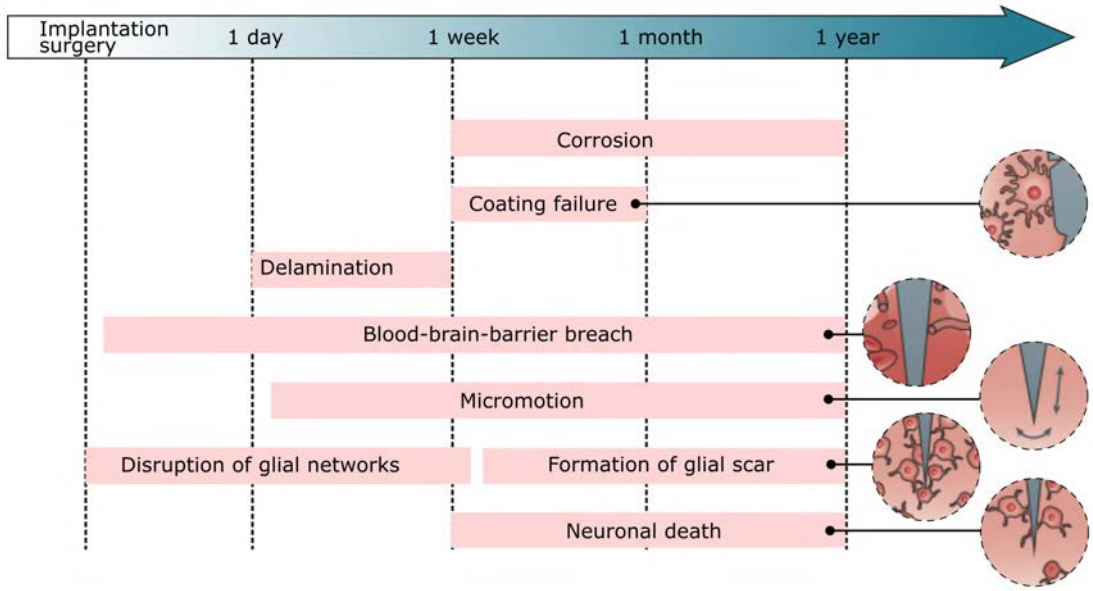

Figure 1.5: Typical causes of failure of rigid neural probes over implantation time in the brain. Adapted from [36]

Main challenge: Foreign body response

A major challenge is the demonstration of the capability to record long term signals in chronic implantations using microelectronics. A characteristic brain's response to any invasive intracortical microelectrodes is the rejection of the device via the

foreign-body response (FBR), with complete loss of electrode functionality as final outcome. To the best of our knowledge and irrespectively of the many differences in the type of device or microelectrodes, in the sterilization method, in the implantation method, there has not yet been the desired outcome of stable recording for more than months [34, 39]. Thus, intracortical microelectrodes are prone to fail on long-term basis, due to tissue reaction around the device [34, 39].

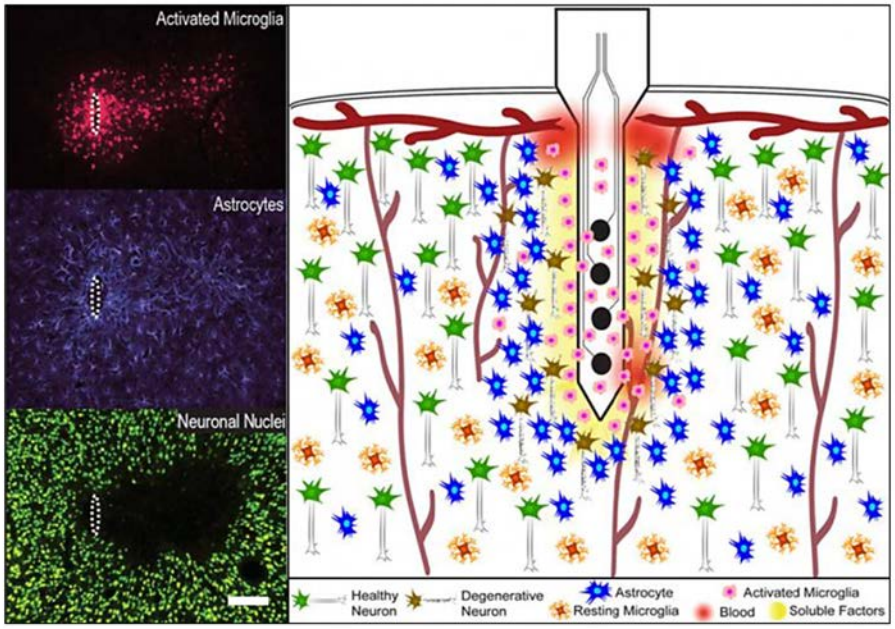

Figure 1.6: The effect of probe implantation inside the brain. (Left) Immunohistochemistry images of activated microglia, astrocytes and neural nuclei. (Right) Illustration of the probe/tissue interface. Briefly, activated microglia are primarily present at the electrode site, releasing pro-inflammatory factors. Astrocytes approach and eventually encapsulate the device (glial scar), while neurodegeneration persists at the interface. Adapted from [35]

When intracortical neural probes are inserted, vascular and cellular tissues inevitably experience damage, which is then followed by multiple immune mechanisms to protect the brain from a foreign body (see Figure 1.6). Some of them are briefly listed below:

1. A coagulation cascade is immediately initiated to restore the wound, during which tissue remodeling starts.

2. The complement system gets activated a part of the immune system that enhances the ability of antibodies and macrophages to remove the damaged cells and pathogens around the injury.

3. Reactive microglia and recruited macrophages release pro-inflammatory cytokines, proteins, like tumor necrosis factor-alpha (TNFα), and interleukines that stimulate further activation of the immune response.

4. The release of pro-inflammatory cytokines attracts new macrophages to the injury site and induces activation of the glial cells, that can lead to gliosis around the probe. Astrocytes, fibroblasts and meningeal cells accumulate around the injury site, forming a dense scar-tissue.

This inflammatory response can be attributed to the following factors [36]:

- The mechanical mismatch between the device and the neural tissue
- The tissue damage during device implantation
- Disruption of the glial networks
- Continuous rupture of the blood-brain barrier (BBB)
- Neurotoxicity of the materials used in the device

Chronic inflammation at the device/tissue interface can lead to the complete loss of the recording functionality[40, 35].

Although the neural activity, particularly LFP signals, can be still measured near the interface, the loss of neurons greatly limits recording performance. Ultimately, the thick scar tissue electrically isolates the entire device from the remaining healthy neural tissue, resulting in the complete loss of the recording function.

1.1.2 Novel materials for next-generation neural interface

Novel neural interfaces promise to enable significant progress in neuroscience and to pave the way for clinical applications in the diagnosis, treatment, and prevention of neurological disorders. The development of recent devices with multimodal functionalities has been driven by innovations in materials engineering, especially the utilization of organic soft materials such as polymers, carbon allotropes, and hydrogels. As discussed above, rigid probes can cause augmented scar formation and gliosis in the surrounding brain tissue. Thus, challenges remain in the development of biocompatible materials and the design of flexible implants for these purposes. The success of novel and minimally invasive clinical implants requires, therefore, the use of advanced materials and miniaturisation of flexible electronic technologies

[39]. Some key requirements and challenges to achieve this are summed up in the following:

1. To minimize foreign-body reaction, next generation neural interfaces should exhibit excellent biocompatibility and mechanical compliance with the neural tissue surrounding the device

2. Adequate and stable signal-to-noise ratio for neural recording. Recording capabilities should allow detection of signals of individual neurons (down to few tens of μV) and of assemblies of neurons (field potentials of few hundreds of μV to mV);

3. Cortical implants should cover large areas (up to few tens of cm^2), with high spatial resolution (hundreds of μm^2 of the active recording site).

4. Intra-cortical implants should be minituarized in size and made of soft material to reduce their invasiveness. Increasing number of recording sites will favour high spatio-temporal resolution in the depth of the brain.

5. For chronic implantation, the neural device should be stable and operational in liquid environments over long periods of time. Challenge of the connector footprint with increasing sensor density, which makes an employment of multiplexed readout circuitry mandatory [41]. Commercial solutions still fail to match these requirements, mostly due to the technological challenge of excessive wiring with increasing array size.

Long-term stability of the implanted devices can be significantly enhanced by improving the mechanical mismatch between the nervous tissues (Young's modulus ranging between 100 Pa and 10 kPa) and the implantable devices (100 GPa for rigid electronics, 5 GPa for thin polyimide based devices, and 1 MPa for silicone-based devices).
Popular choices for developing the next-generations of neural interfaces have been the organic materials, including conductive polymers [42, 43], carbon nanotubes [44], hydrogels including protein based materials and tissue engineered constructs, containing cells[35]. For instance, conductive polymers such as PEDOT (poly(3,4-ethylenedioxythiophene)) and PEDOT mixture with other ionomers (i.e PSS (polystyrene sulfonate)) [45] have been implemented as microelectrodes or as organic electrochemical transitors (OECT) for neural recording [46] and stimulation [47] . Such conductive organic materials offer additional advantages that make them attractive

candidates for neural interfacing, including cytocompatibility and straightforward integration with mechanically flexible substrates [48, 49].
Other very promising materials are those graphene-based. They constitute a versatile platform, that could help address many of the currently unsolved challenges in neural interface design, as mentioned above, due to their robustness, electrical and electrochemical performance and their suitability for integration into flexible devices. Different studies have assessed the biocompatibility of graphene with neural cells and its ability to functionally interface with neuronal tissue. Neurons cultures on 2D graphene substrates have been found to exhibit enhanced adhesion, good viability and improved outgrowth [50, 51, 52]. The issue of biodegradability of graphene and other 2D materials is also important, but much more challenging to determine in a generalized manner. Biodegradation of graphene nanomaterials using enzymes, such as horseradish peroxidase has been reported by few studies [53, 54, 55]. The design of implantable devices should consider material degradability in terms of electrical insulation, exfoliation or tear, especially in cases of long-term implants. Longitudinal assessment studies to address the biocompatibility, biodegradation and overall safety of the graphene-based neural devices is warranted and will be imperative. The conductive properties of graphene planar substrates have been used to electrically stimulate human neural stem cells and hence direct their differentiation toward a neuronal phenotype [56]. It has become apparent that the capacity of graphene to interface with neuronal tissue effectively and functionally, allows also the fabrication of devices for electrical recording. In the next section we present two types of electronic strategies used to record neural activity, namely electrodes and transistors, and present advantages and shortcomings.

1.1.3 Passive vs active sensors for neuroelectrophysiology

Brain activity is commonly classified into slow/infraslow oscillations (frequencies below 1 Hz), local feld potentials (LFPs) - which are considered to originate from spatio-temporal summation of transmembrane currents (frequencies between 1-300 Hz)- and extracellular action potentials of single neurons (frequencies between 300-3000 Hz) (see section 1.2.1). However, available sensing platforms based on electrode technology do not show equally high sensitivity towards neural signals across all the needed frequency bands.
Electrodes have a 1/Z(f) dependence on the impedance (Z(f)), which makes them a popular tool for the detection of high frequency activity such as spikes and LFPs. Therefore, to achieve electrodes able to detect the subtle neural signals, electrode

materials with a high double-layer capacitance (i.e., low interfacial impedance) are needed. Graphene exhibits electrochemical capabilities for neural recording similar to platinum or gold, which have been for long the standard electrode materials for neural recording[57, 58]. Although recent studies have demonstrated the successful recording of local field potentials from rat cortex using graphene [57, 59], the relatively low double layer capacitance of single layer or few layer graphene results in a high impedance, and thus in large thermal noise. This is particularly detrimental to achieve high signal-to-noise ratio with a small microelectrode. Similarly to the case of neural stimulation, the performance of graphene-based materials for recording applications can greatly be improved by using reduced graphene-oxide, or 3D graphene-based-films that increase the specific surface area of the electrode [60, 61]. On the other hand, when the dimensions of a recording electrode reduce to a few tens of microns, its impedance can become so high that the electrode's will suffer from voltage drifts and signal distortion at very low frequencies, as explained below. In electrodes the gain of the recorded signal depends on the ratio between the input impedance of the recording equipment's pre-amplifier, $Z_a(f)$ and the electrode's impedance $Z_e(f)$ (Eq. 1.2) [62]. Signals at the electrode interface (V_{sig}) generate currents (I) that flow to ground through the series combination of the effective electrodes impedance and the effective amplifier input impedance:

$$I(f) = \frac{V_{sig}}{Z_a(f) + Z_e(f)} \tag{1.1}$$

The voltage at the input of the amplifier (V_{in}) is therefore given by:

$$V_{in} = V_{sig} - I(f)Z_a(f) = \frac{V_{sig}Z_a(f)}{Z_a(f) + Z_e(f)} \tag{1.2}$$

Simplifying the electrode/tissue interface as an ideal capacitor, its impedance is a function of the frequency f and the capacitance C_{dl}, the latter one scaling with the electrode's active area:

$$Z_e = \frac{1}{2\pi f C_{dl}} \tag{1.3}$$

Eq. 1.2 shows that Z_a and Z_e form a voltage divider, so that when Z_a is not substantially larger than Z_e, V_{in} will be less than V_{sig}. This signal attenuation will be accompanied by a phase shift between V_{sig} and V_{in} because Z_a and Z_e are complex numbers containing phase and magnitude terms. The $Z_a >> Z_e$, requirement to achieve a voltage gain equal to 1 can be compromised for electrodes with small diameter, especially at very low frequencies, due to the inverse relation between

the electrode impedance and its area (Eq.1.3); this can ultimately lead to high-pass filtering of the recorded signals. Hence, recording slow oscillations with electrodes is challenging due to signal attenuation, and only possible for electrodes with large active area. In addition to gain attenuation, electrodes are also sensitive to baseline drifts, causing artefacts and requiring high-pass filtering to avoid amplifier saturation. Thus, both gain attenuation and baseline drift potentially compromise the recording quality of slow neural activity patterns [62] (see results in section 5.1).

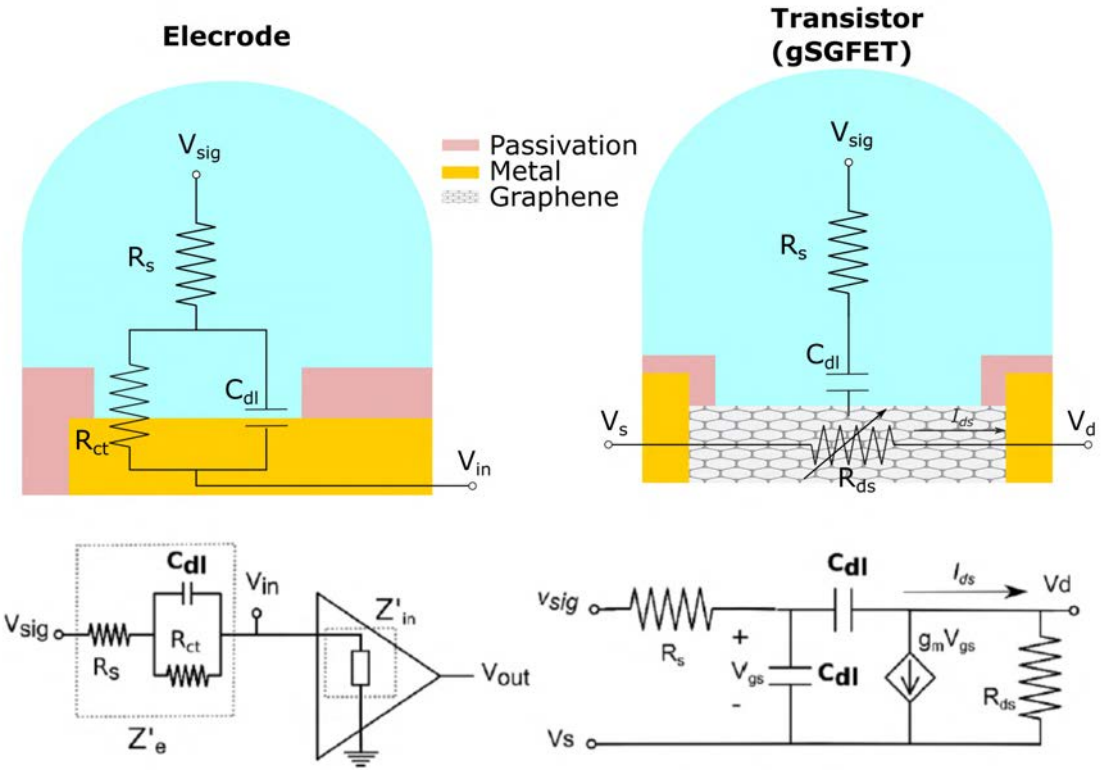

Figure 1.7: Equivalent circuits of signal coupling for electrodes and transistors (gSGFET). For the case using electrodes, its impedance ($Z_e^{'}$) and the amplifier input impedance ($Z_{in}^{'}$) form a voltage divider, which leads to signal attenuation at low frequencies. For an electrode (left), the electrode/electrolyte interface is modelled as a capacitor and a resistor connected in parallel (R_{ct}, C_{dl}). V_{in}, the voltage at the input of the amplifier, is determined by the voltage divider formed by $Z_e^{'}$ and $Z_{in}^{'}$. R_s represents the electrolyte resistance. In the case of a gSGFETs (right), V_{sig} modulates the graphene channel resistance (R_{ds}) by the field effect through the gate capacitance (C_{dl}), which results in current variations ($\delta I_d s$) proportional to the transconductance value at the bias point ($g_m \cdot V_{gs}$), plus the voltage signal V_{sig}, as illustrated in the small-signal model. Adapted from [63]

Hence, sensing platforms using active electronic devices as sensors, such as field-effect transistors (FETs), offer clear advantages as they act as intrinsic amplifiers when translating neural activity into current signals. Recording signals in current

offers more robustness to environmental and pick-up noises. In addition, since the device's bias point is fixed by a reference electrode, it is much less susceptible to artefacts from reference drifts. Further, transistors provide low impedance and can be easily multiplexed, a task that will become necessary when building high density sensing arrays in order to reduce the number of wires to interface the recording electronics [64].

Despite all these advantages of FETs in electrophysiology, the complexity in combining silicon FETs with flexible materials has historically hampered their use for *in vivo* recordings [65]. Moreover, the signal amplification (gain) in FETs is characterised by the transconductance g_m, defined as the variation of the current induced by the variation of the gate bias ($g_m = \frac{\partial I_{DS}}{\partial V_{GS}}$). The value of g_m is therefore considered the sensitivity of a FET sensor. The transconductance depends on the electrical properties of the active material of the FET, and is proportional to the charge carrier mobility (μ) and to the value of the gate capacitance ($g_m \propto \mu \cdot C_d l$, see section 2.3 for more details). Graphene solution-gated field-effect transistors (gSGFETs) have been proposed to potentially overcome most of the previously reported drawbacks [19, 66]. Graphene's mechanical flexibility allows gSGFETs to be embedded in ultra-soft and flexible substrates without loss of performance [67], while its wide electrochemical window and biocompatibility allow direct contact with biological tissues and ensures a safe operation in *in vivo* conditions [18].

Furthermore, graphene-SGFETs exhibit superior transconductance ($\sim$ 2-5 mS/V) compared other SGFETs based on competing material systems, such as Si ($\sim$ 0.2 mS/V), diamond ($\sim$ 0.3 mS/V), or AlGaN/GaN ($\sim$ 0.5 mS/V) [68]; the high values of g_m arise from the combined contribution of the high carrier mobilities in graphene and the large capacitance of the graphene/electrolyte interface [68]. In addition, the two-dimensional nature of graphene provides the highest surface-to-volume ratio possible, making graphene very sensitive to charges at its surface.
One of the reason why graphene microtransistors can record infraslow signals in the brain, is related to the working principle of transistors, which is significantly different from that of electrodes. In gSGFETs, voltage oscillations near the active graphene channel modulate the current flow along it (see Figure 1.7).
The relation between the recorded current (I_{dsrec}) and the signal (V_{sig}) is:

$$I_{dsrec}(V_{gs}, V_{sig}) = I_{ds}(V_{gs}) + \delta I_{ds}(V_{gs}, V_{sig}) = I_{ds}(V_{gs}) + g_m(V_{gs} + V_{sig})V_{sig} \quad (1.4)$$

where I_{ds} is the current at the bias point Vgs, δI_{ds} the current variation induced by the gate signal, and g_m the transconductance. This equation is simplified with the assumption that g_m is frequency independent. In the case of a graphene-electrolyte interface, the gSGFET shows a frequency-independent gain over a wide bandwidth (0.01 Hz - 4 kHz) for signal transduction [69], enabling high-fidelity full bandwidth neural recordings [63, 70]. Figure 1.8 shows a conceptual schematics of the spatiotemporal brain regions covered by the gSGFET-based neural probes and other electrophysiological tools together with the degree of invasiveness (represented by the colour gradient).

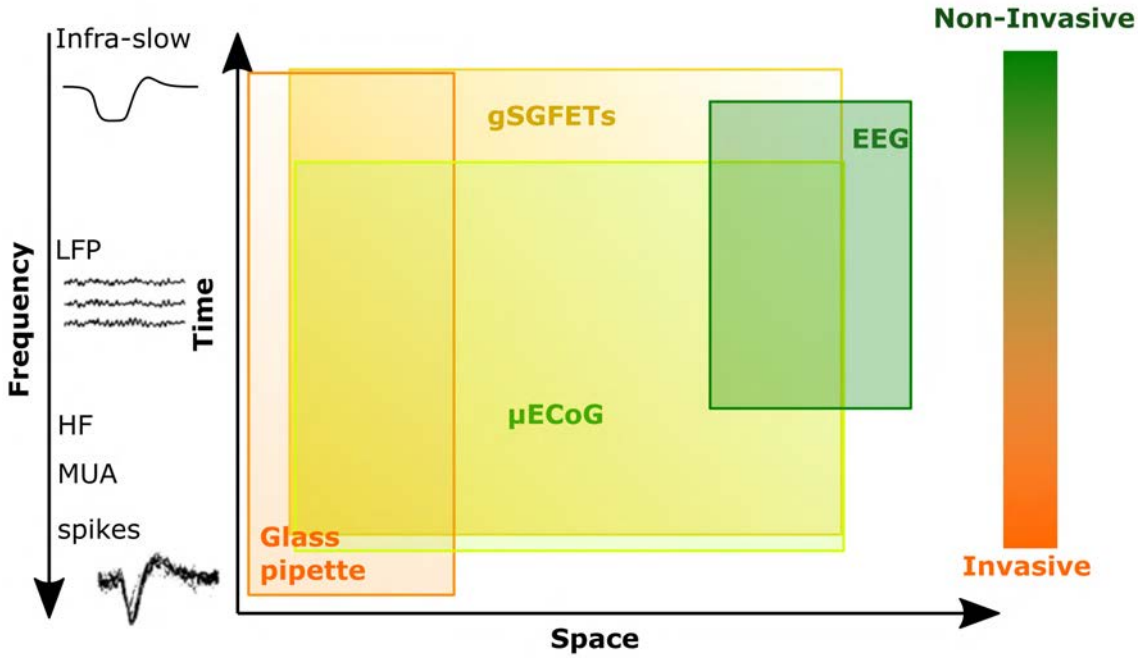

Figure 1.8: Conceptual representation of the spatiotemporal regions covered by the different electrophysiological methods. gSGFETs allow μECoG capabilities (able to record LFP: local field potential, HF: high frequency, MUA: multiunit activity) with additional infra-slow activity detection. Adapted from [71]

Taking advantage of the above-mentioned properties, in this thesis we demonstrate that gSGFETs flexible neural probes are able to record the full bandwidth of the electrophysiological activity in *in vivo* animal experiments (see section 5.1).

1.2 The central nervous system

The central nervous system (CNS) is considered the most complex organ in the human body and is the part of the nervous system containing the brain and the spinal cord. The CNS continuously sends and receives signals to and from the rest of the body to control movement, regulate organs and coordinate cognitive functions. The information is transmitted through a large network of neurons, the electrically active cells of the nervous system. The CNS is connected to the organs, limbs, and skin via the peripheral nervous system (PNS). The PNS consists of the nerves and ganglia outside the brain and spinal cord. Structural changes in the CNS or PNS can lead to malfunction of the human body, greatly affect quality of life and result in neurological disorders.

The brain is physically protected by multiple membrane layers, called the meninges, which include the pia mater, arachnoid mater and the dura mater (Figure 1.9a) [72]. Moreover, the cerebrospinal fluid (CSF), which is located between the arachnoid and pia mater, the skull (bone), the periosteum (connective tissue) and skin protects the brain form shocks and traumas. Furthermore, blood capillaries in the brain have a selective semipermeable membrane, called the blood-brain barrier (BBB) (Figure 1.9b). The BBB is composed by a highly selective barrier that forms tight junctions between the endothelial cells in the vessels and astrocytes cell projections surrounding the endothelial cells. The BBB enables water, glucose and hormones to pass the barrier through passive/active transport, but blocks neurotoxins or bacteria in the blood stream from diffusing in the brain.

The human brain is a soft gel-like tissue, with a bulk elastic moduli between 0.1 to 10 kPa. It has a volume of approximately 1.3 liters and is mostly made up of neurons, glial cells and extracellular matrix (ECM). The ECM is a dense mesh of fibrous proteins, proteoglycans and glycosaminoglysancs, located in between the cells in the interstitial space [72].

Interestingly, the CNS does not contain much collagen, which is normally the most abundant structural protein of the ECM elsewhere in the body. Despite the lack of the mechanically strong collagen, the ECM provides sufficient strength to keep the cells connected and prevent neural deformation or disruption.

Neurons and glial cells.

The brain consists of billions of neurons, a special type of cells able to share information, transmitting electrical and chemical signals between different areas of

the brain and the rest of the body. Although there are various types of neuron with different physical appearances, each neuron contains a cell body (soma) with up to nearly a thousand dendrites and a projection called the axon (Figure 1.9). Basically, the dendrites receive incoming signals and the axon further transmits the signals to neighboring neurons. While the axon is only a few micrometers thick, it can vary in length up to 1 meter [72]. Neurons can be classified according to their function (Figure 1.9b). Signals from the surrounding tissue or organs are received by sensory neurons, which transmit the signals to interneurons. Interneurons then transport and fine-tune the signals throughout the nervous system to eventually reach motor neurons. The motor neurons are connected to muscle fibers and transform the initially received information into a particular action.

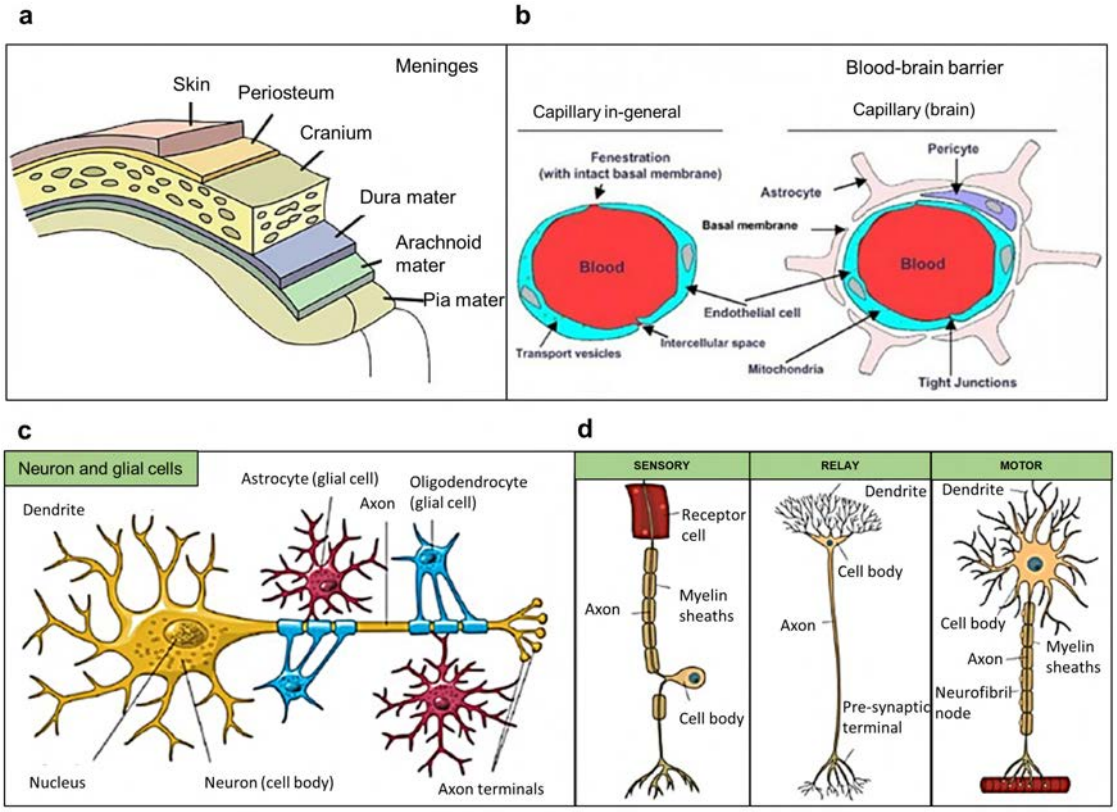

Figure 1.9: a. Illustration of the different meninges. **b**. Comparison of a normal capillary and a blood-brain barrier (BBB) capillary. The addition of tight junctions in between the endothelial cells and astrocyte processions around them, prevent the penetration of neurotoxins or other dangerous species into the brain . **c**. Illustration of a neuron (yellow) supported by astrocytes (red) and oligodendrocytes. **d**. Illustration of the different neuron types. Sensory and motor neurons contain myelin sheaths, while the interneurons (relay neurons) do not [1].

Neurons need the support of glial cells to function correctly. There are three general types of glial cells, called astrocytes, oligodendrocytes and microglia (Figure 1.9c). Astrocytes perform many vital functions, like for example provision of nutrients to the neurons, maintenance of extracellular ion balance, support of endothelial cells that from the blood-brain barrier. Oligodendrocytes produce insulating myelin sheaths which wrap around the axon of the neuron to speed signal transmission. Microglia are the immune cells of the CNS and mediate the foreign body reaction by protecting the brain from any foreign material.

Electrophysiology.
Neurons use electrical and chemical processes to communicate with one another. The signal conduction through the nervous system requires constant transformation of electrical signals into chemical signals and vice versa. The special structure of the neuron allows for efficient transmission of the electrical signal. Dendrites integrate the activity of other neurons and transmit the signal as electrical impulses to the cell body and axon of the neuron. The axon subsequently transmits the impulses away from the cell body towards synaptic terminals. This signal transmission along the axon proceeds at various speeds, depending on the diameter of the axon and whether they are insulated with myelin sheaths or not. The myelin insulating sheath have periodic gaps on the axon of certain neurons (called node of Ranvier) that serves to facilitate the rapid conduction of nerve impulses, as the sheaths themselves are electrical insulators.
The *resting membrane potential* is the difference between the electric potential in the intracellular and extracellular matrices of the cell, when it is not excited (resting state).

Most of the time, neurons have a negative concentration gradient, i.e. more positively charged ions outside than inside the cell membrane. The resting membrane potential is maintained by this negative concentration gradient kept by various membrane proteins (ion pumps), fueled by ATP (active transport). A membrane potential of -70 mV exists, with a negatively charged cell interior compared to the extracellular space.
During signal transmission, an excitation process of the neuron resting membrane

[1]Taken from (**a**) https://teachmeanatomy.info/neuroanatomy/structures/meninges/;(**b**) https://hopes.stanford.edu/cerebrovascular-and-blood-brain-barrier-impairments-in-huntingtons-disease-potential-implications-for-its-pathophysiology/;(**c**) https://www.ninds.nih.gov/Disorders/Patient-Caregiver-Education/Life-and-Death-Neuron; (**d**) https://www.tutor2u.net/psychology/reference/biopsychology-sensory-relay-and-motor-neurons

takes place, in which a dynamic movement (within a millisecond) of electrically charged ions through specific membrane channels produce the **action potential** (AP) [73] (Figure 1.10a). AP is triggered when the membrane potential reaches a threshold of ≈ -55mV; voltage-gated sodium channels of the membrane briefly open and quickly re-close allowing influx of Na+ ions into the cell which depolarizes the membrane potential up to +30mV (depolarisation pahase). During this phase, voltage-gated potassium channels open, causing intracellular potassium to leave the cell and finally repolarizing the membrane potential (repolarisation phase, Figure 1.10a). Thus, the combination of opening and inactivating voltage-gated channels cause a depolarization wave enabling the propagation of the AP.

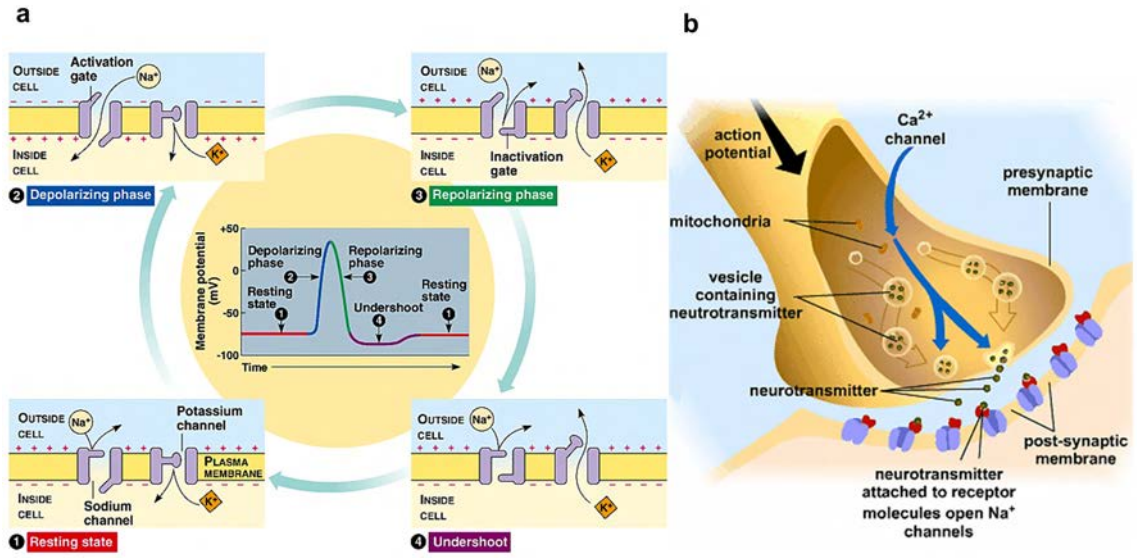

Figure 1.10: a. Illustration of the different stages at the cell membrane during an action potential. **b**. Illustration of the synaptic chemical transmission occurring during an action potential.[2]

When the AP reaches the nerve terminus (presynaptic terminal), the signal is transformed into chemical signals through chemical **synapses** (Figure 1.10b). Calcium ions flow into the pre-synaptic synapse, which causes the release of **neurotransmitters** across the synaptic cleft. The neurotransmitters in the cleft subsequently bind to the receptors of the adjacent neuron (postsynaptic neuron). Then, the receptors open channels enabling the flux of ions inducing a current and triggering a new AP. In the postsynaptic neuron the remaining neurotransmitters at the postsynaptic site are either quickly pumped back into the presynaptic nerve

[2]Figures taken from (a) https://nursing.aliciavance.com/allthingsbody/tag/action/; (b) https://in.pinterest.com/pin/591449363551390485/

terminal, consumed by enzymes near the receptors, or left to diffuse into the surrounding area. Besides this relatively slow chemical transmission, the electrical signals can also be directly transmitted through *electrical synapses*. Such synapses contain pores, known as connexons, through which the ionic charge can flow from the presynaptic neuron to the postsynaptic neuron. Eventually, once the signals reach motor neurons, the electrical signal will be transferred to muscular cells to induce a tangible muscular response. Frequency and amplitude of the electrical impulses to muscular cell, determines the speed of contractions or the pressure feeling on the skin, for instance [74].

1.2.1 Frequencies in the brain

Neuronal activity in the brain gives rise to transmembrane currents that can be measured in the extracellular medium. Although the major contributor of the extracellular signal is the synaptic transmembrane current, other sources, including Na^+ and Ca^{2+} spikes, ionic fluxes through voltage and ligand-gated channels, as well as intrinsic membrane oscillations can substantially shape the extracellular field, called **local field potential** (LFP) [75, 76]. Therefore the characteristics of LFPs, such as amplitude and frequency, depend on the proportional contribution of the multiple sources and various properties of the brain tissue. LFP signals can be further classified into two groups:

1. Rhythmic signals: This neural activity, originates from the synchronized activity of large number of neurons and results in oscillations at frequencies, very different from the firing frequency of individual neurons. There are different types:
   - Slow signals (<1 Hz)
   - Medium signals (δ [0.5-4 Hz], Θ [4-8 Hz], α [8-12 Hz],β [12-30 Hz])
   - Fast signals (γ and **high-**γ, 30-150 Hz)
2. Event-related potentials (ERPs): These are large potential shifts induced for example by an external event in a large neuronal group.

Moreover, the average spiking of small neuronal populations close to the vicinity of the placed microelectrode are called **multiunit activity** (MUA). In order to observe MUA, the LFP signal measured by the microelectrodes need to be band-pass filtered in a frequency range of 400 to a few thousand Hz [77, 78]. Proper

recording of neural activity demands therefore the employment of micro-sensors able to provide high sensitivity over a broad range of frequencies. Besides these defined electrophysiological signals, slow and infra-slow (<0.1 Hz) waves and their interplay with higher frequencies in the brain have recently gain attention due to the development of new tools that facilitate their detection.

1.2.2 Infra-slow activity

More recently, there has been an increasing interest in exploring the very low frequency components (< 0.1 Hz) of the electrophysiological signals, the so-called **infraslow activity** (ISA) [79]. Although the presence of such ISA has been measured in animals for over 50 years [80], consistent fMRI finding of prominent fluctuations at <0.1 Hz during the resting state in human brain revived the interest in ISA [81, 82, 83].

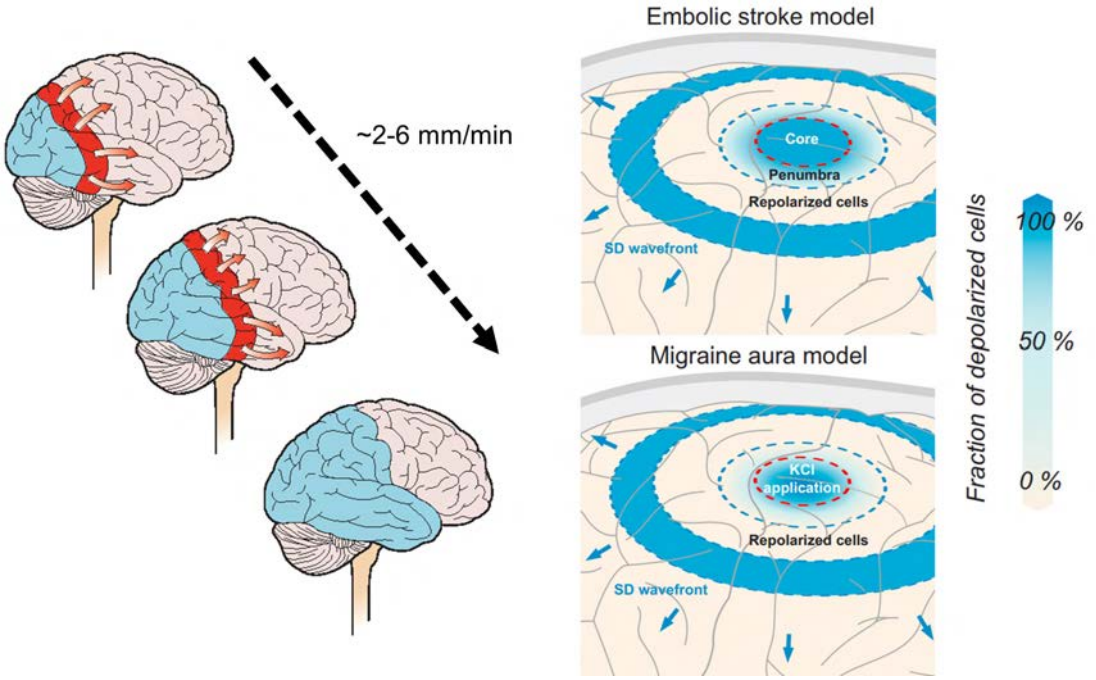

Figure 1.11: Schematics of slowly (∼2-6mm/min) propagating spreading depolarisation waves in the human brain. Examples of SD propagation in embolic stroke model and by application of high potassium (KCl) (Migrane aurea model). In the embolic stroke model, the first SD starts in the ischemic center ∼2–5 min after local circulatory arrest. In the pre-clinical migraine aura model, the first SD starts at the application site of KCl. In both models, the center region remains persistently depolarized thereafter. From the center, the SD runs into the normal, surrounding tissue. Adapted from [84]

As a result, ISA has also been identified in full band electroencephalography recordings in clinical studies (fbEEG, unsing cm-sized metal electrodes) [85, 86].

Notably, this ISA have been shown to be coupled to faster frequencies oscillations, measured with EEG [86]. Consistent with their role in modulating large-scale neuronal network excitability, ISA has been shown to regulate behavioral performance [85], organize electrophysiological sleep-related events, and influence the precipitation of certain types of epileptic seizures [86].

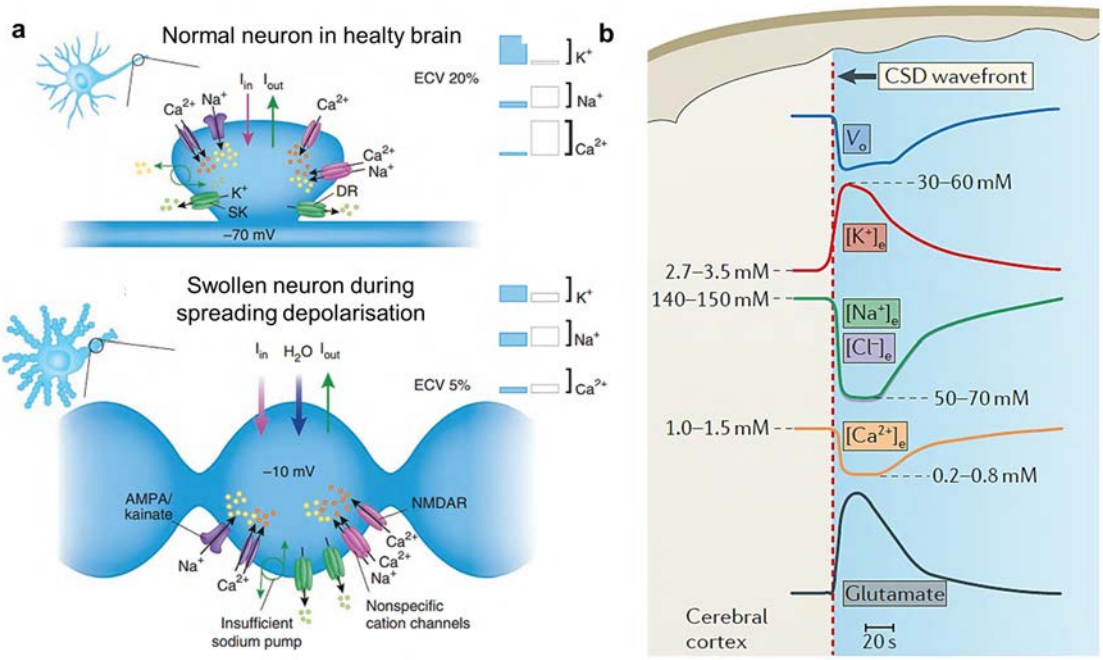

Figure 1.12: a. Mechanisms of spreading depolarization in the neuron. *Top*: in healty brain tissue, ion pumps on the neuron membrane move cations (such as Ca^{2+} and Na^{+}) from the extracellular space into the cell (dendritic inward current I_{in}, pink arrow) and vice versa (dendritic outward current I_{out}, green arrow). This small dendritic currents keep the iso-osmolality across the membrane and steep physiological ion gradients. *Bottom*: the core mechanism of spreading depolarization is the failure of sodium and calcium pumps to provide sufficient dendritic I_{out} to balance the persistent I_{in}. If persistent influx of Na^{+} and Ca^{2+} is more than the outflux of K^{+}, the neuron experiences a near-complete loss of electrochemical energy, almost passive ion distribution across the membrane, intracellular hyperosmolality with cellular swelling and distortion of the dendritic spines, and extracellular hypo-osmolality with extracellular volume (ECV) shrinkage (blue arrow: water follows sodium and calcium influx). The hallmark of this process is near-complete sustained depolarization from -70 to -10 mV. Blue and withe boxes in the legend represent the concentration of K^{+}, Na^{+} and Ca^{2+} inside and outside the neuron membrane respectively. Adapted from [87].
b. Shows changes in the extracellular concentrations of K^{+} ($[K^{+}]_e$), of Na^{+} ($[Na^{+}]_e$), of Cl^{-} ($[Cl^{-}]_e$), of Ca^{2+} ($[Ca^{2+}]_e$) and of glutamate during CSD depolarization. The schematic shows the rapid change of extracellular potential (V_o) at the CSD wavefront and the associated change in ion concentration (left baseline values, right increase/decrease of concentration for the different ions [mM]). Adapted from [88].

A particular example of ISA is **cortical spreading depolarization** (CSD) waves, a slowly propagating wave of near-complete depolarization of neurons and astrocytes followed by a period of electrical activity suppression. CSD has often been observed in individuals suffering stroke, migraine, brain injury, as well as epilepsy [87, 89, 90]. The term spreading depolarization describes a wave in the gray matter of the central nervous system characterized by swelling of neurons, distortion of dendritic spines, a large change of the slow electrical potential and silencing of brain electrical activity [87]. It is known that brain tissue with different degrees of metabolic impairment and/or inhibition of neuronal and glial (Na^+ + K^+) ATPases, is at risk for SD occurrence [87]. Typical phenomena during an SD event are: ion gradients breakdown[91], near-complete sustained depolarization in individual recordings of neurons [92], extreme shunt of neuronal membrane resistance [92], loss of electrical activity [93] and neuronal swelling and distortion of dendritic spines [94] (see Figure 1.12).

Once in this condition, the neurons cannot fire action potentials, as the sustained depolarization is above the threshold at which the membrane channels generate action potentials [95]. As a consequence, spreading depolarization causes brain electrical silence, which was termed spreading depression of brain electrical activity by Aristides Leão in 1944 [93]. In pre-clinical *in vivo* experiments, induction of CSD in normally metabolizing brain tissue can be obtained by increasing the extracellular concentration of K^+ ($[K^+]_e$) above a critical threshold [96] (Figure 1.12b). Depending on the degree of local metabolic impairment of (Na^+ + K^+) ATPase activity, the restoration of the ionic gradients, repolarization of the membrane potential, recovery of synaptic transmission and brain function either occur after a prolonged time compared with CSD (migrane with aurea model) or does not occur at all [97, 87]. CSD causes no cell death nor long-lasting damage in a normally metabolizing brain[98] but it imposes a considerable bioenergetic burden on tissue.

CSD is often triggered in individuals who suffered stroke or brain injury as well as migraines; recent research has shown that CSD plays a significant role in the pathophysiology of epilepsy [87, 84, 90]. Interestingly, in the case of epilepsy both fast activity, at hundreds of Hz or higher, and infraslow activity (ISA), at less than 0.5 Hz can be associated with seizures and epileptiform activity [79, 99]. Moreover, seizure generation has been hypothesised to be induced by a coupled dynamical system, in which there are fast and slow processes [100]. However, the relationship between these two types of brain activity is poorly understood; the effect of SD on the epileptic activity across the cortical laminae and deeper regions of the brain remains largely

unknown [99]. The ability to record simultaneously infraslow activity (<0.1 Hz) and higher frequencies (0.1-600 Hz) using the same recording device, as in the case of gSGFETs, would particularly benefit epilepsy research and the development of novel therapy strategies.

1.3 Epilepsy

> "*I do not believe that the sacred disease is any more divine or sacred than any other disease but, on the contrary, just as other diseases have a nature from which they arise, so this one has a nature and a definite cause. Nevertheless, because it is completely different from other diseases, it has been regarded as a divine visitation by those who, being only human, view it with ignorance and astonishment*"
>
> Hippocrates, 480–323 B.C.E.

The word "epilepsy" comes from the Greek verb *epilambanein*, meaning to "seize" or "take hold of". People in ancient times and in different cultures believed that seizures were induced by gods or by the possession of demons/spirits; therefore, it was considered as a "sacred disease"[101]. One of the first descriptions of epileptic seizures can be traced back to 2,000 B.C. in ancient Akkadian texts, a language widely used in the region of Mesopotamia [102]. Nowadays, epilepsy is one of the most common chronic neurological disorder that affects about 50 million people worldwide, making it the second most common neurological disease after a stroke[103].
Epilepsy manifests as an unusual dynamism of neural networks, which produces synchronised anomalous discharging of neurons leading to recurrent seizures. Seizures are sudden bursts of electrical activity in the brain that temporarily affect its functionality. Depending on which part of the brain is affected, seizures sometimes cause convulsions, muscle spasm or lip smacking, while in others it may cause problems like loss of awareness, blank staring or unusual sensations, emotions and behaviour. They typically pass in a few seconds or minutes. There are thee main types of seizures classified by the International League Against Epilepsy (ILAE): partial, generalized and unclassified (see Fig. 1.13)[104]. **Partial** seizures are usually confined to discrete areas of the cerebral cortex and cause motor, sensory, autonomic, or psychic symptoms, without an obvious alteration in consciousness. These seizures may also be manifested as changes in somatic sensation (e.g., paresthesias or tingling), vision, equilibrium, autonomic function olfactory changes, and hearing. Simple partial seizures can evolve to **complex partial** seizures, by spreading and involving both

cerebral hemispheres, producing a secondary generalisation of seizure, usually of *tonic-clonic* variety. Tonic-clonic seizures involve both tonic (stiffening) and clonic (twitching or jerking) phases of muscle activity with loss of consciousness. On the other hand **generalised** seizures (involving the whole brain) can manifest as *absence seizures* (petit mal), *tonic-clonic seizures* (grand mal), *atonic seizures* and *Myoclonus*. A simple absence seizure is defined as a brief clouding of the sensorium, or loss of consciousness (typically only seconds), without loss of postural control and without postictal confusion. Generalized, tonic–clonic seizures are the main seizure type in approximately 20% of all persons with epilepsy and have been associated with metabolic imbalances [104]. Atonic seizures are characterized by sudden loss of postural muscle tone lasting few seconds. Consciousness is briefly impaired, but there is usually no postictal confusion [104]. Myoclonus is a sudden and brief muscle contraction that may involve one part of the body or the entire body [104]. Not all seizure types can be classified as partial or generalized (**unclassified** seizures); this appears to be true of seizures that occur in neonates and infants [104].

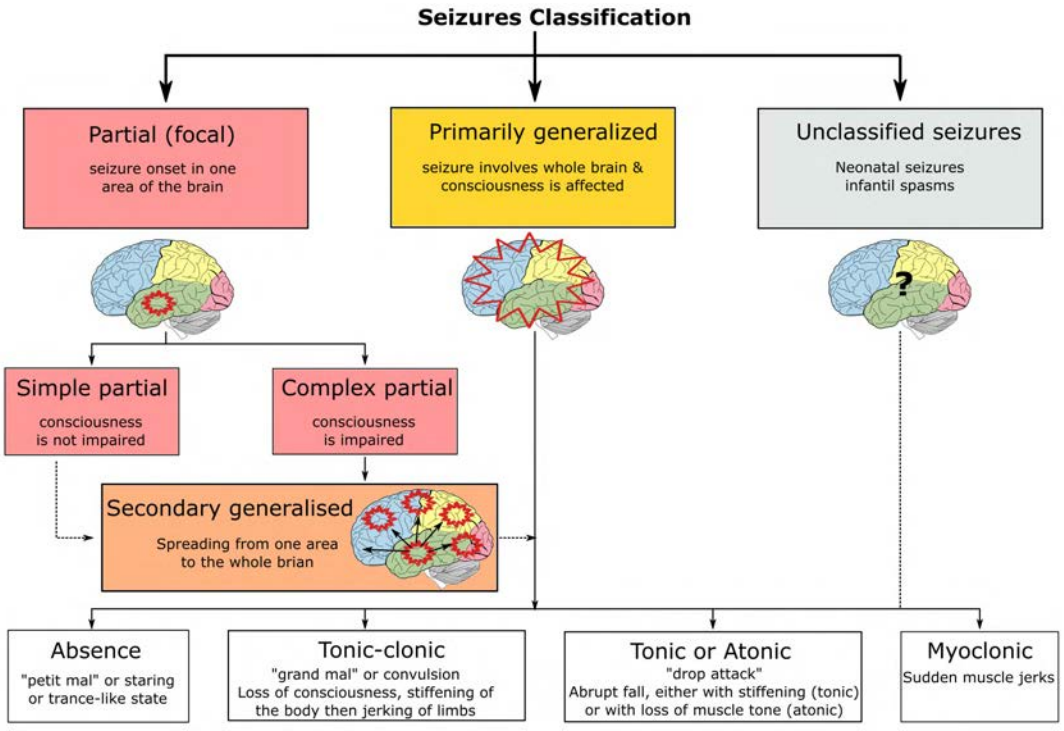

Figure 1.13: Classification of seizure types according to the International Language against Epilepsy (ILAE). Adapted from [105]

Over times, epilepsy generates serious consequences such as automatism, impaired cognition, behavior arrest, unawareness and if not timely diagnosed will lead to insults of the CNS and impaired mental conditions [106].

There are various root-causes of epilepsy, some induced by genetic factors, but it can also result form traumatic brain injuries, stroke, infections in the CNS, high fever or tumors. It has been observed that genetics play an important role in many cases of epilepsy, particularly in very young children, but it can be a factor for people of any age [107].
The two hallmarks of seizure generation are **hyperexcitability** of neurons and **hypersynchrony** of neural circuits. A large variety of mechanisms alters the balance between excitation and inhibition to predispose a local or widespread region of the brain to hyperexcitability and hypersynchrony [108, 109, 110].
Nevertheless, the detailed pathophysiological understanding is incomplete[107]. Clinical and animal studies have indicated the break down of the blood-brain barrier (BBB) as one of the prominent reasons in most cases of epileptic seizures, either caused by some accident or neuronal dysfunctions [111]. In addition, basal membrane thickening, fewer mitochondria in endothelial cells and the presence of abnormal tight junctions have been considered to be other related causes observed in humans studies [112]. Lesions, injuries or surgeries which accidentally damage the BBB support the hypothesis of triggering events causing epilepsy and numerous cognitive impairments [113, 114].
Conventional treatment of epilepsy consists mainly of anticonvulsant drugs[115]; However, a complete cure for the disease has not been found yet [116]. More than 30% of people with epilepsy do not have crisis control (refractory epilepsy), even with the best drugs available [117, 118].
Alternatively, implantable antiepileptic devices are currently under development and in pivotal clinical trials. As therapy, they hold great promises for improving the quality of life for millions of people with epileptic seizures worldwide. The idea of an implantable device against epilepsy originates from the successful implementation of deep brain stimulation (DBS) devices for treatment of Parkinson's disease, primary dystonia and essential tremor [119]. The predictability of seizures, localisation of epileptic focus, and proper monitoring could prevent the sufferings, reduce the casualties, and improve the morbidity in patient's life [116, 120]. The advancements in sensing technologies can overcome these obstacles in order to timely identify the focus of epilepsy. For appropriate sensing, detection, and diagnosis of a disease, highly selective, precise biomarkers are of paramount importance [121]. There are three different categories of biomarkers for epilepsy: **molecular** biomarkers, **neuroimaging** and **electrophysiological** signatures [122]. Molecular biomarkers for epilepsy can be found in blood or tissues and include changes in the ribonucleic

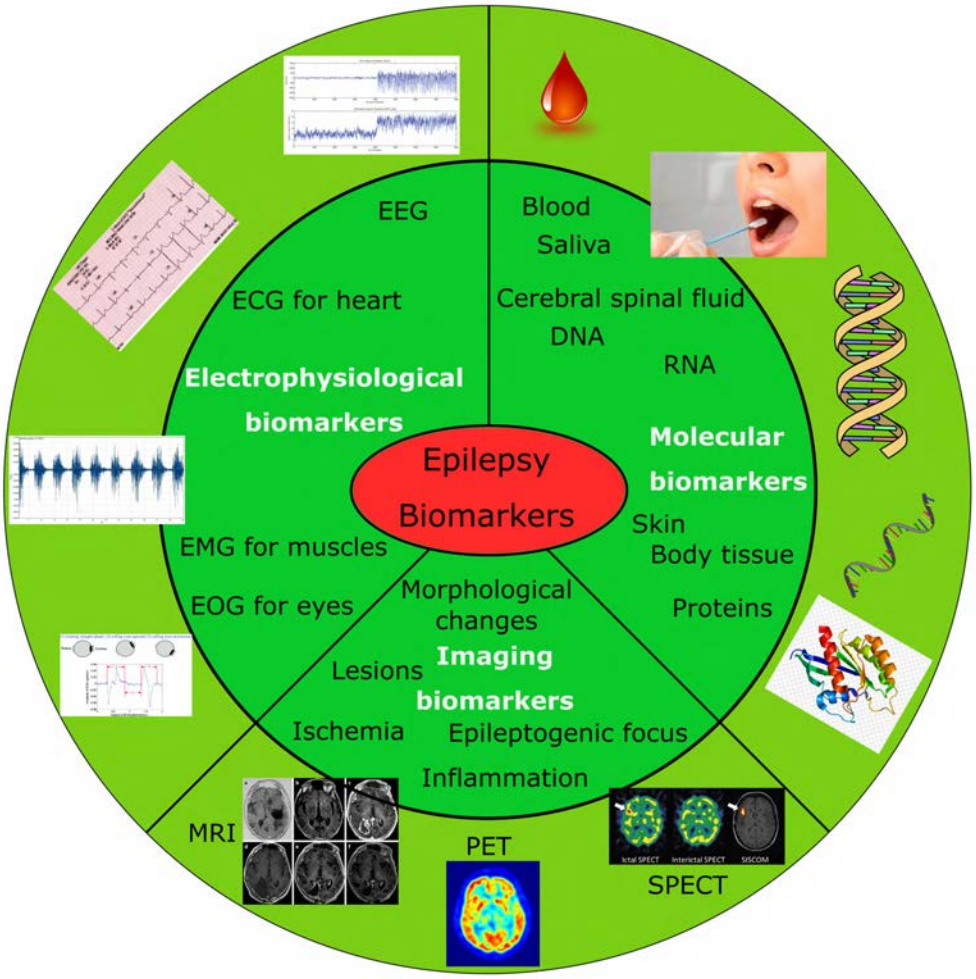

Figure 1.14: Biomarkers for the diagnosis and prediction of epilepsy. Adapted from [121]

acid (RNA) or gene expression, metabolite levels like enzymes, neuropeptides, proteins etc. Their expression and levels correspond to a clear fingerprint of the disorder. Yet, only few of these molecular biomarkers can be related to all types of epilepsy [122]. Non-invasive neuroimaging technologies such as magnetic resonance imaging (MRI) and functional MRI (fMRI) [24], computerized axial tomography (CAT) [123], positron emission tomography (PET), ictal single-photon emission computed tomography (SPECT) [27], and optical coherence tomography (OCT) [124] account for diagnosing of lesions, injury or epileptiform abnormality in the brain [125]. However, *electrophysiology* is one of the most commonly used technique to study the brain and is applied in the clinic to investigate brain dynamics [126, 32] (see Section 1.1.1).

EEG are the most standard analytical techniques for epilepsy diagnosis and detection [121].
For patients with drug-resistant focal epilepsy, surgery is one of the few remaining option in order to achieve seizure freedom. The success of epilepsy surgery relies on the accurate localization and complete resection or disconnection of the epileptogenic zone (EZ), defined as the minimum amount of brain tissue that must be resected to be seizure-free. Therefore, higher spatiotemporal resolutions are needed to identify the seizure-onset zone (SOZ, defined as the area of brain where the seizure is generated) and safely resect the brain tissue [127]. More invasive tools such as intracranial stereotactic electroencephalography (stereo-EEG), electrocorticography (ECoG) and intracerebral probes (depth neural probes), are employed for a higher spatiotemporal localization of the seizure foci. Intraneural (or depth) electrodes are most commonly placed through small burr holes using a stereotactic frame that is attached to the skull; they are used prior to surgery when the SOZ is beneath the cortical surface or there are multiple potential foci [127]. In addition to the higher spatiotemporal resolution that intraneural microelectrodes recordings provide, they are also viewed as an opportunity of direct brain recordings to understand the pathophysiology of epilepsy, since they offer an opportunity to answer questions that cannot be otherwise answered.

1.3.1 Electrophysiological biomarkers for epilepsy

Pathological brain activity associated with epilepsy spans from brief discharges of high frequency (200-600Hz) oscillations [128], to post-seizure infraslow (<0.1Hz) spreading depolarisations (SD) [99]. Electroencephalography recordings in the epileptic brain reveal interictal electrophysiological disturbances that can occur more frequently than seizures, such as **interictal spikes** (IIS) and sharp waves; further, invasive studies have discovered pathological **high-frequency oscillations** (HFOs) [128].
Interictal spikes are brief convulsive electrographic discharges observed between spontaneous recurrent seizures in epileptic patients. The word *interictal* means "between seizures", so "interictal spikes" refers to electrographic spikes that occur between seizures. The relationship between IIS and the seizures has been debated for decades [129]. Also fast activity above the prominent gamma-band (γ [30-150 Hz]), known as HFOs, has been extensively studied as potential biomarkers for epileptogenic tissue: there is evidence showing that resection of brain tissue containing HFOs is associated with good surgical outcomes [129]. HFOs are commonly divided into high-gamma (80–150 Hz), ripples (80–250 Hz), fast ripples (FRs, 250–500 Hz), and

very high-frequency oscillations (VHFOs, 500 Hz to 2 kHz). These ranges are a matter of definition and varies from author to author. It is important to note that *ripples* are also observed in the hippocampus and parahippocampal structures of non-pathological brain of animals and humans [130]. It is therefore crucial for a successful localisation and resection of the EZ to differentiate normal from pathological HFOs associated with seizures.

In contrast to ripples in the normal mammalian brain, fast ripple (and HFOs) in the epileptic hippocampal tissue, have been attributed to brief bursts of population spikes, generated from a cluster of pathologically interconnected neurons [131, 132]. Synchronous principal cell firing, and in some cases interneuron firing, could therefore explain pathological HFOs with central frequencies up to 300 Hz [133]. However, it is more difficult for this neuronal mechanism to explain the occurrence of FR-frequency up to 600 Hz, since no single neuron can fire above 300 Hz [134]. There are many studies that have shown a strong spatial and temporal association between pathological HFOs and IIS in epileptic patients [135, 136]. Recent experimental work, indicates that IIS containing HFOs, as well as HFOs alone, particularly ripple-frequency HFOs[137], localize the SOZ more accurately than IIS alone [136]. Looking at lower frequencies, ISA activity below the delta band - sometimes referred to as DC-shift or ictal baseline shifts (IBS) - can be associated with seizure onset [138, 139] and it is a promising biomarker for pre-surgical evaluation of SOZ [140, 141]. The term DC refer to the requirement of DC-amplifiers implemented with electrodes recordings to view the very low frequency signals, otherwise not measurable due to amplifier saturation (see Section 1.1.3).

Many factors promoting SD such as high extracellular potassium concentration, low magnesium, enhanced synaptic activity or glutamate receptor agonists, promote also seizures; moreover, seizures and SD frequently concur in various experimental models and patients [142].

Recent preclinical studies have linked post-seizure spreading depolarisations to sudden unexplained death in epilepsy (SUDEP) [143, 144] revealing an unexpected importance of ISA and a need to further study and characterise this type of activity in epilepsy.

While SD and seizures can happen concurrently, the inter-layer dynamics and the effect of SD on epileptic activity across the cortical laminae and deeper regions of the brain remain largely unknown. A limitation in studying ISA, either independently or concurrently with higher frequency activity, is the lack of appropriate tools to record it *in vivo* with high spatiotemporal fidelity. To proper measure SD and seizure, full-

band (DC)-coupled recordings are considered the gold standard for their detection. However, the electrodes size plays a limiting role for the use of DC-coupled recordings with electrodes in the range of micro-meters (see Section 1.1.3).
Development of intracranial electroencephalography probes capable of full bandwidth capabilities with high spatiotemporal resolution will be able to provide more accurate electrophysiological biomarkers for epilepsy, eventually enabling a more precise identification of epileptic foci, and thus improving surgical outcome [139].

1.4 Scope of the thesis

In this thesis the capabilities of gSGFETs as sensors to record electrophysiological activity in the brain have been investigated. Micro-fabrication wafer-scale technology was optimized to obtain best signal to noise performance of the graphene based SGFETs. Furthermore, flexible and biocompatible epi-cortical and intracortical devices have been fabricated, and tested in acute in vivo experiment in rats and mice model of epilepsy. Long term functionality is further demonstrated, by chronically implanting intracortical devices for more than 10 weeks in rats with established epilepsy (WAG rats).

The chapters of this PhD thesis are structured as follows:
chapter 2 provides a detailed theoretical description of the properties of graphene and the graphene/electrolyte interface. A description is provided, for the operating principles of the graphene solution-gated field-effect transistors.
In chapter 3 the fabrication procedure is given, as well as the characterization methods, for the transistors (gSGFETs); first for rigid (on a SiO_2 substrates) then also for the flexible neural probes. The final designs of the epi-cortical and intra-cortical SGFETs array probes are provided and illustrated; the developed probes rigidification technique, by means of back-coating with a bioresorbable protein (silk-fibroin), is described in detail. The method was subsequently used as bioresorbable shuttle for brain insertion of the constructed intra-cortical, deep neural probe devices. The electrical validation methods and the results obtained are assessed. It is also demonstrated that the SGFETs array probe functionalities are not affected by repeated rigidification-bioreabsorbation cycles.
In Chapter 4 the sources of electronic noise in gSGFETs are analyzed, and the successful noise reductions obtained by optimizing the contact and channel noises are presented.

Finally in chapter 5, the *in vivo* experiments in rats and mice are presented, demonstrating the full bandwidth capability of the gSGFETs arrays in high fidelity measurements, also of the infraslow neural activity. Full bandwidth properties are demonstrated in awake head-fixed mice model of epilepsy. Furthermore, the long term functionality of the neural probe are presented by chronically implanting the functional devices in a rat model of established epilepsy.
Chapter 6 summarizes the conclusions taken from this PhD work and it gives an outlook for suggested future research activities, in order to continue the development in this field.

During the course of the PhD work the following publications have been produced, in which I am either first author or co-author:

- *Flexible graphene solution-gated field-effect transistors: efficient transducers for micro-electrocorticography*, C. Hébert et al.,Advanced Functional Materials (2018) [70]
- *High-resolution mapping of infraslow cortical brain activity enabled by graphene microtransistors*, E. Masvidal-Codina et al., Nature Materials (2019) 280–288 [63].
- *Improved metal-graphene contacts for low-noise, high-density microtransistor arrays for neural sensing*, N.Schäfer et al., Carbon 161 (2020) 647-655 [145].
- *Full bandwidth electrophysiology of seizures and epileptiform activity enabled by flexible graphene micro-transistor depth neural probes*, A. Bonaccini Calia et al., Nature Nanotechnology (submitted, 2020).
- *Understanding the bias dependence of low frequency noise in single layer graphene FETs*, N. Mavredakis et al., Nanoscale (2018) 14947-14956 [146].
- *Bias dependent variability of low-frequency noise in single-layer graphene FETs*, N. Mavredakis et al., Nanoscale Advances (2020) [147]
- *Impact of contact overlap on transconductance and noise in organic electrochemical transistors*, A. G. G Polyravas et al., Flexible and Printed Electronics (2019) [148].
- *Neural interfaces based on flexible graphene transistors: A new tool for electrophysiology*, A. Guimerà-Brunet et al., IEEE (2019) [71]

2

Properties of Graphene SGFET

This chapter provides some general theoretical concepts essential for understanding the working principle of flexible graphene based SGFET. At first the physical, electronic and optical properties of graphene are presented. Then, the physics of the graphene/electrolyte interface are described, followed by the working mechanism of graphene-based solution-gated field-effect transistor (SGFET). In addition, the theoretical background of the origin of the electronic Flicker noise in graphene is presented and contributions to the SGFETs total noise are outlined and strategies to reduce it discussed.

2.1 Graphene properties

Graphene has attracted the attention of the scientific community around the world and is still an extensively studied material, because of its astonishing mechanical, electrical and chemical properties [149]. The strong carbon-carbon bonds, one of the strongest bonds in nature, give rise to a very high, diamond-like Young's modulus (1 TPa), a breaking strength of 42 N/m^2 [150] and a high intrinsic strength (130 GPa) [150]. Graphene has a formidable heat conductivity, up to 4000 W m/K [151]. The thickness of only one atom layer also results in very high transparency for optical light (97.97%) [152].

Graphene is a two dimensional crystal of sp^2-bonded carbon atoms ordered as honeycomb structure. The overlapping of the p_z orbitals of the neighbouring carbon atoms form a π-orbital, parallel to the graphene sheet. The conduction and valence

band of graphene are formed by the bonding and antibonding states of the π-orbital, respectively (π-state and π^*-state). The graphene lattice can be described using a two atom basis per unit cell with two lattice vectors[153]:

$$\vec{a}_1 = \frac{a}{2}(3, \sqrt{3}) \ , \ \vec{a}_2 = \frac{a}{2}(3, -\sqrt{3}) \tag{2.1}$$

where a = 1.42 Å is the distance between two neighboring carbon atoms (see Figure 2.1a).

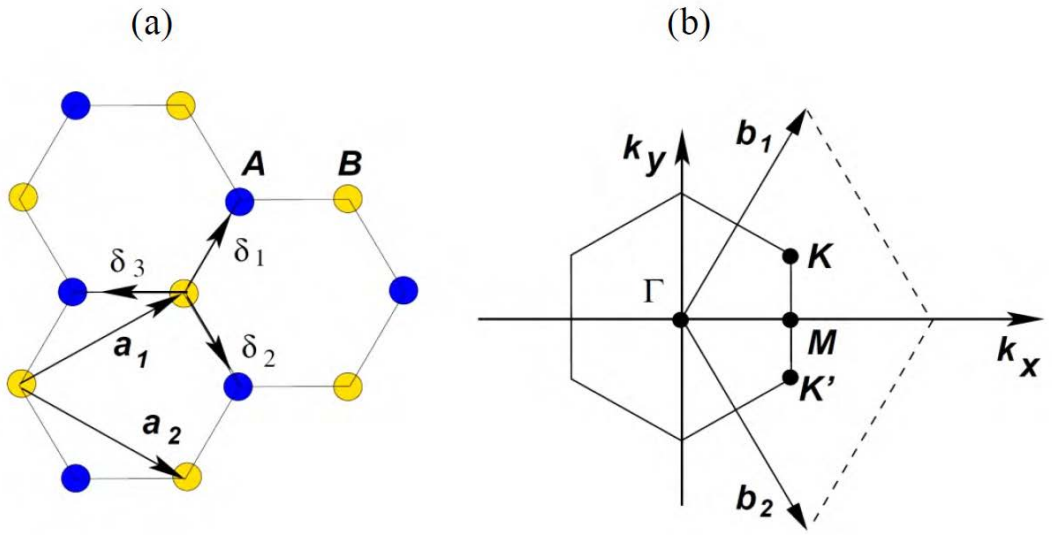

Figure 2.1: (a) The hexagonal lattice structure of graphene. $\vec{a_1}$ and $\vec{a_2}$ are the lattice unit vectors and δ_i, $i = 1, 2, 3$ are the nearest-neighbour vectors at a distance **a**, which corresponds to the carbon-carbon distance. (b) The reciprocal lattice of graphene showing the Brillouin zone and the Dirac points K and K' [154].

Figure 2.1b shows the reciprocal lattice of graphene in k-space with the Brillouine zone. The reciprocal unit vectors of the carbon honeycomb lattice are:

$$\vec{b}_1 = \frac{2\pi}{3a}(1, \sqrt{3}) \ , \ \vec{b}_2 = \frac{2\pi}{3a}(1, -\sqrt{3}) \tag{2.2}$$

The Dirac points are at the six corners of the Brillouin zone, named K and K':

$$\vec{K} = \left(\frac{2\pi}{3a}, \frac{2\pi}{3\sqrt{3}a}\right) \ , \ \vec{K'} = \left(\frac{2\pi}{3a}, -\frac{2\pi}{3\sqrt{3}a}\right) \tag{2.3}$$

They are of great importance for the electronic transport properties of graphene, which become evident when calculating the band structure of graphene. The band

structure was first theoretically postulated by Philip Russell Wallace in 1947[155]. He calculated the band structure of a single layer of graphite using a tight-binding approximation, as a first approximation step to investigate the band structure of graphite. The energy dispersion relation is given by [155]

$$E_{\pm}(\vec{k}) = E_D \pm t\sqrt{3 + f(\vec{k})} - t' f(\vec{k}) \tag{2.4}$$

with $f(\vec{k})$ defined as:

$$f(\vec{k}) = 2\cos\sqrt{3}k_y a + 4\cos\frac{\sqrt{3}}{2}k_y a \cos\frac{3}{2}k_x a \tag{2.5}$$

where $t = 2.75$ eV [154] and $t' = 0.1$ eV [156] are the nearest-and next nearest-neighbor hopping energies. E_D is the energy at the Dirac point. The positive and negative sign apply to the conduction and valence band, respectively. The band structure of graphene is shown in Figure 2.8. The conduction band (grey) and the valence band (red) touch at the six Dirac points. Therefore, graphene is referred to as a semi-metal or zero-bandgap semiconductor. No band gap is a limiting factor for application of graphene transistor for digital circuitry application, since the on/off ratio are typically very low (around 10 at room temperature [157]) compared to more than 10^3 for CMOS transistors [158]. A lot of effort has been dedicated in the past decade to introduce a bandgap in graphene, for instance by hydrogenation [159] or fabrication of graphene nanoribbons [160, 161, 162] or by nanoscale perforation [163]. Although these strategies successfully induced a band gap in graphene, these methods introduced other shortcomings deteriorating graphene's outstanding electronic properties, which are discussed below. Moreover, for bio-sensing application having a bangap is only of minor importance. In the vicinity of the Dirac points (see Figure 2.8b) the energy dispersion relation has a linear dependence [153]:

$$E(\vec{q}) = \pm\hbar v_f \sqrt{\left|\vec{k}\right|^2} \tag{2.6}$$

where $\vec{q} = \vec{k} - \vec{K}$ is the momentum of charge carriers with respect to the Dirac point, $\hbar$ the reduced Planck constant and v_f is the Fermi velocity. This linearity represents a great difference with respect to other semiconductors, in which the energy in k-space at a band minimum or maximum, follows usually a quadratic behaviour.

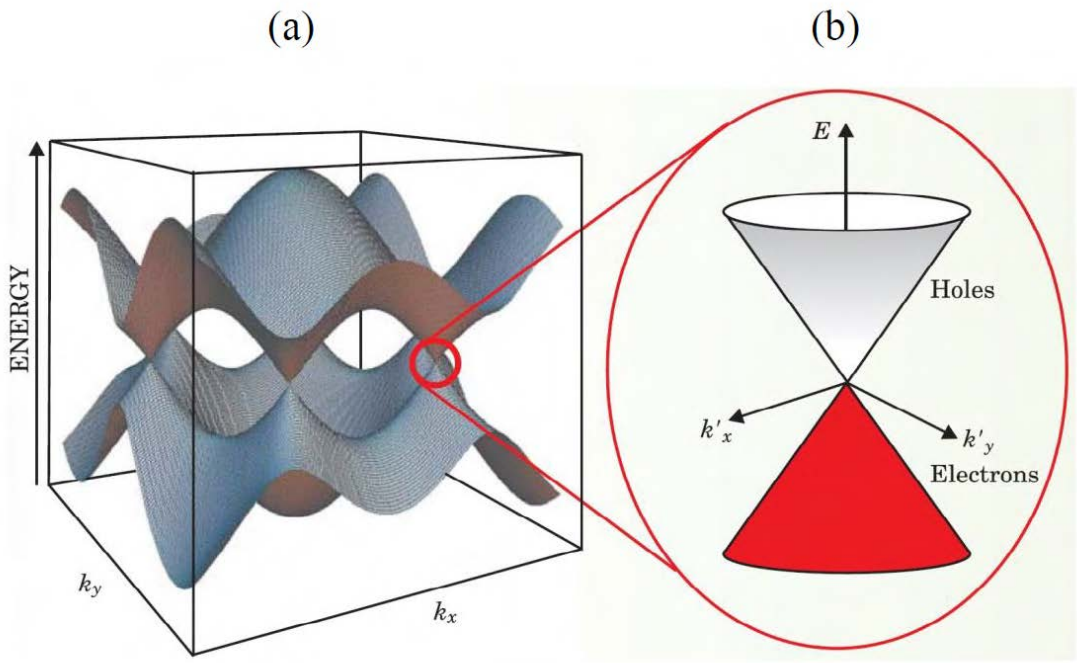

Figure 2.2: (a) Band structure of graphene in the reciprocal space with the valence and conduction band. (b) Around the Dirac point a linear energy dispersion relation is predicted for graphene.

The linearity between energy and momentum allows the charge carriers to have a vanishing effective mass and thus be best described by the Dirac equation for relativistic massless particles, as massless Dirac Fermions in the vicinity of the Dirac points. As a consequence, the expected charge carrier mobility in graphene is extremely high, of approximately $v_f \approx 10^6$ m/s [155]. Experimentally measured mobility of suspended graphene of $\mu = 10^6$ cm^2/Vs at low temperatures [164], values larger than 500 000 cm^2/Vs for encapsulated graphene between hexagonal boron nitride (hBN) lattices, and more than 100 000 cm^2/Vs at room temperature have been reported [165]. These ultra-high mobilities suggest the use of graphene for high-frequency electronics [166, 167] as well as its use for highly sensitive sensors[68]. Another consequence of the band structure is that the expected charge carrier density at the Dirac point is zero. Despite this, a minimum conductivity at the Dirac point of $\sigma_{min} \approx \frac{4e^2}{h}$ has been reported in many experiments [168, 169, 170], where e is the elementary charge and h the Planck constant. The minimum conductivity is related to the scattering mechanism on defects and impurities, as well as on the structure itself [171]. Theoretically, this minimum conductivity at the Dirac-point is explained by the formation of electron hole puddles at zero charge carrier density and

is predicted to be $\sigma_{min} = \frac{4e^2}{\pi h}$ [172]. Still, the exact mechanisms are under debate.
Graphene has also exceptional chemical properties. Due to the high carbon carbon bond energy of 4.9 eV, graphene is chemically very stable. Hence, graphene is stable in liquid environments such as an electrolyte [173, 174], and it has been shown to be biocompatible in recent studies [66, 175].
Due to its unique electrical properties, its outstanding chemical and mechanical stability, as well as bio-compatibility, graphene fulfills important and fundamental requirements for building flexible biosensors. Therefore graphene was chosen as the active material of the flexible transistors fabricated and studied in this experimental thesis.

2.1.1 CVD Graphene growth

There are different ways nowadays to produce two dimensional (2D) crystals (i.e. the family of TMD), including graphene. As already mentioned above, one way is to use mechanical exfoliation in which graphene and 2D-TMDs are detached from their bulk materials (i.e. graphite for graphene), using for instance adhesive tape. The highest quality of 2D materials has been produced by this method[149, 176]. While mechanical exfoliation is still setting the benchmark in terms of crystal-quality and film homogeneity, it does not present a scalable technique when moving towards large-scale fabrication of graphene-based technologies, due to the relatively small obtainable flake size [177, 178].
This is sufficient for fundamental research purposes, however it is not suited for volume production and not compatible with standard CMOS processes. Possible alternatives are the liquid exfoliation of graphene oxide and subsequent reduction [179, 180] and graphene's liquid-phase exfoliation [181, 182]. Such products are already commercially available on a large scale [183] for their application as inks, conductive coatings, supercapacitors, composites (i.e to enhance a material stiffness) and many others [184].
Nevertheless, the rather low charge carrier mobility (100 cm^2/Vs) makes these graphene products not very suitable for studying fundamental physics, or for high mobility electronics devices (such as gSGFETs). Moreover, *epitaxial graphene* has been produced, in which graphene layers are grown on a SiC surface. This was first demonstrated by Berger et al. in 2004 [185]. This method allows the production high quality single layer graphene (SLG) over cm^2 scale areas, with mobility of 5000 cm^2/Vs, up to 20 000 cm^2/Vs(Si-face) and of more than 10 000 cm^2/Vs (C-

face) [186]. Epitaxial graphene enabled studing quantum effects [187]. A bottom-up fabrication of graphene nano ribbons, aiming at creating a bandgap in graphene, has been demonstrated on large scale [188] with mobilities reaching 10^6 cm^2/Vs [189]. Therefore epitaxial graphene is a promising candidate technique for high frequency applications and transistors operating at frequencies larger than 100GHz. The drawbacks of epitaxial graphene are the high costs of SiC wafers and the difficulty of transferring the graphene to other substrates. The transfer problem is particularly a limiting factor for the application in flexible electronics.
Another very promising, cheap and highly-scalable alternative to grow graphene is by a process called *chemical vapor deposition* (CVD). This growth process allows the fabrication of large area, high quality graphene and is based on rather low-cost precursors [190]. Graphene is grown by CVD on a catalytic metal substrate such as copper or nickel [191]. The CVD growth on copper permits the fabrication of large area single layer graphene (SLG) sheets, which can be easily transferred to any other desired substrate. It was discovered that SLG could be grown on iridium[192] and few layer graphene (FLG, <10 layers) could be grown on nickel substrates [193]. The first large scale growth of single layer graphene on copper was demonstrated by Li et al. in 2009 [190]. Afterwards the process was scaled up to 30 inch [194], the grain size was significantly increased to centimetre scale resulting in mobility of 15 000 cm^2/Vs to 30 000 cm^2/Vs at room temperature on hBN substrates [195]. For CVD graphene transferred with a dry transfer technique and sandwiched between hBN flakes mobility larger than 350 000 cm^2/Vs were reported [196, 197]. These high value demonstrate that the obstacle to obtain high mobilities is not the growth process, but rather the choice of the substrate that minimizes carrier scattering.
The process to grow graphene by CVD on copper is briefly described as follows: methane gas flows over a heated copper foil, where it is catalytically decomposed by the copper. Then, the carbon atoms are adsorbed on the copper surface and form the two-dimensional layer of graphene. Due to the very low solubility of carbon in copper only a small amount of the carbon diffuses into the copper foil. This process is self-limited and it results in monoatomic graphene layers, since after a carbon mono-layer is formed over the copper surface, the catalytic effect of copper is suppressed, and no methane can be further decomposed [190]. After growth, the underlying Cu foil can be removed through electrochemical etching, leaving a free standing film of single layer graphene, which can then be transferred onto any target substrate.

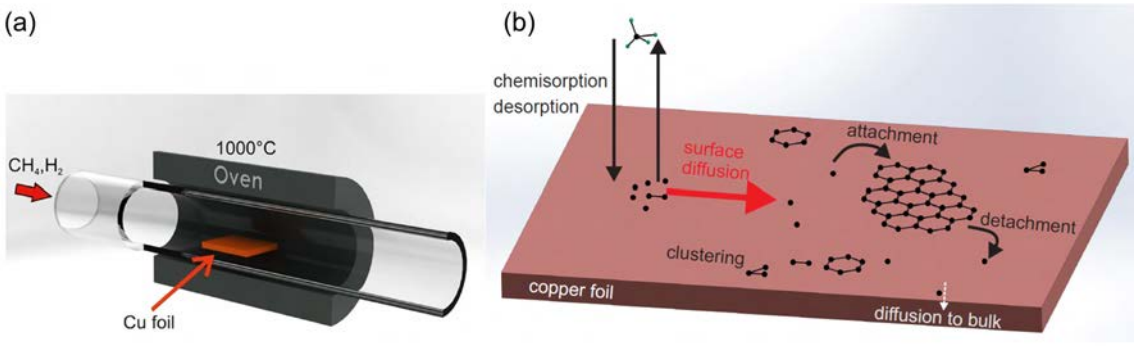

Figure 2.3: (a)Sketch of the CVD setup. The gas mixture enters the glass tube heated by a tubular oven (reactor). The graphene grows on the copper foil, placed in the middle of the oven which is heated around 1000°C. (b) Schematic representation of steps and mechanisms of graphene growth on copper. Adapted from [198]

Figure 2.3a illustrates a typical hot wall reactor set-up for CVD growth, and Figure 2.3b show a schematics of the catalytic decomposition of methane into carbon atoms that nucleates and grow horizontally into single layer graphene [198]. In this work, graphene has been produced by the CVD method on a copper foil, since the microfabrication of the graphene neural probes was developed at 4-inch wafer-scale. A detailed description of the growth mechanism and transfer procedure can be found in section 3.1.

2.1.2 Optical properties

Integration of two-dimensional materials into devices requires the availability of non-destructive characterization techniques, necessary to monitor the crystal quality after growth and throughout the device fabrication process. Raman spectroscopy has become in the last years a common method to investigate the atomic structure and electrical properties of graphene, since it is a non-destructive method, works in situ and can prove sufficiently large scales for our application [199].
Raman spectroscopy was discovered by the Indian scientist C.V. Raman in 1928[200] and has become an important method to characterize material properties, such as degree of crystallinity in solids, doping of semiconductors and strain.
Raman spectroscopy exploits inelastic scattering processes of monochromatic laser light (typically in the visible spectrum), which exhibits resonances with vibrational and rotational low frequency modes in the sample's crystal structure. The incoming excitation photon with wave vector $\vec{k}$ creates a virtual electron-hole pair. Next, the

electron hole pair recombines and adsorbs (anti-Stokes process) or emits (Stokes process) a phonon with wave vector $\vec{q}$ and a photon with wave vector $\vec{k'}$.

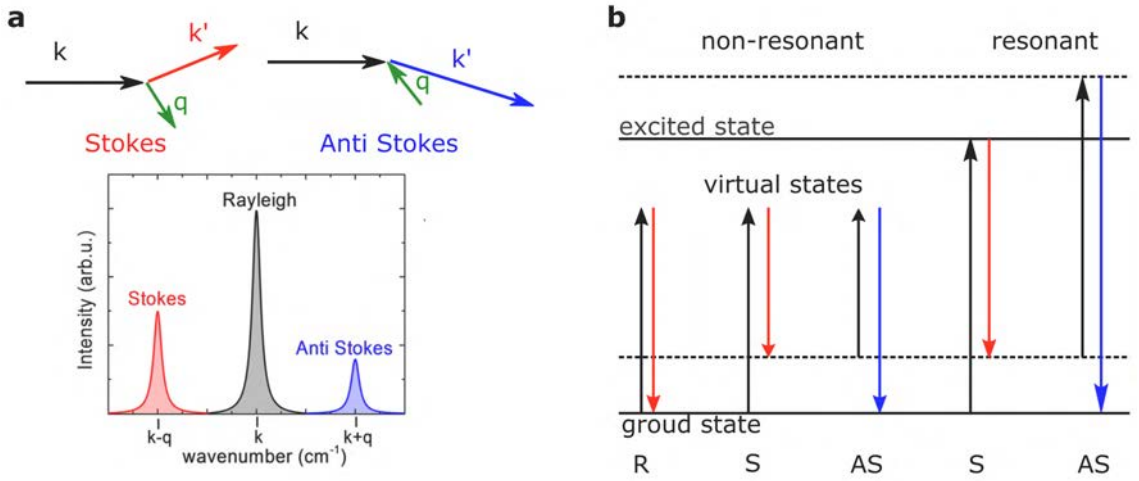

Figure 2.4: a, Conservation of momentum for Stokes and anti-Stokes scattering. *Below*: sketch of a typical Raman spectrum showing signals from Stokes, Rayleigh and anti-Stokes scattering. **b**, Energy diagram of Stokes (S), Anti-Stokes (AS) and Rayleigh scattering (R) for resonant and non-resonant processes with laser energy (black) and the energy of the emitted photon (red: Stokes, blue: anti-strokes). Horizontal straight and dotted lines represents vibrational and electronic states, respectively.

The expressions for momentum and energy conservation that are schematically shown in Figure 2.4 are:

$$\vec{k'} = \vec{k} \pm \vec{q} \tag{2.7}$$

and

$$\hbar\omega_{k'} = \hbar\omega_k \pm \hbar\omega_q \tag{2.8}$$

where $\omega_{k'}$, ω_k and ω_q are the scattered photon, the incident photon and the phonon angular frequencies, respectively. A sketch of a typical Raman spectrum is drawn in Figure 2.4a, showing the redshifted Stokes ($|\vec{k}| - |\vec{q}|$) the blue-shifted anti-Stokes ($|\vec{k}| + |\vec{q}|$) and the elastic Rayleigh (R) scattering mode ($|\vec{k}|$). Figure 2.4b shows the Stokes and anti-Stokes energy diagram for each process. For non-resonant processes the incoming photon (black arrow) excites the system to a virtual state. In the case of a Rayleigh process the system goes back to the ground state without emitting a phonon and the energy of the emitted photon is equal to the energy of the incoming photon. In the Stokes process (S), the system decays to a vibrational state and the energy of the emitted photon is lower (red arrow). In the case of an anti-Stokes process (AS) the system is in a vibrational state upon excitation and then decays

back to the ground state and the energy of the emitted photon is increased (blue arrow). For resonant Raman scattering the system is excited to an electronic excited state and a real electron hole pair is formed. Again, Stokes and anti-Stokes processes are possible. Since graphene has no band gap, Raman scattering in graphene is always resonant. The anti-Stokes process requires phonons to be present in the material, and therefore, it is strongly temperature dependent, according to the Bose-Einstein statistics. An estimate of the intensity ratios of Stokes (I_S) and anti-Stokes (I_{aS}) scattering is given by[201]:

$$\frac{I_S}{I_{aS}} =\propto exp\Big(\frac{\hbar\omega_q}{k_B T}\Big) \tag{2.9}$$

Which means that anti-Stokes scattering is strongly suppressed at room temperature compared to the Stokes process[202]. The Rayleigh band has the highest intensity as it is the most favourable process (see Figure 2.4a).

2.1.3 Raman mode in graphene

In the case of graphene, valuable information concerning the density of defects in the lattice, the number of layers, doping level, the amount of surface contamination and the presence of mechanical strain can be obtained from a proper analysis of its Raman spectrum [203]. The understanding of graphene's Raman spectra can be achieved by studying the phonon dispersion relation depicted in Figure 2.5. The unit cell of monolayer graphene consists of N=2 carbon atoms (see Figure 2.1), and so six (2N+2) phonon dispersion bands are formed [204], with three being acoustic (A) and three being optical (O). One acoustic branch and one optical phonon branch can be interpreted as out-of-plane (o) atomic vibrations. The remaining acoustic and optical phonon branches correspond to in-plane (i) vibrations. These phonon modes are further classified as longitudinal (L) or transverse (T), according to their associated direction of vibration with respect to the surrounding carbon atoms.

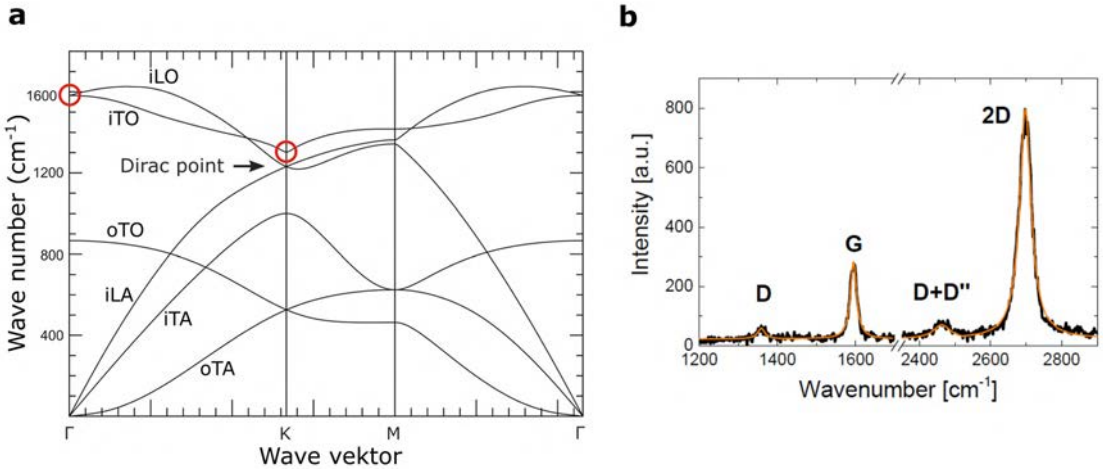

Figure 2.5: a, Computed phonon dispersion relation of graphene along the high symmetry directions $\vec{\Gamma}$,$\vec{M}$ and $\vec{M}\Gamma$. The two-atom basis leads to the formation of three acoustic (A) and three optical (O) phonon branches with one out-of-plane (o) and two in-plane (i) modes per branch. Also to notice the valence and conduction bands, which meet at the K point in reciprocal space (Dirac point). Adopted from [205]. **b**, Raman spectrum of monolayer graphene and its characteristic peaks.

The six phonon modes can thus be assigned to iLO, iTO, oTO, iLA, iTA and oTA, as shown in Figure 2.5a.

Figure 2.5b shows a characteristic Raman spectrum[1] for a CVD grown graphene transferred on a SiO_2 substrate. [2]. Superimposed is a Lorentzian fit of the most prominent peaks in the graphene Raman spectrum, i.e. the D, G, D+D" and 2D.

Figure 2.6 shows schematics for the most important Raman scattering processes in graphene. The **G-peak** approximately at $\sim 1590 cm^{-1}$, historically labeled after graphite, can be measured in all graphitic based materials. It corresponds to high frequency in-plane optical phonons. The lattice vibration can be visualized as two anti-parallel swinging sub-lattices (Figure 2.6) [199]. The **D-peak** appearing typically at $\sim 1350\ cm^{-1}$, it is assigned to the breathing mode of the hexagonal carbon atoms ring. It is generated by in-plane transverse optical phonons (iTO) around the Brilluoin zone corner K, and can be only activated by defects[206, 207].

Due to the vibrational symmetry, it is not visible in case of perfect graphene structure. Yet, it becomes visible for some graphene edges or in presence of structural defects, which make it a reliable indicator to quantify disorder in graphene [206]. The **2D-peak** at ~ 2698 1/cm is considered to be the D-peak overtone, involving

[1]The Raman characterization shown in this work was performed with a solid-state laser at a wavelength of λ =488 nm (light blue), corresponding to an excitation energy of $E_{Laser} = 2,54eV$.

[2]Since the polyimide substrate consists also of carbon atoms, in order to apply Raman spectroscopy the used graphene layer has to be deposited on a substrate such as SiO_2

the resonance of two D-band phonons. The 2D band is therefore a double or triple resonant process. For these resonant processes, which are due to the conservation of the momentum, no defects are necessary for their activation [204, 208].
Another peak that appears in the Raman spectra of single layer graphene is the D+D" band. The latter is also a double resonant process, where an electron is excited near the K point and is scattered to a point near K' by emission of an iTO phonon. Then, an iLA phonon is emitted to go back to K. The intensity of the D+D" is typically low (Figure 2.5) since the probability to emit two phonons in sequence (to fulfil momentum conservation) is also low.
The most important parameters to assess monolayer graphene quality are the I_{2D}/I_G ratio, the absence of the D-band and a narrow 2D-peak. The intensity ratio between G and D peak allows to determine the number of defects in graphene, with a high ratio indicating a low defect density in the graphene.[206].
In addition, the number of graphene layers affects the intensity of the 2D and G peak; a 2D/G ratio larger than 1.5 typically indicates the presence of single layer graphene. For a higher number of layers the ratio decreases.[208]. For multilayer graphene the 2D band splits into several sub-bands, the intensity decreases and the full width half maximum (FWHM) increases, becoming similar to the 2D band of graphite for more than five layers. [208].

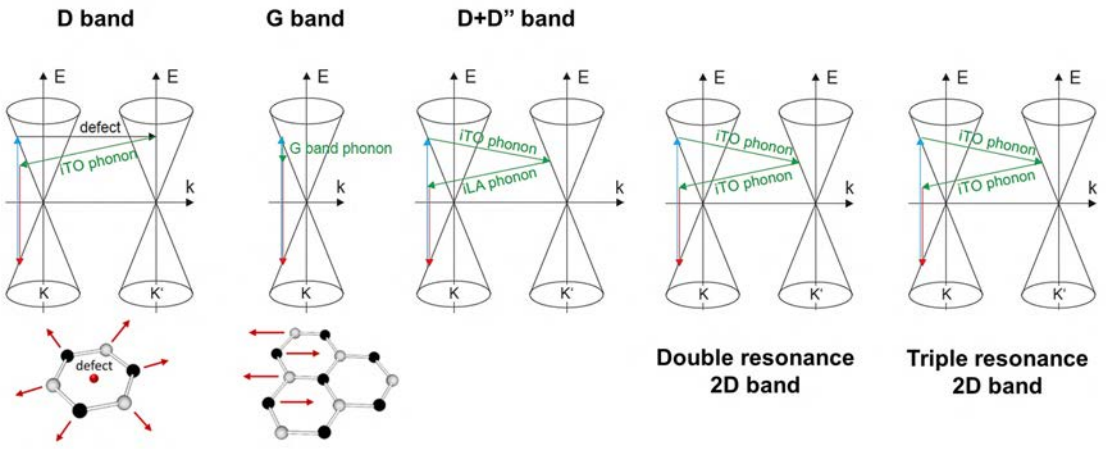

Figure 2.6: Schematic view of the most relevant Raman scattering processes in graphene. Figure adopted from [203].

It has been shown that both strain and doping shifts slightly the peak positions [199]. Inhomogeneous doping (caused by contaminants or defects) leads to the observation of broader peaks and variations in the "D to G intensity ratio.
To investigate the large-scale properties of the CVD grown graphene before its

transfer, we use SEM images and Raman spectra of the grown graphene on copper foil (see Figure 2.7). On Cu, the Raman spectra has a broad fluorescence background, which after subtraction gives the expected single layer graphene bands (Figure 2.7a). The absence of the D Raman peak, activated with disorder, indicates the good quality of the grown samples. Samples are usually characterized in this work with Raman maps with scan area of 30x30 μm^2. Figure 2.7b displays a Raman map of the G-peak intensity, where regions of higher intensity (yellow) correspond to second nucleation centers with characteristic Raman spectrum of multilayer graphene (as shown below). Overall, the grown graphene in this work is represented by the map shown in Figure 2.7b-c, with 92% of the scan area that has a 2D/G intensity ratio of 2.4, and an average 2D FWHM of 28 cm^{-1}, as characteristic of monolayer graphene. We take SEM images of the Cu-foil after the growth of graphene to optically evaluate larger-areas of the samples, in which darker spot indicate second nucleation centres, as shown in Figure 2.7d (yellow arrows).

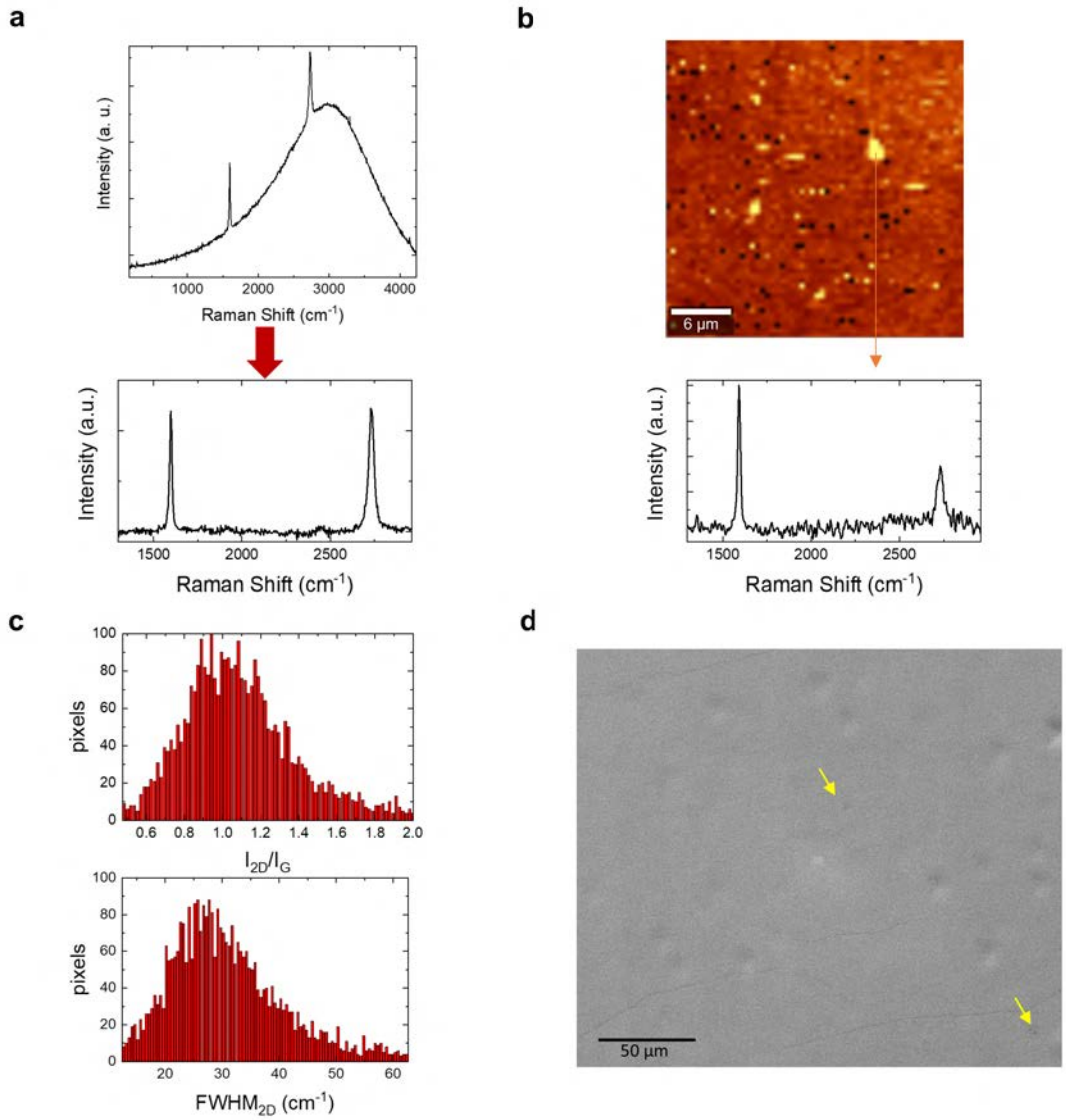

Figure 2.7: **a**, Average Raman spectrum of as grown graphene on copper. Below, a Raman spectrum after copper background subtraction; the two main Raman contributions are observed: G (1596 cm^{-1}) and 2D (2730 cm^{-1}). The absence of the D Raman peak, activated by defects in the graphene, indicates the good quality of the grown samples. **b**, Raman map of the G peak intensity where regions of higher intensity (yellow) correspond to second nucleation centers, with characteristic Raman spectrum like the one shown below. **c**, Histograms of the 2D/G intensity ratio and 2D band width. 92% of the scan area (30x30 μm^2) presents an intensity ratio of 2.4, which is characteristic of monolayer graphene. The average FWHM of the monolayer region is about 28 cm^{-1}. Regions of less than 4 μm^2 that show larger 2D FWHM correspond to the thicker (multilayer) nucleation spots. **d**, Scanning electron microscopy image of as-grown CVD graphene on copper foil; two second nucleation spots can be distinguished.

2.2 Graphene/electrolyte interface

To understand the sensing mechanism of a graphene based SGFET, a closer look at the electrolyte's structure in the vicinity of the graphene interface is necessary. In a simple picture, when an electrode with surface charge σ_S is immersed in an electrolyte, the ions of the opposite charge reassemble and get attracted to its surface. The closest minimum distance d between an ion and the surface is intuitively given by the physical size of its hydration shell. Due to the effective charge separation, this is equivalent to a plate capacitor with capacitance C_H. These ions of opposite charge form a layer referred to as Helmholtz layer. The predicted capacitance $C_H \propto 1/d$ is therefore independent of the applied voltage, which is in contrast to the experimental results [209]. In addition, the effect of the ions in the electrolyte have to be taken into account, in order to correct the measured values at the electrode. Therefore, a diffuse layer of charges in the electrolyte was introduced by Gouy and Chapman [210, 211]. Thermal motion of the ions is responsible for the smear of this layer. In the diffuse layer in the plane parallel to the interface, the concentration n_i of ions species i is described by the Boltzmann distribution:

$$n_i = n_i^0 \exp\left(\frac{-e \cdot z_i \cdot \varphi(x)}{k_B T}\right) \tag{2.10}$$

where n_i^0 is the bulk electrolyte concentration of ion species i, z_i is the ion valence, e the elementary charge, k_B the Boltzmann constant, and T the absolute temperature. $\varphi(x)$ is the electrostatic potential at a distance x from the surface. Therefore, the total charge per volume at a distance x from the solid is given by:

$$\rho(x) = \sum_i n_i z_i e = \sum_i n_i^0 z_i e \exp\left(\frac{-e \cdot z_i \cdot \varphi(x)}{k_B T}\right) \tag{2.11}$$

In order to calculate the potential drop from the electrodes surface to the bulk, the total charge distribution $\rho(x)$ is combined with the Poisson equation:

$$\rho(x) = -\epsilon\epsilon_0 \frac{d^2\varphi}{dx^2} \tag{2.12}$$

giving:

$$\frac{d^2\varphi}{dx^2} = \frac{-e}{\epsilon\epsilon_0} \sum_i n_i^0 z_i \exp\left(\frac{-e \cdot z_i \cdot \varphi(x)}{k_B T}\right) \tag{2.13}$$

By integration with boundary conditions $\varphi_{x=\infty} = 0$ and $\frac{d}{dx}\varphi_{x=\infty} = 0$, the equation is transformed to:

$$\left(\frac{d\varphi}{dx}\right)^2 = \frac{2k_BT}{\epsilon\epsilon_0}\sum_i n_i^0\left[\exp\left(\frac{-e\cdot z_i\cdot\varphi(x)}{k_BT}\right) - 1\right] \tag{2.14}$$

The sum in the upper equation (eq. 2.14) is reduced to two terms, in the case of a symmetric electrolyte[3]

$$\frac{d\varphi}{dx} = -\left(\frac{8k_BTn^0}{\epsilon\epsilon_0}\right)^{1/2}\sinh\left(\frac{z\cdot e\cdot\varphi(x)}{2k_BT}\right) \tag{2.15}$$

This represents the electric field in the electrolyte generated by the ion distribution. Finally, integration leads to the potential in the diffuse layer:

$$\frac{\tanh(ze\varphi/4k_BT)}{\tanh(ze\varphi_{surf}/4k_BT)} = e^{-\kappa x} \tag{2.16}$$

Here $\varphi_{surf} = \varphi_{x=0}$ is the surface potential and κ is the inverse of the Debye screening length L_D defined by:

$$\kappa = \left(\frac{2n^0z^2e^2}{\epsilon_0\epsilon k_BT}\right)^{1/2} = \frac{1}{L_D} \tag{2.17}$$

This characteristic length describes the drop of the potential within the electrolyte and, accordingly, also specifies the distance in which a charge is screened in the electrolyte. The relevant influencing parameters are the ion valence z and the ion concentration n^0. For low ion concentration, L_D is large i.e. the diffuse layer extends widely into the electrolyte, while for high ion concentrations the diffuse layer compresses. For small values of φ_{surf}, equation 2.16 simplifies to

$$\varphi = \varphi_{surf}\cdot e^{-\kappa x} \tag{2.18}$$

using $\tanh(x) = x$ for small values of $x = ze\varphi_{surf}/(4k_BT) < 0.5$. Therefore, equation 2.18 holds for $\varphi_{surf} < 50mV$, considering monovalent ions at $T = 300\,\mathrm{K}$ [209].
In the Gouy-Chapman model the ions in the electrolyte are represented by point-like charges. Stern improved this model by combining it with the concept of the Helmholtz layer [212]. In his modifications, Stern considers the radius of the ion hydration shell as a limiting distance of the charges to the electrode surface.

[3]In a symmetric electrolyte the valency z of the cation and the anion are the same.

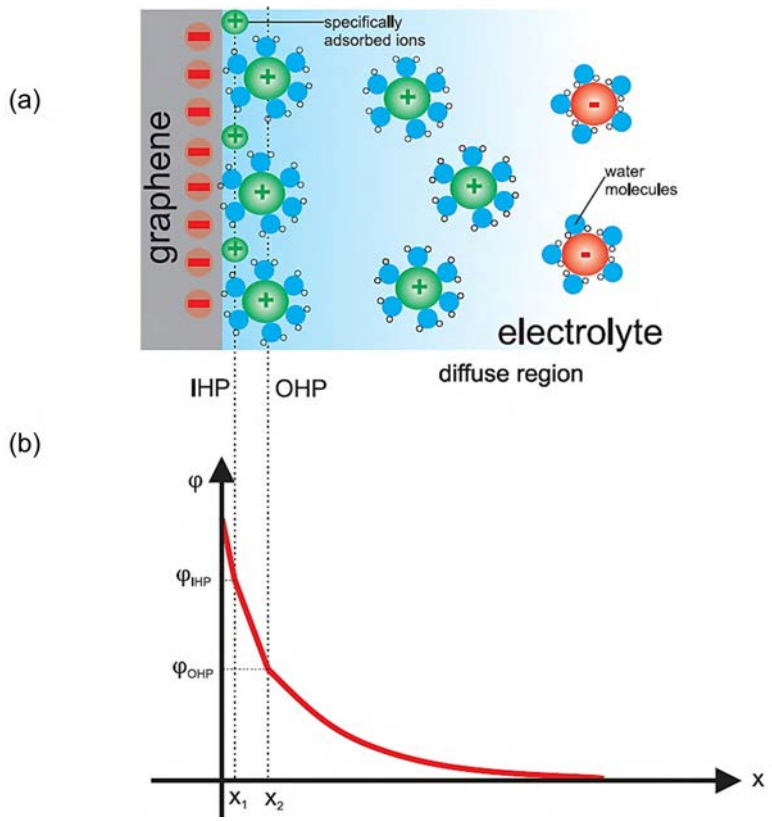

Figure 2.8: a. Schematic representing the Gouy-Chapman-Stern model, in the case of negatively charged graphene in contact with the electrolyte. The specific adsorbed ions are located at the inner Helmholtz plane, the adsorbed hydrated ions at the outer Helmholtz plane, followed by a diffuse layer of hydrated ions. **b**. Elecrostatic potential profile at the graphene electrolyte interface.

In the Gouy-Chapman-Stern model (GCS), the Helmholtz layer at the surface of the electrode is divided into the inner Helmholtz plane (IHP) and the outer Helmholtz plane (OHP), formed by specifically adsorbed and by electrostatically adsorbed ions, respectively. As described above, a diffuse layer of hydrated ions extends into the electrolyte. The potential drops linearly between the surface of the IHP and the OHP, since no charges are in between these layers. The potential profile in the diffuse layer is described by the model presented above (see eq. 2.16 and eq. 2.18).
With the GCS model a double layer capacitance C_{dl} between the electrode and electrolyte can be described by a series connection of the Helmholtz capacitance $C_H = (\frac{1}{C_{OHP}} + \frac{1}{C_{IHP}})^{-1}$ and the diffuse layer capacitance C_{dif}.

$$C_{dl} = \left(\frac{1}{C_{dif}} + \frac{1}{C_H} \right)^{-1} \tag{2.19}$$

The capacitance of a 2D systems with low Density Of State (DOS) can no longer be described classically, as for a plate capacitor in which the capacitance depends only on the geometry of the system and on the dielectric constant; in this case quantum mechanical phenomena have to be considered.

Quantum capacitance.

In graphene, the DOS is low when the Fermi level is close to the Dirac point, so that to properly describe the graphene/electrolyte interfacial capacitance, quantum capacitance [213] has to be accounted for. When an additional charge is brought to the surface of a low DOS system, it has to occupy a higher (available) energy state due to the Pauli exclusion principle. Luryi *et al.* describes such systems by connecting in series the quantum capacitance to the classical capacitance [213]. In metals or systems with high density of states the quantum capacitance is suppressed due to the low energy required to add a charge. However, in graphene, where the DOS is low, such additional energy to add charge carriers required by the Pauli principle becomes relevant. The smaller the quantum capacitance is, the more relevant it becomes.
The quantum capacitance in graphene is defined as $C_Q = \frac{\partial Q}{\partial U_{gr}}$, with $Q = e \cdot (n - p)$ the total charge and U_{gr} the relative position of the Fermi level to the Dirac point. The quantum capacitance of graphene is given by [214]:

$$C_Q = \frac{2e^2 k_B T}{\pi(\hbar v_f)^2} \ln\left(2\left(1 + \cosh\frac{eU_{gr}}{k_B T}\right)\right) \tag{2.20}$$

For $eU_{gr} \gg k_B T$ it simplifies to [215]:

$$C_Q \approx e^2 \frac{2}{\pi} \frac{eU_{gr}}{(\hbar v_f)^2} = \frac{2e^2}{\hbar v_f \sqrt{\pi}} \sqrt{n} \tag{2.21}$$

From this formula it is clear that the quantum capacitance is able reach infinity since it is proportional to the charge carrier density n. The interfacial capacitance C_{int} of the graphene/electrolyte interface is then given by a series connection of the quantum capacitance and the double layer capacitance:

$$C_{int} = \left(\frac{1}{C_{dl}} + \frac{1}{C_Q}\right)^{-1} \tag{2.22}$$

When the Fermi level in graphene is in proximity of the Dirac point, the quantum capacitance is smaller; than the C_{dl} is the main contributor to the interfacial

capacitance. Away from the Dirac point, however, the C_Q increases to infinity and the double layer capacitance C_{dl} becomes dominant C_{int}.

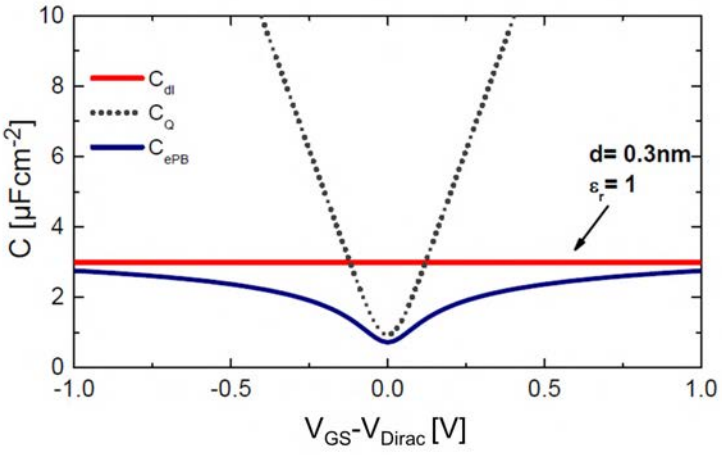

Figure 2.9: Interfacial capacitance obtained from the simulations, using the extended Poisson-Boltzmann (ePB) model (blue line). Both quantum capacitance of the graphene (dotted line), and the electrode electrolyte interfacial capacitance (red line) are considered [216].

Simulations of the graphene/electrolyte interface were performed by Dankerl *et al.* considering the molecular dynamics of water molecules [216]. For the simulation an extended Poisson-Boltzmann model (ePB) was used, that considered the microscopic ordering of water molecules at the hydrophobic graphene surface. With this simulation, capacitances of several µF/cm^2 were calculated [216]. Figure 2.9 shows the interfacial capacitance calculated with the ePB model C_{ePB} (blue line), in comparison to the double layer C_{dl}(red line) and quantum capacitance C_Q (grey dots). The double layer capacitance was obtained considering a hydrophobic gap of 0.3 nm and a dielectric constant $\epsilon = 1$. In the following the simulated values of the interfacial capacitance shown in Figure 2.9 are always used for the calculations.

2.3 Graphene solution gated field effect transistors

Solution-gated field-effect transistors (SGFETs) have been fabricated since many decades and find many applications, especially in the field of biosensing. The first silicon based SGFET was realized by Bergveld in 1970 [217]. As the name anticipate, SGFET is a type of field-effect transistor in which the gate voltage is applied through an electrolyte solution. The main difference between the working principle of a metal-oxide-semiconductor field-effect transistor (MOSFET) and the working principle of a SGFET is the way the current is modulated by the gate bias. In a MOSFET, the current through the transistor is usually gated by a metal, which is separated from the channel by a thin insulating (oxide) layer. By applying a gate voltage, charge carriers are attracted to the substrate/insulator interface forming a conductive channel. If the applied gate bias is reversed the channel is depleted and no current is able to flow.

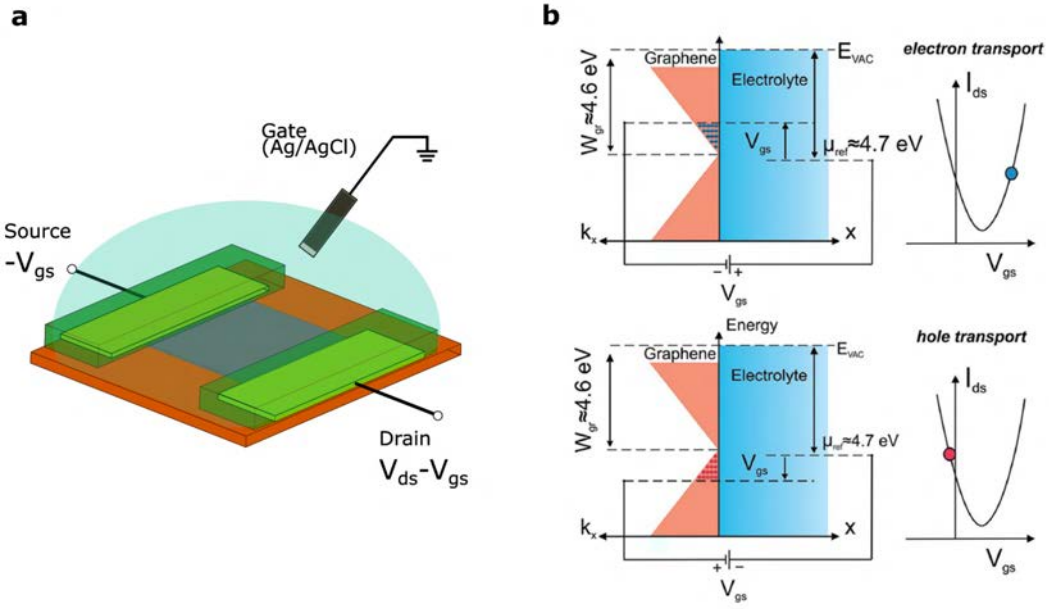

Figure 2.10: Band structure of graphene in contact with the electrolyte. The conductivity can be modulated and the type of charge carriers can be switched between holes and electrons by the applied gate voltage V_{GS}. Here E_{vacuum} is the vacuum energy and $\mu_{reference}$ the electrochemical potential of the reference electrode. **a**. The applied negative voltage between the electrode and the graphene (gate voltage) $V_{GS} < V_{Dirac}$ shifts the Fermi level down into the valence band, which generates holes in the graphene, thereby increasing the current. **b**. For $V_{GS} > V_{Dirac}$, the Fermi level shifts into the conduction band, inducing electrons and thereby increasing the current between drain and source. Adapted from [19]

In a SGFET, on the other hand, the gate voltage is applied by a reference electrode immersed in an electrolyte instead. For both MOSFET and SGFET, the modulated drain-source current I_{DS} depends on the mobility of the active material and the interfacial capacitance [218]:

$$I_{DS} \propto \mu \cdot C_{int} \tag{2.23}$$

The capacitance for the MOSFET is given by the plate-capacitor equation $C = \epsilon\epsilon_0 \frac{A}{d}$ with A being the channel area, d the thickness of the insulating layer and ϵ the dielectric constant of the insulating layer.
In a graphene based SGFET, the active material (graphene) is in direct contact with the electrolyte (Figure 2.10). An insulating layer between the graphene and the electrolyte is not necessary, because of the stability of graphene in a liquid environment and its large electrochemical potential window properties[219]. Values for the graphene/electrolyte interfacial capacitance up to $2\,\mu F/cm^2$ can be reached. This value is high compared to the interfacial capacitance of $0.3\,\mu F/cm^2$ of a silicon based SGFET [68] (see section 2.2).

To operate the transistor, a voltage V_{DS} is applied between the drain and the source contacts and a current flows through the graphene channel. The gate voltage is applied via the electrolytic solution in contact with graphene. The electrolyte (usually sodium-based PBS buffer solutions) is in contact with a reference electrode which applies the gate signal needed to modulate the transistor currents I_{DS} (Figure2.10a). A simplified version of the energy band diagram of the graphene/electrolyte interface explains the modulation of the conductivity of the graphene sheet when sweeping the gate bias(Figure 2.10b). The left part of the schematic shows the band structure of graphene around the K point in contact with the electrolyte. Figure 2.10b shows that by applying a voltage between the reference electrode and graphene, the Fermi level in graphene is shifted, consequently modulating the number of free carriers in graphene. The minimum of free carriers, and thus the minimum of conductivity, is reached when the valence and the conduction band meet at a point called the Dirac point; the gate bias potential at which the Fermi level reaches the Dirac point is V_{Dirac} or also called *charge neutrality point* (V_{CNP} or simply CNP). Depending on the position of the Fermi level with respect to the CNP, the current in the graphene channel will be dominated by holes or electrons.

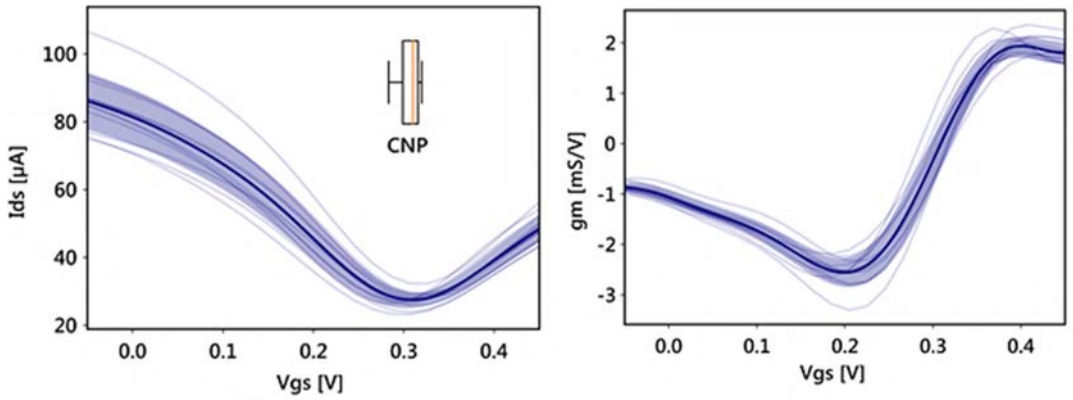

Figure 2.11: Drain source currents as a function of the applied gate voltage(left, $V_{DS} = 100$ mV) and transconductance (right) of a 16 transistors array characterized simultaneously in a PBS buffer solution (10 mM).

Increasing the applied V_{GS} results in a further increase in the number of the charge carriers, resulting in an increase of the current. On the right side of Figure 2.10, I_{DS} is plotted as a function of V_{GS}. The red and blue point represent the resulting current value for the applied V_{GS}. Graphene transistors are thus ambipolar devices, i.e. the transistor current can be carried by either holes or electron charge carriers. The electrochemical potential level of the Ag/AgCl reference electrode is fixed with respect to the vacuum level at $E_{VAC} = 4.7\,\text{eV}$. The work function of pristine graphene is $W_{gr} = 4.6\text{eV}$, very close to E_{VAC} of Ag/AgCl reference electrode [220, 221, 222]. Thus, for undoped graphene a $V_{CNP} = 0.15\text{V}$ is expected. In Figure 2.11 the average transfer curves of a gSGFETs array on a polyimide substrate is shown. The measured V_{CNP} (~ 0.3 V) indicates a p-doping doping in graphene arising from the substrate charge impurities [68]. From the transistor curves, the transconductance can be calculated:

$$g_m = \left.\frac{\partial I_{DS}}{\partial V_{GS}}\right|_{V_{DS}} \tag{2.24}$$

g_m describes the variation of I_{DS} caused by a small change in the gate voltage V_{GS}. The general equation to describe the current density by an applied electric field is [218]:

$$j = -en\mu \cdot E_{DS} \tag{2.25}$$

Here n is the charge carrier density, μ the charge carrier mobility and E_{DS} the applied electric field. The current I_{DS} between the drain and the source, obtained by applying a potential difference V_{DS} in a two dimensional electronic system such as

the graphene layer is given by [218]:

$$I_{DS} = \mu C_{int} \frac{W}{L} \Big(|V_{GS} - V_{CNP}| \cdot V_{DS} - \frac{1}{2} V_{DS}^2 \Big) \tag{2.26}$$

When $V_{DS} << V_{GS}$ the V_{DS}^2 term can be neglected yielding:

$$I_{DS} = \mu C_{int} \frac{W}{L} \Big(|V_{GS} - V_{CNP}| \cdot V_{DS} \Big) \tag{2.27}$$

where W and L are the width and the length of the graphene sheet. In eq.(2.26) the current is derived, given $j = -I_{DS}/W$ and $E_{DS} = V_{DS}/L$. Due to the band structure of graphene, the density of state (DOS) is assumed to be symmetric for holes and electrons. For a graphene SGFET, the charge carrier density n can be derived using the transistor characteristic by:

$$n = \frac{C_{int}}{e} |V_{GS} - V_{CNP}| \tag{2.28}$$

As described in the previous section (2.2), the capacitance C_{int} at the graphene/electrolyte interface depends also on V_{GS}.
From Figure 2.11 it can be observed that g_m slightly decreases for large values of V_{GS} (from -3 to -1 mS/V in the hole regime), which is not explained by eq. 2.27. The reason is the contact resistance R_C, originating from both, the access regions and the contact resistance of the graphene/metal interface. Near the current minimum, the resistance of the gated graphene channel R_{CH} is rather high and the contact resistance can be neglected. For larger gate voltages R_C becomes comparable or larger than R_{CH} and it reduces the transconductance. To obtain an equation that contains R_C and the charge carriers impurities present in the graphene n_0:

$$R_{CH} = \frac{V_{DS}}{I_{DS}} = \frac{L}{W \cdot n_{tot} e \mu} \tag{2.29}$$

where the total charge carrier density in graphene, n_{tot}, is given by:

$$n_{tot} = \sqrt{n_0^2 + \Big(\frac{C_{int}}{e} \Big(V_{GS} - V_{CNP} \Big) \Big)^2} \tag{2.30}$$

The contact resistance is thus summed to get the total resistance as:

$$R_{tot} = R_C + R_{Ch} = R_C + \frac{L}{W \cdot n_{tot} e \mu} \tag{2.31}$$

and using eq. (2.28) we get the new expression for I_{DS} :

$$I_{DS} = \frac{V_{DS}}{R_{tot}} = V_{DS}\Big(\frac{L}{W}\frac{1}{\sqrt{n_0^2 + n^2}}\frac{1}{e\mu} + R_C\Big)^{-1} \tag{2.32}$$

With this set of equations we can characterize the electrical properties of the graphene SGFETs fabricated in this work, starting from the basic transistor characteristics. Figure 2.11 shows typical I_{DS} and g_m values for the gSGFET on polyimide (PI) which was fabricated during the thesis work. The homogeneity of the CNP value (around 0.3V), shows that the graphene is slightly p-doped by the charges trapped in the substrate and from residuals of fabrication debris.

As already mentioned, the current through a graphene based SGFET can reach a minimum value, but the device cannot be switched completely off - in contrast to a silicon based SGFET. The reason for that is that graphene has no bandgap (see Section 2.1.1). For sensors applications the on/off ratio is not as relevant as for digital electronics applications; the transconductance (eq.(2.24)), which express the sensitivity of the transistor's drain source current to small changes in the gate potential, is indeed the most relevant parameter. High values of interfacial capacitance and mobility allow graphene SGFET to have a very high transconductance, and thus allows the realization of very sensitive devices. Compared to other SGFET technologies, graphene based SGFETs provide superior values of transconductance compared to other SGFETs [68]. Transconductance values of up to 4 mSV^{-1} (actually, this value corresponds to the transconductance normalized by the drain–source voltage) for a transistor of 20×10 μm^2 have been reported [223]. Moreover, such high transconductance allows to use drain–source bias voltages of graphene field-effect transistors in a narrow potential window below 100 mV. This feature is particularly important for neural interfaces, because:

- High applied voltages (above 1 V) can have a significant influence on neural activity
- Low bias voltages result in low power consumption, a critical issue for chronic applications where the devices require an external battery.

For the *in vivo* experiments described in this work, the drain–source voltage is usually fixed at 50 mV, leading to typical drain–source currents of 25 μA. The input power is thus around 1.25 μW for a single transistor. Given that the channel resistance is around $1k\Omega$, this results in a local heating power of 0.625 μW. The gate voltage was fixed at around 100 mV where the transconductance was found to be the highest

on the transistor curve. This gating voltage was found to be even closer to 0 V in a previous report [223, 70]. A low input power is of utmost importance, in terms of thermal dissipation and power consumption, to ensure the scalability of transistor arrays in which hundreds of recording transistors will be operating simultaneously. Apart from high transconductance values, which is linked to the signal sensitivity, the intrinsic noise of graphene SGFET has to be taken into consideration and minimized, in order to improve the signal-to-noise ratio of a sensor. In section 4.1 we introduce some basic concept and different sources of noise that hampers the gSGFET performances, which have been tackled as part of the thesis work.

3

Technology of graphene neural interfaces

This chapter provides a short overview on the micro-fabrication and operation of graphene-SGFETs arrays. Furthermore, different fabrication strategies to increase the signal-to-noise of the gSGFETs, as described in the next chapter, are presented together with their Raman spectrum and electrical characterisations.

Moreover, the design and fabrication steps to produce ultra-flexible graphene neural sensors for *in vivo* experiments (Chapter 5) are discussed together with their characterisation. The last part of this chapter introduces the two experimental setups used in this work for the device characterisation and for the electrical noise measurements; an overview of the data processing methodology is also presented.

3.1 Microfabrication of gSGFETs arrays

Graphene growth

Graphene was grown by chemical vapor deposition (CVD) on a copper foil[1] (size 4.5 cm x 7 cm). First the Cu foil was electropolished for 5 min in a solution (1 L of H_2O, 0.5 L of H_3PO_4, 0.5 L of ethanol, 0.1 L of isopropanol and 10 g of urea) at a constant current density of 62 mA/cm^2 and subsequently loaded into a horizontal quartz tube (length of 160 cm and diameter of 6 cm) heated by a three-zone oven (see Figure 3.1). A thermal annealing step was performed for 1 h at 1050 ^{o}C (under

[1] 25 μm thick Alfa Aesar coated

400 sccm Argon flow at 100 mbar pressure) to stabilize the temperature and remove any contaminants from the copper foil. Then, mass flow controllers filled the heated quartz tube with a gas mixture of 1000 sccm of Argon, 200 sccm of hydrogen and 2 sccm of methane, for the graphene growth phase (10 min, at 12 mbar pressure, Figure 3.1). After a cooling step of few hours, in which the sample is then quenched down to room temperature by removing the tube from the heating zone, the copper/graphene sample is extracted.

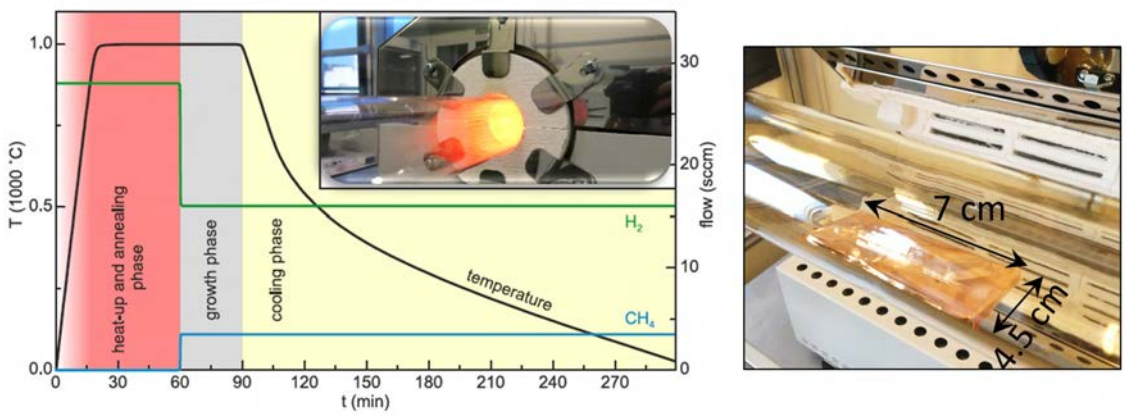

Figure 3.1: Growth of graphene by CVD. The process starts with a cleaning process of the copper foil to remove any contamination; it is followed by the actual growth of graphene with methane gas and ends with a cooling step. Inset picture shows the operating CVD-reactor during the growth process. Right: picture of the copper foil in the reactor quartz tube.

Right after the growth, the quality and uniformity of the graphene monolayer is assessed by scanning electron microscopy (SEM) and Raman spectroscopy (30 μm x 30 μm mapping). The grown CVD graphene layers usually exhibit a domain size between 10 μm and 20 μm, low defect density and high uniformity across the entire sample. The averaged full-width-half-maximum of the 2D Raman peaks of the used samples was found to be around 33 cm^{-1}, indicating a low percentage of second nucleation (Figure 3.2). Once the quality of the grown graphene is assessed by SEM and by Raman spectroscopy, the copper/graphene sample is ready for the transfer to any substrate.

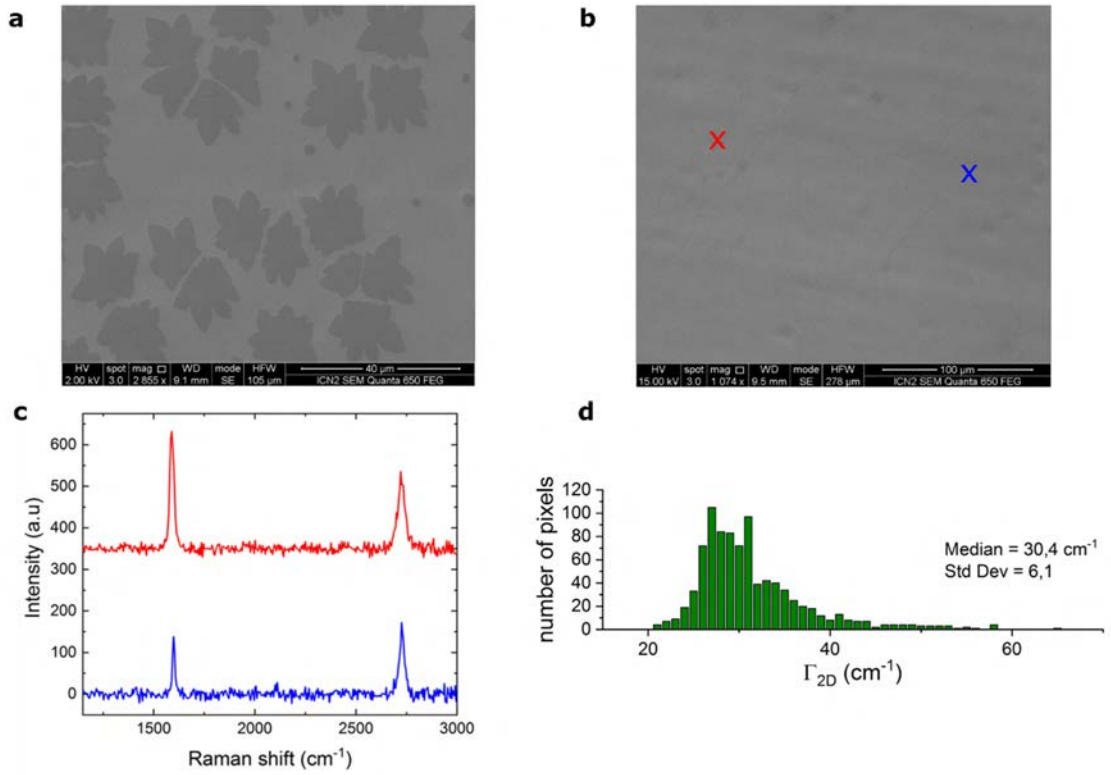

Figure 3.2: **a**. SEM picture of an open graphene layer after short growth time (2 min) showing domain sizes around 10 μm to 20 μm. **b**. SEM picture of a closed graphene layer after a full growth cycle (10 min). **c**. Typical Raman spectra for a region of single layer graphene (blue) and a region with second nucleation (red), crosses in **b** indicate positions. **d**. Histogram of the full-width half-maximum of the 2D Raman peak Γ_{2D} over an area of 30 μm x 30 μm in the center of the sample.

Transfer of graphene

To transfer the graphene film, poly(methyl methacrylate) (PMMA A4) was spun onto the graphene/Cu stack and dried at room temperature for 12 h. Afterwards, the backside graphene was removed by oxygen plasma and the sample was kept floating for at least 6 h in solution of $FeCl_3$/HCl to remove the copper. Subsequently, the sample was cleaned several times in deionized water, before being transferred onto the substrate. The wafer was then dried and thermally annealed in ultra-high vacuum (30 min at 40 ^{o}C, then gradually increased to 180 ^{o}C), before the PMMA was dissolved in acetone and isopropanol.

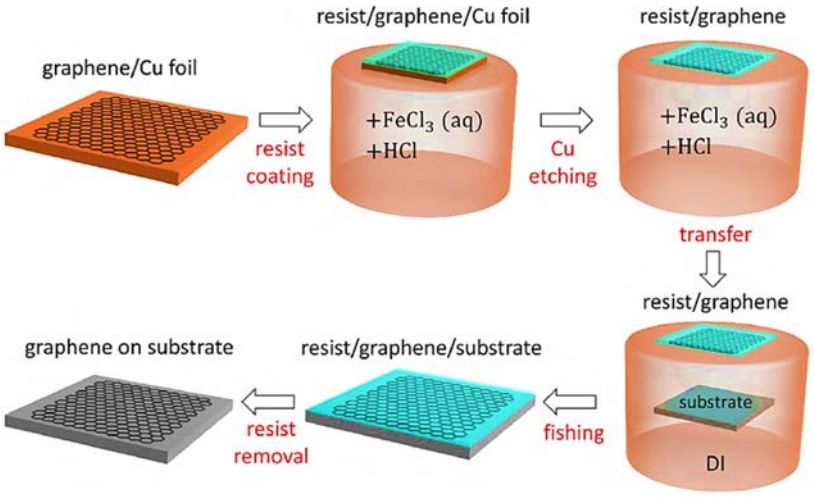

Figure 3.3: Schematic of the polymer-assisted, wet chemical etching transfer of graphene from copper foil to an arbitrary substrate. The transfer steps are: resist coating, Cu etching, transfer to DI water, fishing onto the final substrate and resist removal. Adapted from [224]

Fabrication process

In order to produce high-quality flexible devices of graphene-SGFETs for neural sensing, the electronic properties of test devices fabricated on rigid substrates were first assessed. In this section, a brief description of the different processing steps is given, starting from the bare substrate, until the electrical insulation of the device. The gSGFET were fabricated by contact photolithography on 4 inch Si/SiO2 wafers. Figure 3.4 shows the schematic microfabrication flow used in this work to produce the Device Under Test (DUT) arrays of gSGFETs. First, the wafer is cleaned with solvents by placing it in an ultrasonic acetone bath for 10 minutes, then rinsed in isopropyl alcohol (IPA) and dry blown using nitrogen. Afterwards, the rigid substrate is placed for 15 minutes in an oxygen-plasma (1.4 mbar, 200 W), to make the surface more hydrophilic. Subsequently, a photoresist[2] was spin coated, illuminated through a chromium mask and developed[3] with the contact metal layer structure. Then 20 nm of Ti and 200nm of Au are evaporated using an e-beam evaporator and patterned by means of lift-off, with ultrasonic vibration in an acetone bath (Figure 3.4 step (II)).

[2]negative photoresist AZ 5214E - MicroChemicals GmbH
[3]AZ 726MIF Developer - MicroChemicals GmbH

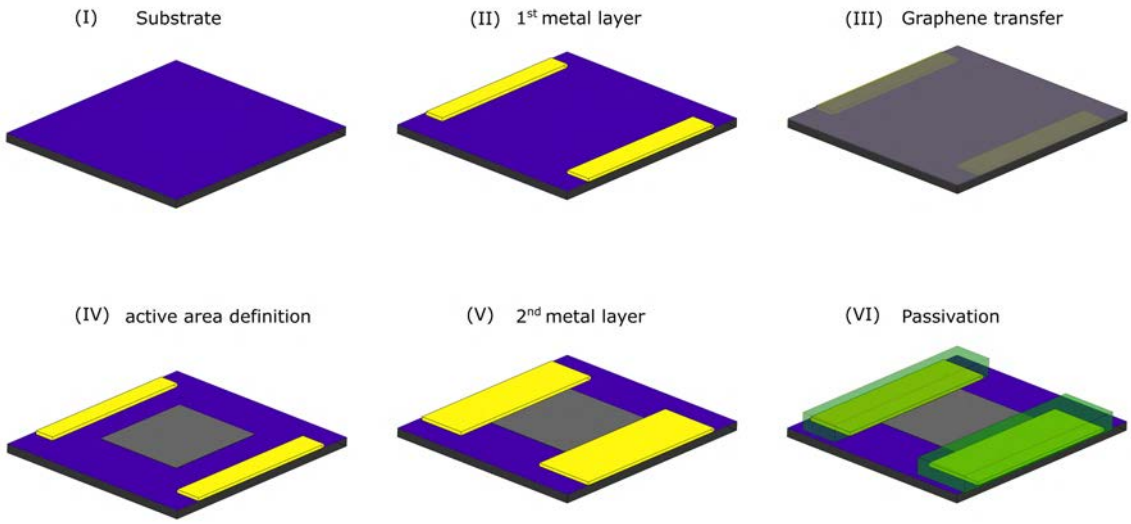

Figure 3.4: Fabrication steps for a graphene SGFET on rigid SiO_2 substrate. On top of the SiO_2 substrate (**I**) a first layer of metal contacts (Ti/Au, yellow) were deposited and defined by liftoff (**II**). Subsequently, CVD graphene is transferred (**III**) and structured by means of reactive ion etching (RIE) (**IV**). After definition, a second metal layer top-contacted the active graphene area (**V**). Finally, the graphene-SGFET was passivated with an insulating resist (green) (**VI**).

Then, CVD grown graphene was transferred on top of the wafer (see above), spin coated and patterned with a photoresist[4] in order to protect the active area of the transistors. Then, the graphene is etched by oxygen deep reactive-ion etching (DRIE for 1 min at 150 W, Figure 3.4 step (III-IV)). The photoresist is then removed in a heated acetone bath (40°C) for more than one hour and rinsed in IPA. Subsequently, photolitography is performed again in order to obtain the structure of the second metal contacts (20 nm Ni and 200 nm Au) by means of e-beam evaporation and lift-off (Figure 3.4 step (V)).
While the first metal contacts are not in contact with the graphene channel, the second metal layer contacts the graphene from above. Two masks are used for the metal leads to avoid strain in the graphene transferred on the pre-patterned wafer (particularly at the source-drain contact step) and to have a top contact type of configuration for the gSGFETs. In order to avoid damage of the graphene active area, the lift-off in step (V) was performed by softening the photoresist in an acetone bath for more than one hour and by flushing the structure with acetone using a syringe (instead of using a ultrasonic bath like in step (II)), before rinsing with IPA.
To note, in this step (from step IV to step V in Figure 3.4) the contact improvement

[4]HiPR6512 photoresist, FujiFilm

method using UVO was applied (results shown in section 4.3); before the metal evaporation on top of the pre-patterned protective photoresist, the wafer was exposed to UV-ozone[5] [225] for the removal of residuals at the graphene/metal interface.
At the end of the process an insulating and chemically stable photoepoxy resin (SU8[6]) covers all the sample, with the exception of the graphene active area and the bond pads. SU8 is widely used for manufacturing of micromechanical structures and components in the area of micro-system technologies (MEMS) due to its relatively simple processing and its outstanding material properties[226]. To deposit and lithographically pattern the passivation layer, SU8 is spin coated (30 s at 3000 rpm) and a first pre-exposure bake (PEB) is done where the sample is baked 5 min at 65°C, followed by 15 min at 95°C on the hotplate. It is important to increase slowly the hotplate temperature (5 °C/min), because the SU8 easily cracks or produces bubbles, when an accelerate cross-linkage of the epoxy resign occurs.

At the end an hard bake step of 2h in nitrogen atmosphere is performed to smooth the surface and allow the cracks in the SU8 to melt and merge. Thus, at this point in the process the graphene SGFETs are all insulated, apart from the active area of the transistor, which stays exposed to the environment (sensing area, see Figure 3.4 step (V)). More detailed information about the fabrication parameter can be found in the Appendix A.1.

Double transferred graphene SGFETs

Another type of transistor configuration we explored during this work is the double-transferred (DT) graphene configuration. In the following I mention only the changes needed to the process flow for fabricating SL gSGFETs. As the name says, the device have been fabricated by doing a double transfer of the CVD grown graphene at step (III), shown in Figure 3.4. After transferring the first layer of graphene and removing the PMMA (as described above), a second graphene/PMMA stack is carefully overlapped to the first layer. A thermal ramp is performed first at 40°C for 2h then to 180°C in an annealing oven in order for the graphene/PMMA stack to release tension and conform to the substrate. The wafer is then cleaned with organic solvents (2h in Acetone, 30 min in IPA) and blow dry with nitrogen. Then, the graphene in the channel region is protected by the photoresist and exposed for a longer period of time to oxygen RIE (300W, 4min).

[5]Jelight Model 42
[6]SU8-2005 MicroChem

Encapsulated hBN-graphene-hBN SGFETs

For the case of hBN encapsulation, CVD-grown multilayer hBN has been transferred pre and post graphene transfer, to form a top and bottom encapsulation. After transferring graphene, hBN is transferred on top of the multilayer stack. Thorough surface cleaning with organic solvents and thermal treatments have been applied to remove organic residues from the multiple transfers. The RIE exposure to define the channel of the FET, was prolonged to 7min at 300W to ensure properly definition of the hBN-graphene-hBN layers.

Hydrophobic coating with HMDS

For the case of the hydrophobic coating, the silicon wafers (with 285 nm thermal oxide layer) have been pre-treated in oxygen plasma to clean the surface and subsequently placed on a hot-plate (100^{o}C) in an HMDS saturated atmosphere for several minutes. After this treatment, the graphene layer has been immediately transferred onto the coated substrate, in order to minimize the exposure of the coated surface to the environment, considering the high volatility of the surface functionalization.

Mask and Design

In order to study the dependence of the gSGFETs with geometrical factors in terms of conductivity and electrical noise, DUTs containing arrays of transistors with different shapes were fabricated. Figure 3.5a shows the design of the fabricated gSGFET-DUT, containing 60 transistors, pair-wise connected to a common drain. The DUT contains different squared transistors (green box, 100x100 μm; 60x60 μm; 10x10 μm; 5x5 μm) and transistors with fixed width (W=40μm) and different length. Each side of the mask contains two types of transistor with the same length (orange box). Pictures of the fabricated gSGFET are shown in Figure 3.5b-c. The different lengths allow to not only find the best WxL ratio for maximizing the sensor SNR , but also enables us to extract the sheet and contact resistance using the transfer length method (see section 3.3).

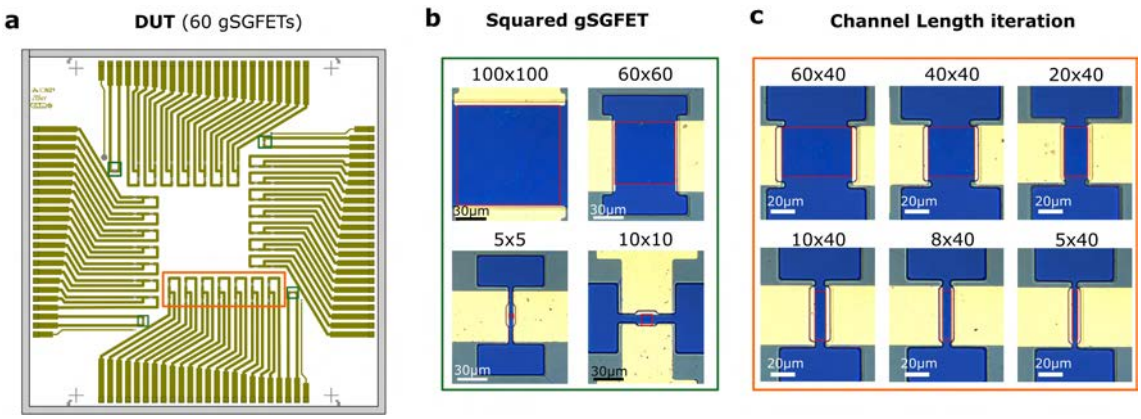

Figure 3.5: DUT design and pictures of gSGFETs with different aspect ratios (Length x Width, units in μm). (**a**), DUT design containing arrays of gSGFETs with different squared active areas (**b**) and various length iterations (**c**).

3.2 Fabrication and design of flexible neural probes

The fabrication of the flexible epi-cortical and depth probes is similar to the process described above, with the exception of having an additional polyimide layer deposited initially on top of the sacrificial SiO_2 substrate, to act as the final ultra-thin flexible substrate. To avoid repetition of previously explained steps, only the additional steps will be discussed in this section. The reader is referred to the Appendix A.1.2 for the full fabrication procedure and parameters.

3.2.1 Epi-cortical and flexible depth neural probes

The polyimide precursor (polyamic acid) is dissolved in an N-methyl-2-pyrrolidone (NMP) base solvent that have to be spin-coated on a rigid substrate and then thermally cured[7]. In order to obtain a clean rigid substrate onto which the PI 2611 can be spin coated, the rigid substrate has to be cleaned with solvents. Therefore, it is placed in acetone in an ultrasonic bath for 10 minutes, then rinsed in IPA and dry blown using nitrogen. Afterwards, the rigid substrate is placed for 15 minutes in an oxygen-plasma (1.4 mbar, 200 W), to make it hydrophilic. Then it is heated at 100°C during 5 min on a hotplate, in order to remove water molecules. After that, the wafer is cooled down by blowing nitrogen and the polyimide precursor is spin coated (three steps: at 4000 rpm for 30 s and at 6000 rpm for 60 s, followed by 2 s at

[7]PI 2611,HD MicroSystems

9000 rpm[8]). The rotation speed of the spinner is chosen in order to get a polyimide layer of 10 μm thickness.
Finally, the polyimide has to be thermally cured in order to remove the NMP solvent: the wafer is placed on a hotplate in a nitrogen atmosphere, and the temperature is increased using a temperature ramp of (2.5°C/min) up to 200°C. After 30 minutes at 200°C, the temperature is further increased to 350°C for 1 hour. Finally, the sample is cooled down on the hotplate until room temperature is reached.

As described above, the metal contacts are then formed by e-beam evaporation, then patterned by means of photolithography and lift off. The first metal deposition is performed before the graphene transfer (Ti/Au, 20 nm/200 nm), and then second layer metal deposition as top contact (Ni/Au, 20 nm/200 nm) after the definition of the graphene channel by deep-RIE Figure 3.6 steps (III-VI)). Thick metal tr are important in order to decrease the resistance of the metal track; if too resistive, the metal tracks can have a negative impact on the performance of the gSGFETs.
All metal contacts and leads are then covered by the chemically stable and insulating SU8 resin layer(Figure 3.6 steps (VII)). To ensure complete coverage of the gold contacts, a small region of the graphene in the channel is also covered by the insulating SU8 resin to reduce potential leakage currents through any exposed metals. The graphene close to the metal contact covered by the SU8 is commonly called *access region* which, in the transistors on the neural probes produced during this work, has a length of $3\mu m$. In order to release the finalised gSGFETs-neural probes, a step is needed to cut the PI in the shape of the probe. Therefore the wafer is covered by a thick ($\approx 16\mu m$) protective photoresist[9] and patterned in such a way that the probe structures border remains uncovered.

[8]The last step is performed to avoid the formation of edge beads on the wafer
[9]Photoresist AZ 9260 - MicroChemicals GmbH

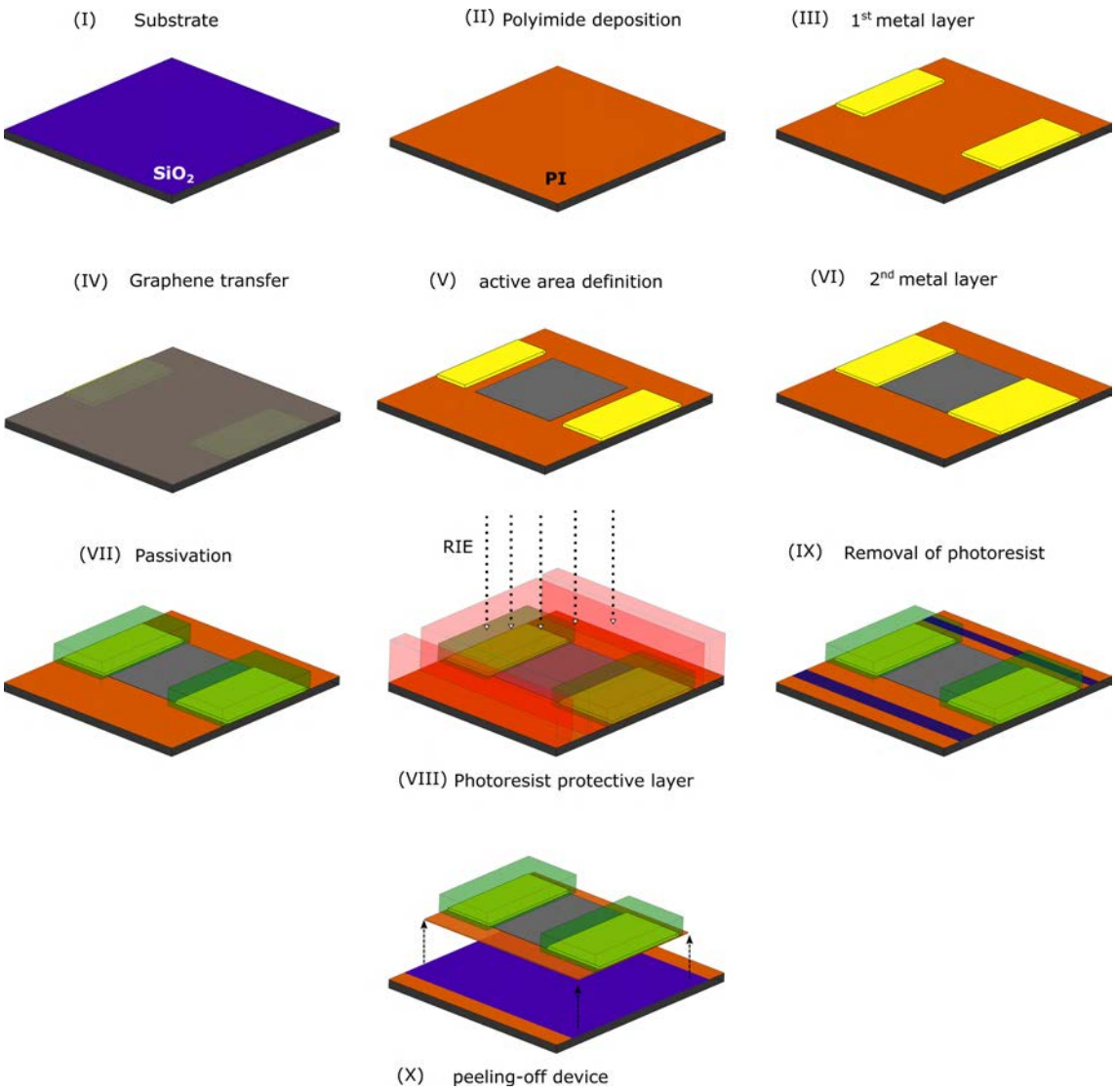

Figure 3.6: Fabrication flow of flexible graphene neural probes. On top of the SiO_2 substrate (**I**), a $\approx 10\mu$m PI layer is spin coated and cured (**II**). Then, a first layer of metal contacts (Ti/Au, yellow) is deposited and defined by liftoff, followed by the transfer and definition of graphene (active material) (**III-V**). After the second metal layer deposition and passivation of the device (**VI-VII**), a thick protective photoresist is spin-coated and patterned on top of the device structure (**VIII**). After RIE, the photoresist is removed and the neural probes can be easily peeled from the SiO_2 substrate (**IX-X**).

Then, the wafer is placed in a DRIE for more than $\approx$ 40 min until the SiO_2 substrate is clearly observable at the probes edges. Subsequently, the photoresist is shortly dissolved in acetone for 10min, and in IPA for more than 1h, to ensure its complete removal and to avoid damaging the cured SU8 passivation layer. Finally, the PI-based neural probes with all the top stacked structures fabricated are released

one by one from the supporting SiO_2 substrate, by carefully peeling them off (Figure 3.6 steps (VIII-X)).

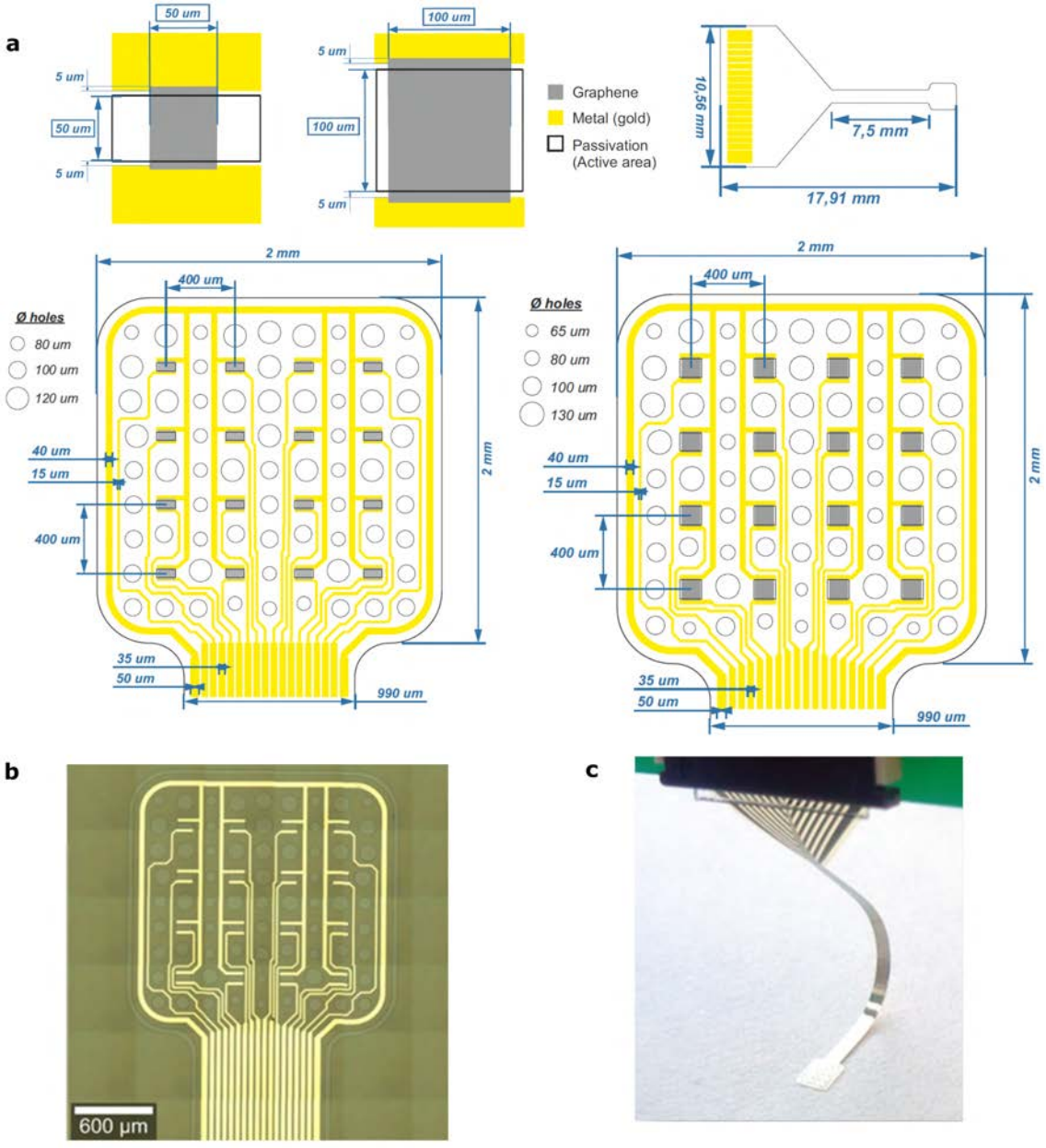

Figure 3.7: a. Design of the epi-cortical flexible graphene neural probes, showing the two micro-transistor sizes (LxW: 50x100 μm^2 and 100x100 μm^2), the dimensions of the probe and of the gSGFET array. **b**. Optical microscope images of the active area of a 4×4 gSGFET array. **c**. Photograph of the neural probe after peeling off from the wafer and being introduced into a zero insertion force connector (ZIF).

Figure 3.7 shows the design of the epi-cortical neural probe used for microelectrocorticography (μECoG) in this thesis work. The device consist of an array of 4x4

transistors equally spaced at a distance of 400 μm. Probes with transistors of two different active area have been fabricated on the same wafer: one with large sensors (LxW: 100x1000μm^2) and one with smaller sensors (LxW: 50x100μm^2), intended for different resolutions of cortical neural activity.
These devices were fabricated using the above mentioned fabrication processes, and are intended for pre-clinical *in vivo* μECoG in rats and mice. The holes in the probe facilitate the positioning and adherence of the gSGFETs array to the brain tissue.
Figure 3.8 shows a prototype of intra-cortical neural probe. A serpentine-like, common drain metal track, connects all gSGFETs (LxW: 30x80 μm^2) on the linear array. The shank is 1.3mm in length and has been designed to sample and record through the cortical laminea of the rodent's brain cortex.

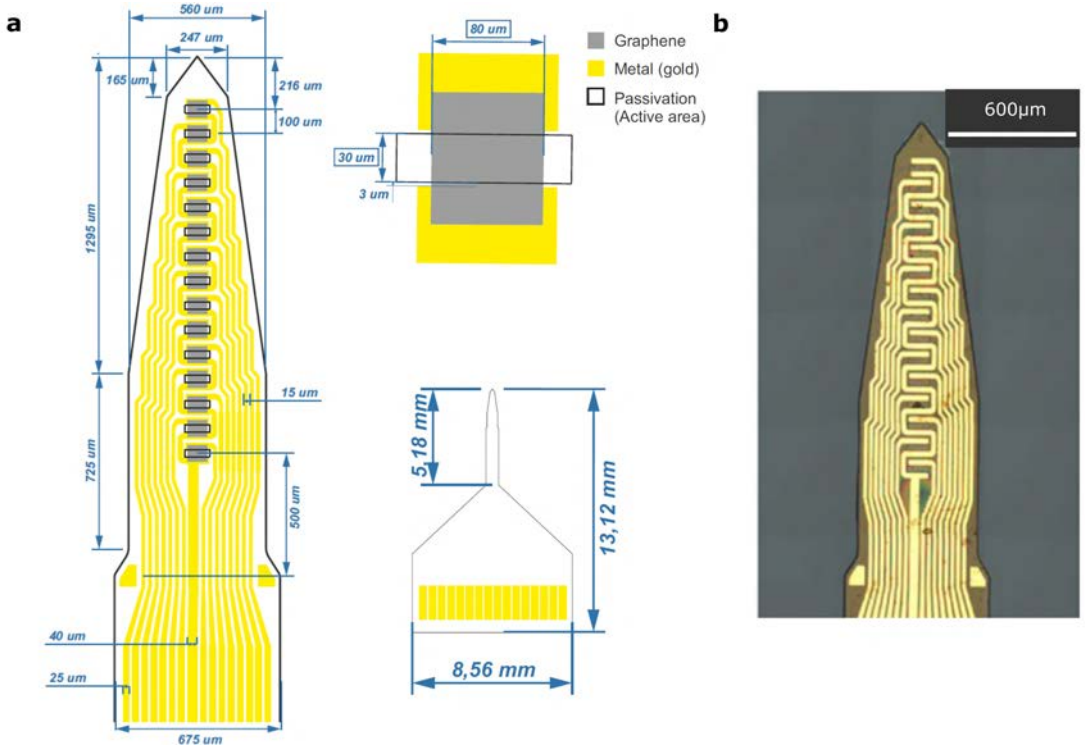

Figure 3.8: a. Design scheme of an intra-cortical flexible neural probe (v3.0), showing the micro-transistor size (LxW: 80x30μm), with all the relevant dimensions of the probe and gSGFET linear array. **b**. Optical microscope images of the intra-cortical neural probe showing the 15-channel gSGFET linear array.

Although the probe is very thin, the shanks width of this intra-cortical prototype is relatively large and could lead to significant brain damage during insertion. A limiting factor when shrinking the probe width is the width and spacing of the metal tracks that contact the graphene transistors. In the case of passive electrodes the width of the metal track is not normally an issue, in the case of the active gSGFETs

the situation is very different: if the metal tracks are too narrow, the additional series resistance introduced by the metal tracks can potentially lower the performance of the sensor. Therefore, to shrink the shank width to values comparable to those of the state of the art intra-cortical and depth technologies for mice studies (<200μm), a two layer metal track, connected via-holes, was developed and successfully implemented.

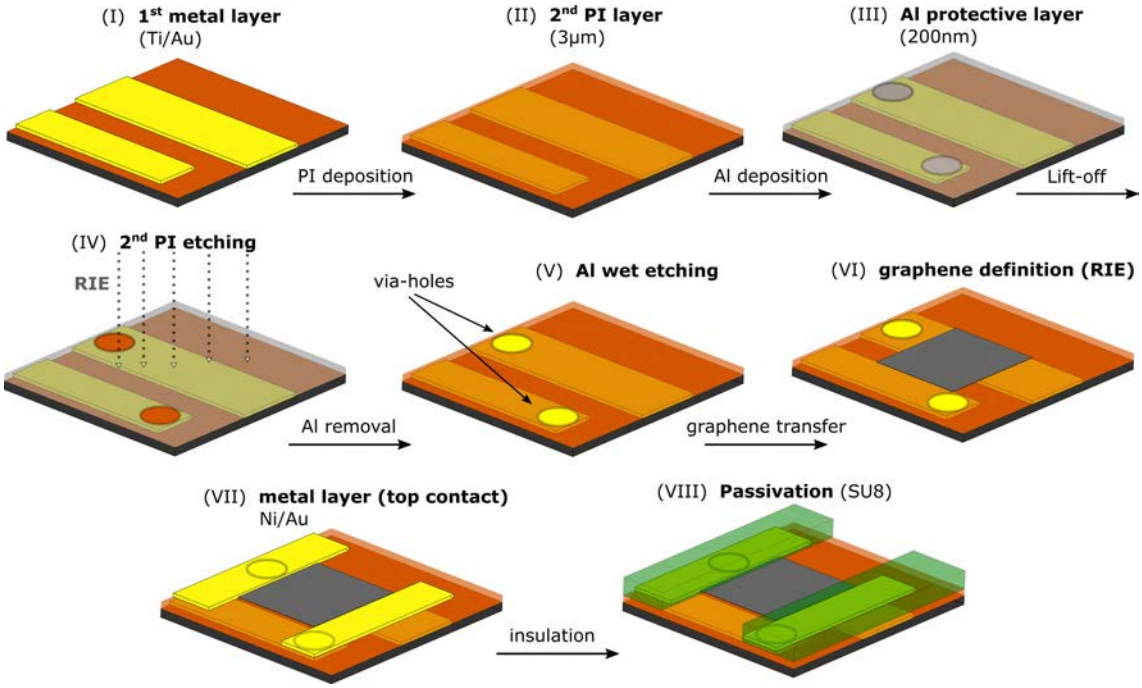

Figure 3.9: Fabrication flow of the gDNP (v4.0), illustrating how the via-hole enables creating a two-layer metal stacking, separated by a PI insulating layer. A second layer of PI is spin-coated on top of the first metal layer (**I-II**). An aluminum mask is used to form the via-holes, each across the 2nd PI layer (**III-IV**). Then the Al layer is wet etched and graphene is transferred and defined by oxygen-RIE (**V-VI**). After deposition of the second metal layer, the via-hole interconnects the two metal layers with the source and the drain of the transistor (**VII**). Finally the device is passivated, cut and peeled off from the wafer.

Thus, additional steps had to be added to the fabrication flow presented in Figure 3.6. Figure 3.9 shows schematically the additional steps to fabricate gDNPs (v4.0). After the formation of the first layer of metal tracks (Ti/Au, 20/200 nm), a thin second layer ($\approx 3\mu$m) of PI is spin-coated and cured on the wafer (Figure 3.9 steps I-II). To pattern the via-holes, we followed the AZ5214 image reversal protocol from previous steps, using a clear field mask with opaque circles only, e-beam evaporated 200 nm aluminum and proceed with its lift off in acetone (Figure 3.9(III-IV)). Subsequently the wafer is placed in the RIE (mixuture of Ar/O_2-RIE, power 1200W, 10min) and the 2nd PI layer is etched only in the exposed Al-openings

(Figure 3.9(IV)). Then, the aluminum is chemically removed using a NI555 stripper (Microchemicals GmbH) at 60 ºC for 1 hour, followed by a rinse in isopropyl alcohol for 30s, ethanol for another 30s and finally blew them dry with nitrogen (step (V)). As described above, graphene is then transferred and the active area of the gSGFET is defined by a short oxygen-RIE (1 min, 150 W). Subsequently, the top metal layer (Ni/Au, 20/200nm) is deposited to form the drain and source of the graphene channel, overlapping at the same time the via-holes. Once the contact between the two metal layers are achieved, the device are passivated with the SU8 resin (step (VIII)), protected with AZ 9260, cut by means of RIE (> 40min exposure) and peeled off from the wafer, as described earlier.

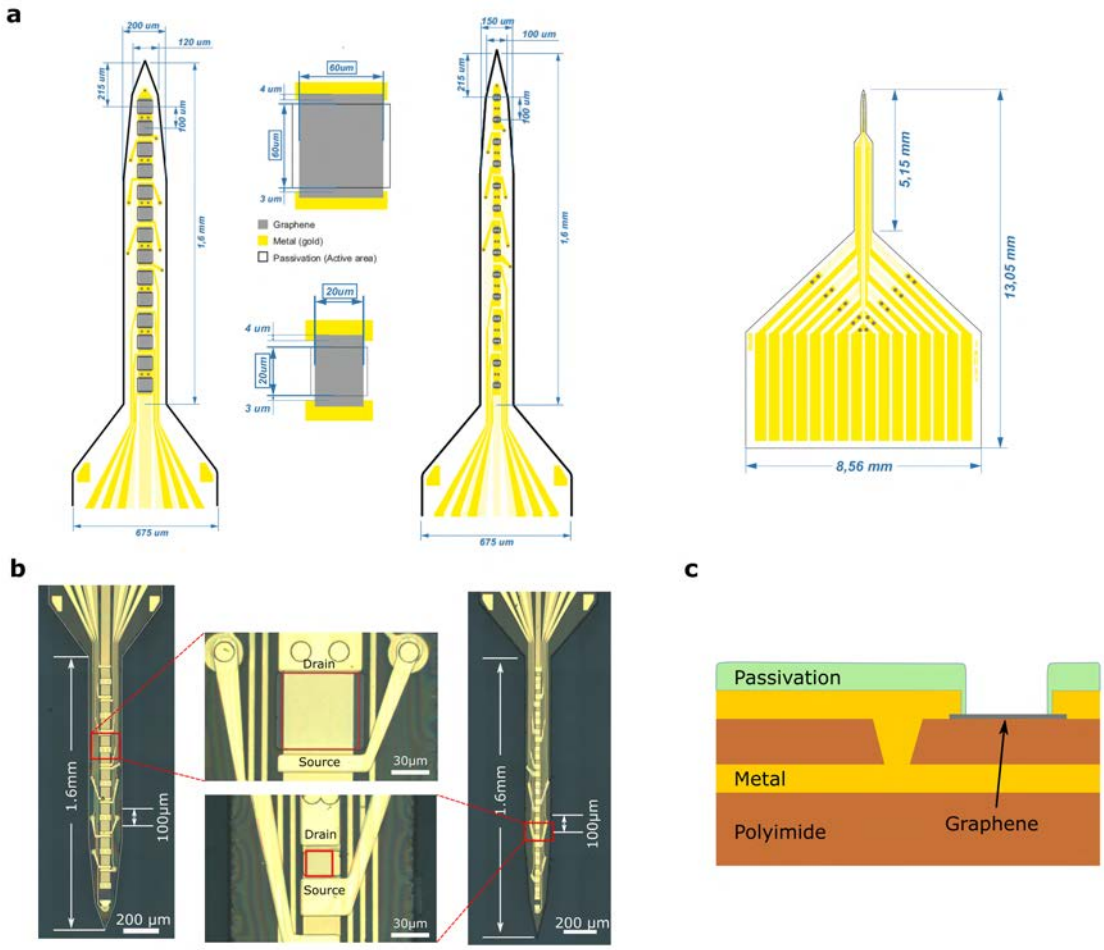

Figure 3.10: a. Design of the new version of of intra-cortical flexible graphene neural probes (gDNP, v4.0) with a narrow width of 200μm and 150μm, for the gSGFETs with size 60x60μm^2 and 20x20μm^2 respectively. **b**. Optical microscope images of the two probes type, with 14 gSGFETs linearly distributed (pitch 100μm) along the 1.6mm shank. in the middle, the magnified images of each gSGFETs type. **c**. Schematic of a gSGFET cross section, showing the via-holes in the second PI layer of the probe interconnecting the metal leads of the underneath layer.

Figure 3.10 shows the design of the flexible intra-cortical probes (gDNP, v4.0) fabricated using the metal interconnection strategy described above (Figure 3.9) As it can be observed, there is a significant reduction of the shank width (200μm and 150μm) compared to the first produced prototype (gDNP_v3.0, Figure 3.8).
Two design of gDNP (v4.0) have been fabricated, one with a larger sensing area (60x60 μm^2) and one with smaller one (20x20 μm^2), with the same shank length (1.6 mm) in order to reach also hippocampal structures in mice brain (see section 5.2). Figure 3.10b illustrates the optical micrographs of the two gDNP with the magnification of one transistor on the shank (red squares). The via holes (small metal circles) are clearly visible and interconnect the common drain track (embedded in the PI substrate, underneath the graphene channel) as well as the source tracks with the metal contacting the graphene from top. Figure 3.10c show a schematic of the cross section of a gSGFET, illustrating how the via holes enable the interconnection of metal tracks on different layers.

3.3 Electrical characterisation

This section describes the assessment of the electrical performance of the fabricated DUTs on rigid substrate as well as the fabricated flexible neural probes in saline solution. The measurements were carried out in a 100 mM phosphate buffer saline (PBS) solution, using a Ag/AgCl electrode as reference electrode (gate of the gSGFET).

3.3.1 Characterization setup

To interface the gSGFETs with suitable electronics capable of providing the desired bias point and to measure the current, a customized recording system was used during this thesis work.

The custom electronics setup (Figure 3.11) provides for the current-to-voltage conversion and for the independent bias control of each channel (up to 16 channels). It also splits the converted signals into DC (frequency <0.1 HZ) and AC (0.1 Hz < frequency < 5 kHz) components. To perform the devices characterizations, both DC and AC signals were managed by the data acquisition system[10]. Figure 3.11 shows a schematics of the electronics used, illustrating the different components; the signal is to be transformed first into voltage and then filtered. The DC-components are used

[10]National Instruments USB- 6353

to measure the transfer curves and the AC signal is used to characterise the power spectral density (PSD) as well as to obtain the transconductance spectroscopy ($g_m$vs frequency). The latter was obtained by applying a sinusoidal signal in the reference gate electrode. This signal contains several harmonics in the frequency range of study. Then, the AC acquired signal was demodulated to obtain the transconductance for each evaluated frequency.

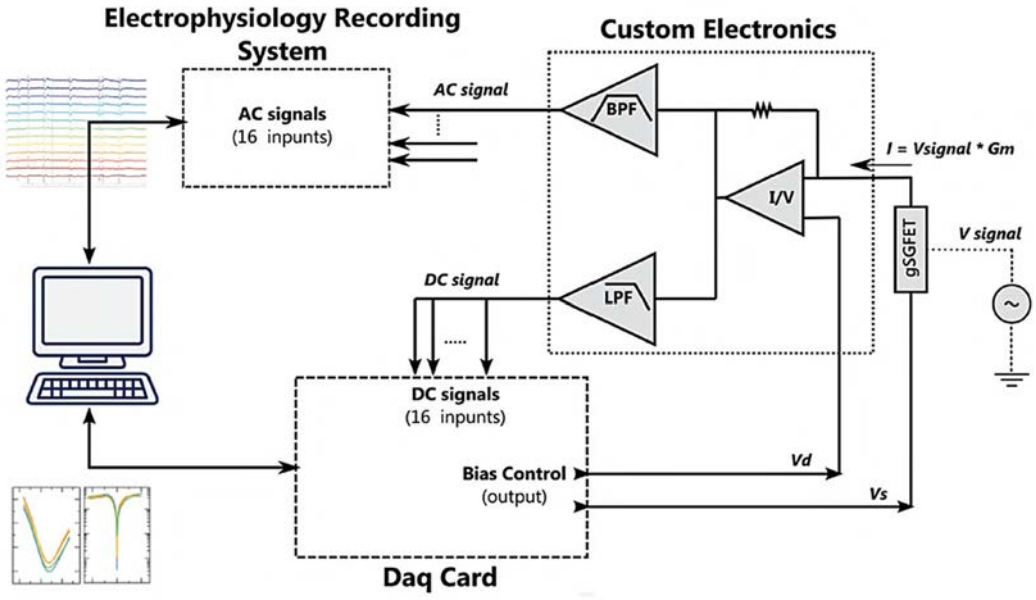

Figure 3.11: Schematic of the custom characterization setup used to characterise arrays of gSGFETs and to interface commercial neural recording systems. The custom electonics converts the signal current into voltage (I/V), then splits it in two frequency bands with a low pass filter (LPF) and a band pass filter (BPF), before the acquisition via the DAQ-card (or via the electrophysiology recording system during *in vivo* experiments). Adapted from [70]

At each bias point (V_{GS}), the stabilisation of the current was ensured by acquiring only after the time derivative of 1 s of averaged current was below $5 \cdot 10^{-7} As^{-1}$. This setup also enables us to measure the leakage current (I_{GS}), which is measured for the whole array and corresponds to the sum of the individual leakage currents of all transistors in the array (range on nA). For in vivo recordings the AC signals can be directly acquired by a commercial electrophysiological recording system while the DC signals and bias control were managed by a data acquisition system (DAQ-card).

3.3.2 DUTs characterisation

Measurements of the I_{DS} currents of the graphene transistors were performed in common gate mode with a fixed drain–source voltage (V_{DS} = 50 mV), varying the gate–source voltage (V_{GS}), versus a Ag/AgCl reference electrode in 0.01 M PBS solution. To characterise the DUTs, a custom wedge probe consisting of 24 tips (separated by 300μm) was used to contact the pads of the gSGFETs array and apply source and drain biases. A PDMS well was designed to fit on top of each DUT and to contain the electrolyte during the characterisation. An Ag/AgCl reference electrode was immersed in the well during the simultaneous characterisation (Figure 3.12a). Moreover the characterisation setup has been placed in a Faraday cage to reduce the pick-up of environmental noise (pick-up noise) during the characterization.

Transfer length method - gSGFET

The different transistor length on each DUT enables to obtain the sheet resistivity of graphene at different V_{GS} polarisation potentials, via the transfer length method (TLM) . The contact resistance (R_C) and the sheet resistance (R_{sh}) values shown in section 4.3 have been extracted by applying the TLM to different devices of 2.5 μm, 5 μm, 8 μm, 10 μm, 20 μm and 40 μm channel length (L) and 40 μm channel width (W) (Figure 3.12b-c). For each length, the resistance value has been extracted from the mean value of several measurements and fit with a linear regression model to extract the values for R_C and R_{sh}. Figure 3.12d shows the average transfer curves of gSGFET with different lengths on a DUTs (I_{DS} vs (V_{GS}-CNP)). The corresponding resistance at V_{GS} = 0.1V gate voltage bias is shown in Figure 3.12e, where the slope of the linear fit correspond to R_{sh}/W, its value at L=0 to $2R_C$ and the x-axis crossing to the transfer length $-2L_T$.

Figure 3.12f displays the corresponding total resistance for each gSGFET together with R_C extracted by the TLM method. It is clear that for very short devices R_C becomes a dominant contribution. To further improve the accuracy of this approach, outlier resistance values which strongly deviate from the median of each transistor type (outside the 25$^{\text{th}}$ and 75$^{\text{th}}$ percentile) were not used in the analysis.

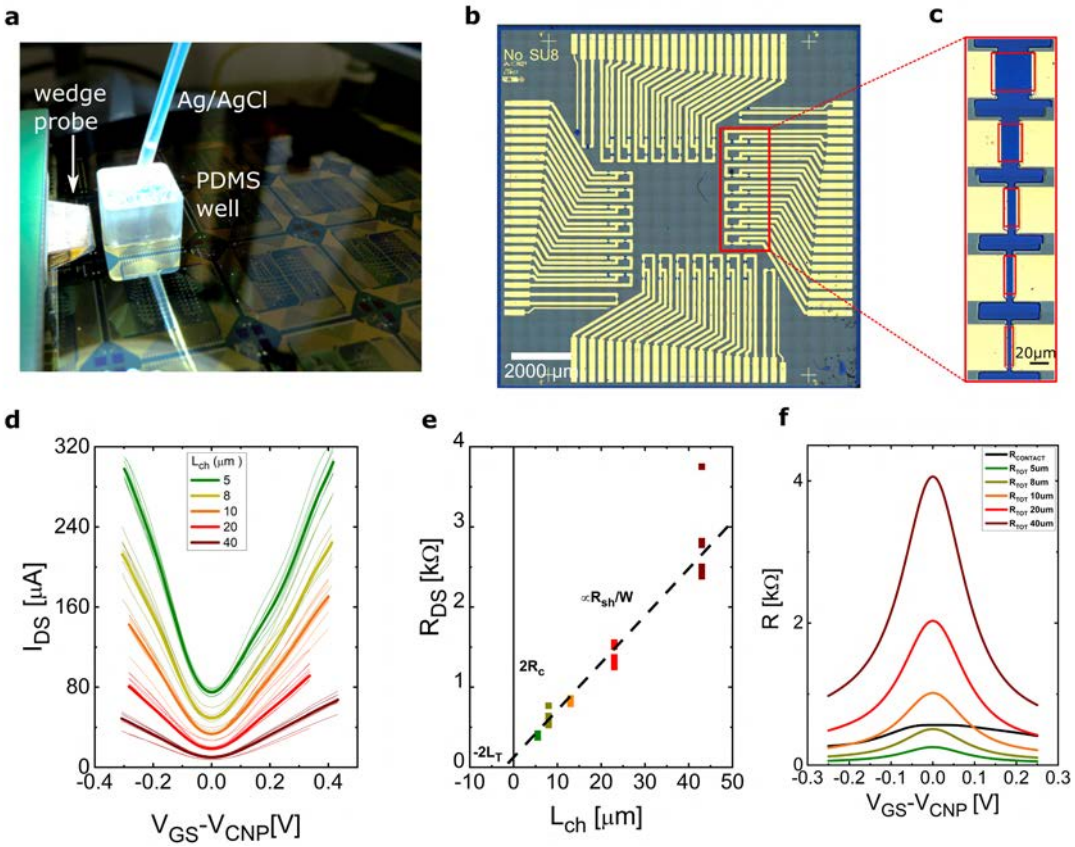

Figure 3.12: a. Picture of the simultaneous characterisation of the transistor array on a DUT. A PDMS well containing the electrolyte (PBS) is placed on top of the DUT. An Ag/AgCl reference electrode is immersed in the electrolyte applying the gate voltage. A wedge probe with 24 tips is lowered onto the DUTs with a micro-positioner. **b**. Micrograph of a fabricated DUTs, containing arrays of gSGFETs with different lengths (**c**). **d**. Average I_{DS} characteristics of gSGFETs with different L. **f**. The corresponding resistance is plotted together with the contact resistance R_C, assessed via TLM-method. The linear fit of the resistance values at $V_{GS} = -0.1$V enables to assess the values of R_C and R_{sh} (**e**).

3.3.3 Double transferred graphene SGFETs

The formation of double layer graphene by means of a double transfer (DT) using two single graphene layers grown by a chemical vapor deposition method was structurally and optically characterised by AFM and Raman spectroscopy, before doing the electrical characterisation. In Figure 3.13a-c we show two indicative Raman maps of single transferred CVD graphene and double transferred CVD graphene after removal from PMMA with organic solvents and thermal annealing.
The average Raman spectra are plotted on top of each other in Figure 3.13a for SL-gr (red), and DT-gr (light blue, blue).

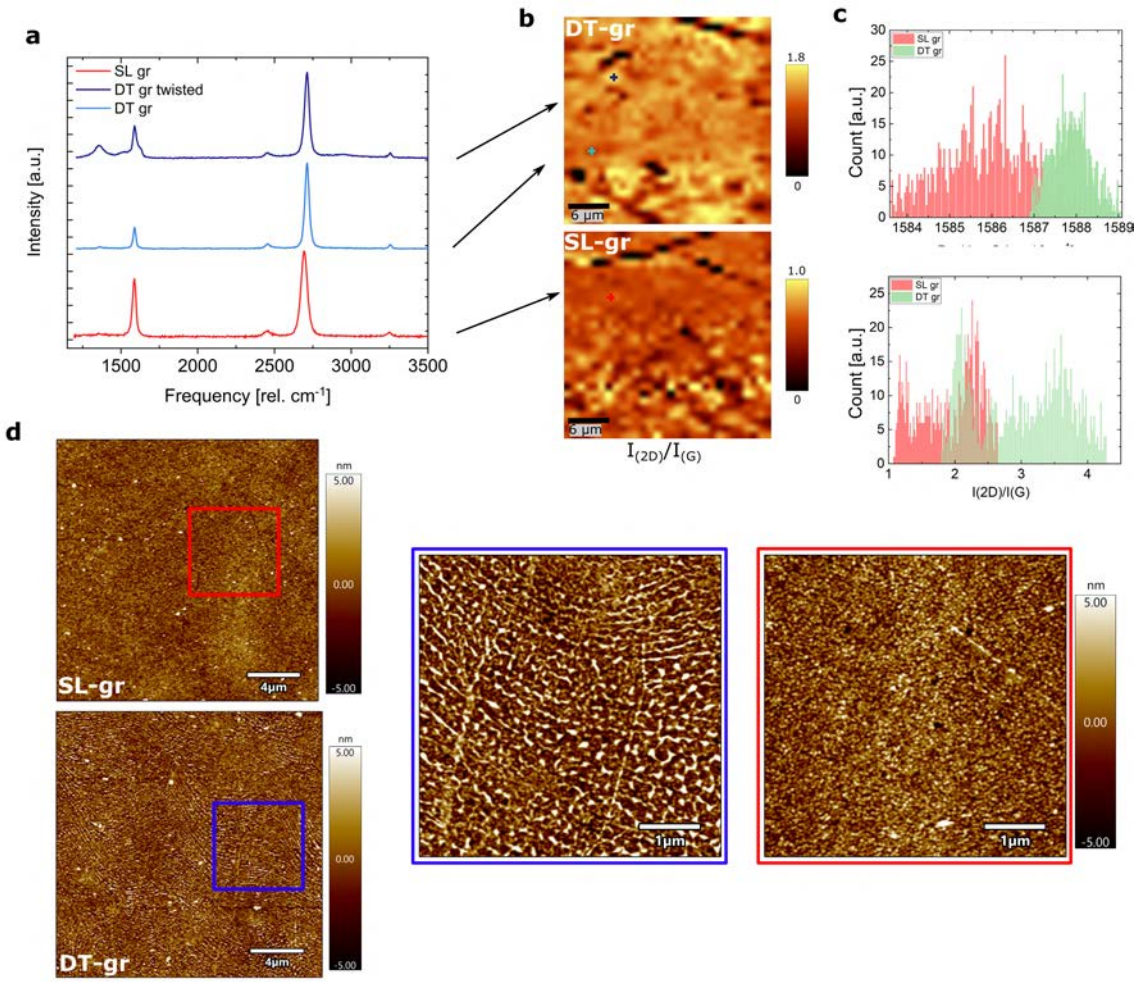

Figure 3.13: a-c, Raman maps of single layer graphene (SL-gr) and double transferred graphene (DT-gr). **a**. average Raman spectra for SL-gr (red) and DT-gr (light blue, blue), extracted from the mapped area shown in (**b**). The colored maps clearly indicate an increase in the intensity ratios of the 2D/G band for DT-gr. **c**. Histograms of the 2D/G intensity ratios and G-band position for SL-gr and DT-gr. **d**. Surface roughness of the SL-gr and DT-gr layers measured by AFM. Lower root-mean-square value in SL-gr of 1.55 nm (red box) are observed compared to the more "wrinkly" DT-gr surface with rms values of 2.25nm (blue box).

The red spectrum is characteristic of CVD single layer graphene discussed in section 2.1.3. When a second CVD SLG is transferred, the characteristic Raman spectrum is shown in light blue. The average spectrum of DT-gr shows an increase of the 2D band intensity, as expected from the literature and in clear contrast to exfoliated BLG [227, 228]. As shown in the I2D/IG Raman maps and the corresponding histograms (Figure 3.13b-c), most of the scanned area present a I2D/IG larger than SLG. This result indicates that the electronic coupling between two sequentially transferred SLG sheets is not perfect. This result is also supported by

the increase of the G band frequency from SLG to DT-gr, presented in the histogram in Figure 3.13c. If the electronic coupling between layers was strong like in exfoliated BLG, the G band center frequency should decrease when moving from monolayer to bilayer graphene[229]; The observed G-band position in our DT-gr indicates a predominant strain effect between adjacent layers. Moreover, we can appreciate in some regions of the scanned area, that the Raman spectrum presents defect-related peaks: D, D' and D+G. From this observation we can conclude that the electronic coupling between layers in certain regions is strong; both graphene layers sub-lattices present a rotational angle, which generates a Moiré pattern supercell. This give rise to double-resonant processes, leading to the appearance of extra Raman peaks, even in absence of structural defects [230].
The roughness of the SL-gr and DT-gr are assessed by AFM measurements. DT-gr presents more wrinkles and a higher root-mean-squared value of roughness (2.25 nm) compared to the more flat SL-gr (rms: 1.55 nm) (Figure 3.13d). The wrinkles are also observed in the Raman maps (Figure 3.13b) suggesting that the DT-gr can be considered as an amorphous irregular bilayer graphene with regions having mixed electrical properties. Yet, the average electrical properties in the DT-gr micro-shaped transistor channel do keep similar behaviors as SL-gr.
In the following, the transport characteristics of DT-graphene SGFETs are compared with those of single layer graphene SGFETs, showing a very similar behavior. Figure 3.14a shows the transfer curves of SL- an DT-SGFETs (WxL: 40 μm x 20 μm) measured by applying a V_{DS} of 20mV. The transconductance in the valence band (V_{GS}<CNP) as well as in the conduction band (V_{GS}>CNP) are very similar for both type of devices (Figure 3.14b). Yet, there is a shift of the CNP towards more negative values for DT-gSGFETs (CNP at 0.1V), indicating a different doping of the graphene layer, likely arising from the different lattice substrate interaction.

Furthermore, from the TLM analysis the sheet resistance R_{Sh} in the DT-gSGFETs is reduced to half of the value of SL-gSGFETs, as expected in bilayer graphene[228]. The broader R_{Sh} vs V_{GS} curve for DT-gSGFETs compared to the SL-gSGFETs, is to be tentatively attributed to the lowered charged carrier mobility in the DT-graphene. Moreover, this result indicates for DT-gSGFETs an increase in charge carriers in the graphene structure, thus confirming the electrical interaction (as the Raman maps showed) between the two CVD graphene sheets. The improved channel noise performance of the DT-gSGFETs compared to SL gSGFETs is presented and discussed in the next chapter.

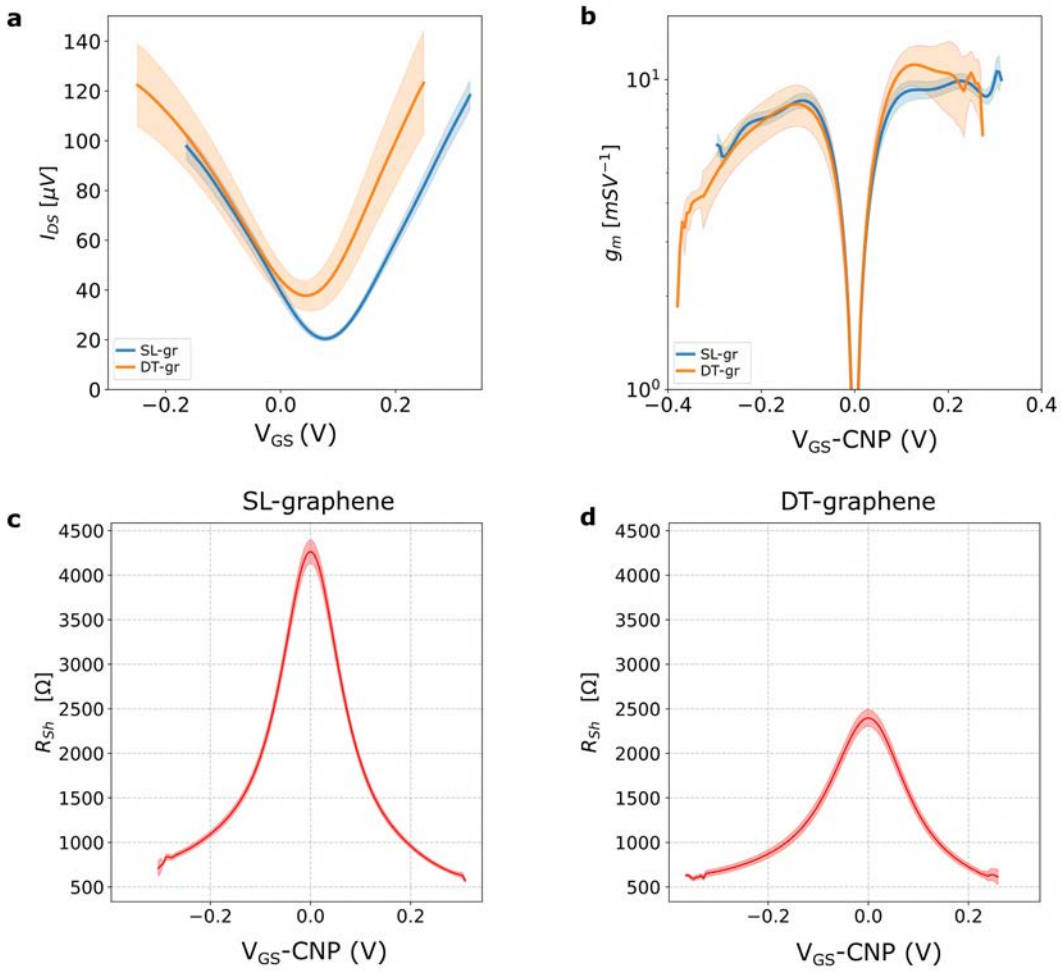

Figure 3.14: a. Transfer characteristics of SL gSGFETs (blue) and DT-gSGFETs (orange) for 40 μm x 20 μm transistors and corresponding normalized transconductance (**b**) showing very similar behaviors. Sheet resistance R_{Sh} for SL-gr (**c**) and DT-gr (**d**) derived with the TLM method, shows lower values of R_{Sh} around the CNP, as expected for bilayer graphene.

3.3.4 Neural probe characterisation

The probes were characterised using the same electronic setup described above. The flexible neural probe are connected to the customized electronics via a 16-contact zero insertion force (ZIF) connector (Figure 3.15). As for laboratory or *in vivo* acute experiments the size of the PCB is not a problem; for chronic experiments, where the neural probe-PCB need to be fixed on the rats head, the size and weight need to

be considered. Figure 3.15 **c** show a gDNP inserted in a small PCB with Omnetics connectors[11] designed for chronic implantation.

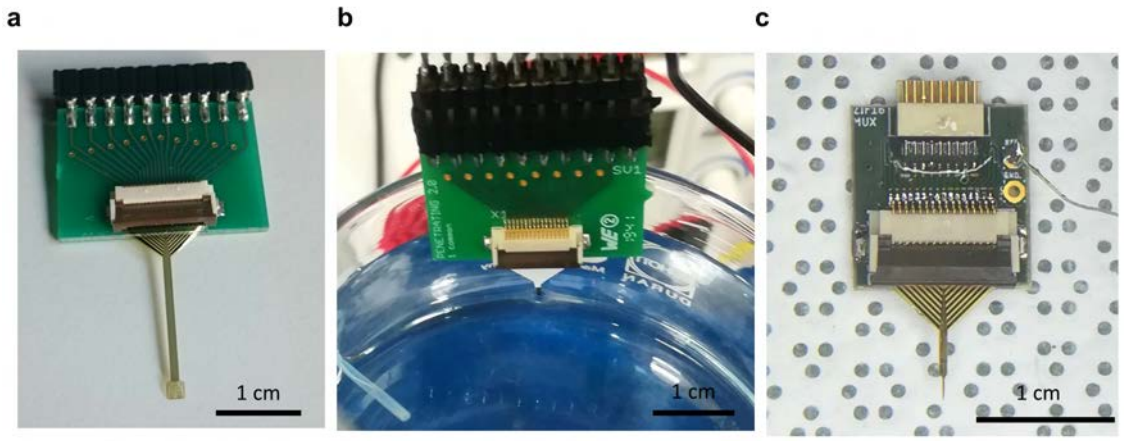

Figure 3.15: PCB used to connect the flexible neural devices to the electronics. **a**. Picture of an epi-cortical probe inserted in a PCB and a gDNP during an electrical characterisation (**b**). **c**. gDNP inserted in smaller PCB with Omnetic connection for chronic experiments. The reference Ag/AgCl wire is bonded to a ground pin on the PCB.

Before any *in vivo* experiment, all devices were characterised in PBS solution. The characterization consisted in measuring the transfer curve of all gSGFETs in each array, at fixed drain–source voltage (V_{DS}). The small dispersion of the charge neutrality point obtained (CNP $= 243.6 \pm 6.1$ mV), indicates a good homogeneity of the transistors (Figure 3.16a). For neural probes, it is important to have a small CNP dispersion to obtain near-optimal recording performance for all gSGFETs of the same array (since V_{GS} and V_{DS} are shared). The leakage current (I_{GS}) for all gSGFETs in the array was also measured, and found to be in the nano-ampere range throughout the voltage sweep (Figure 3.16b), demonstrating the good insulation from the passivation layer and the low electrochemical reactivity of the graphene.

[11] Omnetics Connector Corporation

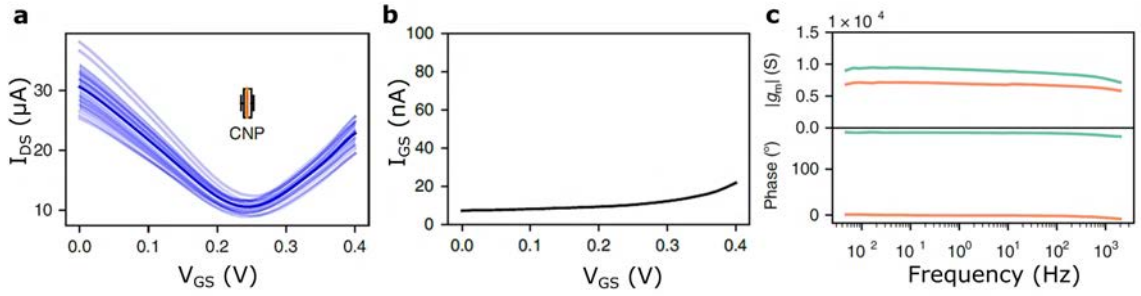

Figure 3.16: a. representative gSGFET transfer curves of an epi-cortical probe (blue lines), I_{DS} vs gate–source voltage (V_{GS}), together with the mean (dark blue) and standard deviation (blue shade). The boxplot inset shows CNP dispersion (centre line, median; box limits, upper and lower quartiles). **b**. Leakage current (I_{GS}) of all gSGFETs in the array throughout the voltage sweep. **c**. Frequency response of the transconductance at two different points of the transfer curve. When V_{GS} is lower than the CNP (green) the gm is negative, resulting in a signal inversion (180° phase); and when V_{GS} is higher than the CNP (orange) the g_m is positive and thus results in no inversion (0° phase). Independently of the branch of the transfer curve where a gSGFET is polarized, the modulus of g_m is similar to the steady-state value for a wide bandwidth (≈ 0–1 kHz).

Furthermore, we also investigated the frequency response of the transconductance (g_m), which indicates the efficiency of the signal coupling ($\delta I_{DS}/\delta V_{GS}$). The negative g_m for V_{GS} values lower than the CNP results in an inversion (180° phase) of the signals measured in that bias regime, while forV_{GS} values higher than the CNP the signal phase is preserved. In both cases, we obtained constant g_m values in a wide frequency bandwidth (Figure 3.16c). Several wafers of graphene flexible neural probes have been fabricated during the course of this PhD, iterating the fabrication processes based on the characterization results. Figure 3.17a and Figure 3.18a show the average performances (shadow represents standard deviation) of all the fabricated devices present on one of the wafers. The histograms (Figure 3.17b and Figure 3.18b) show the values of transconductance, the position of the CNP and the field-effect mobility[12], as deduced from the transfer characteristics (see equation 2.32). The high transconductance values (1-2 mS/V) and FET mobility, which ranges between 2000-4000 cm^2/Vs, are in good agreement with previous work [68].

[12]The FET mobility assumes $R_C = 300\Omega$ and a defect density $n_0 = 1 \cdot 10^{11} cm^{-2}$

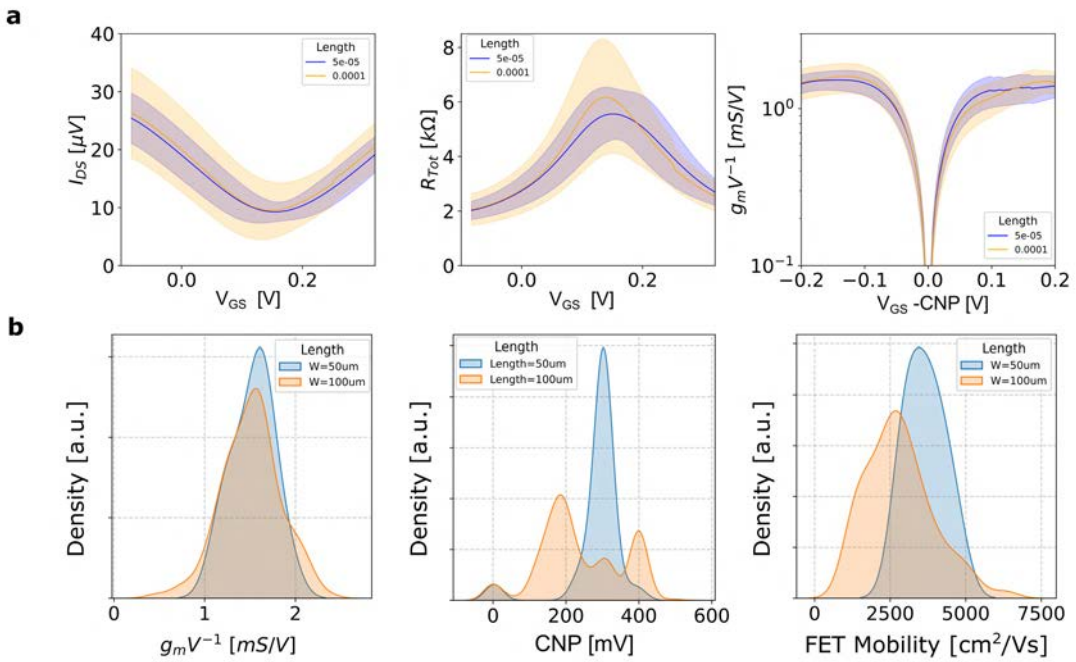

Figure 3.17: Statistical analysis of all fabricated epi-cortial probes present on one wafer. **a**. Average values of I_{DS} of R_{Tot} and g_m/V_{DS} for probes with active area of 100x100 μm^2 (orange) and of 100x50 μm^2 (blue). **b**. The histograms of all fabricated devices on a wafer (1-σ outlayers removed) show the distribution of the transconductance, the position of the CNP and the field-effect mobility of the sGFETs arrays.

From the statistical overview, the epi-cortical probes (Figure 3.17) as well as the gDNP (Figure 3.18) show very good homogeneity across devices in terms of position of the CNP (200-350 mV) and values of transconductance; together with the high fabrication yield per wafer (80-85%), the development work shows a very solid, advanced technology for neural activity recording devices. The gDNP have a higher resistance compared to the epi-cortical probes and a flattening of the V-shape transfer curve occurs at high $|V_{GS}|$ values. We attribute this increase in resistance to the much narrower metal leads at the tip of the gDNP probe (metal track width=5μm) compared to the epicortical probes (metal track width=25μm).

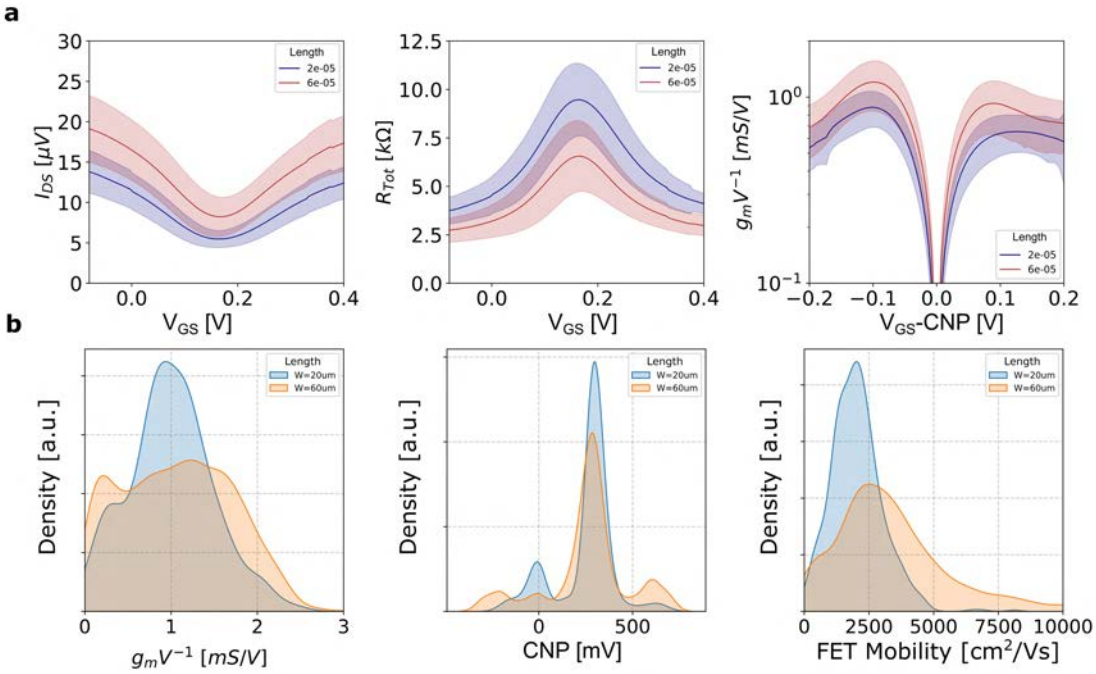

Figure 3.18: Statistical analysis of all fabricated gDNP 4.0 on a wafer. **a**. Average values of I_{DS} of R_{Tot} and g_m/V_{DS} for gDNP with active area of 60x60 μm^2 (red) and of 20x20 μm^2 (navy). **b**. The histograms of all fabricated devices on a wafer (1-σ outlayers removed) show the distribution of the transconductance, the position of the CNP and the field-effect mobility of the sGFETs arrays.

3.4 A bioresorbable shuttle for penetration of a flexible gDNP in-vivo

Flexibility is very advantageous for the epi-cortical probes and can facilitate the placement of the sensors on the cortex of the neural tissue. However for gDNPs, the flexibility becomes an obstacle for the device insertion, since the probe need to penetrate the outer skin layers of the cortex (i.e. the dura mater). In this section, I present a short overview of current insertion strategies of flexible polimeric depth probes, and describe the protocol developed in this thesis work to insert the gDNP in rodents brain.

3.4.1 Short overview on current state of the art

The development of flexible and softer neural depth probes constructed from polymer shanks is thought to overcome the large mechanical mismatch and micro-motion between rigid probes (E=200 GPa) and soft brain tissue (E=0.4–15 kPa), which

is one of the main cause of the long-term inflammatory response causing neuronal loss and scar formation around the implants, followed by gradual degradation of the recording quality, which limits the chronic recording capabilities [231, 35, 232] (section 1.1.1).
The same flexibility that is desirable for a sensor device once in the brain, makes its implantation challenging. Many strategies have been used to insert flexible neural probes including temporarily attachment to a hard shuttle, such as silicon [233, 234], diamond[235] and tungsten[236]. The advantage of these shuttle methods with rigid shanks, is the ability to penetrate very deeply; however the low yield from insertion, the brittleness of thin crystals, and the damage caused to the neural tissue, are the main drawbacks of this technique.
Another possibility is the use bioresorbable polymers, which temporarily coat the neural probes, keep them rigid during insertion, and after reaching the desired location in the brain dissolve. This we call a bioresorbable shuttle. Biocompatibility of these substances is of utmost importance, as any aggravation of the immune response to the coated probe by surrounding tissue detracts from the quality and lifetime the neural recordings. Coatings used to stiffen flexible neural probes during insertion include polyethylene glycol (PEG) [237, 238, 239], gelatin [240, 241], tyrosine-derived polymers [242, 243], carboxy-methyl-cellulose (CMC) [244], saccharose [245], and maltose [246]. Another candidate as bioresorbable shuttle, that slowly dissolves in the brain after implantation is silk-fibroin (SF)[247, 248, 239] a protein extracted from the Bombyx mori silk worm cocoons.

SF was recognized by the US Food and Drug Administration (FDA) as a biomaterial and used as surgical suture [249]. Compared with other natural biopolymers, SF is promising, due to its excellent mechanical properties, extremely good biocompatibility, biodegradability, and the versatility of structural re-adjustments. It has been engineered as scaffolds, as coating, as hydrogels, sponges, electro-spun fibers as well as micro/nanospheres for biomedical applications [250, 251, 252]. Moreover, it has been shown that SF is degraded by enzymes such as protease and that its byproducts have low antigenicity and non-inflammatory characteristics[253, 254, 255]. Its dissolving time and rigidity can be therefore tuned, in order to reach the trade-off between solubility and rigidity.
It has therefore been chosen as bioresorbable shuttle material, for the probe insertion strategy in this thesis study. In the next section more details about the properties of silk fibroin are presented.

3.4.2 Silk-fibroin

Overview. Bombyx Mori's (silkworm) silk is a unique material, which has been used in the traditional textile industry for more than 4000 years; Silk is admired for its soft, pearly luster and good mechanical properties. Physicians have used silk as a suture material for centuries, and it has recently gained attention as biomaterial because it has several desirable properties. Silks are commonly defined as protein polymers, which are biosynthesized by specialized epithelial cells in the glands of arthropods, such as silkworms, spiders, scorpions, mites, and bees, and then spun into fibers during the arthropods metamorphosis. The majority of silks are spun in air, but some aquatic insects produce silks with different compositions that are spun under water. Natural silks can provide structural roles in cocoon formation, web formation, traps, nest building, safety lines and egg protection.
Although, physicians have used the silk as a suture material for centuries, in recent years silk from Bombyx Mori (silkworm) has been discussed extensively due to its biocompatibility, robust mechanical performance, control over the degree of crystallinity, tunable degradation, ease of processing, sufficient supply and ease of acquisition from the mature sericulture industry. Silk fibroin (SF) is a protein material studied in tissue engineering, biomedical devices, and for drug release. SF patterned films,[256, 257] thin films,[258, 259] blend films,[260] sponge tissue scaffolds,[261, 262] nanofibers,[263, 264] microspheres,[265, 266] nanoparticles,[267] and different gels including hydrogels,[268] electro-gels,[269] and vortex gels[270] have been studied in the past decade, allowing the transition of this biopolymer from the traditional textile industry to a broad range of biomedical applications. To date, the best quality SF as natural polymers and biomaterials is still obtained from silk cocoons (Figure 3.19a).

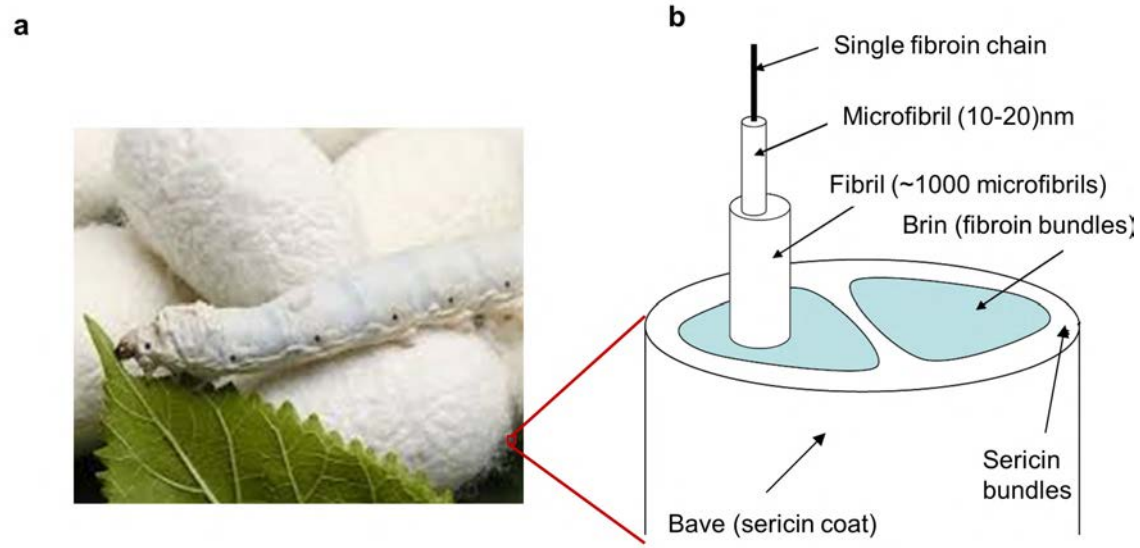

Figure 3.19: a Picture of a Bombix mori silk worm spinning the coocons.[13] **b** The structure of B. mori silk thread (single fiber) [271, 272]

Silk is composed of two major proteins: silk fibroin (SF) (approximately 75%) and sericin (approximately 25%). The silk fibre has been shown to be composed of two protein-monofilaments (named **brins**) embedded in the sericin coating (Figure 3.19b) [273, 274]. The brins are fibroin filaments made up of bundles of nanofibrils (called **microfibrils**), approx 5 nm in diameter, with a microfibrils diameter of around 100 nm [274, 275, 272, 271, 276]. The elements of the supramolecular structure of silk fibers are macrofibrils (or **fibrils**) with a width of up to 6.5×10^5 nm [276]. The formed silk fibroin fibers are about 10–25 μm in diameter [272, 271, 276]. The glue-like sericin protein wraps around fibroin, acting as an adhesive binder to keep the structural integrity of the fibers[277, 278] (Figure 3.19b); Depending on its structural composition, the molecular weight of degummed SF can vary between 84 kDa and ∼350 kDa[279, 277, 280], while in sericins it is between 10 and 300 kDa, rich in amino acid serine[277].

To extract the fibroin proteins, SF is usually purified from sericins by a thermo-chemical treatment, also known as degumming process, in which silk cocoons are boiled in an alkaline solution [281, 253, 282, 280]. The end result is an aqueous solution of pure silk fibroin, proteins with a semi-crystalline structure that provides stiffness and strength.

[13] image taken from http://www.todayifoundout.com/index.php/2014/10/real-silk-made/

The chemical composition of fibroin, contains primarily glycine (Gly, 43mol%), alanine (Ala, 30mol%), and serine (Ser, 12mol%), as well as other amino acids (such as tyrosine (Tyr, 4.8 mol%), and valine (Val 2.5 mol%) [282].

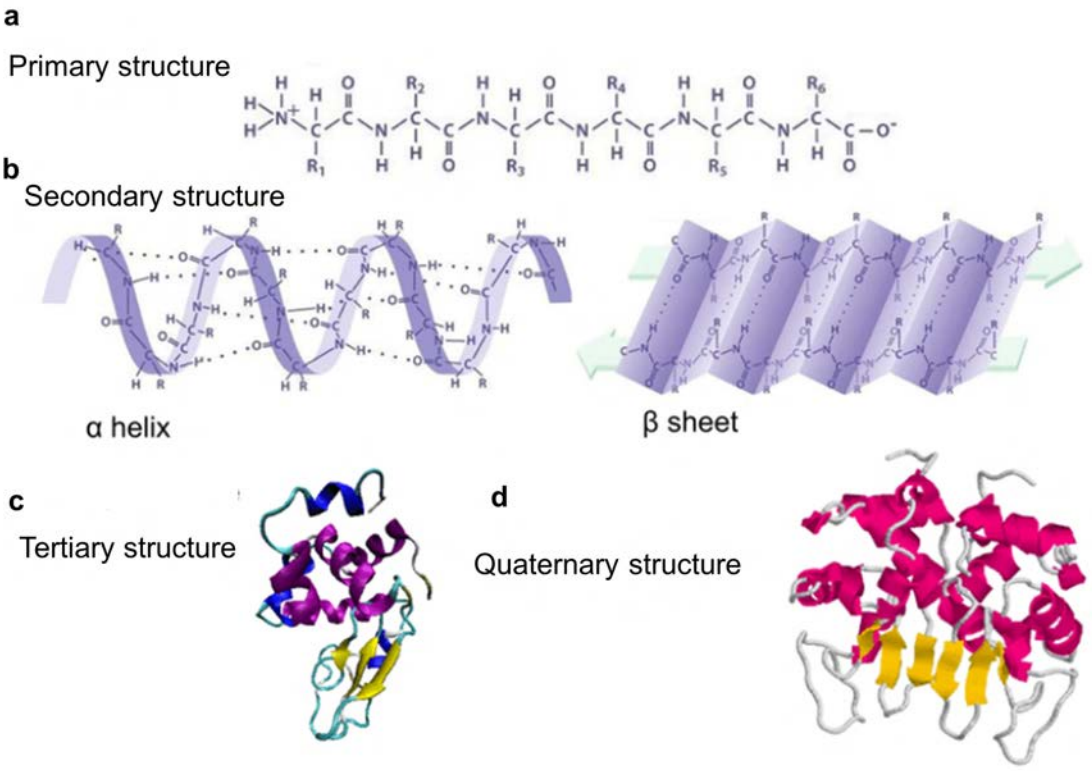

Figure 3.20: Different hierarchical structures in proteins. **a**. Primary structure: Polypeptide chain. **b**. Secondary structure elements: (Left) α-helix. (Right) Antiparallel β-sheet. **c**. Tertiary structure: Folded protein with different secondary structure elements present. **d**. Quaternary structure: Association of two tertiary structure subdomains. Adapted from [283].

Generally speaking, the proteins structure can be divided into four levels: the primary structure, the secondary structure, the tertiary structure, and the quaternary structure [283]. The genetic sequence of amino acids is called primary structure [284, 285]. Figure 3.20a shows the model of the primary structure, where the aminoacid units form a peptide string. The aminoacid residues can have interaction with each other by forming hydrogen bonds; this induces the protein chain to form intermediate protein structure called secondary structure. Amids and hydrogen atoms bond very efficiently with each other, forming secondary structures by the shapes of helices, sheets, turns, or coils [284, 285].
For instance, in the α-helix structure the polypeptide backbone is forced to coil in

a right-handed helix, where the hydrogen bonding occurs between successive turns of the helix (Figure 3.20b). Another widely observed secondary structure is beta sheets (β-sheet), in which the hydrogen-bond-connected strands of polypeptide are stretched out and lay either parallel or anti-parallel to one another (see Figure 3.21a) [283, 284, 285].

Tertiary structure is a well-defined 3D structure with a special biological function, formed when various elements of the secondary structure pack tightly together. The protein chains are held together by weak interactions, like a tightly-packed snowball, between the side chains; therefore, heat or exposure to chemicals could cause them easily to be "denatured" from their original tertiary structures. Figure 3.20c shows a model of the tertiary structure, inside which some portions are α-helix and others are β-sheet secondary structures[283].

In addition to the tertiary structures, multiple-subunit proteins can form a larger quaternary structure, which normally contains several tertiary structures or many functional protein 3-D structures. Those quaternary structures sometimes could have an ion or a small molecule core around which the tertiary structures group. Figure 3.20d shows a model of the quaternary structure which formed by combining two tertiary structures [283]. The main crystal structures of silkworm SF are silk I (non-crystalline, hydrophilic regions) and silk II (crystalline, hydrophobic regions). The little and unstable silk III structure also exists in regenerated SF solution at the air/water interface (see Figure 3.21b).

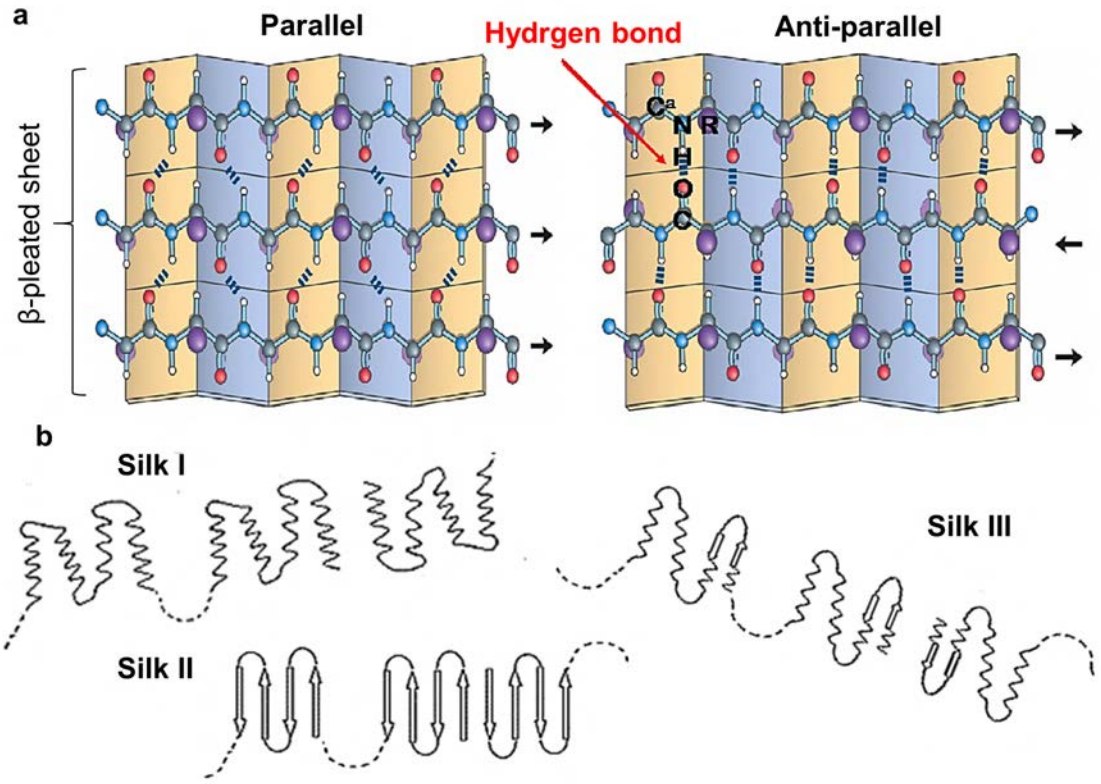

Figure 3.21: a, Chemical pattern of SF anti-parallel β-sheet crystalline. The intra-chain hydrogen bonding pattern produce parallel and anti-parallel β-strands. Atoms colors: white-hydrogen, red-oxygen, blue-nitrogen, grey-carbon, purple-amino acid side group. Reproduced from [284]. **b**, Crystal structures found in SF. In region I, the heavy-chain fibroin consists mainly of Silk I structure, which includes helix (solid helical curve) and β-turn (solid loop line) structures. The dashed line shows the hydrophilic spacer sequence. In silk II, the secondary structure is predominantly anti-parallel β-sheet. The arrows indicate β-strands. In silk III, the helix structure appears again. Adapted from [286].

Silk I is a metastable structure with crank or S zigzag structure spatial conformation, belonging to the orthorhombic system. Silk II is an anti-parallel β-sheet structure, belonging to the monoclinic system. The β-sheets are arranged so that the methyl groups and hydrogen groups of opposing sheets interact to form the intersheet stacking in the crystals. Strong inter- and intra-chain hydrogen bonds, plus Van der Waals forces, can generate thermodynamically stable crystalline structures. Crystallinity, transition kinetics, thermal, mechanical, and biodegradation properties of proteins such as SF, are investigated by Fourier transform infrared spectroscopy (FTIR), differential scanning calorimetry (DSC), uniaxial tensile studies, contact angle, X-ray diffractions (XRD) and enzymatic degradation studies among others. To induce an amorphous to silk I or silk II (β-sheet) conformational transition,

aqueous SF is treated via methanol (by immersion in an alcohol, such as methanol or ethanol), via potassium phosphate treatment or via water annealing. Alcohol immersion is simple and quick but can leave organic solvents or trapped ions residuals which are not ideal, specially for biomedical applications. Water is the most important solvent of proteins in nature. Water molecules plasticize protein structures with hydrogen bonds and also promote solvent-induced crystallization. Water molecules disrupt intermolecular cohesive forces between protein chains, reduce steric hindrance for movement and reorientation,and thus enhance chain mobility of noncrystalline domains in proteins. Therefore, a large reduction in the glass-transition temperature (T_g) is favored in a protein-water system. Hence, water annealing is preferred as "green" solvent for biomedical application in which SF is involved [287]. High contents of β-sheets in the SF renders the biomaterial less soluble in water. To extend the use of silk proteins as biomaterial, the option to form water-stable silk-based materials with reduced β-sheet formations is desirable. The temperature dependence of the silk glass transition as a function of water content has been widely reported in the literature. X. Hu et al. [287] reported high levels of SF crystallinity, up to 60%, by a temperature controlled water vapor annealing process , whereby the silk materials are incubated in a humid environment for several hours, with pressure control. J. Magoshi et al. [288] obtained the phase diagram of aqueous SF crystallized by water annealing (Figure 3.22a). By applying different drying temperatures and varying the initial SF concentration, the study showed degrees of cristallinity of 33-40% (Figure 3.22a).

Figure 3.22b shows the crystallization time (defined as the time needed to complete the crystallization) vs. the drying temperature of aqueous SF solution. Clearly the crystallisation time changes dramatically at around 50 ^{o}C, at the α- to β-transition. It is also clear that the α-form requires a longer crystallization time while for β-formation the crystallisation time is shorter (1-3h). X-ray diffraction images (see Figure 3.22c) illustrate different diffraction patterns obtained in three different SF structures, amorphous (T), α-form characteristic of silk I regions (M), and β-form silk II region (B)[288].

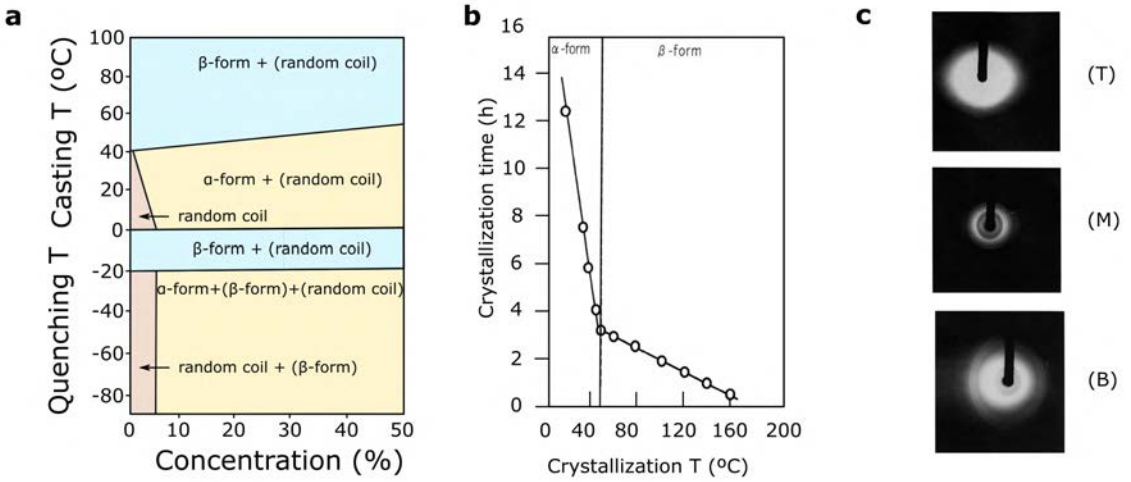

Figure 3.22: **a**. Phase diagram of B. mori SF, illustrating the relationship between conformation, quenching or casting temperature and concentration. **b**. Crystallization time vs. drying temperature of liquid SF. The crystallization dynamics change around 50ºC, which corresponds to the α-to-β-form transition temperature. **c**, X-ray diffraction patterns of SF: (T) amorphous, (M) α-form (silk fibroin I) and (B) β-form (SF II). Adapted from [288].

Although studies with water annealing use different thicknesses and shapes of the samples (which affects the crystallinity kinetics), it was generally found that with the increase in the annealing temperature, the kinetics of the β-sheet crystal formation increased gradually[288, 287, 289]. The structural changes induced by the different crystallization strategies confer different physical and chemical properties to the SF biomaterial. However, the glass transition in fibroins is influenced not only by the temperature but also by the environmental relative humidity (RH). The elastic modulus in fibroin has been found to span by two orders of magnitude between dry fibers, $E_{Dry} \approx$=10 GPa and wet fibers$E_{Wet} \approx 0.01$ GPa [290, 291, 292, 293].
Fast water-degradability of SF is not very convenient when stiffening should ensure insertion in the brain tissue. On the other hand, SF offers ways to control and delay the uptake of water, even to make SF water resistant[289]. Water stable silk films have been produced either in high content of silk I and silk II by water annealing [289]. Controlling structures of regenerated SF without the use of organic solvents may have useful applications in biomedical engineering, including wound dressings, tissue regeneration and bioresorbable shuttle for neural interfaces.
In this work we have used SF to back-coat the graphene depth neural probe (gDNP) with water-annealed SF, as means of insertion in the brain of rodents for *in vivo* experiments. The next section describes the methodology (which has been inspired

from previous reported studies [239]) and present the characterisation of the depth probes after silk-coating.

3.4.3 Fabrication of a Bioresorbable Fibroin Shuttle

The graphene depth neural probes (gDNPs) are highly flexible compared to traditional rigid depth electrodes. Although the flexibility is highly advantageous once the probes are inserted into the tissue, it also implies a challenge during insertion.

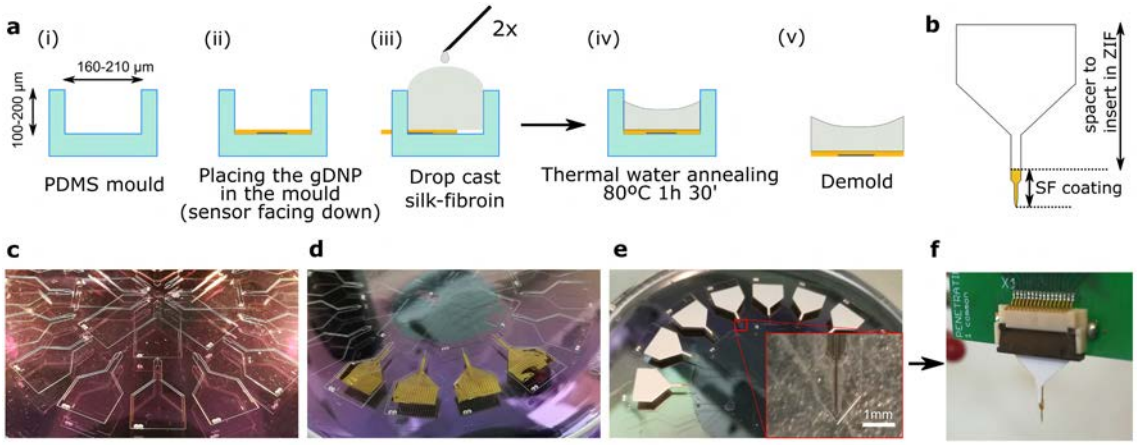

Figure 3.23: a. Back-coating stiffening procedure: (i) a PDMS mould is used, microstructured with the shape of the gDNP; (ii) placement of the gDNP with sensors facing down wards; (iii) drop-casting of the SF by filling the mould's trench. Double coat after 20min, then place on a hotplate and increase slowly the temperature to 80ºC; (iv) curing step of the SF at 80C for 1h and 30min; (v) remove from hotplate and gently demould the gDNP.**b**. The tip of the gDNP is back-coated with SF; a plastic spacer with the same shape of the probe is attached in the upper part of the gDNP. **c-e**. Pictures of the PDMS mould following the steps described in (**a**). After placement of the gDNP in the mould (**d**), an adhesive spacer is sticked to the back side of the flexible gDNP (**e**), providing rigidity of the gDNP base when inserted in the ZIF-connector (**f**).

Therefore, to insert these probes we temporarily stiffen the gDNP using silk-fibroin (SF)[247, 294]. As discussed in the previous section, SF offers excellent mechanical properties, extremely good biocompatibility, biodegradability, and the versatility of structural readjustments[289, 281, 253]. Further, the byproducts of the SF degradation by enzymes (e.g. proteases) have low antigenicity and non-inflammatory characteristics[254, 255].

The stiffening technique developed consists of a moulding process in which the gDNP is back-coated with cured SF, allowing the preparation of a rigid, straight shank with a defined shape and thickness. Moreover, the SF back-coating strategy enable immediate recordings in the brain tissue during and after the insertion, whereas

other coating strategies need first a latency time in order for the biopolymer to dissolve and expose the electrodes to the tissue.
A soft-lithography technique was used to prepare a micro-structured polydimethylsiloxane (PDMS) mould, which was designed with the shape of the neural probes (5μm of space between the probes edges and the PDMS walls to facilitate the alignment of the gDNP). To fabricate the moulds, PDMS is cast on a standard 4-inch silicon wafer with pre-patterned 100 μm and 200 μm thick SU8 (SU8-2050) epoxy resin. More details about the fabrication of the SU-8 master-mould can be found in the Appendix A.4.1.

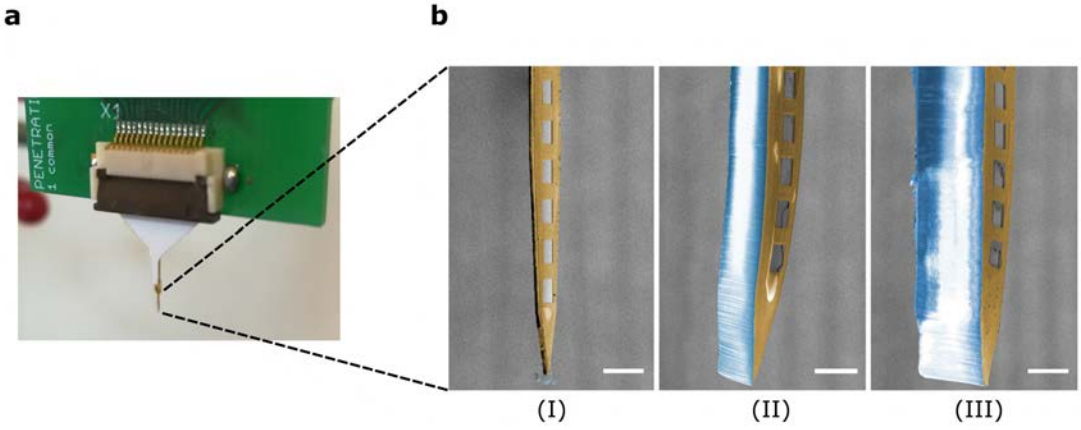

Figure 3.24: a, After demoulding the back-coated gDNP, the probe is place in the ZIF of the custom PCB to interface the electronics. **b**, Blow up of the SF coated tip. Coloured SEM images of the gDNP; (I) uncoated, (II) back coated with $\sim$ 80μm and (III) with $\sim$ 150μm thick silk-fibroin. Scale bar=100μm.

The back-coating procedure is as follows: first, the probe is placed in the PDMS mould trench previously filled with water, with the transistor side facing down (Figure 3.23a (i-ii)). Through surface tension the probe self-aligns in the mould. After evaporation of the water, a pre-thawed silk fibroin solution [14] ($\sim$ 5μl) was applied via a syringe to the mould's trench. The gDNP shank is double coated in drying intervals of 20 minutes. Then, the mould with the probes are placed on a hotplate with a glass cover, first at 50 ^{o}C for 15 min (to evaporate the water, avoiding curling of the gDNP) then ramping the temperature to 80 ^{o}C for at least 1h 30 minutes (iii-iv). The SF was then dried at room temperature for more than 12h (step (iv) in Figure 3.23a) in a low moisture desiccator chamber, as previously reported [247, 294]. After curing, the coated probe can be easily removed from the PDMS mould (v).

[14] Sigma Aldrich, Silk, Fibroin Solution 50 mg/mL

By increasing the duration of the water annealing step and of the temperature,it was possible to control the dissolution time of the SF-shuttle compared to SF cured at room temperature. The moisture absorption amount of the SF-coated gDNP was calculated around 7% after one day at 25 ^{o}C for 24 h (see Appendix A.4.2 for more details). Absorption of moisture on the SF-coating can soften the gDNP. Therefore, in order to maintain their mechanical rigidity, the gDNP should be stored either at 37 ^{o}C in a drying cabinet, in a vacuum cabinet or in a desiccator, before their insertion into the brain.
The coating thickness of the silk fibroin on flexible polyimide probe was evaluated using a scanning electron microscope (SEM). With this SF stiffening technique, we were able tune the thickness of the SF by controlling the mould's trench depth (PDMS depth of 100 and 200 μm, respectively), achieving two typical thicknesses of $80 \pm 10\mu$m and $150 \pm 12\mu$m (n=5), as shown in the scanning electron microscopy image of Figure 3.24.

The average silk mass on the polyimide tip was estimated by measuring the actual weight of the coated and uncoated gDNP; for the 150 μm-thick coating it was estimated as $198 \pm 13\mu$g (n=5). In the *in vivo* experiments presented in chapter 5.2 we successfully implanted several flexible gDNPs in the brain of mice and rats, always using a 150 μm thick SF back-coating cured at 80^{o}C.

3.4.4 Water stability of SF coatings

Although the SF coating can stiffen the ultra-thin polyimide gDNP for their insertion into the brain, the coating is expected to soften in the presence of water. This softening has been investigated by inserting the coated gDNP in an agarose brain model and observed by optical microscopic analysis. SF coated gDNP loses its mechanical integrity in presence of water or when inserted in agarose gel; The degradation of the rigid SF occurs within a minute (see Figure 3.25). Video frames of a SF-coated gDNP inserted in an agarose brain model (Figure 3.25b) show the fast water absorption (<10 s) of SF after complete insertion (insertion speed: 400 μm/s); it also shows the collapsing of the SF in small residue beads which often stays in the solution for a longer period of time. As observed from the gDNP after removal from agar gel (180 s), SF is completely delaminated from the polymeric shank, therefore making the SF coated probes only suitable for single-time insertion.
In water, most of the SF coatings are degraded within five minutes and delaminated from the gDNP shank surface (Figure 3.25c). However, as SF is not water soluble, the degraded products often stays in the solution as small residue parts for a longer

period of time. SEM images of the gDNP surface after 1h in water, further indicate that there are only few nano-scopic SF residuals attached to it, making the SF coating of the neural probes a procedure that can be easily repeated and cleaned without the use of aggressive organic solvents (Figure 3.25d).

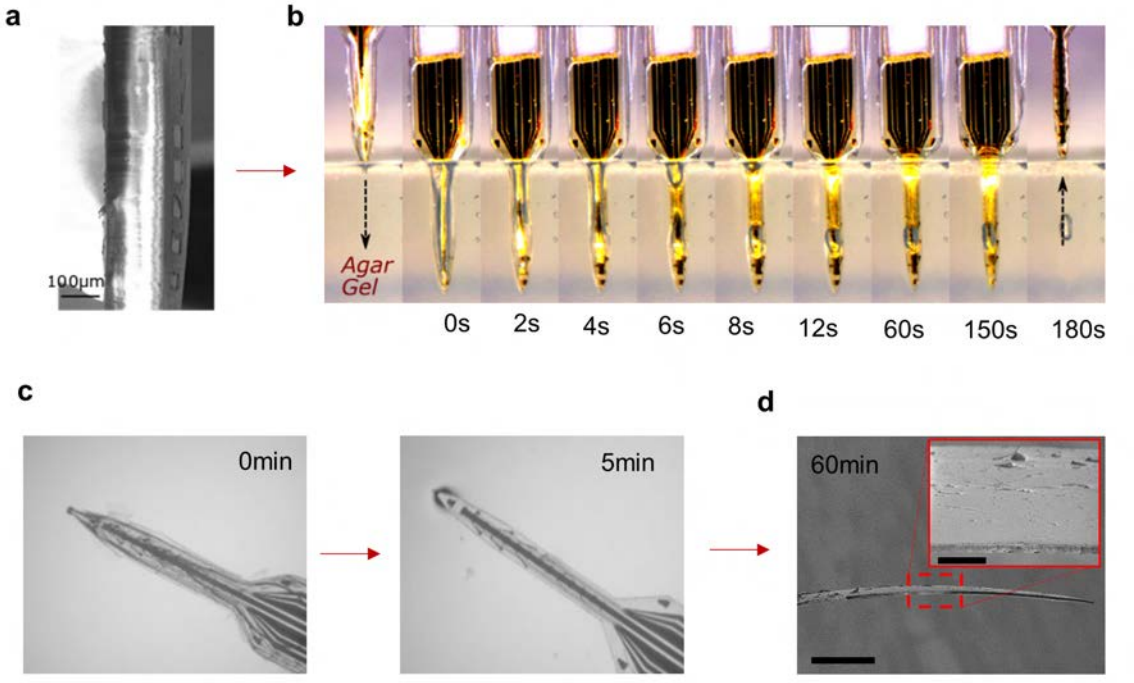

Figure 3.25: **a**. SEM image of the SF back-coated gDNP, inserted in agarose gel. **b**. Image sequence of a SF coated gDNP, at different time points during degradation in 0.6% agarose gel brain model. **c**. Optical images of the SF-coated gDNP in water. Most of the SF coatings are degraded within five minutes and delaminated from the gDNP surface. **d**. SEM image of a SF coated gDNP. The gDNP surface is completely cleaned from the SF after 1h in distilled water (scale bar: 200 μm). Inset showing a blow up image of the water cleaned gDNP surface (scale bar: 50 μm)

Contact angle measurements show that the cured SF (80 ^{o}C for 1h and 30min) is hydrophilic (<90^{o}), indicating the presence of α-form domains (see section 3.4.2). The contact angle value is less than 90^{o}, which implies that water can sufficiently wet the silk fibroin surface. Moreover, the contact angle value was varying from 62.84^{o} to 48.01^{o} within 20s time, which shows the increasing absorption of water on the SF in surface with time[295].

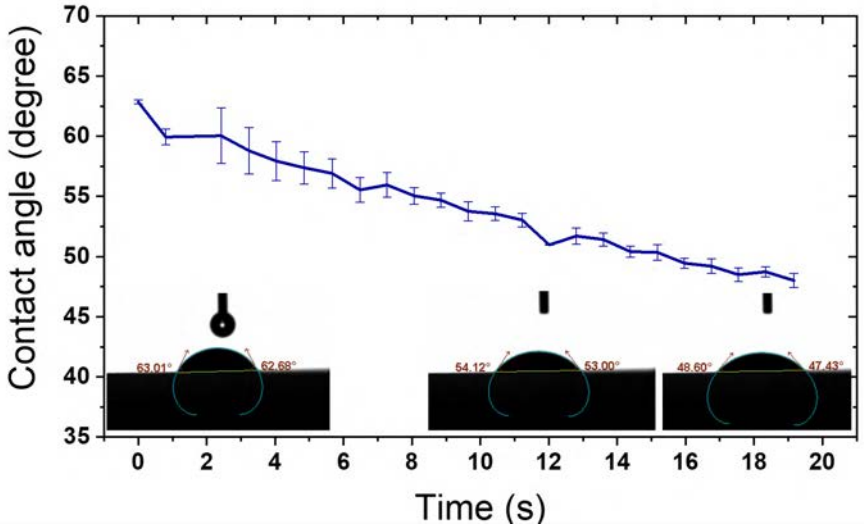

Figure 3.26: Contact angle measurement for silk fibroin coating cured at 80 ºC for 1h and 30min

3.4.5 Structural properties of SF coatings

The smoothness of the SF coating was evaluated using atomic force microscopy (AFM). According to the topographic images from the Figure 3.27, a densely packed beadlike features were observed with an average roughness of around 2-3 nm.

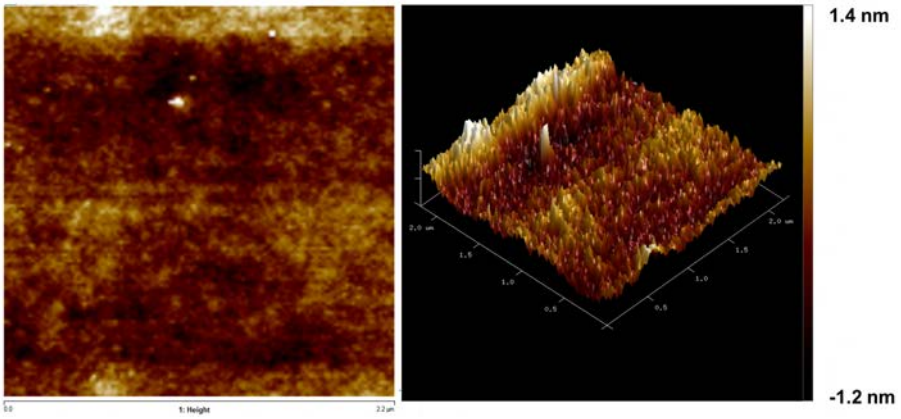

Figure 3.27: AFM analysis of silk fibroin coating.

Spectral analyses of the cured SF were performed in order to assess the physical properties of the SF structure, in particular the degree of crystallinity, which is related to the formation of β-sheets in SF (Section 3.4.2). Therefore, Fourier transform infrared spectroscopy and X-ray diffraction measurement were used, to characterize the SF films that were treated with thermal water-annealing, as described in section 3.4.3. Figure 3.28a shows the FTIR spectra of the SF coating, which exhibited

absorption bands at 1644 cm^1 to amide I (CO stretching), 1521 cm^1 to amide II (NH in plane bending), and 1231 cm^1 to amide III (NH deformation and CN stretching), which were all attributed to amorphous structure [296, 297]. The broader absorption peaks around 3282 cm^1 indicated the formation of amide-A bonding within the β-sheets [298]. The absorption band at 1,053 and 967 cm^1 regions further indicated the -gly-gly- and -gly-ala- structure formation within β-sheets [299].
The amorphous structure of the SF film was further confirmed by XRD pattern (Figure 3.28b). The diffraction peak was exhibited at 20.68º and corresponding d-spacing is calculated as 0.429 nm, which further indicates the presence of β-sheets formations [300]. Both spectral analyses confirm that the SF used for the insertion of the gDNP in the brain is made of amorphous fibroin, containing predominantly α-form and few regions of β-sheets.

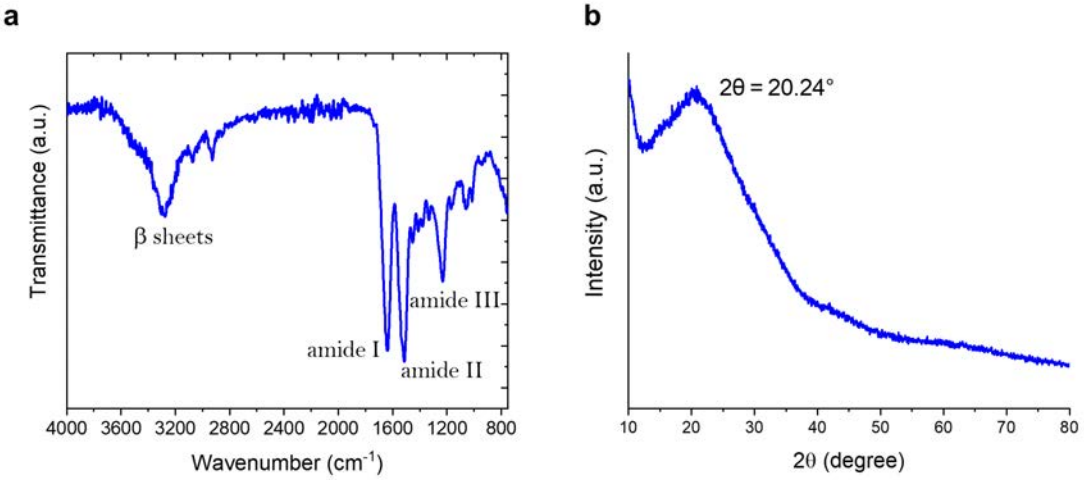

Figure 3.28: a. FTIR spectra and **b**. XRD analysis of the silk fibroin coating used.

3.4.6 Mechanical Characterisation

Standard compression tests against a hard silicon (Si) substrate were performed to assess the mechanical properties of our SF-coated gDNP probes. Buckling experiments were carried out in a UMIS nanonindenter[15]. A custom clamp was fabricated to fix the probes at the end of the indenter shaft that, in turn, was connected to the actuator and load cell (Figure 3.29a). Applied force vs displacement was measured until the probe started buckling and eventually broke down. An initial linear increase in force is observed for both coating thicknesses tested, while the probes remained

[15]UMIS nanoindenter from Fischer-Cripps Laboratories

straight before buckling (green box in Figure 3.29b). Continued application of force results in buckling and bending (orange box in Figure 3.29b), characterized by a peak in the force-displacement curve. The obtained peak forces, 101±21 mN for the 150 μm thick SF and 29±13 mN for 80 μm thick SF, are in good agreement with the previously reported values of peak forces of similar SF-coated neural probes [247, 239].

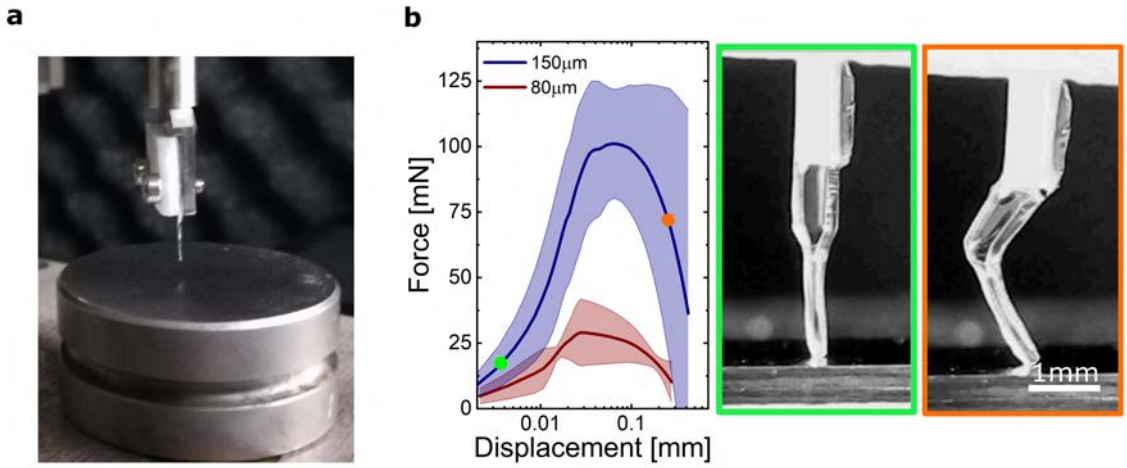

Figure 3.29: a. Buckling load test set up, showing the probe fixed to the nanoindenter with a custom made clamp. **b**. Averaged compression force vs displacement for the gDNP coated with two SF thicknesses (coloured areas are standard deviations, n=10 trials); the optical images correspond to two different conditions of the experiment.

For the uncoated gDNP, the nano-indenter was out of the measurable range (0.5 mN); this indicates that the gDNP without a SF-shuttle cannot be inserted in the brain, since the peak force value is less than 0.5 mN.
We additionally measured the Young's modulus of the SF cured at 80 ºC by means of nano-indentation tests. SF was drop casted on a 2x2 cm^2 Si chip and water-annealed. The indentation measurements were performed using a Nanoindentation Tester[16] equipped with a Berkovich pyramidal-shaped diamond tip. A maximum load of 5 mN was applied, with a loading segment of 30 s followed by a load holding segment of 10 s and an unloading segment of 30 s. The hardness and reduced Young's modulus are reported as an average value of at least twenty indentations, performed on top of each sample (in the central region). Young's modulus values in the range of 10 GPa where measured for 80 ºC cured SF (see Figure 3.30).

[16]NHT2 Nanoindentation Tester from Anton-Paar

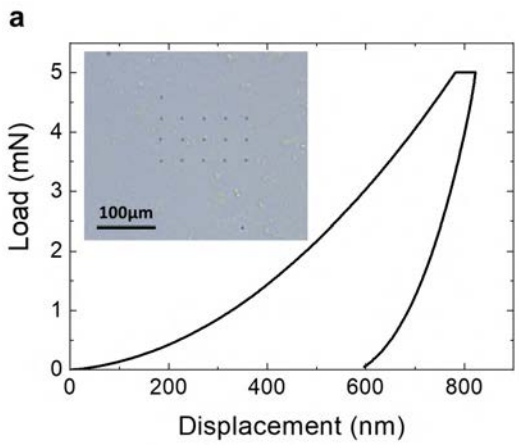

b

SF water-annealed (@80°C 1h 30min)		
Sample	**H(MPa)**	**Er(GPa)**
SF 1	369±7	10.7±0.4
SF 2	365±2	10.1±0.1

Figure 3.30: a. Representative indentation curve from the series of measurements performed to assess the hardness (H) and reduced Young's modulus (Er) of silk-fibroin cured at 80 °C for 1h 30min on a SiO2 chip (2cm x 2cm). Inset: microscope image of the indentation sites on the SF sample. **b**. The table shows the extracted values of H and Er as an average value of twenty indentations.

These values are measured for SF coatings in dry state, whilst in a real scenario the SF starts dissolving while being inserted. In order to find out the elasticity of wet SF, more sensitive atomic force microscopy (AFM) based indentation measurements were performed (details in Appendix A.4.2). To prepare the sample for AFM indentation, based on the mechanical properties measurement, SF was drop cast on a clean glass slide and water-annealed on a hot plate. The SF was then immersed in deionized water just before the measurements and the measurements were made in randomly selected 10 μm $\times$ 10 μm areas. The SF coating exhibited a uniform elastic modulus distribution. The Young's modulus of the SF coating was derived as 12±3.5 KPa, which shows a good match with the Young's modulus of the brain tissue [301].

3.4.7 Electrical validation of SF-coated gDNPs

In order to evaluate the effect of the stiffening and insertion procedures on the device performance, we electrically characterized the gDNPs before and after the SF stiffening process, as well as before and after insertion and removal from an agarose gel brain model.

Figure 3.31 shows the averaged values of the normalized G_m as well as the effective gate noise (V_{RMS}) of all 14 transistors on a representative gDNP, confirming that neither the stiffening process nor the insertion in an agarose brain model impair gDNP performance in terms of transconductance nor noise.

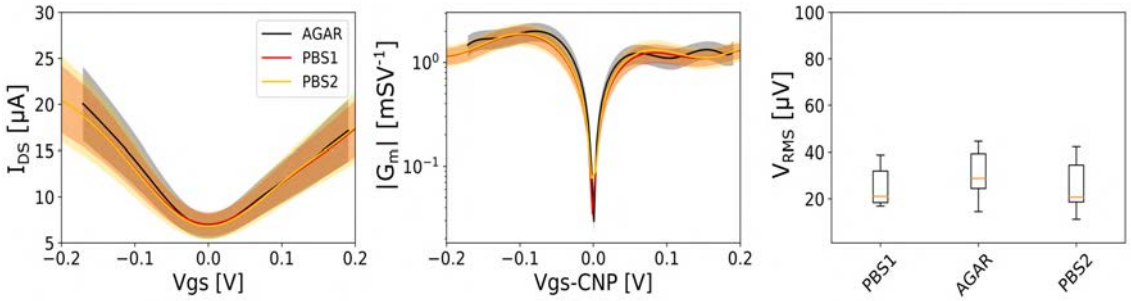

Figure 3.31: Functional assessment: Averaged transfer curve (I_{DS} vs V_{gs}) and transconductance (G_m vs V_{gs}) of a gDNP characterized before back-coating in 100mM Phosphate-buffered saline (PBS1); then an agarose gel brain model (AGAR), after been coated with SF; Finally characterised again in PBS (PBS2).

To assess how many times the gDNP can be coated and inserted in a brain-like tissue (such as agarose gel), gDNPs were iteratively coated and inserted for several times and characterized in terms of transfer curves and electric noise. Figure 3.32a-b shows the average value of I_{DS} and g_m of all working gSGFETs on a representative gDNP, inserted up to four times in agar. No significant signs of device degradation are observed. Moreover, Figure 3.32c-e show small oscillations in the mean values of the g_m, current noise I_{RMS} and effective gate noise V_{RMS} at peak-transconductance. The flexible gDNP may potentially be re-used for more than one time in acute experiments, which makes the developed technology even more appealing for neurologist and potential users interested in brain studies. These results underline the stability of the fabricated gDNP, that can be coated with SF, water annealed up to 80 ºC, inserted through the different layers of rodents brain and re-used without impairment of performances.
Furthermore, we could assess the performance of SF back-coated gDNP after their usage in the *in vivo* experiments presented in section 5.2.

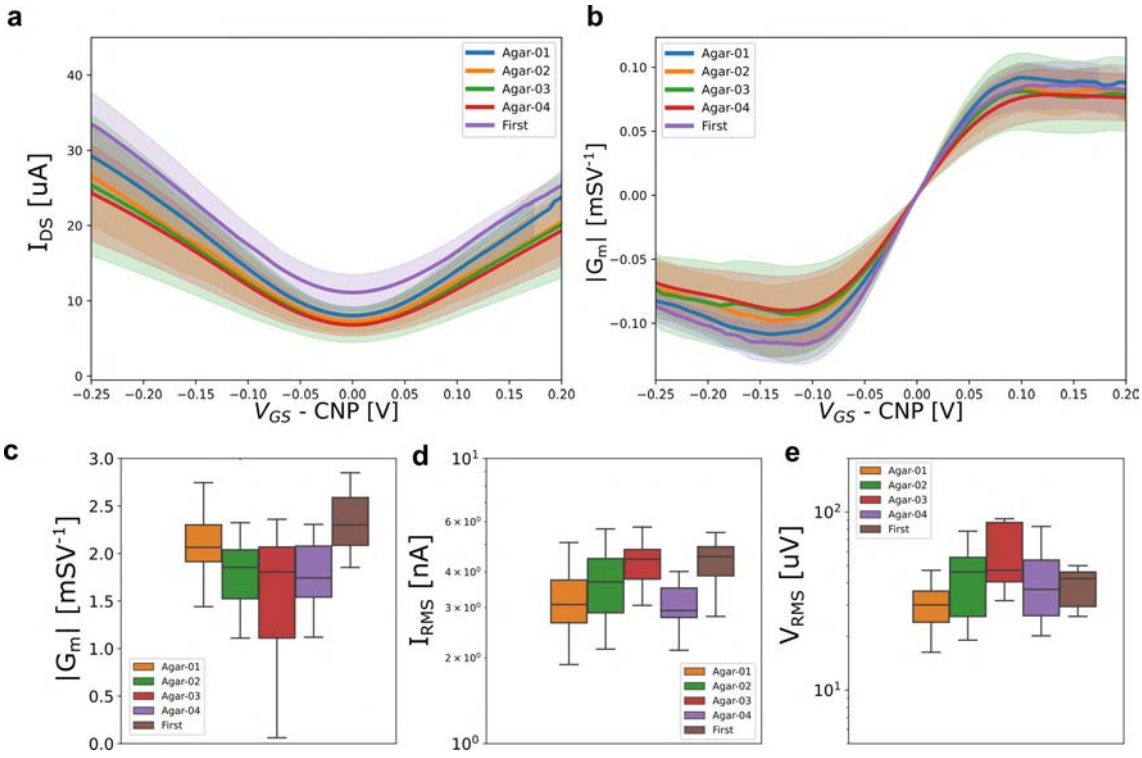

Figure 3.32: Multiple insertion in Agar. **a-b**. Averaged transfer curve (I_{DS}) and transconductance (g_m) of a gDNP characterized before back-coating in 100mM Phosphate-buffered saline (First), then inserted in agarose gel, cleaned from the residual SF, coated again and re-inserted in agarose gel after coating with SF; The iteration as been done four times. Boxplots illustrating the mean values and standard deviations of g_m (**c**), I_{RMS} current noise (**d**) and V_{RMS} gate noise at peak-transconductance (V_{DS}=-0.1V) over the iterative insertions (**e**).

To summarize, in this chapter we showed the finely tuned fabrication steps and the characterisations done for gSGFETs for rigid substrates, as well as for flexible neural probes. Besides SL-graphene SGFETs, also DT-graphene, hBN encapsulated graphene and graphene on self assembled HMDS layer SGFETs have been produced during this work.

Epicortical and intracortical (gDNPs) operational devices have been fabricated with high yield on wafer-scale, for in vivo experiments. Moreover, a silk-fibroin based stiffening protocol has been developed and studied, enabling a bioresorbable shuttle functionality for penetration of a flexible gDNP, with *ex vivo* assessment of electrical performances. It has been further demonstrated that the same gDNP device maintains electrical performance through several cycles of SF stiffening coatings and dissolution, which can be an asset for such devices. In the next chapter, the noise study on the fabricated gSGFETs is presented and results discussed.

4

Improving the Detection Limit of gSGFETs

In an electronic system, noise is defined as a random fluctuation of the electrical signal. Intrinsic noise is present in any electrical circuit; it degenerates the quality of the measured signal and cannot be completely avoided. All sensors have a basic or limiting noise level. For a sensor device, the signal to noise ratio in a measurement is the parameter to tackle. Studying, characterizing and minimizing the noise, thus, is fundamental in order to determine the quality of a sensor. In electronic devices, the noise can be generated by different mechanisms[302]. There are **external noise** sources like the interference noise which is generated by coupling from the environment and **internal noise** sources, for instance thermal noise. External noise is difficult to reproduce and can only be avoided by changing the environmnet or the location of the measuring system or for instance in the case of electro-magnetic noise, by shielding the setup and connectors with Faraday cage methods. On the other hand, the internal noise is intrinsic to the system under investigation and cannot be avoided, unless the system is modified. Interestingly, the study of the internal noise can provide information on the physical transport processes taking place in an electronic device. In this thesis, the intrinsic low frequency noise of graphene SGFETs was investigated and succesfully reduced, with substantial experimental efforts. Different strategies were pursued and experimented, to increase the SNR of the gSGFET by reducing the electrical intrinsic noise limit; contributions from the contacts resistance and channel noise have been addressed. To reduce the contacts noise, as we will show,

an ultra-violet ozone (UVO) treatment at the graphene-metal interface can reduce the contribution to the intrinsic noise and increase the homogeneity of the gSGFET sensors. Channel intrinsic noise reduction was pursued by tailoring the fabrication of 2D heterostructures, such as the stacking hBN-graphene or a double-transferred CVD graphene.

4.1 Intrinsic Low-Frequency Noise

The intrinsic low-frequency noise present in transistors is of critical importance to many electronic applications, and has inspired intense research since the advent of the semiconductor industry [303]. Electronic noise plays a particularly important role for new emerging graphene-based technologies such as biologic sensors, photodetectors and high-frequency devices[304], as their functionality relies often on the high carrier mobility properties of graphene and the accurate control of the number of charge carriers in the density of state (DOS) of graphene. For our application, due to the small amplitude of the neural activity measured by ECoG and intracranial-ECoG, low noise plays a paramount role when developing graphene-based neural sensors. Therefore, its origin have to be well understood in order to minimize its impact.

There are different sources of intrinsic noise in electronic devices, including thermal noise, Flicker or 1/f-noise, shot noise and generation-recombination (G-R) noise. **Thermal noise** (also called Johnson-Nyquist noise), is generated by random thermal motion of charge carriers inside the conductor, it is independent of the applied voltage and found in any electronic device. The current power spectrum of the thermal noise depends, apart from the temperature T, also on the resistance R of the conductive material and is given by [305]:

$$S_I = \frac{4k_B T}{R} \tag{4.1}$$

with k_B the Boltzman constant; S_I relates to the average kinetic energy of the system electrons. Thermal noise is nearly equal at all frequencies of the spectrum of interest. Another noise source is the **shot noise**. It appears in all low-current devices that include barriers, for example across a p-n junction or in transistors[305]. It is produced by the random arrival of electrons or holes at the output element. The shot noise can be described using the Schottky's theorem [303], and its current power spectrum

scales linearly with the current through the device:

$$S_I = 2e \langle I \rangle \tag{4.2}$$

where $\langle I \rangle$ is the average value of the electrical current, and e the electron elementary charge constant.
Thermal and shot noise types have their origin in the random motion of charge carriers and their spectral density does not depend on the frequency f, therefore both are the source of *white noise*.
G-R noise is a noise process specific for semiconductors and is caused by the statistical generation and recombination of charge carriers from trapping state (usually defects, dopants atoms or molecules) in the vicinity of the semiconductor [303]. This charge fluctuation causes voltage/current fluctuations at low frequencies and its spectral density is described by the Lorentzian function [303]:

$$S_I(f) = \frac{S_0}{1 + (2\pi f \tau)^2} \tag{4.3}$$

where S_0 is the frequency independent portion of $S_I(f)$ observed at $f < (2\pi\tau)^{\breve{}1}$ and τ is the time constant associated with a specific trapping state. . The most important contribution at low frequencies, however, arises from **Flicker-noise** which for most semiconductors shows an inverse proportionality to the frequency (thus also called **1/f-noise**)[305].:

$$S_I = a \cdot f^b \tag{4.4}$$

With a being the noise amplitude at f=0, and tipically $-1.5 < b < -0.5$.
The normalized amplitude of 1/f noise typically scales inversely with the channel volume, or, in the case of two-dimensional materials with the channel area[306, 304]. While the origin of 1/f noise is not completely understood, it is commonly agreed that the statistical fluctuations of electrical current (see eq. 4.5) which originate from either fluctuations in the mobility μ of charge carriers (the dominant source in metals) or fluctuations in their number N (as for semiconductors).

$$I \propto eN\mu \Rightarrow \propto e(\delta N)\mu + qN(\delta\mu) \tag{4.5}$$

A figure of merit for the 1/f noise, which initially was introduced specifically for the mobility fluctuations model and then extended also for other 1/f mechanisms, is

the Hooge parameter α_H, based on his empirical formula:

$$\frac{S_R}{R^2} = \frac{\alpha_H}{N \cdot f} \tag{4.6}$$

where $S_R \sim (\delta R)^2$ is the power spectral density of the fluctuations in the value of the resistance ($S_R/R^2 = S_I/I^2 = S_V/V^2$) and V is the voltage. The Hooge parameter α_H, varies from one system to another, and is often observed to be close to 10^3 10^2 for thin films of simple metals [306].

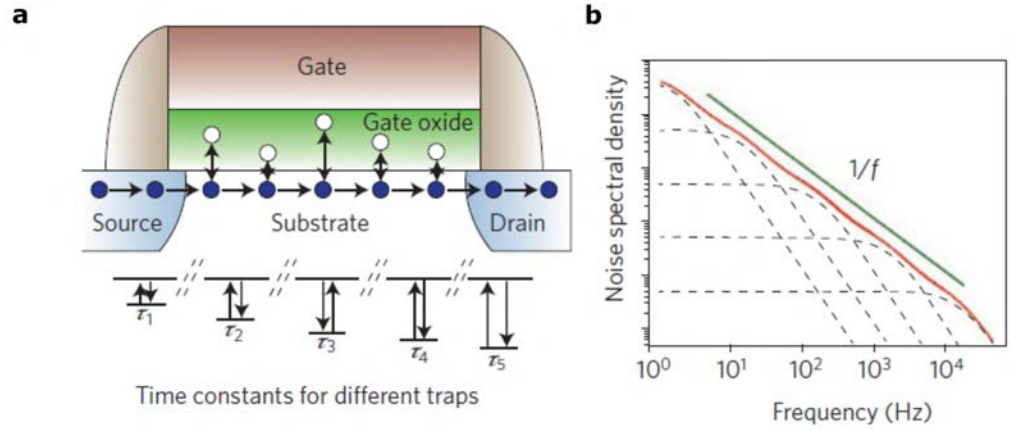

Figure 4.1: a, Schematic of a Si-CMOS device, showing charge traps in the oxide layer producing G-R noise with different lifetimes τ_i in the total current of the transistor. **b**, The 1/f noise in the McWhorter model is obtained as superposition of the Lorentzian shapes of each charge trap with its respective decay time. Taken from [304]

When charge carrier fluctuations (δN) dominate, the 1/f-shape has been explained in MOSFET devices using the McWorther model (eq. 4.7), which assumes a superposition of G-R noise contributions with changing trap times between τ_1 and τ_2,typically due to a varying distance of the trapping centres located in the oxyde layer from the channel where charges contribute to the current. The superposition of this trapping-detrapping mechanisms, gives rise to the 1/f shape of the noise power spectrum $S_N(\omega)$ in the range of frequencies $1/\tau_2 < \omega < 1/\tau_1$ (Figure 4.1) [307] Here $\omega = 2\pi f$ is the angular frequency. Introducing a density distribution of lifetimes, $g(\tau_N) = (\tau_N \cdot \ln(\tau_2/\tau_1))^{-1}$, one can write the spectral density of the number fluctuations S_N, in the form:

$$S_N(\omega) = \overline{4\delta N^2} \int_{\tau_2}^{\tau_1} g(\tau_N) \cdot \frac{\tau_N}{1 + (\omega\tau_N)^2} d\tau_N \tag{4.7}$$

In a MOSFET therefore, the 1/f noise dominates at the low frequency regime and its origin is attributed, as explained above, to charge fluctuations due to the random trapping and detrapping of the mobile carriers at Si/SiO_2 interface [308]. This hypothesis can be formulated in terms of an equation (eq. 4.8) which is derived to account for oxide trap induced noise in Si devices [309, 310, 311]. Thus, normalized noise power $\frac{S_I}{I^2} = \frac{S_R}{R^2}$ in MOS transistors is derived from the the McWorther charge traps noise model[309]:

$$\frac{S_R}{R^2} \approx \frac{\lambda \kappa_B T N_t}{f \cdot \alpha \cdot A_{Ch} \cdot n^2} \tag{4.8}$$

Where S_R is the PSD of the resistance, α is the charge tunneling constant (tunneling of charges through the oxide barrier to the conduction band), N_t is the number of charge trap state, A_{Ch} the active area of the transistor (in our case LxW), n the density of charge carriers and $\kappa_B T$ the thermodynamic energy of the system. Charge carrier noise is often also described as surface noise, as it becomes more pronounced for thin channel materials, due to increasing influence of proximity charge traps.
Mobility noise can be referred to as volume noise as it prevails in bulk materials [312]. Mobility fluctuations are related to energy fluctuations and are conditioned by random non-elastic scattering and generation-recombination processes. In particular, mobility fluctuations come into existence as a result of random electron-phonon and phonon-phonon scattering processes[306, 313].
In the case of graphene, however, this differentiation between the two distinct noise sources is challenging, as it features both metallic and semiconducting properties, which can lead to comparable or combined contributions of either type of 1/f noise[304]. However, their geometric dependency makes graphene-based devices more prone to be dominated by charge carrier noise, unless the channel material is decoupled from proximity traps. Strategies so far proposed to reduce 1/f noise in graphene devices includes: channel encapsulation with insulating materials (such as hBN or thin oxide layers) [314, 315], fabrication of free-standing sheets or stacking of multiple graphene layers [316].
The presence of two dominant noise origins, combined with additional noise contributions arising from the graphene/metal interface (Contact-noise S_{R_C}), also leads to a complex gate-bias dependence of 1/f noise in graphene FETs, which neither follows the Hooge's nor the McWorther's model.
For gSGFET, it has been shown that an expanded charge-noise model can be used instead[147]; it allows differentiating between a low carrier density regime, in which the noise is mostly generated by trapping-detrapping mechanisms, and a regime of

high carrier density, where scattering processes within the channel dominate the noise amplitude [317].
While there is a clear dependence of the level of current noise on the charge carrier density, and therefore the bias point in the case of carrier density fluctuations, the case of mobility fluctuations is nearly gate-independent. This complex bias dependence typically results in a M-shape behaviour of the current noise in monolayer graphene FETs for varying V_{GS}, with a minimum at the charge neutrality point (CNP)[147, 317, 304]. In devices where the contact noise S_{R_C} contributes significantly, this transitions into a V-shape behaviour with monotonic noise increases away from the CNP[304, 318].

In this work, low noise gSGFETs have been developed by addressing both, the channel and the contact contributions to the overall 1/f noise in graphene FETs. All noise measurements were done with the electronic setup described in Section 3.3. The electronics was powered by DC batteries and placed in a Faraday cage during the transistor characterisation, to avoid pick-up noise. For the measurements, V_{DS} has been kept constant (usually at 50 mV while V_{GS} was swept in steps of $\approx$ 100 mV.

4.2 Basic analytic tools to study noise

In order to investigate the electronic noise, the drain-source current I_{DS}, resulting from the applied V_{DS} and V_{GS} bias voltages, is recorded over time and evaluated in the frequency domain. To this end, the *power spectral density* (PSD) of the transistor current $S_I(f)$ is calculated by using the Fourier transform. For a time discrete signal $x[n]$ the discrete Fourier transformation (DFT) is given by:

$$\mathcal{F}(x[n]) = x(k) = \sum_{n=0}^{N-1} x[n] e^{i(2\pi/N)nk} \tag{4.9}$$

The transformed spectrum is periodic and symmetric with a frequency resolution $\Delta f = f_s/N$, being f_s the sampling frequency and N the number of samples. The PSD is then obtain by:

$$S_{xx} = \frac{1}{T}|\mathcal{F}(x)|^2 \tag{4.10}$$

With the period $T = N \cdot f_s$. For the PSD of the gSGFET current I_{DS}:

$$S_I(f) = \frac{2}{T}\overline{\mathcal{F}(I(t))\mathcal{F}^*(I(t))} \tag{4.11}$$

where T is the averaging time, $\mathcal{F}(I(t))$ and $\mathcal{F}^*(I(t))$ are the Fourier transform and its complex conjugate of the current fluctuation in time $I(t)$.
The PSD is computed using the Welch's method, with the *Pyhton Scipy* built-in library function[1], which calculates an estimate of the PSD by dividing the data into overlapping segments, computing a modified periodogram for each segment and averaging the periodograms. An inverse dependence on the frequency (1/f noise) was found for graphene SGFETs on SiO_2 and on PI substrates, as observed for many semiconductors devices (see Section 4.1).
As already mentioned, the amplitude of the noise varies with the applied gate voltage V_{GS}. To quantify and better understand the 1/f noise, the PSD(f) was fitted by:

$$S_I = \frac{a}{f^b} + c \tag{4.12}$$

with a and b being fitting parameters of the 1/f noise, and c a constant to consider thermal and pick-up noises. To exclude the effects of the high pass filter of the setup in low frequency ranges (1-7kHz) and the thermal noise contribution at high frequencies, the noise data is usually fit between 5Hz and 5kHz. Figure 4.2 illustrates the dependence of the PSD vs V_{GS}, in a sample gSGFET (active area=40x40μm). Values for b between -0.7 and -1.2 were obtained, depending on the applied V_{GS}, in agreement with previous reports (Figure 4.2c).[304, 317]

[1] scipy.signal.welch() - https://docs.scipy.org/doc/scipy/reference/generated/scipy.signal.welch.html

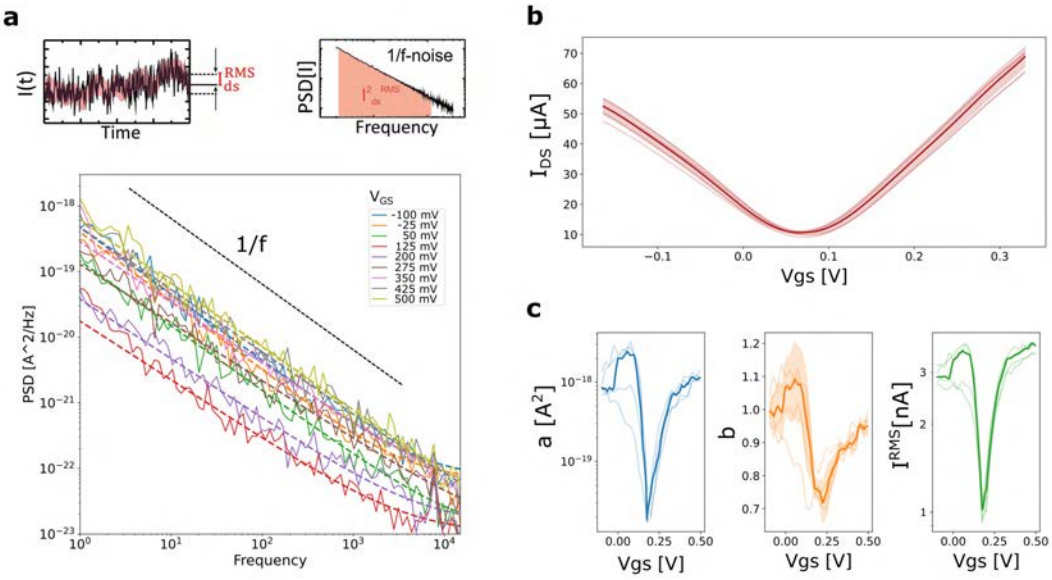

Figure 4.2: 1/f quantification in gSGFETs. **a**. 1/f noise is calculated from the I_{DS} fluctuations in time. The integral of the PSD over a frequency range corresponds to $(I_{RMS})^2$ (red shadow in upper graphs). The 1/f has a V_{GS} dependence and is fitted considering the thermal noise (dotted line). **b-c** Shows the variation of the noise parameters a,b, and I_{RMS} along the transistors transfer curves (**b**) for several gSGFETs produced during the thesis work on a SiO_2 substrate (area=40x40 μm^2,line is the mean, shadow the standard deviation).

To quantify the noise amplitude, the parameter a can be used as estimate of the PSD at 1 Hz. The amplitude of the current noise fluctuation can be evaluated also by integrating the PSD over the frequency of interest:

$$I_{RMS} = \sqrt{\int_{f_1}^{f_2} S_I \, df} \tag{4.13}$$

For sensing applications the most meaningful noise parameter is the so-called root-mean-square (RMS) gate noise defined as:

$$V_{RMS} = \sqrt{\int_{f_1}^{f_2} \frac{S_I}{g_m^2} \, df} = |\frac{I_{RMS}}{g_m}| \tag{4.14}$$

Here it is assumed that the transconductance g_m is constant over the frequency range of integration. For biological signals, the integration limits in this work are usually set to $f_1 = 1$ Hz to $f_2 = 7$ kHz. The V_{RMS} is not a peak-to-peak value of the electronic noise, but the root mean square (RMS) of the noise, over a period of time, for non-symmetric functions such as the random 1/f fluctuations (see Figure 4.2a). Any physiological signal that is smaller than the V_{RMS} cannot be detected by the

gSGFET, since it will be buried in noise. Consequently, the RMS gate noise can be used as an upper limit for the detection resolution.

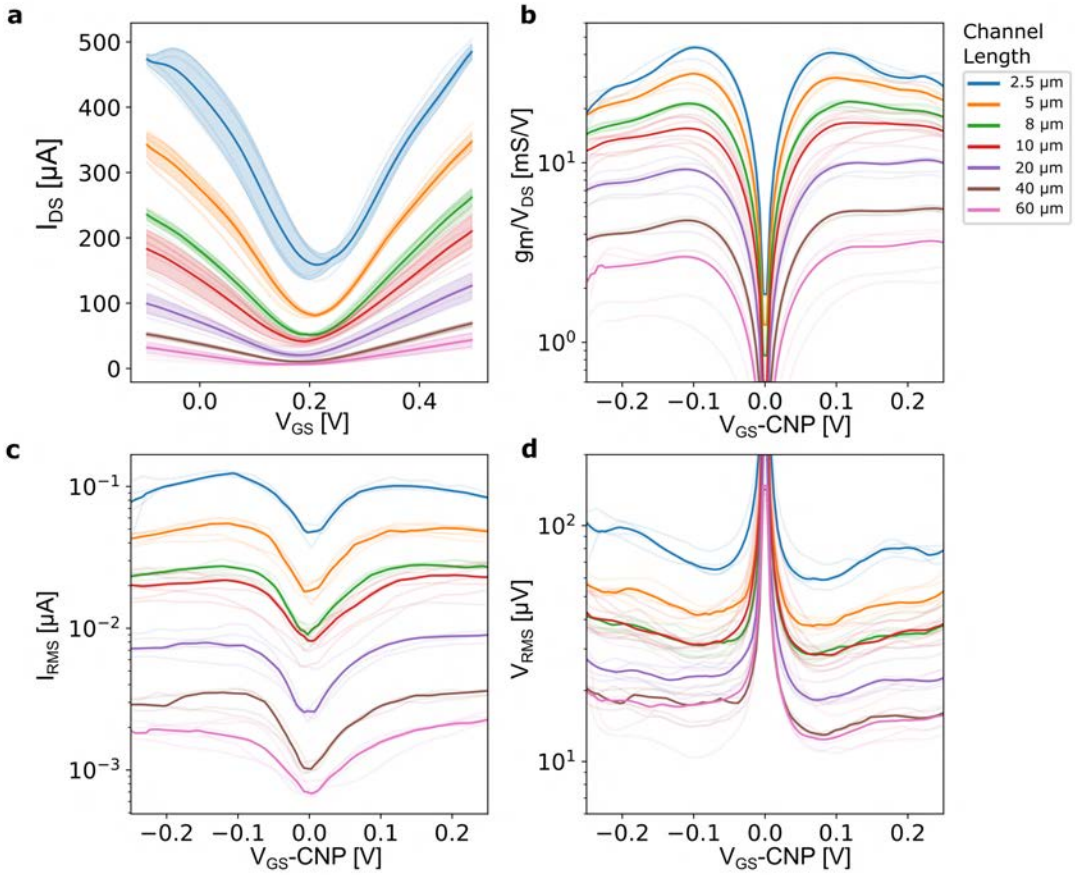

Figure 4.3: Noise characterisation of gSGFETs on a SiO_2 substrate with fixed width (W=40μm) and different lengths. The amplification of the gSGFET varies with the length of the graphene channel (from L=60 μm to L=2.5 μm). (**a-b**) shows the average I_{DS} current (dark line, four transistors each line) and normalized transconductance g_m/V_{DS} for different gSGFET channel lengths. (**c-d**) Current noise (I_{RMS}) and effective gate noise (V_{RMS}) for different channel lengths.

Figure 4.3 shows the I_{RMS} and V_{RMS} of graphene SGFETs as a function of the gate voltage. It also shows the I_{DS} currents and the amplification (g_m/V) of the gSGFETs, for a fixed width (W=40μm) and different lengths of the transistor channel. The transconductance increases with the geometrical factor W/L; however, the current noise I_{RMS} and the corresponding effective gate noise V_{RMS} also increase with smaller areas. It should be noted that the I_{RMS} scales with $1/\sqrt{A_{Ch}}$ (see eq. 4.8 and Figure 4.4). Values down to tens μV are obtained close to the CNP for gSGFETs, in good agreement with previous reports [66].

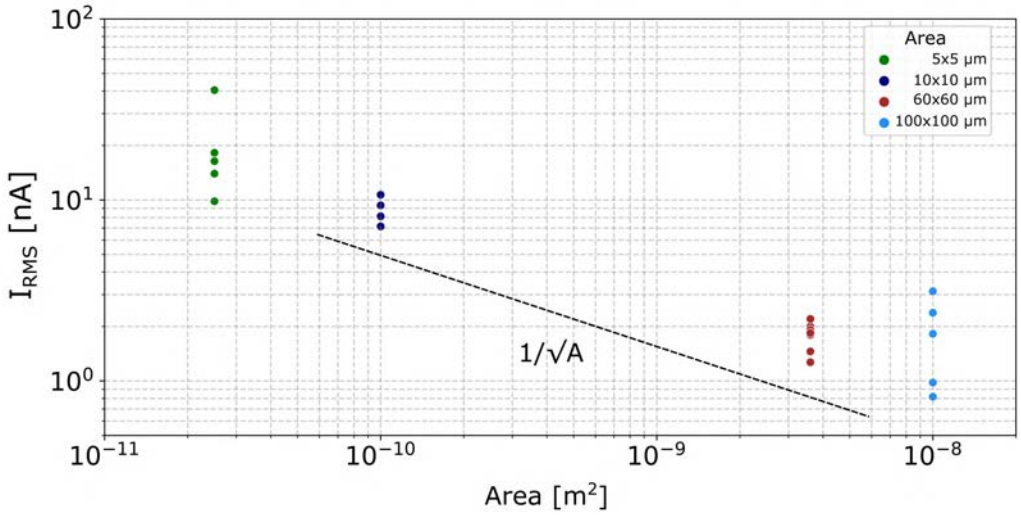

Figure 4.4: I_{RMS} ($V_{gs} = -0.1$) vs active area of squared gSGFETs. The current noise scales with $1/\sqrt{A}$.

The next section describes some strategies developed in the frame of this PhD, that enabled us to reach the important target of reducing the contact resistance and decrease the noise generated at the graphene/metal interface of the gSGFETs. The work, done also in collaboration with other PhDs in the team, has been published this year in the journal *Carbon* with the title: *Improved metal-graphene contacts for low-noise, high-density microtransistor arrays for neural sensing* [145].

4.3 Contact noise

Poor metal contact interfaces are one of the main limitations preventing unhampered access to the full potential of two-dimensional materials in electronics [319]. Contact noise results from time-dependent resistance fluctuations at the metal-channel interface and becomes more relevant with increasing contact resistance R_C. High R_C has a negative impact on the performance of graphene FETs. In the case of graphene, it has been explained by the work function mismatch between graphene and contacting metals, by the lack of dangling bonds at metal-graphene interface and the low density of states in graphene, which results in a poor charge carrier injection [319, 222, 320]. Common strategies to reduce contact resistance include the controlled creation of defects in the graphene lattice through its exposure to oxygen plasma [321] or ozone [225], and the use of contact metals which interact strongly with graphene (e.g. nickel or palladium) [322, 323, 324].
In order to lower the metal-graphene contact resistance in wafer-scale gSGFET

technology, we used the treatment of the exposed contact region of graphene to ultra-violet ozone (UVO) prior to metal deposition (Figure 4.5). This technique has previously been reported to significantly improve charge injection through both surface cleaning of micro-fabrication residues (i.e. photoresists residues) and defect creation in the graphene sheet[225, 325].

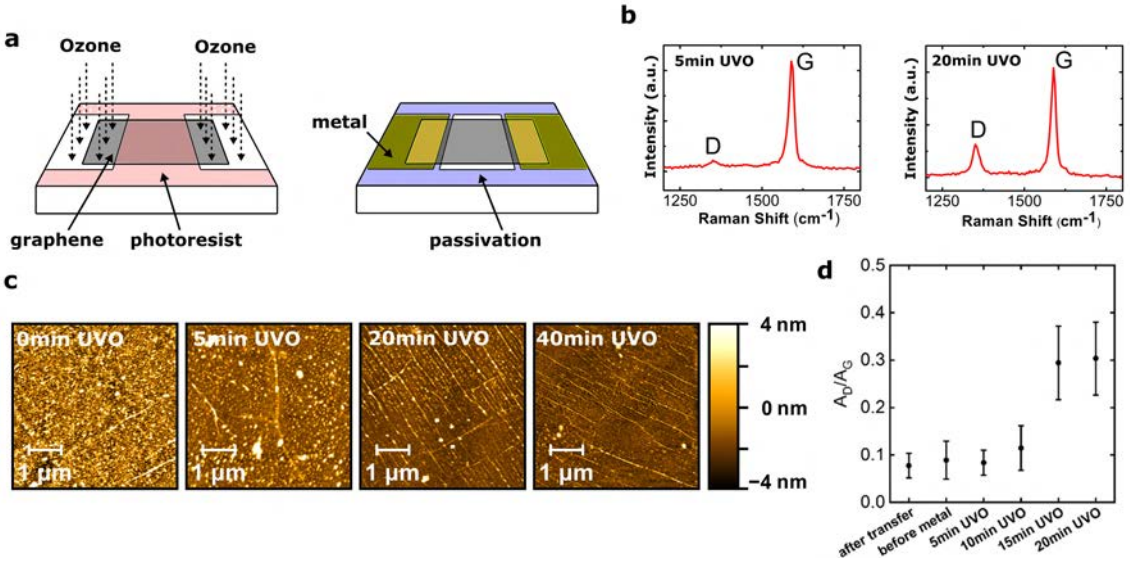

Figure 4.5: a. Schematic of device fabrication with ultra-violet ozone (UVO) applied to the graphene contact region prior to the metal deposition. **b**. Raman spectra after 5 min and 20 min UVO treatment show an increase of the D-peak for longer treatments. **c**. Surface roughness of the graphene layers measured by AFM. The lowering of the surface roughness root-mean-square value from 2.1 nm to 1.1 nm for 20 min UVO treatment indicates an effective cleaning of surface residues. **d**. Ratio of peak intensities of the D-band and G-band of single-layer graphene used as an indicator for the amount of residues and defects in the graphene sheet for different UVO exposure times. Adapted from [145]

Figure 4.5b and d show the evolution of A_D/A_G as a function of UVO treatment duration. The Raman spectra show a clear increase of peak amplitude of the D-peak, which can be attributed to a breaking of sp^2-bonds in the graphene lattice. In this work, UVO treatment has been applied at room temperature and due to the small size of the exposed contact region, surrounded by areas covered with photoresist, defects in the graphene film at the contacts are expected to be induced at a slow rate. In the case of the 20 min UVO duration, the resulting low D/G-ratio (0.3) together with the absence of a noticeable D'-band indicates a low defect density, predominantly with a sp^3-type nature [207, 326]. Since the sp^2 orbitals hinder charge injection along the z-plane [327], the creation of defects by long UVO treatments improves the charge injection, which results in a decrease of contact resistance. These

results are in good agreement with previous studies [225]; however, the duration of the UVO treatments certainly depends on the particular experimental setup used for the UVO treatment.
The change in surface topology resulting from the UVO treatment was analyzed by atomic force microscopy (AFM). Figure 4.5c illustrates the surface roughness of the graphene measured at the contact region, before and after different treatments. The rms roughness of the scanned areas lowers from 2.1 nm for no-treatment (0min UVO) to 1.1 nm for 20min and to 0.8nm for 40 min UVO treatment, indicating a continuous and significant cleaning of the graphene surface.
The transfer length method (TLM, see section 3.3) was used to assess the values of the contact resistance R_C and the sheet resistance R_{Sh} of the channel in our wafer-scale fabricated gSGFETs (see Section 3.1). Figure 4.6a-b, shows R_C and R_{Sh} of the graphene channel for 20min UVO exposure compared to the no-treatement scenario. It is worth to note that, the TLM method assumes a constant sheet resistance per unit area across the whole transistor channel. However, this assumption is only correct for cases in which the applied gate bias is much larger than the drain-source bias ($V_{GS} >> V_{DS}$). While this is mostly true for FET designs that use a relatively thick dielectrics, solution-gated FETs are operated at much lower V_{GS}. In gSGFETs, the potential difference between channel and gate is not constant but changes gradually along the channel, which leads to a non-uniform sheet resistance; this can result in unreliable values for R_C, in particular in the vicinity of the CNP (grey shaded region of Figure 4.6a).

The R_C far away from the CNP (Figure 4.6a) yields values around 3-4 $k\Omega$ for the case of a non-treated contacts and reaches a value as low as 0.6 $k\Omega$ for a 20-30 min UVO treatment. Longer treatments result in an increase of R_C, as a high defect density in the UVO treated graphene sheet eventually reduces the charge conduction. As expected, R_{Sh} remains independent of the UVO treatment, since the channel region is protected by the photoresist during exposure.

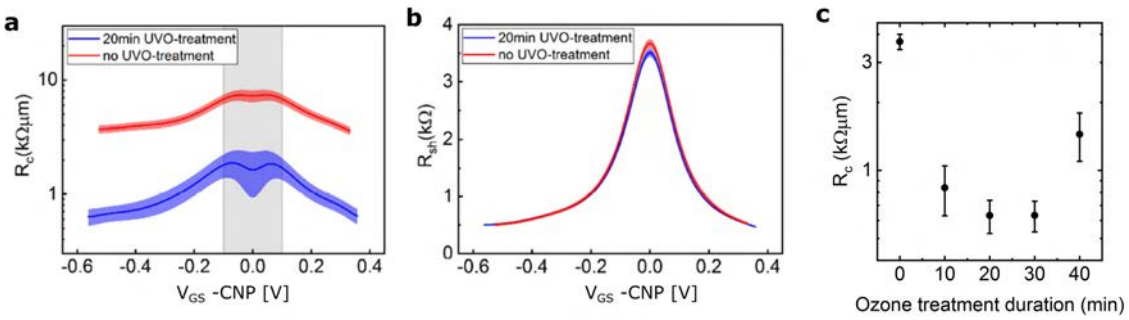

Figure 4.6: R_C (**a**) and R_{Sh} (**b**) measured as a function of applied gate bias for UVO-treated and non-treated devices. The shaded region close to the CNP does not yield reliable values for R_C, as here the applied gate bias reaches similar values than the drain-source bias ($V_{DS} = 20$ mV), leading to a non-constant R_{Sh} along the channel. **c.** R_C (obtained at -0.5V from CNP) as a function of UVO-treatment duration, showing optimal results for 20min and 30min UVO exposure. Adapted from [145]

In sensing applications, the contact resistance in gSGFETs is of critical importance for their proper operation. Poor current injection at contacts reduce the linearity of the transfer characteristics causing signal distortions, lowering of the signal-to-noise ratio of the recorded signal and limiting the sensor homogeneity. Figure 4.7 illustrates the effect and importance of improved contact resistance on the performance of the gSGFET. For non-treated gSGFET, the $I_{DS} - V_{GS}$ curve shows a flattening of the V-shape away from the CNP due to the contribution of the contact resistance. This limits the linear regime of the device's around the operation point (usually at peak-transconductance) leading to significant distortion of the transduced signal thus affecting the signal fidelity. In addition, it lowers the transconductance g_m. We can observe a two-fold increase of peak-g_m, thanks to contacts improvement. (Figure 4.7b).

More important than the transconductance, however, is the observed reduction, and less variation across an extended bias window of the effective gate noise V_{RMS}, as a consequence of the reduced R_C, particularly for short graphene channels (Figure 4.7c). The effects of the UVO treatment becomes more pronounced when moving further away from the CNP: V_{RMS} remains fairly constant in the case of low R_C and increases rapidly for devices with high R_C (grey area in Figure 4.7c). This is particularly interesting when operating the gSGFET *in vivo*, which typically requires using a common bias point for all devices. Both, increased g_m and decreased current noise I_{RMS}, allows for improved signal-to-noise ratio (SNR) of the gSGFETs sensors (Figure 4.7c).

As described in the previous section (see section 4.1), the improvement of the electric

noise strongly depends on the device's geometry (see Figure 4.7d), being most pronounced for short channel lengths. In addition to electric noise reduction, the dispersion of the noise across several devices strongly improves as well with the UVO treatment. Device homogeneity is important in sensor arrays since it allows uniform recording quality of all sites on the array.

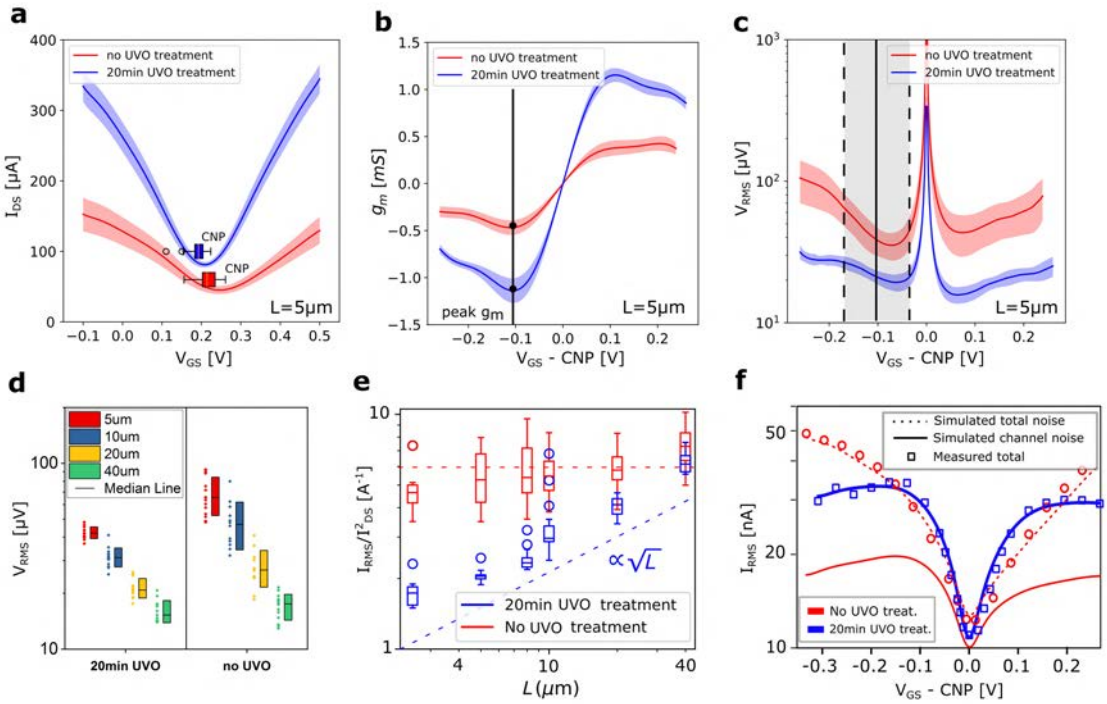

Figure 4.7: Average value and standard deviation of transfer curves for drain-source current I_{DS} (**a**), transconductance g_m (**b**) and effective gate noise V_{RMS} (**c**) for devices of 5μm channel length and 40 μm channel width. **d**. Statistical variation of V_{RMS} values at peak transconductance ($V_{GS} = CNP - 0.1$ V) for devices of different channel length for no-treatment and 20min UVO reatment. **e**. Dependence of the normalized current noise I_{RMS}/I_{DS}^2 ($V_{GS} = CNP - 0.1$ V) versus the channel length (L) for devices with non-treated and treated contacts. **f**. Experimentally measured integrated current noise I_{RMS} versus V_{GS}, plotted for non-treated and treated contacts in devices of 5μm channel length. The lines correspond to the fitting of the experimental data with a model that considers the contributions of the channel noise only (solid line) and of both, channel and contact noise (dashed line). Adapted from [145]

The improvement in device performance resulting from the contact treatment directly leads to two questions:

- What is the contribution of the contact noise compared to the channel noise?
- What is the root cause of the contact noise improvement?

The total normalized noise S_I/I_{DS}^2 generated in a gSGFET includes the contribution of the contacts (S_{R_C}) and the channel ($S_{R_{Ch}}$). The contributions of these terms to the measured current noise can be added linearly with the proper normalization:

$$\frac{S_I}{I_{DS}^2} = \frac{S_{R_C} + S_{R_{Ch}}}{R_T^2} \tag{4.15}$$

Here R_T is the total resistance of the transistor. The dependence of each of these terms on the channel width (W) and length (L) will determine their relative contribution to the total noise for different geometries. The geometrical dependence of S_{R_C} and S_{R_Ch} can be expressed explicitly :

$$\frac{S_I \cdot f}{I_{DS}^4} = \left(\frac{k_{R_C}}{W^3} + \frac{k_{R_{Ch}} \cdot L}{W^3}\right) \cdot V_{DS}^{-2} \tag{4.16}$$

where k_{R_C} and $k_{R_{Ch}}$ include all the constants which are independent of the channel dimensions for S_{R_C} and $S_{R_{Ch}}$ respectively. The relative contribution of each term can therefore be identified by evaluating the dependence of noise ($I_{RMS} \propto \sqrt{S_I}$) on L. Thus, I_{RMS} exhibit a $\propto \sqrt{L}$ when channel noise dominates, and should remain constant with L if contacts are the dominant source (see also Appendix A.3).
Plotting the experimentally measured normalized current noise (I_{RMS}/I_{DS}^2) for devices of varying channel length, the noise in devices with untreated contacts remain fairly constant. However, devices with UVO-treated contacts (20 min treatment duration) show a transition from this approximately L-independent regime to a $\propto \sqrt{L}$ regime (Figure 4.7e). While for gSGFETs with channel length of around L=60 μm both noise sources contribute equally to the total normalized noise, for devices with shorter channels the normalized current noise is significantly lower in the case of UVO-treated contacts (Figure 4.7e).
To further explore the transition from a contact noise to a channel noise dominated regime, the gate-bias dependence of the measured total noise was modelled using a channel noise model for gSGFETs [147] and adding the contact noise contribution to it [145]. It can be seen in Figure 4.7f how for untreated devices the channel noise model strongly underestimated the measured current noise, meaning that for most of the V_{GS}-range contact noise is dominant. Conversely, for UVO-treated devices the contact noise model fit the experimental data as contact noise is suppressed. It should be noted that when contact noise contributions prevails, the I_{RMS} curve displays a V-shape, whereas it changes towards the M-shape characteristic for dominating channel noise. A transition line equivalent circuit model is proposed [145] for simulating the improvement of both the metal-graphene R_C and the resulting contact noise S_C.

Increased z-plane charge injection due to the removal of fabrication residues and defect creation during the UVO treatment leads to current crowding at the contact edges, shortening the length of the graphene sheet under the contacts in which the current passes through. More details about the model can be found in [145].

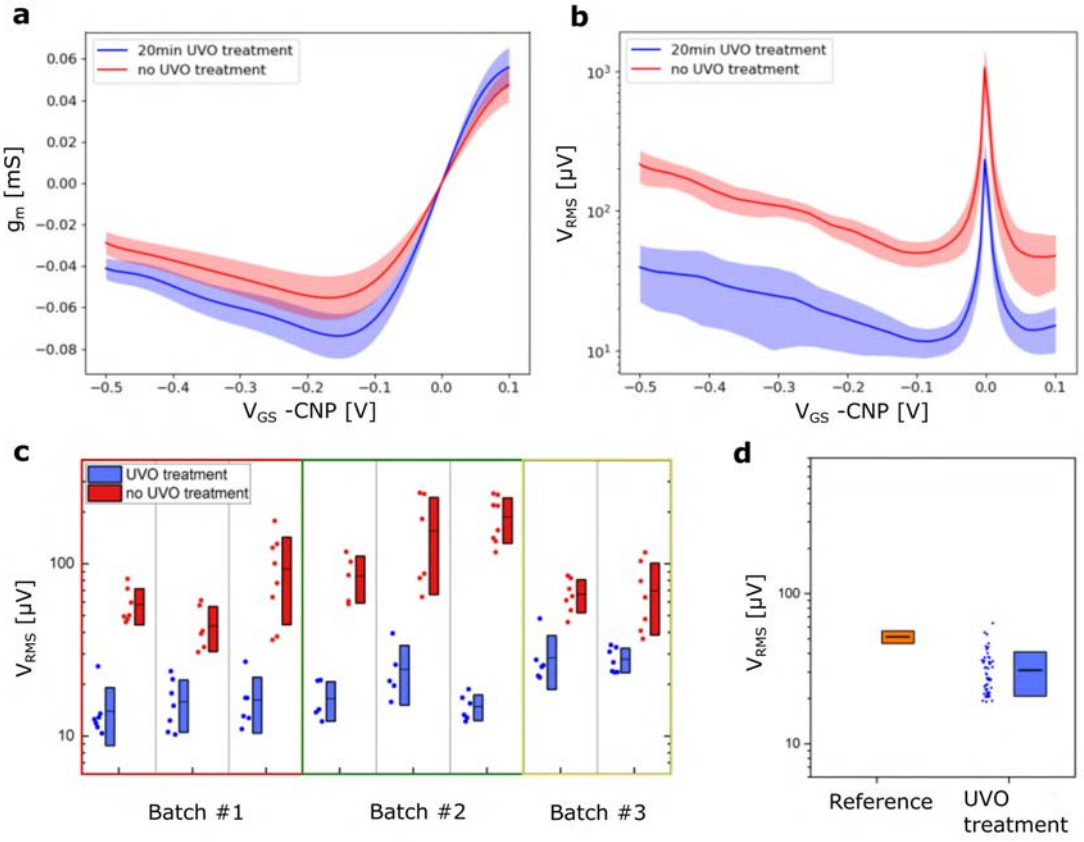

Figure 4.8: a. Average values of transconductance g_m and effective gate noise V_{RMS} (**b**) as a function of applied gate bias V_{GS} for a flexible epi-cortical probe treated with 20min UVO (blue) and one not treated (red). **c**. Comparison of the effective gate noise V_{RMS} (integrated from 1 Hz to 100 Hz) for different neural probes (WxL: 20 μm x 20 μm) across several wafers (grouped in fabrication batch) indicates the high repeatability of the technique. For each batch (grouped in color boxed), probes from two independent wafers are compared. For each device the mean value and standard deviation as well as the individual data points are shown. **d**, V_{RMS} mean value (integrated from 1 Hz to 5 kHz) and standard deviation obtained with the UVO contact improvement presented in this work compared to previously reported noise values for gSGFETs with a "sandwich-contact" configuration (graphene sheet contacted from bottom and top) [70].

The contact improvement study on rigid SiO_2 substrates was successfully implemented also for the final application, the flexible graphene neural probes.

Figure 4.8a shows average g_m for epi-cortical probes treated and non-treated with UVO at contacts. A clear decrease in the detection limit is also observed in the UVO treated flexible graphene probes compared to the non-treated ones (Figure 4.8b). As repeatability is an essential criterion when introducing technology improvements for large-scale device fabrication, we also assessed the reliability of the UVO treatment to provide low contact resistance and reduced contact noise in gSGFETs. Therefore, the procedure has been applied to independent wafers undergoing identical process flows (apart of the UVO-treatment step). Figure 4.8c compares the effective gate noise of UVO-treated and non-treated gSGFETS (WxL: 20 μm x 20 μm) of several devices on independent wafers fabricated in different batches (grouped by colour boxes). While small variations in measured noise values can be seen between different devices, which are attributed to non-identical graphene quality and changes in the amount of surface residues, the mean noise value of the UVO-treated gSGFETs always compares highly favorably towards the one of the untreated devices. In previous work [70], a mean effective gate noise value of 21 μV $\pm$ 2 μV (integrated from 1 Hz to 5 kHz) has been reported for gSGFETs of size 30 μm x 80 μm. To compare this noise value to the one obtained for UVO-treated gSGFETs, renormalization by a surface ratio term has been taken into account for the $1/\sqrt{A}$ dependence of flicker-noise, yielding an expected mean V_{RMS} of 52 μV $\pm$ 5 μV for devices of size 20 μm x 20 μm. Figure 4.8d compares this predicted noise value to the ones measured for gSGFETs with the UVO contact improvement, showing the clear impact the treatment has on the noise performance.

The flexible neural probe devices with improved SNR were also successfully used, in this thesis work, for *in vivo* experiments with epileptic rodents models (Section 5.2).

4.4 Channel noise

In the above section, the impact of contact noise and channel noise on the overall 1/f noise in gSGFETs has been closely investigated and discussed. The UV-ozone contact treatment has been presented as a reliable method to reduce high contact resistance and contact noise in gSGFETs.

As a further step towards ultra-low noise sensors, channel noise has been addressed and lowered as well. As previously mentioned, channel noise in gSGFETs was found to be dominated by charge carrier fluctuations due to trap states in the underlying graphene substrate or surface contaminants [52, 147]. Strategies to isolate

the graphene channel from the hampering influence of trap charges in its vicinity, include the engineering of free-standing channels [328] and the use of buffer materials. Popular materials reported in the literature, are high quality thin dielectrics, such as multiple or single layers of hexagonal-boron nitride (hBN). hBN is an electrical two-dimensional insulator which can be obtained by either mechanical exfoliation or CVD growth [329, 330, 331]. It has been demonstrated that 1/f noise in graphene transistors can be strongly suppressed, when the graphene channel is encapsulated between two layers of hBN, due to the lower density of impurities and trap sites in the hBN layer compared to thermal oxides [52, 315].
In recent years, hBN has been extensively studied and used for encapsulation purposes and as gate dielectric in graphene FETs due to its atomically thin surface and its minimal lattice mismatch with graphene [329]. Apart from reducing the noise, studies show that hBN strongly improves the device's carrier mobility due to screening from dominant scattering sources such as charge impurities and surface phonons [329, 332, 333].
Bilayer graphene transistors have also served as a mean to reduce the intrinsic 1/f noise in graphene [317, 334]. More recently also doubled transferred (DT) CVD graphene in field effect transistors configuration showed similar characteristics than single layer graphene FET but with decreased noise amplitude [335, 228]. The noise reduction is understood to result from an increase of charge carriers in the channel, from screening of adsorbed molecules and charge traps in the substrate or in the graphene surface. To demonstrate this hypothesis, we fabricated a DT-gSGFETs following the fabrication steps described in section 3.1.
As for other reported strategies for noise reduction in graphene, self-assembled monolayer (SAMs) is considered, which turn the SiO_2 substrate surface hydrophobic; such as hexamethyldisilazane (HMDS), allowing for electrostatic screening of charges [336, 337, 338, 339]. Furthermore, surface adsorbates such as hydroxyl groups, which attach to either the silicon substrate or defects in the graphene surface, facilitate subsequent bonding of e.g. dipolar molecules, which in turn have been identified as a primary cause for non-uniform doping and transfer curve hysteresis in graphene FETs [315].

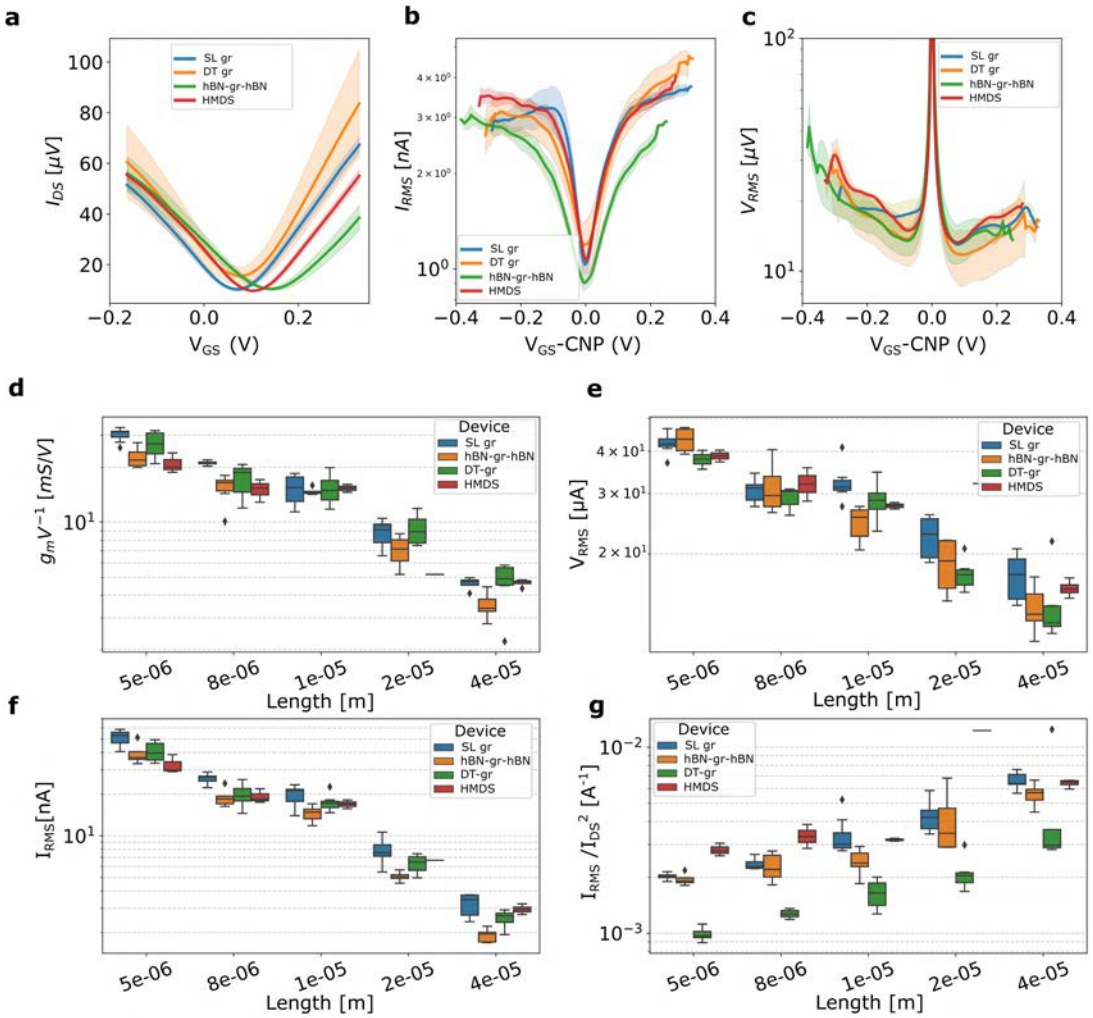

Figure 4.9: Average value and standard deviation of transfer curves for: **a**. Drain-source current I_{DS}, **b**. Integrated current noise I_{RMS} and **c**. Effective gate noise V_{RMS} for an applied drain-source bias V_{DS} of 40 mV and device 40 μm x 40 μm channel size. All noise values where calculated for an integration range from 1 Hz to 5000 Hz. (d-**g**) Boxplot of noise parameters: **d** transconductance g_m/V ,**e** V_{RMS}, **f** I_{RMS} and **g** normalised current noise I_{RMS}/I_{DS}^2 at peak transconductance ($V_{GS} = CNP - 0.1$ V) for several channel lengths (5 μm, 10 μm, 20 μm and 40 μm) and constant channel width of 40 μm for a graphene channel either directly placed on the SiO2 wafer (SL gr), with an HMDS buffer layer (HMDS), encapsulated in hBN (hBN-gr-hBN) and for double transfer graphene (DT-gr).

Coating the silicon wafer before graphene transfer with hydrophobic surface-modifying agents (such as HMDS), can prevent the attachment of such adsorbates, thus inhibiting degradation of the electric properties of the graphene FET. A threefold increase in carrier mobility has been linked to the successful screening of the graphene lattice as a result of such hydrophobic treatment [336]. For the case of hBN encapsulation, CVD-grown multilayer hBN has been transferred pre and post

graphene transfer to form a top and bottom encapsulation, in order to protect the channel from substrate defects as well as from the adsorbates from the contacting electrolyte.

For more details about the fabrication see section 3.1. All devices used in this study have been treated at the graphene/contact interface with UV-ozone, as described in the previous section; in this way, we can ensure that the predominant 1/f noise contribution originates in the channel.

Figure 4.9d-g, shows the transconductance and noise parameters (V_{RMS}, I_{RMS}, I_{RMS}/I_{DS}^2) at peak g_m for various engineered gSGFETs with varying length. The improvement resulting from the different strategies to influence channel noise is most clear for devices with long channels, suggesting that for short channels contact noise might still strongly contribute. For longer channels (>20μm), the lowest values for V_{RMS} and I_{RMS} are reached by the encapsulated graphene (hBN-gr-hBN) and the DT-graphene SGFETs. Evidence of the noise reduction in DT-graphene and hBN-graphene-hBN is more clear in Figure 4.9g, where the normalised integrated I_{RMS}/I_{DS}^2 noise is plotted for all lengths. While the HMDS-treated surface apparently did not significantly improve the noise performance compared to graphene directly placed on the SiO_2 substrate, the bilateral hBN encapsulation shows a positive impact on V_{RMS}. Transfer characteristics of the four types of gSGFETs are compared in Figure 4.9a for the case of transistors with a long channel length (40 μm). The differences in the CNP position is an indication of the different doping level of graphene: HMDS and encapsulated hBN transistors exhibit higher p-type doping than the control (graphene on SiO_2) or the double transfer graphene. The bias-dependence of the integrated current noise (Figure 4.9b)reveals a slight change from a M-shaped dependence (for devices directly fabricated on SiO_2), which is characteristic for noise dominated by the channel region, to a V-shape, which indicates in this case a significant reduction of channel noise, hence a dominance of the residual contact noise.

Channel encapsulation is further expected to augment the charge carrier mobility in graphene FETs, which in turn should result in higher transconductance; however, Figure 4.9d shows comparable values to the case of single layer graphene. This can be explained by the transconductance not only being proportional to the charge-carrier mobility but also the double-layer capacitance at the graphene electrolyte interface, which is likely to decrease due to the thickness of the top hBN layer separating the ions from the channel. Supporting this explanation, a small reduction in of g_m is also observed for DT-gSGFETs.

Thus, fabrication strategies based on DT graphene and channel encapsulation with multilayer hBN lead to a decrease of both, sensitivity and intrinsic noise of the device; yet an overall positive effect on the SNR (V_{RMS}) remains, as can be seen in Figure 4.9e. In contrast to the results reported in the literature [315], hBN encapsulation in our case increased the amount and dispersion of p-type doping of the devices, compared to a plain SiO_2 substrate (Figure 4.9a); this can indicate that either a large amount of organic residues from the transfer process remained between the stacked layers or that the CVD-grown multilayer hBN has a high density of defects. Yet, the preliminary results obtained suggest that DT-graphene and hBN encapsulation are very promising strategies for channel noise mitigation, to obtain ultra-low noise gSGFETs.

In order to optimize the results of this study, it is suggested a further improvement of the fabrication procedure to provide a contamination-free stacking of layers, as well as improving the quality of the hBN synthesized by CVD growth. Also, the thickness of the top encapsulation layer has to be fine-tuned, ideally providing sufficient protection from adsorbates and surface contamination without decreasing the double-layer capacitance and thereby the sensitivity of the sensor.

5

In-vivo experiments and full bandwidth recordings

This chapter illustrates the *in vivo* experiments conducted to assess the potential of the flexible neural probes developed in this PhD. First, the chapter discusses the electro-corticographic recording performed with epi-cortical probes in anesthetised rats, in which cortical spreading depressions (CSDs) are chemically induced by appling KCl in the cortex. The results highlight the ability to map CSD and demonstrate that the gSGFETs are able to record with high fidelity infraslow signals together with signals in the typical local field potential bandwidth.

In a second section, the chapter summarizes the *in vivo* experiments performed in awake pre-clinical rodent models of induced seizures and chronic epilepsy, reporting full-bandwidth recordings using the developed gDNP technology. It is shown that gDNPs can reliably record and map with high spatial resolution seizures, post-ictal spreading depolarisation, and high frequency epileptic activity, through cortical laminae to the CA1 layer of the hippocampus, in a living mouse model of chemically-induced seizures.

In the third part, the chapter demonstrates the operational functionality of chronically implanted devices for over 10 weeks, by recording with high fidelity spontaneous spike-wave discharges and associated infraslow activity in a rat model of absence of epilepsy[1]. In addition to the chronic functional validation of the gDNP, an extensive

[1]All *in vivo* experiments with epileptic rodents were conducted at the *Department of Clinical and Experimental Epilepsy, Queen Square Institute of Neurology* at UCL in London in collaboration with Dr. Rob Wykes and Dr. Trevor M. Smith who performed all surgeries.

chronic biocompatibility study has been conducted[2] to assess any potential neuro-inflammation caused by the invasive nature of the penetrating neural probes and by the residual silk-fibroin in the neural tissue. The data is discussed and compared to recordings using competing technologies. Altogether, this chapter highlights the successful suitability of this technology for *in vivo* electrophysiology research, in particular, to examine the contributions of infraslow activity to seizure initiation and termination. This chapter is based on the following publications achieved in the course of the PhD work:'High-resolution mapping of infraslow cortical brain activity enabled by graphene microtransistors'[63] and "*Full bandwidth electrophysiology of seizures and epileptiform activity enabled by flexible graphene micro-transistor depth neural probes*" (submitted).

5.1 High-resolution mapping of infraslow cortical brain activity

To show the capabilities of graphene transistors to record *in vivo* electrophysiological signals in the infraslow (<0.1 Hz) frequency regime, cortical spreading depolarisation (CSD) was induced and recorded with the epicortical 4x4 graphene SGFETs array prepared for this activity (see Section 3.2).

Experimentally, two craniotomies were performed over the left hemisphere of isoflurane-anaesthetized Wistar rats: a larger craniotomy over the primary somatosensory cortex, where the epicortical probe was placed, and a smaller one in the frontal cortex, where 5 mM KCl was applied locally to induce CSD (Figure 5.1). Figure 5.2 shows a sequence of four induced CSDs, recorded in both the LPF and BPF bandwidth with on of the gSGEFTs of the epicortical array. The graphene transistors were polarized in the hole conduction regime, that is $V_{gs} <$ CNP (negative g_m), resulting in an inversion of the recorded LPF and BPF current signals with respect to the voltage signal occurring at the gate. The LPF signal shows the very slow CSD event whereas the BPF signal corresponds to the local field potential (> 0.1 Hz), revealing the silencing of LFP activity characteristic of CSD [90]. The wide-band electrophysiological signal is obtained after the the LPF and BPF are combined and calibrated (see Figure 5.2, see also Appendix A.5.3). The calibration procedure enables us to eliminate both, the variations associated with the different

[2]The biocompatibility study was performed at the *Nanomedicine Lab, Faculty of Biology Medicine Health National Graphene Institute* in Manchester in collaboration with Prof. Kostas Kostarelos, Dr. Matthew Drummond, Dr. Sinead Savage and Dr. Katharine Barr

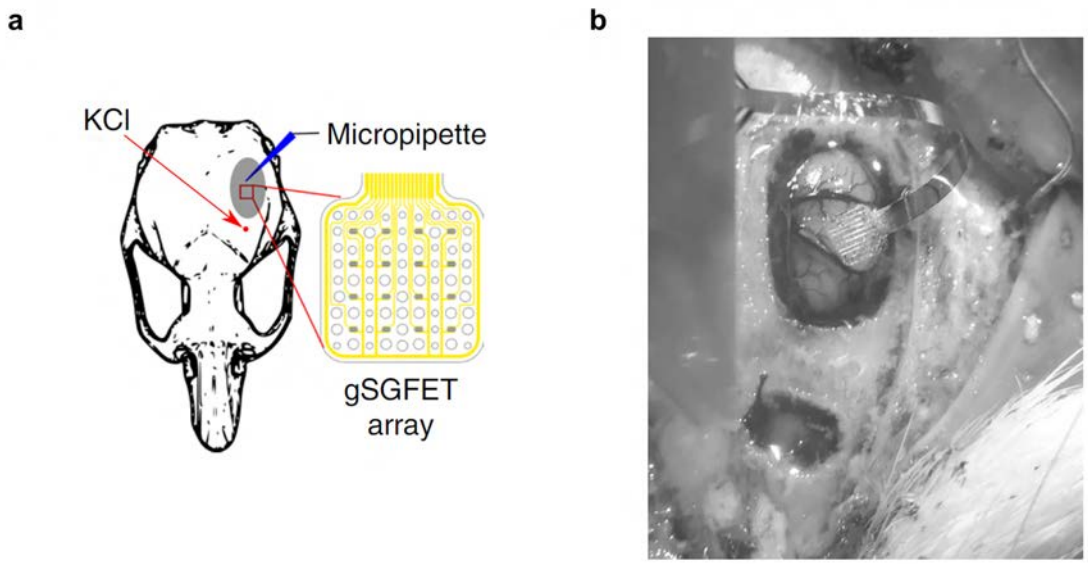

Figure 5.1: a, Schematic of a rat skull showing the location of the epi-cortical probe, the glass micropipette used to compare recordings and the point where KCl is applied to induce CSDs. **b**, Photograph of the craniotomy over the anaesthetized Wistar rats and the positioning of the flexible epi-cortical probe as well as the second smaller craniatomy site where KCl is applied. From [63]

current levels (of each transistors on the array), and the g_m differences at the bias point between the transistors. Every recorded CSD event is generally preceded by a small positive shift of 1-2 mV, followed by a steep negative change (≈-20 mV), which slowly recovers during the next minutes.

In order to evaluate the fidelity of the infra-slow activity recorded with the graphene SGFETs, an experiment has been designed to compare the performance with a solution filled glass micropipette with a Ag/AgCl wire as well as with other microelectrodes (see Figure 5.3).

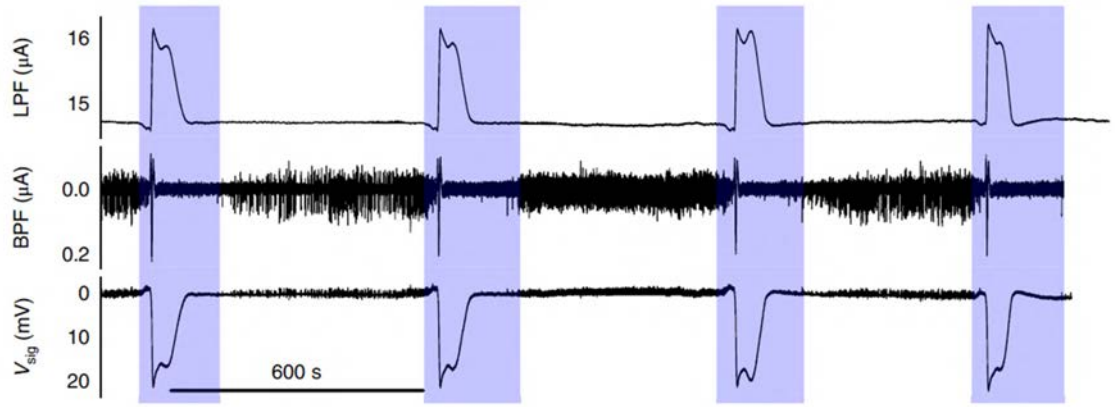

Figure 5.2: The transistor current in the low-pass filtered (LPF) and band-pass filtered (BPF) bands are combined to reconstruct (taking into account the current-to-voltage conversion) the wide frequency band signal. The plot illustrates electrophysiological recordings obtained with a gSGFET epicortical array during the induction of four CSD events (blue shade). From top to bottom: LPF, BPF and voltage-converted wide-band signal. From [63]

To this end the epicortical gSGFET array and a neural probe consisting of microelectrodes grouped in triodes were placed close to each other on the cortex to simultanously record the induced CSD. The microelectrode consists of gold microelectrodes of 50μm diameter 200μm apart; one microelectrode of each triode was modified by deposition of platinum black to lower its impedance [340, 341, 342]. More details about the design and fabrication of the neural electrodes can be found in the Appendix Figure A.6 and in the publication of E. Masvidal-Codina et al. [63]. Polarisation-induced drift is one of the intrinsic limitations of microelectrode technology to record correctly ISA (see Section 1.1.3). A representative recording is illustrated in Figure 5.3a, showing that the recordings with gold and platinum black microelectrodes exhibit very large and diverse baseline offsets as well as oscillations and drifts; the gSGFET signals, on the other hand, are very stable. This base line drifts together with the large voltage offsets, can eventually saturate the amplifiers of the electronics used to record the signal. More importantly it makes it very challenging to determine the real CSD characteristics, such as voltage amplitude and waveform, as the required high-pass filter used to remove such effects will alter the signal shape.

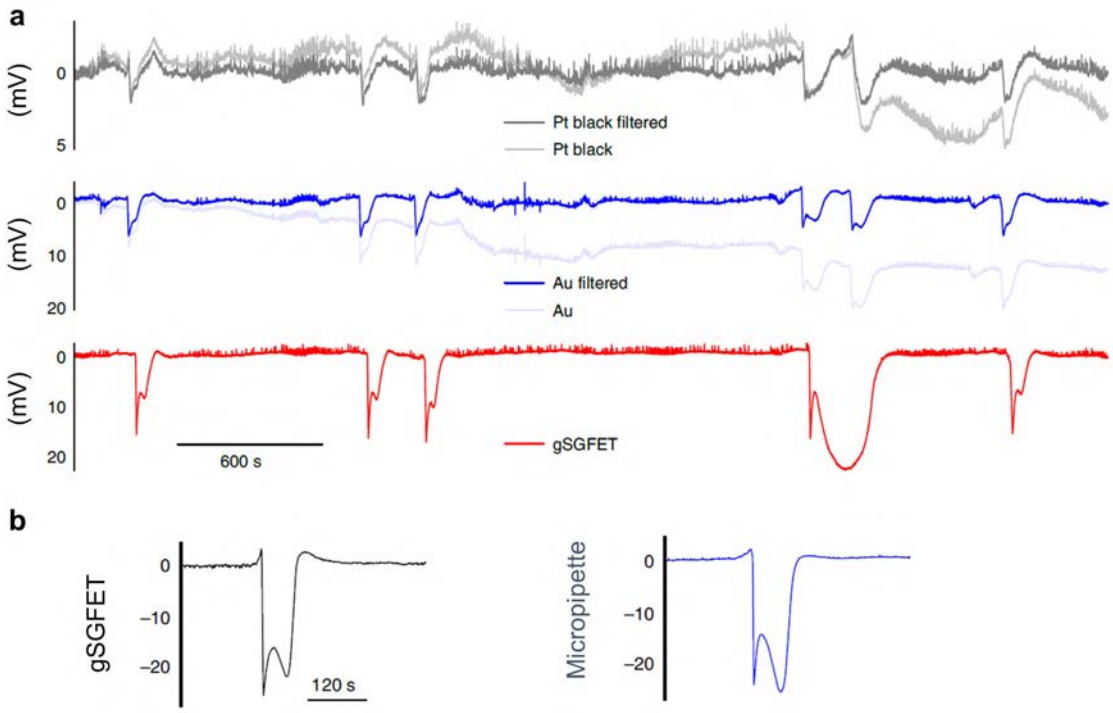

Figure 5.3: a, CSD recordings with gSGFETs and passive micro-electrodes technology. DC-offset removed recordings of a representative channel of each type (Pt-black, Au, and gSGFET) and the same signal filtered at 0.002 Hz to remove oscillations and drift; the gSGFET signal does not require any filtering and is therefore not distorted. **b**, Comparison of a CSD signal recorded by a graphene transistor (black) and a solution-filled glass micropipette with a Ag/AgCl wire (blue). From [63]

The gSGFETs can record significantly higher amplitudes for the CSD events (-13.3 ± 1.8 mV) compared to gold (-4.7 ± 1.6 mV) and platinum black (-3.0 ± 0.7 mV) microelectrodes. To avoid polarisation induced drifts, ISA is usually recorded in preclinical studies using solution-filled glass micropipettes with Ag/AgCl wires which limits the spatial resolution to just a few-point measurements. In order to confirm the fidelity of the CSD recordings of the gSGFET technology, simultaneous recordings with a solution filled glass micropipette with a Ag/AgCl wire were also conducted. The *in vivo* measurement configuration, showing the location of the gsGFET and micropipette is depicted in Figure 5.1a. As shown in Figure 5.3b, the infraslow deflection associated with CSD and measured by gSGFETs has a very similar shape, magnitude and temporal duration than the signal recorded by a micropipette (Figure 5.3b). The cross-correlation of the low frequency (< 5 Hz) component of two measured CSD event gives a similarity of $(85 \pm 1)\%$ between all gSGFETs and the micropipette (see Appendix Figure A.8).

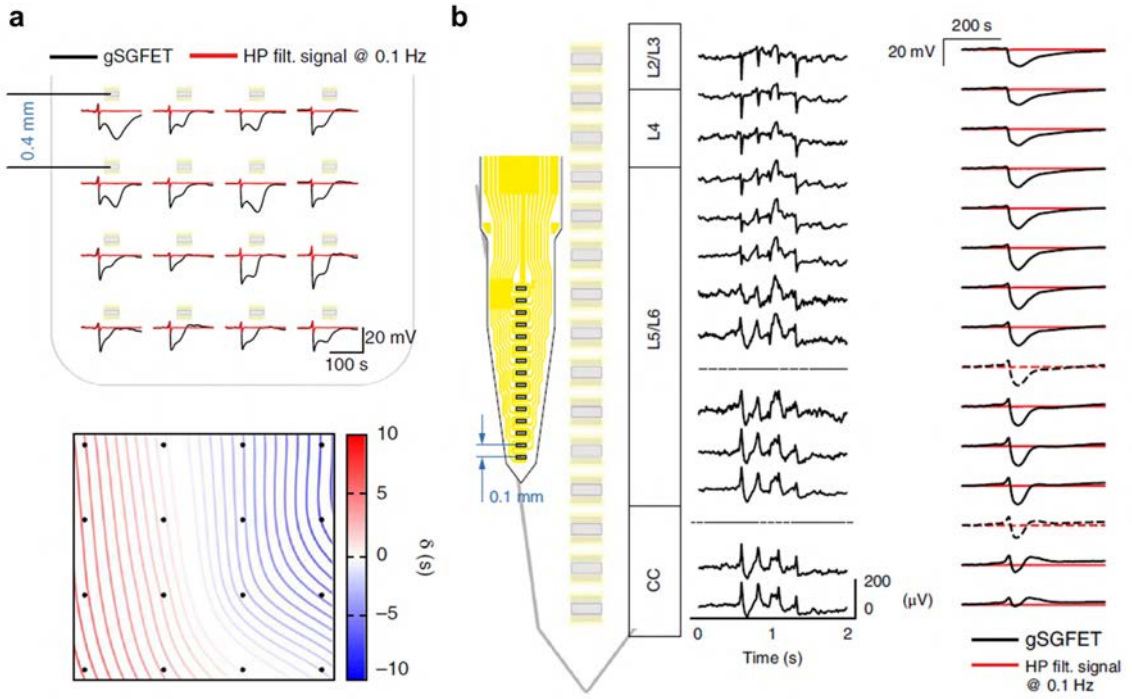

Figure 5.4: a, Infralow-frequency signals recorded by a 4x4, 400μm grid spacing, gSGFET array (black lines) during the occurrence of a CSD event. The contour plot (below) shows the time delays of the onset of CSD with respect to the mean time, illustrating the spatiotemporal course of the CSD. **b**, Layout of the 15-channel graphene intra-cortical probe (100μm distance between transistors) together with the local field potential (high pass filter >0.5 Hz) and infralow-frequency recordings during the occurrence of a CSD event. The dashed lines have been interpolated from nearby transistors. Depth position is indicated by the layer number and corpus callosum (CC). **a-b**, High-pass filtered recordings at 0.1 Hz are included (red) to illustrate the loss of signal information in conventional microelectrode recordings. From [63].

We also performed in vivo experiments with gDNP (gDNP_3.0, see Section 3.2) probes consisting of a linear array of 15 gSGFETs spanning the entire depth of a rat cortex. As an example of the potential of gSGFET technology, we mapped the propagation of CSD events epicortically and intra-cortically in separate experiments, and compared the signals with what is observed in conventional high-pass filtered recordings (Figure 5.4). The recording of the CSD event with the gSGFET array reveals the initiation and termination as well as propagation speed and direction of the depolarisation wave. The mean duration of CSD events is 47 ± 8 s and the speed of propagation 8 ± 1 mm min^{-1} (n = 10 CSDs collected from two different subjects). Interestingly, even though CSDs were induced from the surface of the cortex, the CSD occurs and propagate across the whole cortex depth (Figure 5.4b). A transition from a superficial long depolarization to a shorter depolarization preceded and followed

by hyperpolarization in the deeper layers can be clearly observed. Importantly, this information is lost in conventional microelectrode recordings, where only the CSD onset is observed due to the high-pass filter in the recording electronics.
These *in vivo* results in anesthetised Wistar rats, showed that the graphene transistor technology developed is able to record neural signals in a wide electrophysiological bandwidth, from infralow (< 0.1 Hz) frequencies to the typical local field potential bandwidth, similar to solution-filled glass micropipettes but with the capability of overcoming their spatial sampling limitations.
The ability to record simultaneously infraslow activity (<0.1 Hz) and higher frequencies (0.1-600 Hz) using the same recording electrode would particularly benefit epilepsy research. In the next section *in vivo* recordings using graphene depth neural probes in awake rodent model of epilepsy are displayed and discussed.

5.2 Recordings in an awake epileptic rodent model

The work presented in this section is a leap forward, in which further advance from the above described initial proof-of-concept study is presented; thus, the usefulness of this technology in more relevant awake animal models of seizures and established epilepsy is demonstrated.

Experimental results obtained with specifically developed multichannel flexible graphene depth neural probes (gDNP) to detect and map ISA through different cortical layers and subcortical regions, whilst simultaneously recording epileptiform activity in more conventional frequency bands (1-150 Hz) and up to higher frequencies (150-600 Hz that are found to occur in the epileptic brain) are presented. The gDNP (gDNP_4.0, see Section 3.2) used here, has been designed to have a narrower tip (200μm) compared to the wider intra-cortical probe (gDNP_3.0) used the first time as proof-of-concept; also the insertion strategy has been greatly improved making use of bioresorbable silk-fibroin .

The full bandwidth, recording capability of intracortical gSGFETs was assessed by implanting a gDNP into awake, head-fixed mice in which chemoconvulsant drug was focally injected to produce seizures. After *in-situ* back-coating with silk-fibroin (See Section 3.4), the gDNP was carefully connected to the electronics and lowered using a micromanipulator. The gDNP tip was placed just above the dura, over right hemisphere visual cortex (V1) and lowered until the tip reached hippocampal tissue ($\sim$2 mm into the brain). A reference wire ($Ag/AgCl_2$) was placed in the ipsilateral

motor cortex (Figure 5.5 a-c). The reference electrode in contact with the mouse skull is necessary to provide the bias to the transistors and obtain a "DC characterisation" (the transfer curves of the transistors) and, thus, for the calibration of the measured signal. Since transistors are active devices, the reference electrode allows choosing the optimal operation voltage V_{gs} of the transistor (at the maximum transconductance $g_{m,MAX}$ potential) and the point of highest signal to noise ratio (SNR) for the best operation of the neural transducers before each recording session (see Section 2.3). To induce network discharges and synchronous neuronal bursting 200 nL of 4-AP (50

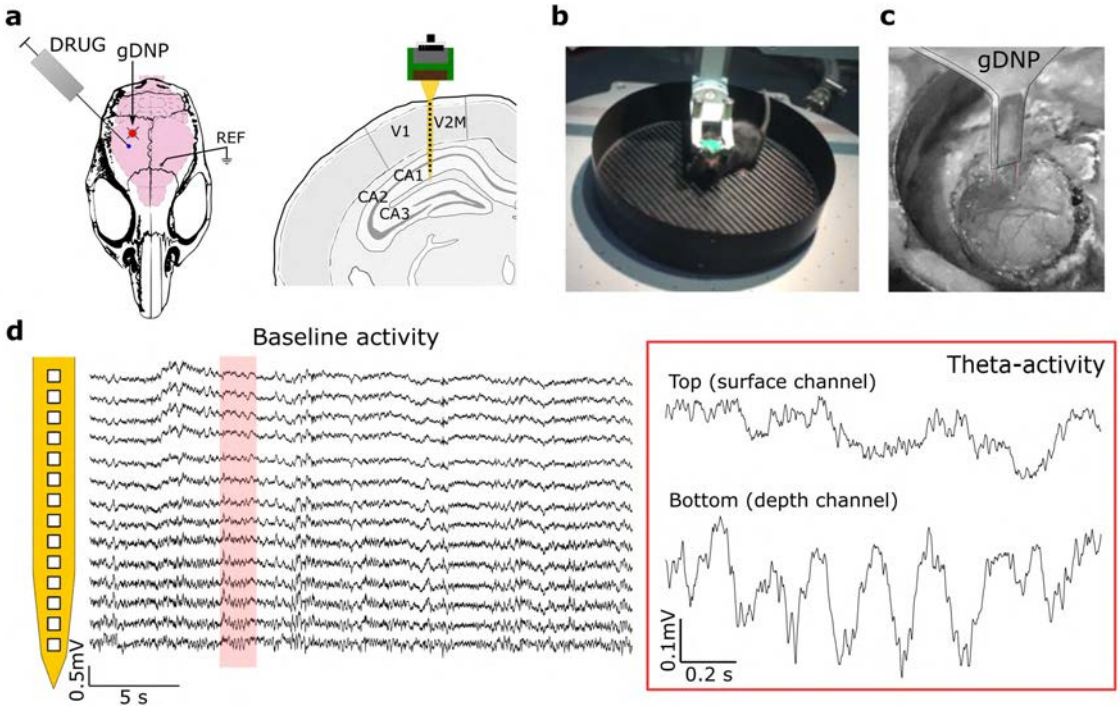

Figure 5.5: **a**, Schematic of a mouse skull with location of the gDNP and the needle used to inject the chemoconvulsant drug. Right, coronal view of the mouse brain with the localisation of the gDNP in the visual cortex. **b**, Photographs of the free-moving head-fixed mouse undergoing habituation training in the Neurotar frame with air-supported carbon-fibre frame. **c**, Photograph of the craniotomy site after the silk-fibroin coated gDNP has been successfully inserted. **d**, Probe shape with recordings during baseline activity (prior to drug injection) showing theta activity in the lower channels of the shank when the animal was moving, confirming that the lowest channels reached the hippocampus.

mM), a selective blocker of Kv1 potassium channels [343, 344] was locally injected into the cortex area adjacent to the gDNP (Figure 5.5 a). Before the injection of the chemiconvulsant, baseline neural activity (defined as the non-pathological brain state) was always recorded for 10-20 min post implantation mostly for:

1. Allowing the sensors to adapt to the neural tissue environment and the transistor current to stabilize. The chage neutrality point of the graphene SGFET shifts

possibly due to the ions and molecules that adsorbs on its suface (see Section 2.3)

2. Measuring physiological activity of a healthy brain state, which allow us to determine the SNR of the devices, when compared to *post-mortem* recordings.[3]

3. Estimating the position of the shank in the brain; this can be done by looking for layer specific activity i.e. hippocampal *theta* rhythm associated with animal movement.

Figure 5.5d shows the 14 traces recorded with a gDNP during baseline characterisation. The *theta* activity recorded in the bottom channel (see Figure 5.5d) confirmed that the gDNP reached the CA1 hippocampal cell body and thus had not buckled during insertion. This is confirmed by the histological analysis of fixed brain sections (obtained after the *in vivo* experiment, see Appendix Figure A.7).

[3] After an acute experiment, the animal is culled. The Senosors are then reoved from the recording site. Before the removal of the sensors, recordings are done to have a "zero-activity" baseline. This we call *post-mortem* recordings

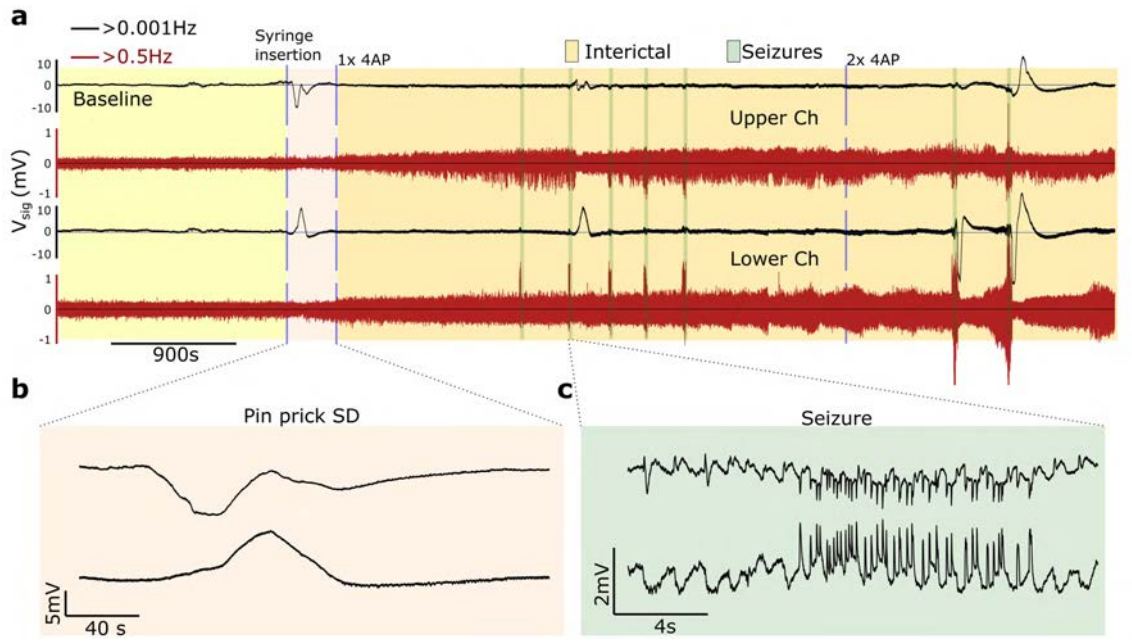

Figure 5.6: a, Long electrophysiological recording (120 mins) of two channels on the gDNP array (top: visual cortex, bottom: hippocampus). The wide bandwidth ($f > 0.001$ Hz, black) signal illustrates the drift-free stability of the gDNP recordings over a long period of time. It is shown for comparison the HP filtered signal >0.5 Hz (dark red) that would be recorded by conventional electrodes. The long recording contains several conditions including baseline activity, pin-prick SD, increased neuronal activity after 4-AP injection and seizures, some of them followed by a post-ictal SD. **b**, High resolution of the pinprick SD (beige) and **c** seizure activity shown for the uppermost and lowest channels of the gDNP (green).

Figure 5.6 displays 2 hours of an electrophysiological recording session (only the uppermost and the lowest channels of the implanted gDNP are displayed); the complete data set is shown in Appendix (Figure A.9). The ability of the graphene transistors to have long and stable full-bandwidth recordings without the need for electronic off-set readjustments overcomes the corresponding limitation of DC-coupled passive electrodes [345].

The black lines correspond to the wide bandwidth signal (HP > 0.001 Hz) and the red lines to the signal high-pass filtered above 0.5 Hz (which is the expected signal recorded by AC-coupled electrodes)[346]. The coloured regions correspond to different experimental conditions during the recording: baseline (yellow), needle-induced pin-prick SD[347] (beige), interictal activity (orange) induced by chemoconvulsant drugs, and seizures (green). After injection of 4-AP, epileptiform spiking evolved; five seizures (over 60 minutes) were elicited in this example, one of which was followed by a post-ictal SD. A second cortical injection of 4-AP induced two additional seizures, both followed by post-ictal SDs that were detected first in the hippocampus. In 5

different mice injected with 4-AP, an average number of 7 ± 3 seizures were recorded in 60 min post drug injection. SDs could be observed in this chemoconvulsant model either in superficial cortical layers or, the hippocampus (Figure 5.6).

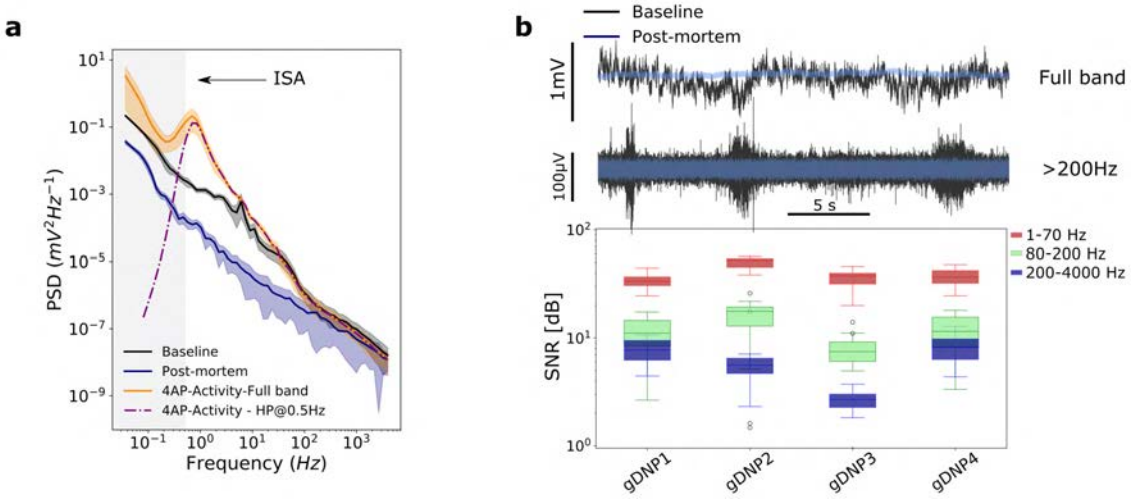

Figure 5.7: a. Averaged PSD over the electrophysiological recordings of all transistors during baseline, epileptiform activity, same activity HP filtered at 0.5 Hz (purple dashed-line) and post-mortem. The grey area highlights the low frequency part (<0.5 Hz) that is usually missed with conventional AC-coupled recordings. **b**. Comparison of a baseline activity (black) and a post-mortem (blue) in one channel of the gDNP (top: full band, bottom: HP>200 Hz). Lowest plot shows SNR evaluation for 4 *in vivo* experiments performed with 4 different gDNPs. The SNR is calculated for different bands: LFP (1-70 Hz), high frequency (80-200 Hz) and very high frequency (200-4000 Hz) and is the averaged SNR for all channels on each gDNP.

After the acute experiment was ended, *post-mortem* recordings were acquired to characterize the noise level of the gDNP in the activity-free brain state and, consequently, to quantify the detection limit of the gDNP. Figure 5.7 displays the averaged power spectral density (PSD) calculated using the recordings of all channels in the gDNP, and obtained for different brain states (baseline, after injection of 4-AP, and post-mortem). Compared to the baseline PSD, the large amplitude of the PSD at low frequencies (< 5 Hz) after 4-AP injection is an indication of the interictal and infraslow activity in the epileptic brain. The dash-dot line in Figure 5.7a corresponds to the activity recorded after injection of 4-AP, but with a typical HP filter of 0.5Hz, found in many AC-coupled recording systems, thus revealing the loss of ISA signal (grey area) expected for AC-coupled electrodes. In order to assess the detection limit in the conventional frequency bands (>1Hz), the recordings of the baseline were directly compared with *post-mortem* recordings. For instance, applying a digital filter (> 200 Hz) and comparing *post-mortem* with baseline validates the ability of

gDNP to record spontaneous high-frequency activity arising from groups of neurons in a non-pathological brain state (Figure 5.7**b**). Beyond this qualitative comparison, we have calculated the signal-to-noise ratio (SNR) in three different bands, 1-70Hz, 80-200Hz, and 200-4000 Hz for different gDNPs implanted in four animals. The SNR is calculated as root-mean square (RMS) amplitude ratio of the baseline and *post-mortem recordings*, filtered in the three different bands (see Appendix A.6.6). These results show that the gDNPs are able to record typical electrophysiological signal bandwidths with SNR ratios well above 1 dB (Figure 5.7b).

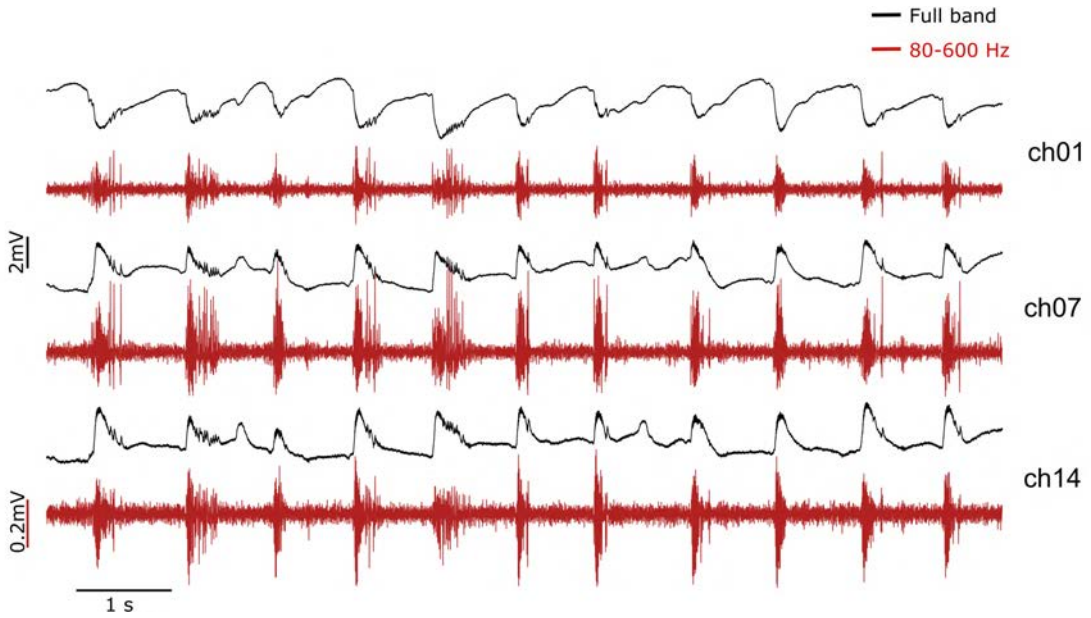

Figure 5.8: Interictal activity with associated HFOs in three different channels of a gDNP (ch01, ch07, ch14, red curves BPF 80 Hz–600 Hz). This type of activity was usually recorded between seizure events in the chemically-induced pathological mouse brain.

Interictal activity and associated HFOs (>80 Hz) are electrophysiological biomarkers used by neurologists to identify and diagnose epilepsy[128, 348] (see also Section 1.3.1). Figure 5.8 illustrates inter-ictal spikes coupled with localised HFOs experimentally recorded by three of the transistors of a gDNP, each located at a different brains depth. Filtering between 80 – 600 Hz (red curves in Figure 5.8a) reveals layer-specific bursting of HFOs and sharp wave ripples, during interictal spikes with characteristic oscillations of 200-300 Hz and 400-600 Hz in the cortical and hippocampal channels respectively [75] (see also Appendix Figure A.11); entrained inter-ictal epileptiform activity was found in all channels before each seizure. Two different pro-convulsive drugs (4-AP or picrotoxin PTX) were used to induce and evaluate epileptic activity. Figure 5.9 illustrates characteristic examples of sharp

wave ripples and HFOs induced by 4-AP and by PTX recorded by the lowest channel of the gDNP (hippocampal CA1 region). The HFO and ripple traces shown in Figure 5.9 exhibit high-frequency tones up to 600 Hz. The filtered traces (>200 Hz) are compared to the original traces (full-bandwidth) in order to verify that the activity actually corresponds to epileptic ripples and are not harmonics due to digital filtering.

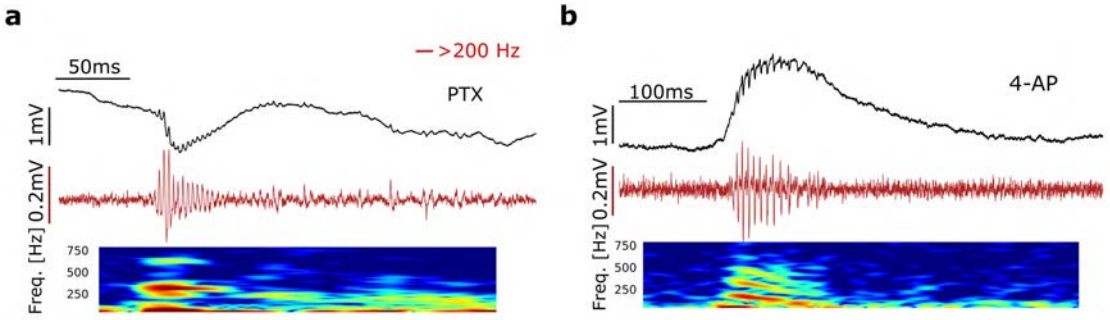

Figure 5.9: Sharp-wave ripples and HFO recorded in the hippocampus induced by (**a**) 4-AP and (**b**) PTX (full-band: black; HP>200 Hz: red); the figure also shows the corresponding spectrograms in the frequency range 10-800 Hz. Color map of the power: red=$4 * 10^{-4}$mV^2 - dark blue= $3 * 10^{-7}$mV^2.

5.2.1 Validation of infraslow activity recordings with glass micropipette

The fidelity of recorded ISA activity in the depth of the brain was validated by simultaneous recordings using a DC-coupled solution-filled glass micropipette, which is considered the gold-standard for ISA recordings. After the insertion of the gDNP, we positioned the pipette above the cortical surface before insertion approximately 400μm into the cortex. The head-stage was provided with the same reference as the gDNP, a chlorinated silver wire touching the ipsilateral motor cortex (see Appendix Section A.6.4 for more details). Figure 5.10a shows the full-bandwidth recording obtained with the gDNP (black lines) and the micropipette (green line) after injection of the 4-AP chemoconvulsant.

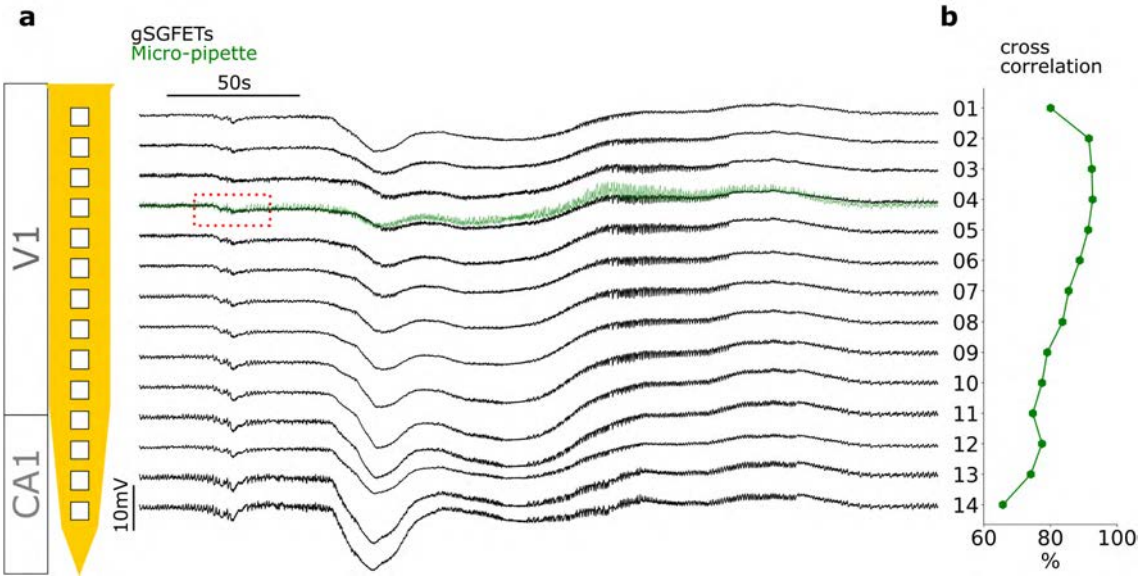

Figure 5.10: a, Full bandwidth recording with a gDNP across the visual cortex (V1) and hippocampal cell body (CA1) showing epileptiform activity followed by an SD event (black). Superimposed (green) the signal measured with the glass micropipette. The red box indicates the seizure initiation area; an amplification of this area is shown in the next figure. **b**, low frequency cross-correlation (< 5 Hz), between the micropipette and each of the transistors in the gDNP.

Both recordings reveal DC shifts preceding the seizure and a high amplitude ISA occurring after the seizure. The ISA deflection measured by the gDNP has a similar shape, magnitude and temporal duration as the signal recorded by the glass micropipette. A cross-correlation analysis (signal filtered <5 Hz) of the signal recorded by the glass micropipette and the 14 gDNP transistors demonstrates a very high correlation (above 90%) for channels Ch03 and Ch04, both located at the same cortical depth than the micropipette (Figure 5.10b).
The seizure start, marked by a red-dashed box in Figure 5.10a, is shown in more detail in Figure 5.11. In this part of the recording, the seizure onset is anticipated by inter-ictal spikes (1 Hz) without any high frequency component (associated HFOs); then, by a negative DC shift (~ 2 mV) and a high frequency tone at around $250-300$ Hz that was measured by both the micropipette and the transistor.

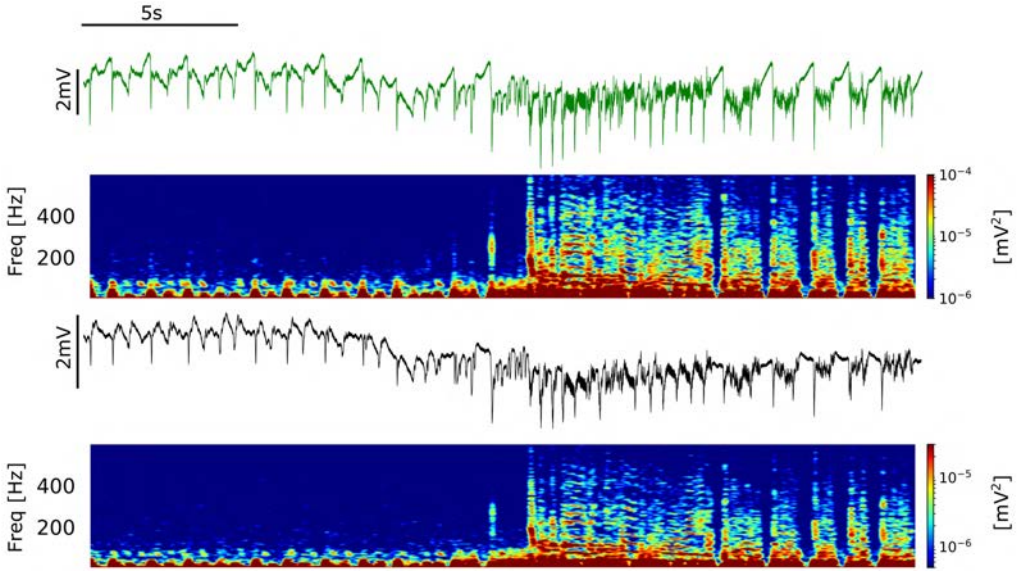

Figure 5.11: Micro-pipette electrode (green) and gDNP transistor Ch04 (black) and their respectively spectrograms (freq. range $1 - 600$Hz). This part of the recording shows the seizure onset preceded by a DC-shift and high frequency tone around $250 - 300$Hz recorded with both the micro-pipette and transistor.

Although inserted at $\sim$ 1 mm from each other, the recorded activity by the micropipette and the gDNP transistor (Ch04) is very similar in shape; also similar frequency tones at higher frequency up to 600 Hz can be seen in their spectrograms at seizure onset (Figure 5.11). This representative examples of the simultaneous recordings in the depth of the awake-mouse brain, validate the fidelity of the full bandwidth frequency recordings enabled by the flexible gDNP technology.

5.2.2 Concurrent spreading depression and seizure

The advantage of the gDNPs to monitor concurrent infraslow and high-frequency activity, is illustrated in Figure 5.12a, which shows a post-ictal spreading depression (SD) arising from the hippocampus. The black line is the full bandwidth recording, the red line the digitally filtered signal with a high-pass at 0.5Hz and in purple the RMS of the high frequency part of the recording (200 Hz, sliding integration window 100μs). In this part of recording, the seizure is preceded by a phase of entrained interictal epileptiform activity with HFOs and ripples. Interestingly, the power of the HFOs and ripples increases approaching the seizure, with a maximum at seizure onset (purpule line). A DC shift just before the seizure event followed by a SD with the highest amplitude in the hippocampus (-21 mV) was recorded along the vertical laminae. High frequency activity with entrained interictal epileptiform

activity appears again at the hyperpolarisation wave onset (Figure 5.12a), this time with higher amplitude in the superficial cortical layers. The layer-dependent silencing of the neural activity by the hippocampal SD is represented in Figure 5.12b in terms of activity variation [%], which is calculated taking into account only the frequencies > 0.5 Hz. We calculate the activity variation by dividing the averaged RMS values during the pre-ictal phase and during the post-ictal SD. The right plot in Figure 5.12b shows the layer-dependent amplitude of the SD and the following hyperpolarization along the vertical profile (see Appendix Figure A.12 and Section A.6.6), revealing that the silencing of the neural activity in the hippocampus is correlated with the amplitude and subsequent hyperpolarization wave of the SD.

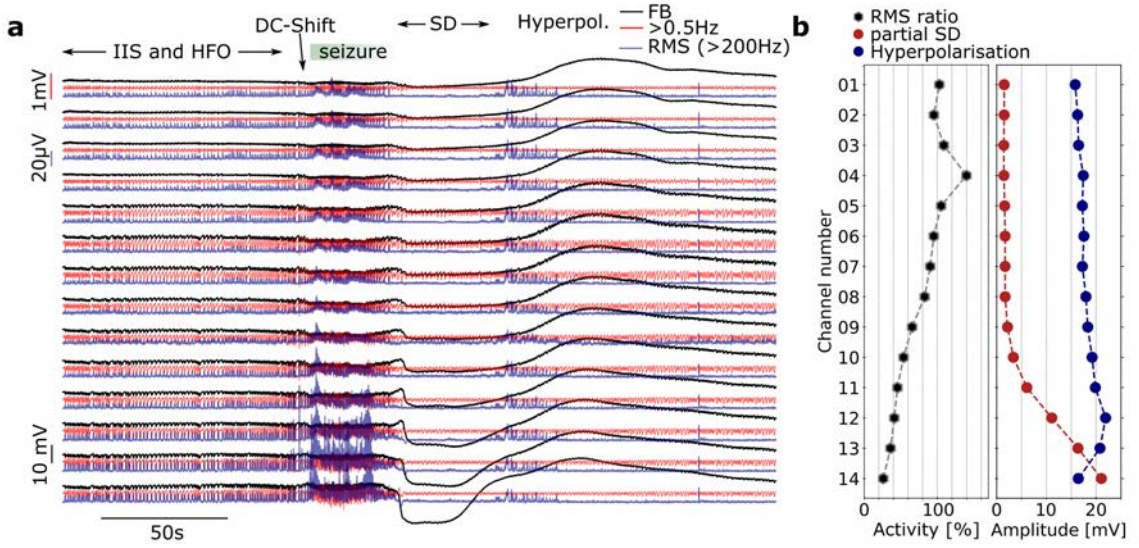

Figure 5.12: a Electrophysiological full band recordings (black curves), HP filtered at 0.5 Hz (red curves) and RMS of the high frequency activity (HP 200Hz, sliding window 100μs) from the cortex (top channel) to hippocampus (bottom channel) illustrating different phases prior and after a seizure event. During the pre-ictal phase: intericta spikes (IIS) asociated with HFOs, pre-ictal DC-shift, seizure, post-ictal spreading depression (SD) arising from the hippocampus followed by a long hyperpolarisation period. **b** Neural activity variation (before seizure and during SD) and amplitudes of the SD and hyperpolarisation waves concurrent with the seizure across the vertical profile. Neural activity variation is calculated for each channel by comparing the RMS amplitude of the activity before and during the SD.

Silencing of neural activity in the hippocampus by the SD is visualized with more clarity in Figure 5.13, where the spectrograms of the upper and lowest channels are depicted. Notice the higher frequencies as well as increased power of the neural activity recorded in the CA1 region (Ch14) during the pre-ictal phase and during the seizure as expected for neurons of the hippocampus[75].

Moreover, full bandwidth recordings with the gDNP, allow to perform current source

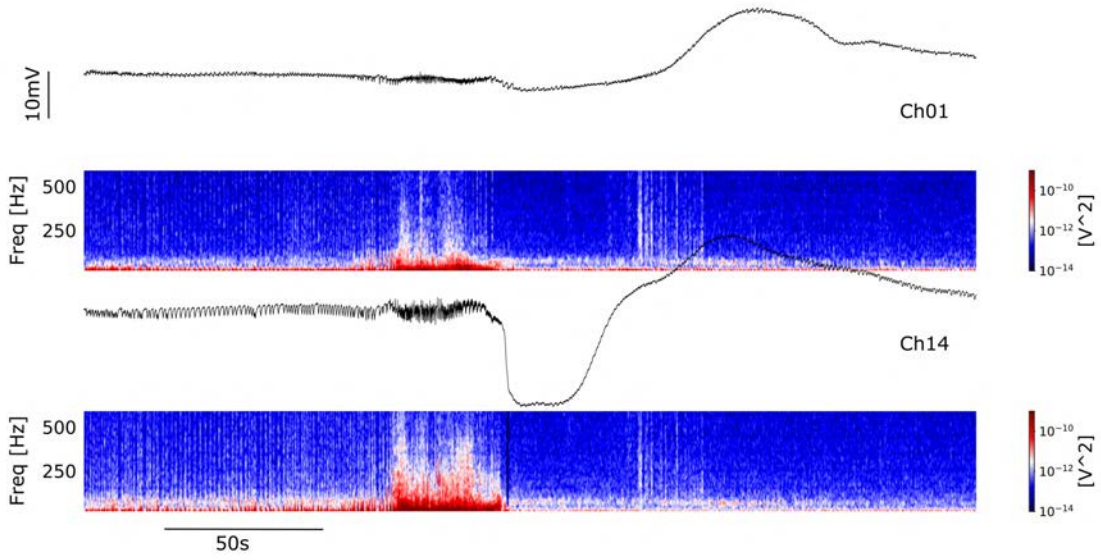

Figure 5.13: Neural silencing during the hippocampal SD is illustrated by the spectrograms (range $1-600$ Hz) of the uppermost and lowest channels of the gDNP (Ch01, Ch14). Notice the greater power and higher frequency activity of the neurons in the CA1 region measured by the lowest channel during the pre-ictal phase.

density analysis (CSD) to identify current sources and current sinks through the cortical laminae.

CSD analysis is a class of methods to analyse the extracellular electric potentials recorded at multiple sites which leads to an estimates of current sources generating the measured potentials. When net positive current enters the cell we speak of **current sink** and it corresponds to negative CSD. When net negative current enters the cell we speak of **current source** and it corresponds to positive CSD. It is usually applied to the lower frequency part of the extracellular potential (LFP, < 70Hz)[349]. CSD analysis of the data in Figure 5.12 (see Appendix A.6.6 for further details) reveals a large net ionic sink in the hippocampal extracellular space after the seizure, followed by a large source at the beginning of the hyperpolarization wave (Figure 5.14). Enlarging the seizure onset region, 4 sink and source regions can be identified through the laminae profile. CSD analysis computed without the infraslow components ($0.5\text{Hz} < f < 70\text{Hz}$) fails to report the ionic sinks preceding and during the seizure in the bottom layers (Figure 5.14, AC-coupled panel), illustrating the importance of using full-bandwidth recordings for CSD analysis to avoid misinterpretation of the extracellular potential sinks and sources. To date, this type of full-bandwidth recording and CSD analyses with high spatio-temporal resolution are quite rare to

find due to the difficulties metal electrodes have to record low-frequencies without been affected by voltage-drifts (see Section 1.1.3).

In Figure 5.15a we show more examples of seizures and concurrent ISA recorded

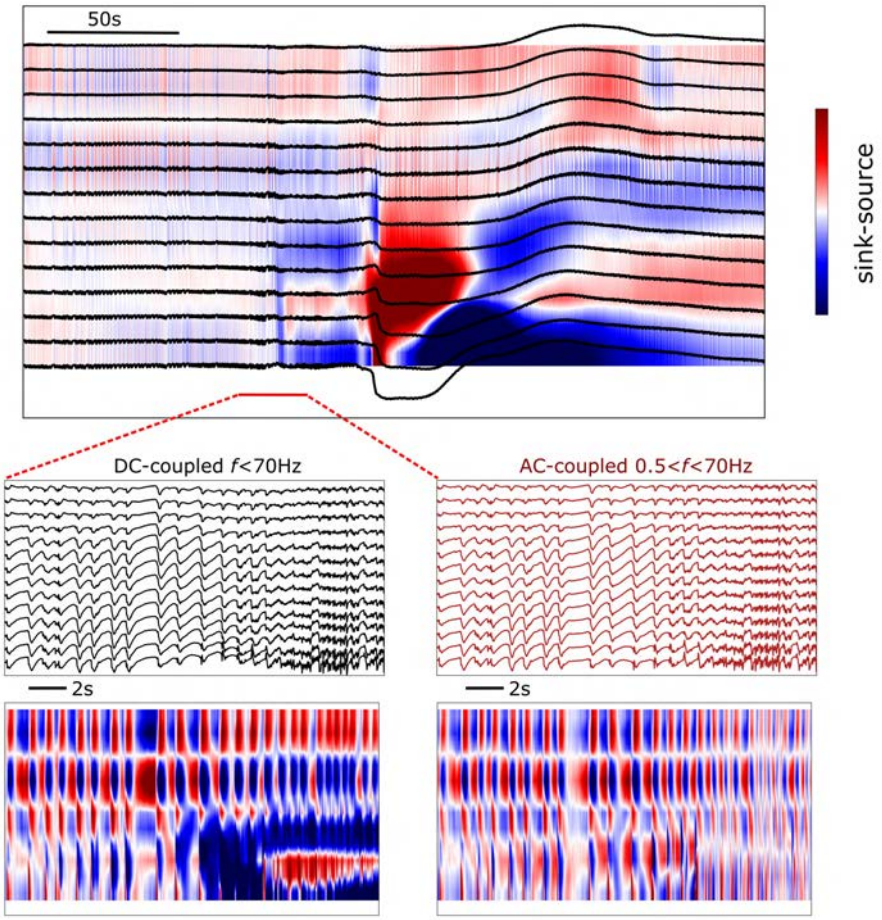

Figure 5.14: Current-source density (CSD) analysis of the low frequency activity (< 10 Hz), showing source and sinks in the hippocampus during the SD. Below: blow up of the pre-ictal to seizure transition (< 70 Hz), showing dipoles in the different layers of the cortex and hippocampus. The two graphs correspond to the CSD analysis performed with (left) and without (right) the contribution of low frequency components.

with the gDNP technology in three different awake mice. The corresponding CSD analysis (signal low pass filtered < 10 Hz) is displayed below each data set (Figure 5.15b). Large source and sink currents can be observed along the cortical laminae and hippocampal cell body during each SD events (Figure 5.15b). Although the detailed interpretation of the the CSD analysis is out of the scope of this thesis, this data confirms the unprecedented performance of this technology in the study of epilepsy; identification of source and sinks together with the seizure localisation and propagation analysis could lead to a better understanding of the interplay between

SD and seizure in epilepsy. Apart from epilepsy, CSD analysis of full bandwidth recordings with gSGFETs depth probes, will surely improve the identification of source activation in a variety of focal neurological disorders [350].

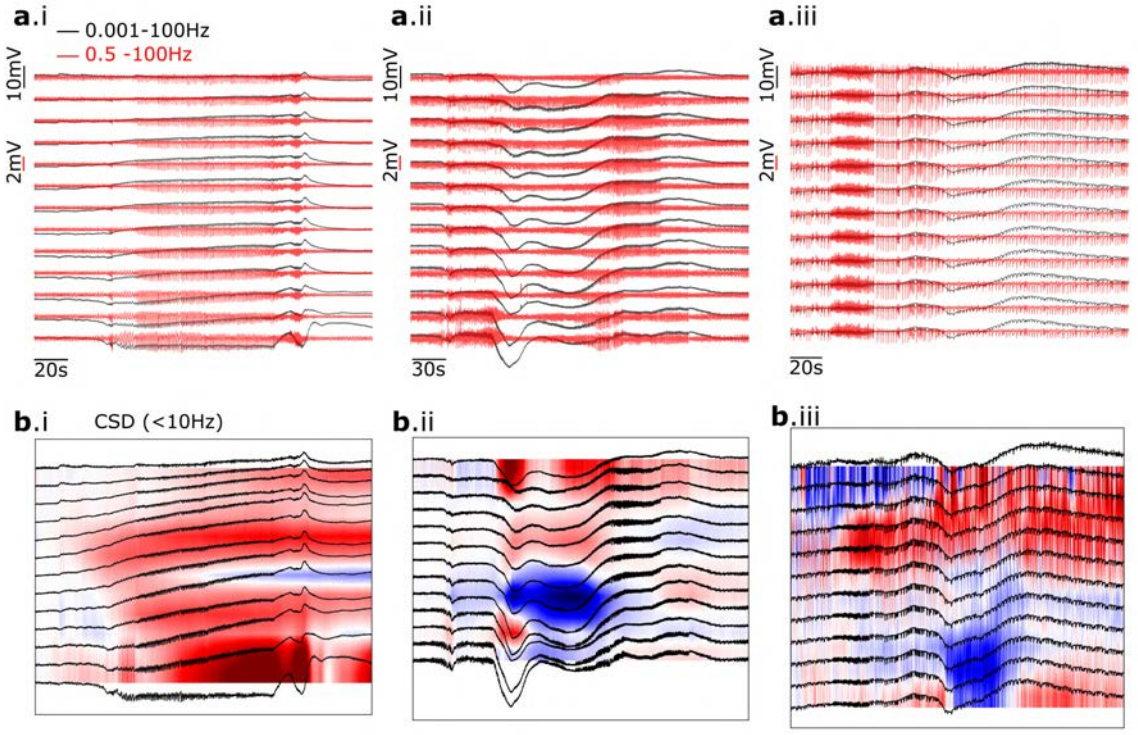

Figure 5.15: **a**.i-iii, profile recording during seizure events in three different mice showing seizure and spreading depolarisation. In black the signal is HP $>$ 0.01 Hz allowing detection of the ISA oscillations otherwise hidden to conventional electrodes due to HP filtering (red $>$ 0.5 Hz). **a**.i-ii, 4-AP was injected to elicit epileptiform activity; **a**.iii PTX was used as chemoconvulsant to induce epileptiform activity. **b**.i-iii, Current source density analysis (CSD) of the low-passed filtered full bandwidth recording ($<$ 10 Hz) shown in (a) depicting different ionic dynamism during seizure in the three different in-vivo experiments.

5.2.3 Pre-ictal DC-shift and seizure

DC shifts can be associated with seizures [138] but are usually removed from recordings due to the requirement for high-pass filtering applied to conventional AC-coupled electrodes[346]. During the first 60 min after 4-AP injection, negative DC-shifts starting before seizure onset were found in cortical channels in two different mice. In Figure 5.16a one representative trace shows seizures and DC-shifts for two different bands: DC-coupled low-pass filtered recording (<0.1Hz) black and banpass filtered (4-12Hz, red). Using this two bands we extracted the DC-shift onset (blue line) and the seizure onset (red line); the seizure onset is clearly anticipated by the

DC information. The DC-shift persist during the whole seizure event and return to baseline values once the seizure stops (green line). Maximum DC-shift amplitudes where observed in the lower cortical layers (Ch10) in both mice (Mo1 with n=4 seizures events and Mo2 with n=3 seizure). Moreover the highest time difference between DC-shift start and seizure start is also observed in the lower channels (see Figure 5.16b). Negative DC-shifts with amplitude of 1mV (0.5/1.5 mV) preceded seizure onset at deep cortical layers by 2.6s (3.5s/1.9s)[4].

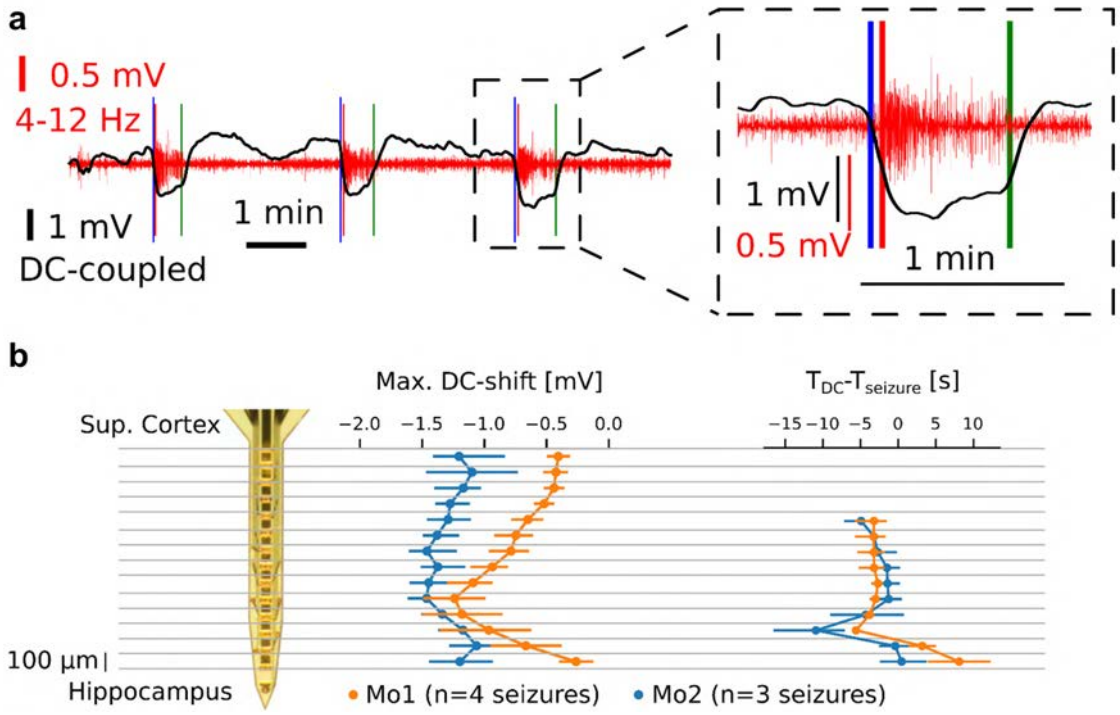

Figure 5.16: DC-shifts precede seizures at the injection site after 4-AP injection in awake mice. **a**, Representative trace as recorded by an intracortical gSGFET showing seizures and DC-shifts after injection of 200 nL of 50mM 4-Aminopyridine. Data is shown for two different bands: DC-coupled low-pass filtered recording (<0.1 Hz) black and banpass filtered (4-12 Hz, red). Coloured lines indicate the DC-shift onset (T_{DC}, blue), the seizure onset ($T_{seizure}$, red) and seizure end (green). One event is zoomed to facilitate assessing that DC-shift precede seizure onset. **b**, Peak DC-shift amplitude and delay between DC-shift and seizure onsets ($T_{DC} - T_{seizure}$) for each transistor for two different experiments (blue, n=4 seizures; and orange, n=3 seizures). Dots represent the mean and bars the standard deviation.

Observation of pre-ictal DC-shifts with polarity and amplitude dependence along the cortical layer was recorded. Here amplitudes of the DC-shift range between 0.5-3 mV. Figure 5.17 shows a seizure event preceded by a DS-shift and followed by a SD; recordings are shown at three different depths, from the visual cortex

[4]Values expressed as median (25%/75%)

to the hippocampus, comparing the signal in full-band (black curves), HP filtered >0.5Hz (red curves), and LP filtered < 0.5Hz (green curves). DC-shifts preceding

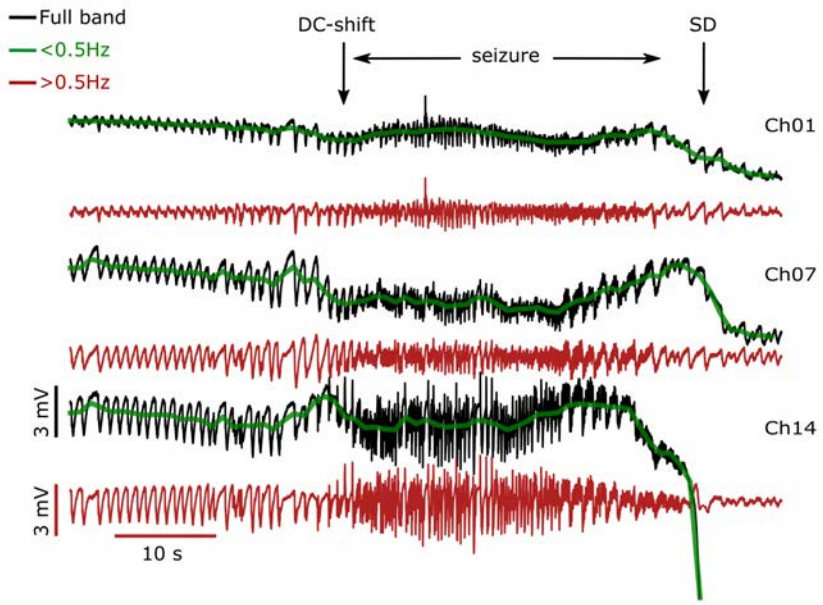

Figure 5.17: Three channels (Ch01, Ch07, Ch14) showing full band recording (black) and high-pass filtered (> 0.5 Hz, red) of a seizure followed by a hippocampal SD; in green the low-frequency component of the recording (< 0.5 Hz) overlapped to the full bandwidth signal, showing an ictal DC shift associated with a seizure, and followed by the SD.

seizures need to be statistacally analysed in more animal experiments with gDNPs. Nevertheless, this preliminary results highlights the importance of recording slow and infraslow activity in epilepsy, potentially leading to an implantable device able to anticipate a seizure event in patients.

5.3 Chronic implantation and long lasting validation of technology

In this part of the work we discuss the stability and chronic functionality of gDNP, defined by the ability to keep high signal-to-noise ratio recordings spontaneous epileptiform activity over time. We implanted gDNPs in the right-hemisphere somatosensory cortex of WAG-Rij rats (n=4), a rodent model of absence epilepsy [351], and perform chronic full-bandwidth recordings over a 10-week period. WAG-Rij rats exhibit frequent spontaneous spike-and-wave discharges (SWDs), a characteristic thalamocortical oscillation between 8-10 Hz [351]. Implanted animals were connected 1-2 times per week for tethered recordings, using a commutator to enable free movement of the rats (see Figure 5.18).

Transistor curves were measured in each recording session to assess device stability,

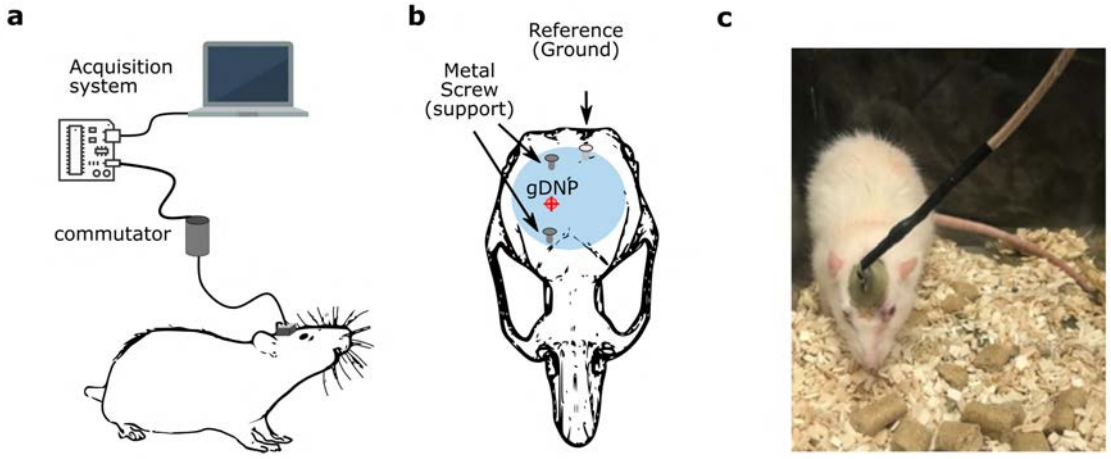

Figure 5.18: a, Schematic of a WAG-Rij rat tethered via a commutator and the electronics for the data acquisition. **b**, Schematic of the rat skull with the approximate location of the gDNP together with the Ag/AgCl reference wire and the screw to stabilize the implanted device. **c**, Photograph of the WAG-Rij rat and the chronic implanted gDNP connected to the electronics.

changes at the device/tissue interface and importantly, to permit selection of an optimal Vgs to maximise SNR; this feature is possible with active sensor devices [19]. Figure 5.19 shows the averaged transfer curves (each one is the average of the 14 transistors) of a gDNP measured over 10 weeks (see also Appendix Figure A.14). The stability of the transistors' performance is illustrated in Figure 5.19b, which depicts the position of the CNP and the maximum value of g_m over the implantation period. The averaged g_m value remains approximately constant over the whole study.

Since g_m is directly related to the tissue/graphene interfacial capacitance and to the carrier mobility in graphene, the g_m stability strongly suggests little or no variation of these two parameters. The CNP (Figure 5.19b) shows a significant shift (200 mV) during the few first days after implantation, which then remains stable for the rest of the experiment. We tentatively attribute the initial shift to the adsorption of negatively charged species, which reduce the intrinsic p-type doping of the graphene transistors[19].

The long-term functionality of the gDNP was assessed by evaluating the quality of

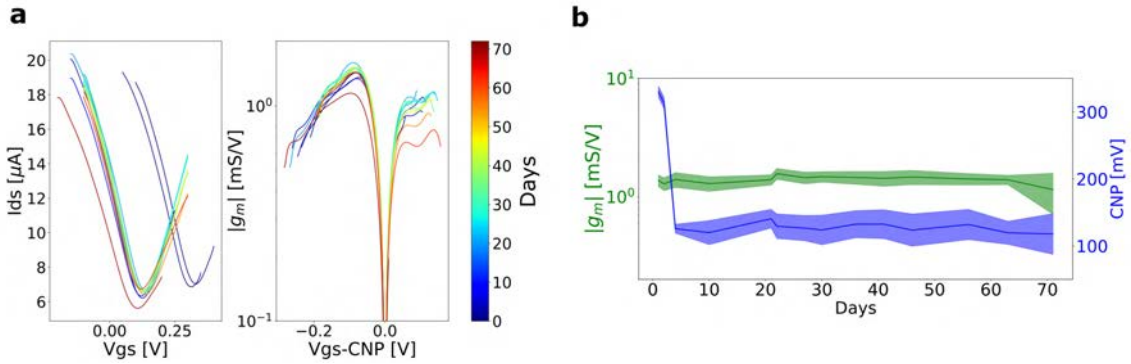

Figure 5.19: **a**, Averaged transfer curves of all transistors of the gDNP over the implantation time together with it transconductance g_m. **b**, Averaged values of the maximum transconductance g_m (green) and the charge neutrality point (CNP, blue) of the transistors transfer curves.

the recorded signals over the implantation period using two parameters:

1. The normalized SWD power amplitude.
2. The transistor noise (V_{RMS}).

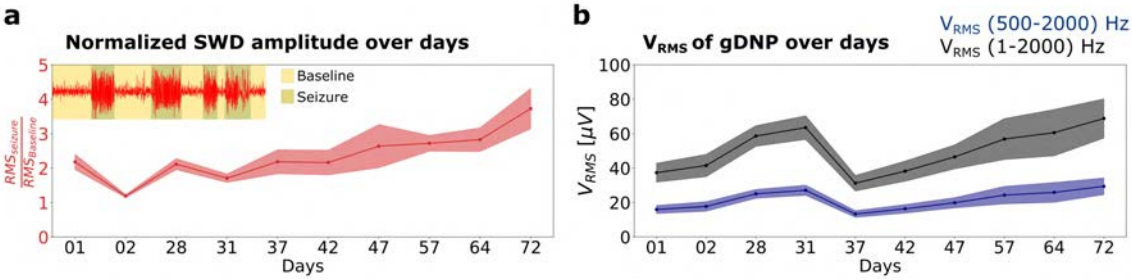

Figure 5.20: **a**, Normalized SWD activity over implantation time, calculated as the ratio of the SWD activity and baseline activity. Inset: example of SWDs events (red), highlighting the periods considered baseline and SWD. **b**, The average V_{RMS} noise in the bandwidth between $1 - 2000$ Hz (black) of all channels over the implantation period is extrapolated from the average V_{RMS} noise in the bandwidth between $500 - 2000$ Hz (blue).

Normalized SWD power amplitude is defined as the RMS (calculated in the frequency band $1-500$ Hz) of the SWD activity normalized by the baseline activity (non-SWD periods, see inset of Figure 5.20a and Appendix Figure A.10). V_{RMS} over time is extracted by averaging the RMS values at very high frequency ($500-2000$ Hz) in the non-SWDs periods of the recording, where the power of neural activity is expected to be closer to the transistor's electric noise. Then, assuming an 1/f type of noise, the V_{RMS} value is extrapolated to lower frequencies (1-2000 Hz, black line, see Figure 5.20b) For further calculation details, refer to Appendix Figure A.10.
Figure 5.20 the variation of these two parameters over time is shown, demonstrating the ability of the implanted devices to monitor seizure activity with high fidelity during the whole implantation period. The slight increase in the normalized SWD activity could result from a strengthened coupling between neural tissue and the gDNP or from an increase in the seizure power and duration as the animal ages [352].

5.3.1 Correlations between ISA and SWDs

The WAG Rij rat chronic model of absence epilepsy offers the possibility to investigate correlations between infraslow activity and SWD events. Because of the full-bandwidth capability of the gDNP, we were able to observe DC shifts (< 0.5 Hz) associated with SWDs, and a correlation between the amplitude and polarity of the DC shift with the depth of the neocortex layers.

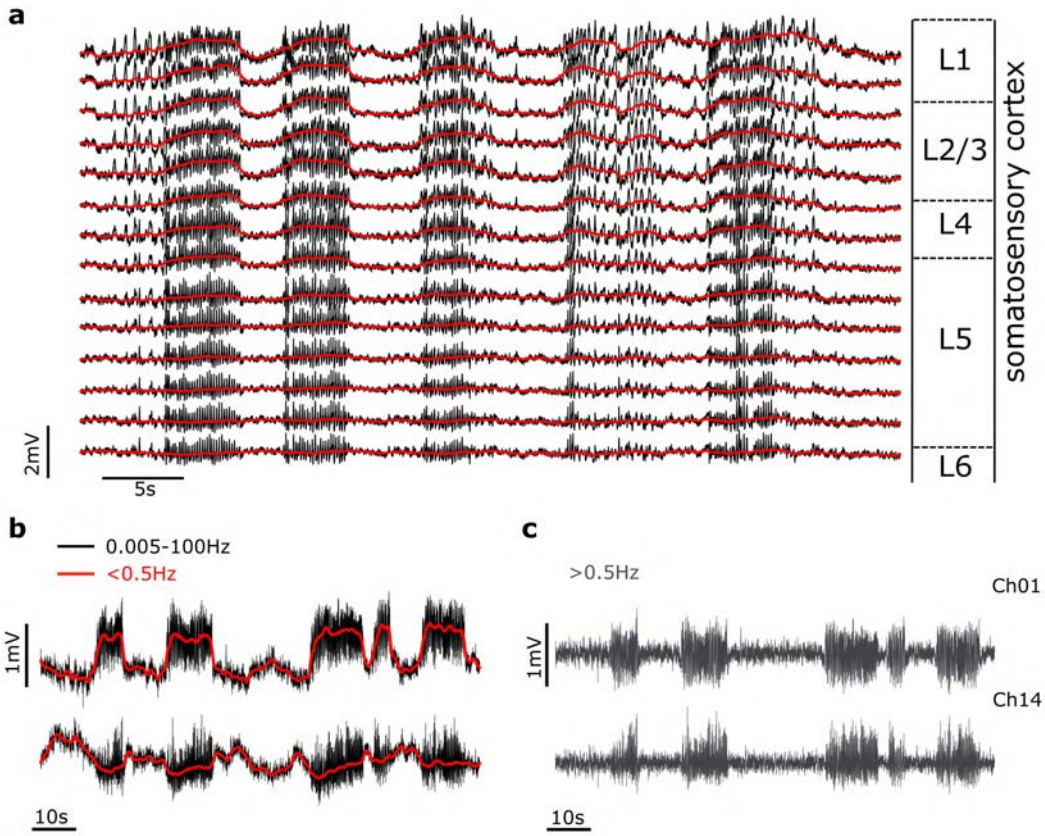

Figure 5.21: **a**, Profile recording across the cortical laminae, illustrating SWDs. Overlapped low frequency component (< 0.5 Hz red) of the signal showing a gradient in amplitude along the rat's cortex. Largest DC shifts are observed in the more superficial layers. **b**, SWD in the uppermost and lowest channels of the gDNP; ISA component (red$<$0.5 Hz) overlapped to the 0.005-100 Hz signal (black). **c**, Same signal filtered above 0.5 Hz, showing how the low frequency component would be lost with commonly used AC-coupled electrodes.

In this experiment we observed a positive DC shift ($\approx$1.5 mV) in the superficial layers L1, L2/L3, and L5 to a lesser degree, and a negative DC shift in the lowest cortical layers (see Figure 5.21a). Figure 5.21b shows the uppermost and lowest channel with opposite associated DC shifts during each SWDs.

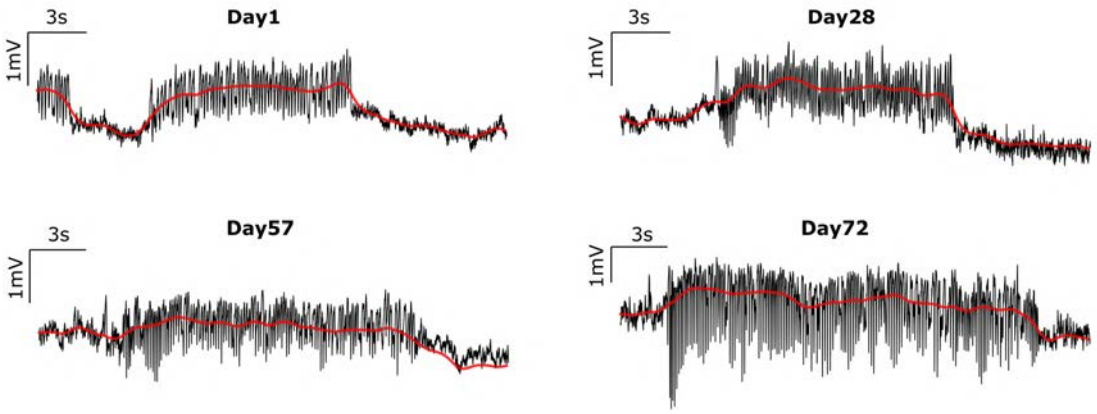

Figure 5.22: Illustrative SWD events measured by the same channel at days 1, 28, 57, and 72. Overlapped in red the low frequency component (< 0.5Hz) showing that the ISA and SWD were consistently recorded over the whole implantation time.

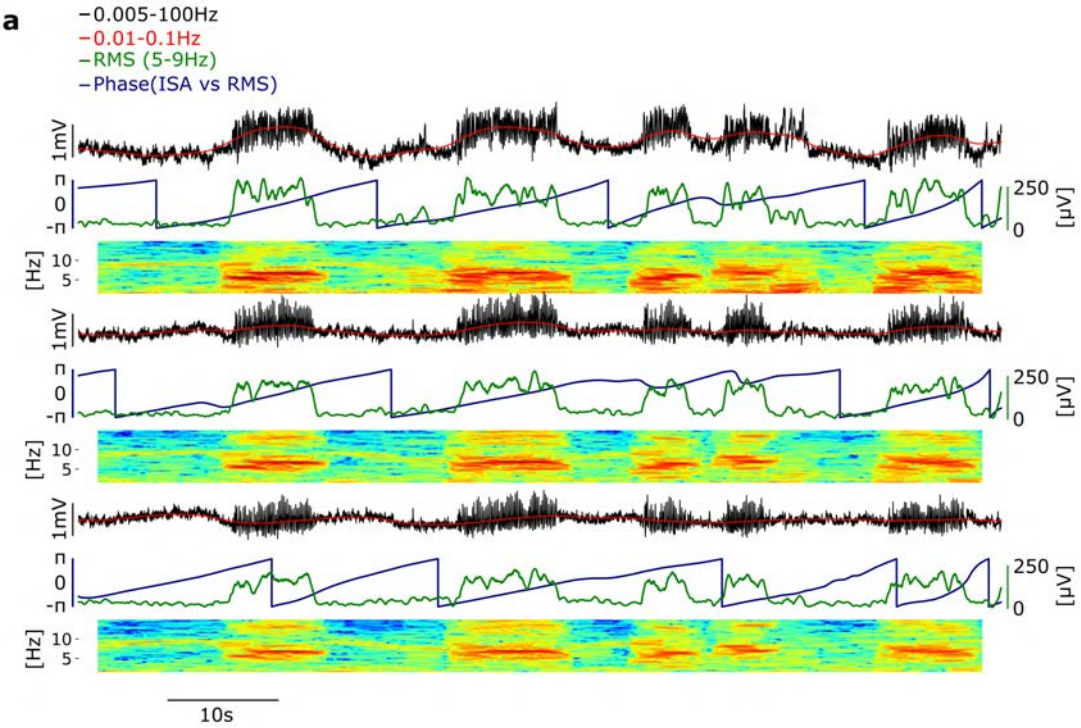

Figure 5.23: Three channels along the gDNP (Ch01, Ch07, Ch14) showing the phase (blue) of the ISA (red, $0.01 - 0.1$ Hz) with the associated SWD shifts with depth in the rat cortex. In green the RMS of the SWDs ($5 - 9$ Hz band).

The latter is not observed after application of a HP-filter (>0.5 Hz) as typically used with conventional AC-coupled microelectrodes (Figure 5.21c). The observed correlation between the SWDs and ISA, and layer-dependent polarity of the DC

shift persist over the implantation period, as shown in Figure 5.22 which depicts representative seizure events showing SWDs and DC shifts over time.
In order to do a more quantitative analysis, the phase of the ISA (blue, limited to the $0.01 - 0.1$ Hz band) and the power amplitude of the neural activity associated to the SWDs (green, 5-9 Hz) together with their spectrograms (range 1-14 Hz) is shown in Figure 5.23 for three channels (Ch01,Ch07,Ch14).
Interestingly, a ISA-phase dependence during the SWD is found, shifting with the position of the sensor along the cortical laminae: a positive DC-shift in the upper cortical layers and a negative for the lower layers is observed (see also Figure A.14). In order to quantify the observation, the power (RMS) as well as amplitude (mV) distribution of the neural activity between $5 - 9$ Hz (corresponding to a prominent oscillation during SWDs) is plotted for each channel versus its ISA phase BP-filtered between $0.01 - 0.1$ Hz (see Figure 5.24a-b). The histograms in Figure 5.24a-b are calculated over a recording time of 1600 s (with approx. 145 SWD events), showing a clear inversion of the DC-shift during the SWDs in the lower layer of the neocortex (see Appendix Section A.6.6 and Figure A.14). This correlation between ISA and SWD was also observed in the other implanted WAG-Rij rats (n=4, see Appendix Figure A.15).

gDNPs are therefore a promising electrophysiology tool to gain further understanding of the influence of thalamocortical oscillations in SWD generation[353]. Further, the ISA-phase correlation with the SWD, together with the concurrent DC-shift with seizure observed in the mouse epilepsy model (see previous section 5.2.3) are confirming once more the potential of this technology to anticipate seizure events, with possible future implication for therapeutic devices in epilepsy.

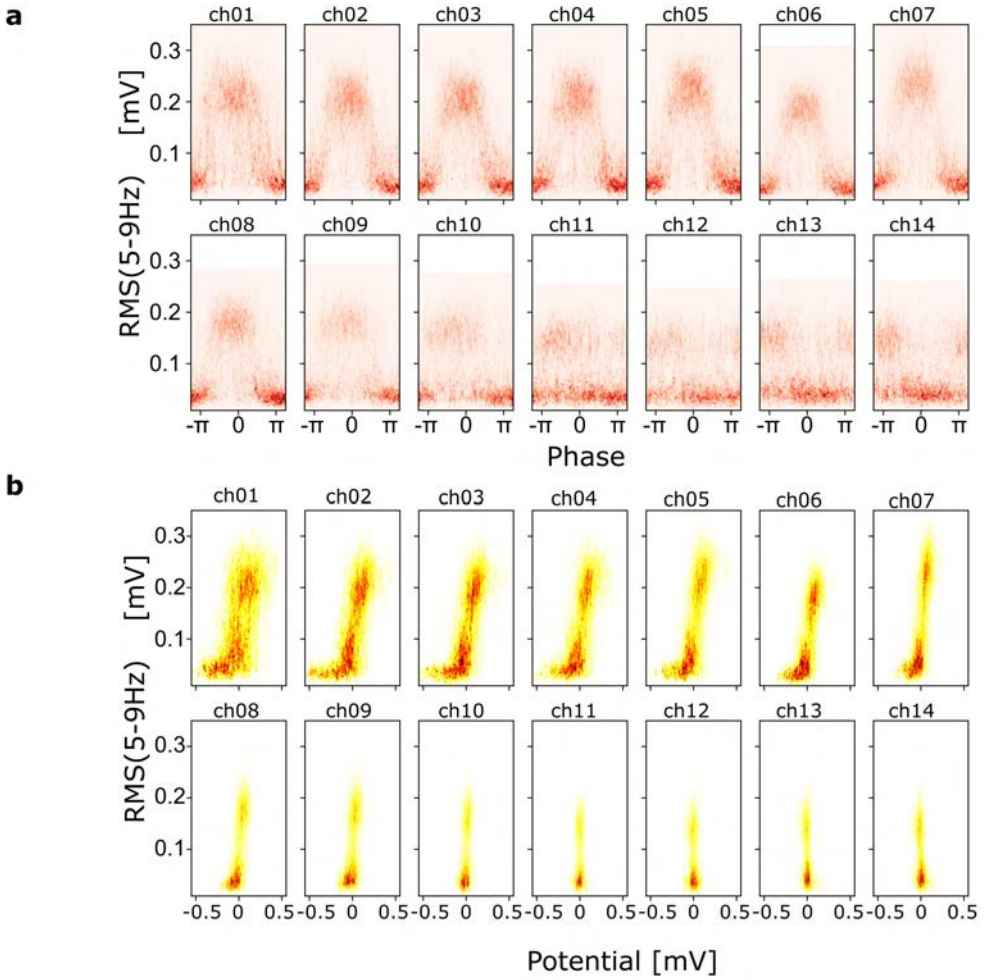

Figure 5.24: a-b, Density distribution of the RMS values of SWDs vs ISA phase and ISA amplitude for all channels evaluated in a long recording (1600s); a clear correlation between ISA phase and SWD power and a phase inversion in the deeper cortex layers is observed. **a**, y-axes correspond to the RMS (5-9 Hz) associated with the SWD and the x-axes represent the phase of the ISA (red represents higher density);**b**, Histograms for all channels of the gDNP of the RMS (5-9 Hz) with ISA amplitude (BPF: 0.01-0.1 Hz).

5.3.2 Biocompatibility study

In addition to the chronic functional validation of the gDNP, we conducted an extensive chronic biocompatibility study to assess any potential neuro-inflammation caused by the invasive nature of the penetrating neural probes, the presence of CVD graphene, or by the SF following implantation. To this end, gDNPs with or without graphene at the recording sites (to act as a control) were implanted in adult, male Sprague-Dawley rats (n=20). The most comparable clinically relevant device on the market, a Neuronexus 32 channel iridium penetrating electrode, was also assessed at the longest implantation timepoint for histological analysis. This was not an exact match for our manufactured devices, due to the narrower dimensions of the neuronexus device; however this device remain fully rigid, so they give a comparison against the flexible electronics used[5]. Histological and immunohistochemical studies were conducted at 2, 6, and 12 weeks' post-implantation and compared to the contralateral hemisphere, without device implantation. More specific details about the surgery and the immunohistochemical analysis can be found in Appendix A.7. Histological analysis of astrocyte cells (glial fibrillary acidic protein, GFAP) associated with inflammation showed no significant increase in cell presence in the area directly surrounding the probe site for the graphene devices compared with the no-graphene gDNP at 12 weeks post implantation and at any timepoint (see Figure 5.25 and Appendix Figure A.17).

Pro-inflammatory cytokines in the brain were assessed at 2, 6 and 12 weeks post implantation for both the graphene and no-graphene devices, compared to the contralateral hemisphere which was not implanted. A bead-based multiplex ELISA kit was run, allowing to have insight into the amount of interleukin proteins in the brain tissue associated with inflammatory response (see Appendix A.7).

Markers which included markers for interleukin-17 alpha (IL-17a), interleukin-33 (IL-33), interleukin-1a (IL-1a) and interleukin-1beta (IL-1b) showed no sign of an inflammatory response at any timepoint, regardless of the device used (Figure 5.26 and Appendix FigureA.16).

[5]Experiments performed at The University of Manchester, supervised by Prof. Kostas Kostarelos and Dr.Sinead Savage

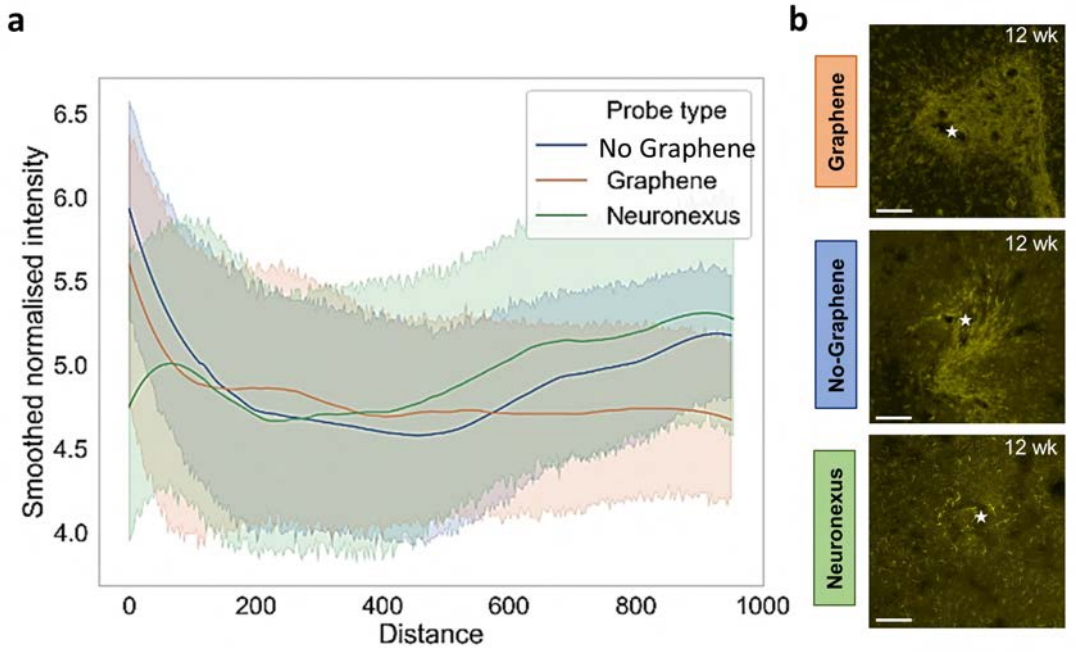

Figure 5.25: a Fluorescence intensity in the region surrounding implantation site at 12 weeks post-implantation as a measure of positive astrocyte cells (GFAP). There was no significant increase in astrocyte presence after implantation of the graphene device (orange) compared with the No-graphene (blue) and the rigid Neuronexus (green) probes. **b**, Exemplary fluorescent images of GFAP, in the area of insertion at 12 weeks post implantation (the star mark shows the insertion point). Brain sections were selected for staining at an approximate site depth of 0.8mm. Scale bar is 200μm.

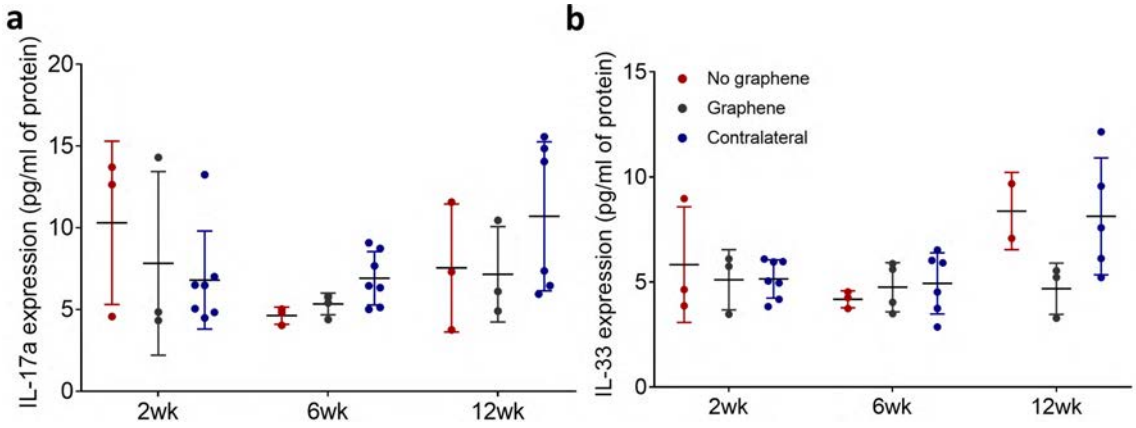

Figure 5.26: The presence of pro-inflammatory cytokines, such as IL-17a (**a**) and IL-33 (**b**) were not increased by the presence of graphene in the flexible gDNP implanted for 2, 6 or 12 weeks. ELISA data for pro-inflammatory markers showed no evidence of increased neuro-inflammation for either no-graphene or graphene devices at any timepoint, even when compared to the contralateral hemisphere, where there was no device implanted.

Microglial activation state was assessed by morphological analysis of cells stained for ionized calcium binding adaptor molecule 1 (Iba-1), a marker for microglia. There was no significant increase in the percentage of activated microglia present in the area surrounding the implantation site in the presence of graphene-based gDNP, compared with the gDNP without graphene (Figure 5.27). Microglial cell counts showed that there were a greater number of microglial cells present in the area surrounding device implantation at 2 weeks, but that this number subsided by 6 weeks. At 12 weeks, there was a similar number of microglial cells in the area for all devices implanted, however there was a slightly lower percentage of activated microglial cells in animals implanted with Neuronexus devices (Figure 5.27a).

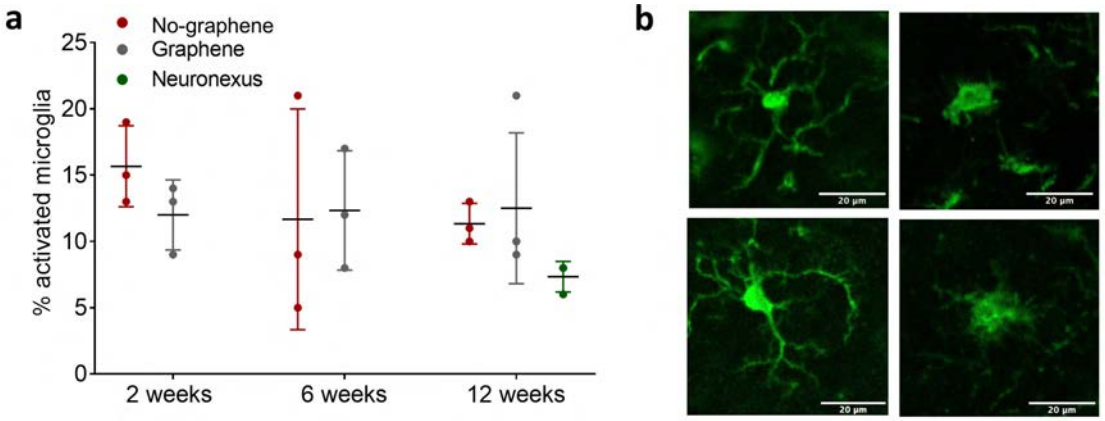

Figure 5.27: a, Time evolution (2, 6, 12 weeks) of activated microglia in the vicinity of the implanted probes (in an area of 0.7 mm^2) obtained for the two types of probes (graphene, no-graphene) and for the rigid Neuronexus probe (at 12 weeks, as benchmark). **b**,Two examples of microglial activation. Fluorescence images: from left to right, non-activated and activated microglia, respectively. Scale bar: 20μm

At the longest timepoint, 12 weeks post implantation, there was also no significant difference between the flexible probe and the rigid probe, showing that these devices are comparable to devices on the market, despite the larger size of the flexible gDNP (Figure 5.27a and Appendix Figure A.18).
Altogether, the chronic biocompatibility study indicates that gDNPs are suitable for chronic implantation, inducing no significant damage nor neuroinflammatory response.

6

Conclusions and Outlook

6.1 Conclusions

The aim of this thesis was to further develop and optimize state-of-the-art neural sensors using CVD-graphene transistors, which have a large potential for a novel class of flexible, brain-machine interfaces (BMIs). Graphene's large interfacial capacitance, its record-high charge carrier mobility and stable interface with aqueous solutions, allows it to sense ionic and enzymatic dynamics in its vicinity. This sensitivity, combined with its mechanical flexibility and biocompatibility, make graphene a very attractive material for bio-sensing applications. Thanks to its unique set of properties, graphene is considered as a transducer with very high potential for next generation neural interfaces.
The thesis work presented has involved at first to assess the requirements for brain neural interfaces for intracortical electrophysiology, aiming e.g. at *in vivo* application to epilepsy studies; then, review the state of the art of the devices used so far; after that, to iteratively develop the graphene-based technology necessary to fulfill the requirements, demonstrate its feasibility and provide a roadmap for the integration of the graphene solution-gated field-effect transistor (gSGFET) technology into epi-cortical and intra-cortical μECoG arrays, achieving high spatio-temporal resolution.

It was chosen to improve the signal-to-noise (SNR) of the gSGFETs by decreasing its intrinsic 1/f noise, understanding its root causes, and then tailoring the fabrication processes. In the attempt to lower the intrinsic electronic noise, an exhaustive

analysis of 1/f noise in gSGFETs has allowed to unveil the contributions of the graphene FET transistor channel and of the contacts region resistances, whose relative importance depends on the device geometry. The contacts region is found to be the prevalent source for 1/f noise in devices with short graphene channel; on the other end, channel noise becomes more significant at increasing graphene channel lengths.
As for the gSGFET contacts noise, our results point out the importance of applying an ultra-violet ozone (UVO) treatment at the graphene-metal interface; this treatment has two main effects, surface residue cleaning and controlled defect creation in the graphene sheet underneath the metal contacts. As a result, it leads to lowered contact resistance (R_C), increased linearity of signal transduction, and the homogeneity across devices. This has effectively improved the sensitivity of the neural interface and reduced the contact contribution to the intrinsic noise.
As for the reduction of the gSGFET channel noise, three methods were investigated: (1) the encapsulation of graphene in multi-layer hexagonal-boron nitride (hBN); (2) self assembled monolayer of hexamethyldisilazane (HMDS) onto the SiO_2 substrate and (3), double transfer graphene (DT) gSGFETs. The electronic properties of single layer (SL) gSGFETs have been compared against the gSGFETs produced with the three above-mentioned methods, revealing better SNR performances for encapsulated-hBN and DT-gSGFETs in case of longer graphene channels (L>20 μm).

The wafer-scale fabrication of graphene SGFETs was optimized first on rigid substrates and then on the flexible polymeric substrate polyimide (PI). The optimization enabled the production of homogeneous and high yield (>80%) gSGFETs with high SNR. The SGFETs produced have been extensively characterised in terms of their electrical performance, electronic noise and frequency response, while improving and iterating the processes, to obtain qualified devices.
For the *in-vivo* demonstrations, ultra flexible ($\approx 15\mu$m thick) polyimide-embedded epi-cortical and intra-cortical neural probes, consisting of micro-transistors arrays, were designed and fabricated as transducers for micro-electrocorticography (μECoG).

Besides having improved the sensitivity of the devices, we had to tackle the problem of how to insert flexible intracortical devices in the brain. In order to do so, a low invasive insertion strategy was developed in the frame of this PhD work. It consists in a stiffening procedure, based on the bioresorbable protein silk fibroin (SF). This strategy enabled us to have μm-precision control on the thickness and the shape

of the SF-shuttle, which then dissolves in the brain within seconds after insertion, restoring the gDNP to its soft, flexible nature, neither provoking damages to the cells, nor gDNP functional degradations. Besides, we have verified and demonstrated the re-usability of flexible gDNP for more than one SF-coating.

In the frame of the PhD work, the arrays of gSGFETs developed have been applied and tested in relevant awake rodant models of seizures and of established epilepsy. We have presented, analyzed and discussed the experiments, done with the multichannel flexible gDNP produced. The *in vivo* experiments have allowed the detection and mapping of ISA through different cortical layers and subcortical regions, whilst simultaneously recording epileptiform activity in more conventional frequency bands (1-600Hz). It has been demonstrated that this novel technology can record with unprecedented stability and spatio-temporal resolution electrophysiological biomarkers related to epilepsy, including interictal spikes, pre-ictal DC shifts, seizures, high frequency oscillations (HFO) and post-ictal spreading depolarisation.
Besides *in vivo* acute and short-term experiments, we have also conducted an extensive study on the chronic implantation of the gDNP in rats, demonstrating long term recording stability in operation as well as the remarkable biocompatibility of the implanted gDNP.
Altogether, the chronic functionality and biocompatibility studies done confirm that gDNPs are indeed suitable for chronic implantation, inducing no significant damage nor neuroinflammatory response even at 10 weeks after implantation.

To recap, the gSGFET transistor devices have been improved by reducing the contacts noise and the channel noise, via finely tailoring fabrication and process issues. Flexible neural arrays of gSFGFETs have been fabricated, minimizing the shank width of the gDNP by a two metal layer method, interconnected via-holes. A silk fibroin bioresorbable shuttle method has been devised and tailored to allow the insertion of the gDNP in the brain, without buckling, with excellent biological response. It has been demonstrated that the gNDP remains fully operational in the brain, even after 10 weeks of implantation. *In vivo* experiments have given unprecedented and novel electropysiological results on the seizures and epilepsy conditions, published and currently in use in the corresponding field of preclinical neurosciece, opening the path for future discoveries.

6.2 Outlook

Measuring the full bandwidth of neuronal activity in the brain (including infraslow activity as well as activity >0.1 Hz) with high spatiotemporal resolution, also thanks to the newly developed gDNP neural interfaces, will contribute to the advancement of our understanding of the healthy and of the diseased brains. This is particularly relevant in diseases such as epilepsy, for which very broad electrical activity is observed. For instance, while SD and seizures can occur concurrently, the inter layer dynamics and the effect of SD on epileptic activity across the cortical laminae and deeper regions of the brain remain largely unknown, typically due to the lack of suitable technology able to measure this broad activity.
Together with a validation of chronic functionality of implanted gDNPs, this work underlines very distinct advantages of the developed graphene technology for *in-vivo* epilepsy research. The demonstrated graphene sensor technology can help a better understanding of seizure initiation and termination, and to gain insight into the nature of post-seizure spreading depolarisations, which have been recently implied in sudden, unexplained death in epilepsy cases (SUDEP) [143, 144].
To be noted that the capability to measure infraslow activities with high spatial sampling resolution does not depend on a given transistor size but is preserved among a wide range of device sizes, which brings freedom when designing an array for a given application.
Exploiting the optical transparency of graphene, it is possible to envision the future combination of epi-cortical and gDNP probes with imaging techniques, such as laser speckle contrast imaging (LSCI) or calcium imaging techniques [59, 354], to map infraslow electrophysiological signals. This combination of techniques would enable a 3D full bandwidth electrophysiological recording, potentially leading to a better understanding of neural and neurovascular coupling phenomena. Also the combination of electrical neural recordings with recent advancement in optogenetics, in which genetic modified neurons in the brain can be selectively excited/inhibited with light, will provide a complementary information to electrophysiology experiments and studies [59, 355].

As for aspects that should need further development, we highlight the necessity to fabricate gDNP with longer shanks, which will enable full bandwidth recordings in even deeper regions of the brain, such as the hippocampus and the thalamus. For such purpose, the insertion strategy need to be further refined and optimized,

looking e.g. for other bio-polymers or hydrogels with lower dissolution rate than the presented silk-fibroin, which can not reach deeper than ≈ 2 mm without buckling.
Another area of future development concerns the fabrication of arrays with very high number of elements. The nature of the gSGFET as an active electrical component with intrinsic signal amplification allows the realization of multiplexed sensor arrays, without requiring integrated addressing circuitry, thus reducing the number of needed electrical connections [64, 41]. Consequently, in addition to their potential as efficient full bandwidth transducers of neural activity, gSGFETs also show great promise as building blocks for multiplexed brain-machine interfaces, with large sensor numbers (>1000 sensors). The integration of the multiplexed strategy in epicortical probes or in multi-shanks depth neural probes with high density linear arrays, might soon surpass many comparable technologies, for what regards the number of sensors and the detectable spectral bandwidth in the time domain.
If the challenges of translating gSGFET technology to the clinics, such as chronic, safe operation and human compatibility, are overcome, gSGFETs could be applied in neurointensive care monitoring [356] or for CSD intraoperative monitoring, since there is evidence that CSD may occur during neurosurgical procedures [357].
Besides epilepsy research, the graphene sensor technology is expected to advance our understanding of neurological diseases, and could easily be applied to study disorders associated with infraslow activity - including traumatic brain injury, stroke and migraine [90].
Measuring the full bandwidth of neuronal activity in the brain with high spatio-temporal resolution will surely help to advance our understanding of the normal and/or the pathological brain, eventually contributing to improve the diagnosis of brain disorders and, ultimately, the therapies for those suffering from them.

References

[1] Marco Piccolino. “Luigi Galvani’s path to animal electricity”. en. In: *C. R. Biol.* 329.5-6 (May 2006), pp. 303–318.

[2] Nicholas G Hatsopoulos and John P Donoghue. “The science of neural interface systems”. en. In: *Annu. Rev. Neurosci.* 32 (2009), pp. 249–266.

[3] Joel S Perlmutter and Jonathan W Mink. “Deep brain stimulation”. en. In: *Annu. Rev. Neurosci.* 29 (2006), pp. 229–257.

[4] Angelo Lavano Attilio Della. *Deep Brain Stimulation for Treatment-Resistant Depression: Review of the Literature*. 2015.

[5] Alik S Widge, Donald A Malone, and Darin D Dougherty. *Closing the Loop on Deep Brain Stimulation for Treatment-Resistant Depression*. 2018.

[6] Serge Picaud and José-Alain Sahel. *Retinal prostheses: Clinical results and future challenges*. 2014.

[7] Gregg A Tabot et al. “Restoring the sense of touch with a prosthetic hand through a brain interface”. en. In: *Proc. Natl. Acad. Sci. U. S. A.* 110.45 (Nov. 2013), pp. 18279–18284.

[8] Sharlene N Flesher et al. “Intracortical microstimulation of human somatosensory cortex”. en. In: *Sci. Transl. Med.* 8.361 (Oct. 2016), 361ra141.

[9] David J Payne et al. *Drugs for bad bugs: confronting the challenges of antibacterial discovery*. 2007.

[10] Long Yang, Yuanchang Li, and Ying Fang. “Nanodevices for cellular interfaces and electrophysiological recording”. en. In: *Adv. Mater.* 25.28 (July 2013), pp. 3881–3887.

[11] Edward F Chang. “Towards large-scale, human-based, mesoscopic neurotechnologies”. en. In: *Neuron* 86.1 (Apr. 2015), pp. 68–78.

[12] Mikhail A Lebedev and Miguel A L Nicolelis. “Brain–machine interfaces: past, present and future”. In: *Trends Neurosci.* 29.9 (Sept. 2006), pp. 536–546.

[13] Meel Velliste et al. *Cortical control of a prosthetic arm for self-feeding*. 2008.

[14] Jennifer L Collinger et al. "Collaborative approach in the development of high-performance brain-computer interfaces for a neuroprosthetic arm: translation from animal models to human control". en. In: *Clin. Transl. Sci.* 7.1 (Feb. 2014), pp. 52–59.

[15] Anirudh Vallabhaneni, Tao Wang, and Bin He. *Brain—Computer Interface*.

[16] Jonathan S Brumberg and Frank H Guenther. "Development of speech prostheses: current status and recent advances". In: *Expert Rev. Med. Devices* 7.5 (Sept. 2010), pp. 667–679.

[17] Hassan Akbari et al. "Towards reconstructing intelligible speech from the human auditory cortex". en. In: *Sci. Rep.* 9.1 (Jan. 2019), p. 874.

[18] Kostas Kostarelos et al. *Graphene in the Design and Engineering of Next-Generation Neural Interfaces*. 2017.

[19] Lucas Heinrich Hess. "Graphene Transistors for Biosensing and Bioelectronics". PhD thesis. Technische Universität München, 2014.

[20] Boris Rosin et al. "Closed-Loop Deep Brain Stimulation Is Superior in Ameliorating Parkinsonism". In: *Neuron* 72.2 (Oct. 2011), pp. 370–384.

[21] Antal Berényi et al. "Closed-loop control of epilepsy by transcranial electrical stimulation". en. In: *Science* 337.6095 (Aug. 2012), pp. 735–737.

[22] Dietrich Haubenberger and Johanna Thompson-Westra. *Faculty Opinions recommendation of Stimulating at the right time: phase-specific deep brain stimulation*. 2017.

[23] Oliver Müller and Stefan Rotter. "Neurotechnology: Current Developments and Ethical Issues". en. In: *Front. Syst. Neurosci.* 11 (Dec. 2017), p. 93.

[24] Chandrasekharan Kesavadas and Bejoy Thomas. "Clinical applications of functional MRI in epilepsy". en. In: *Indian J. Radiol. Imaging* 18.3 (Aug. 2008), pp. 210–217.

[25] Thomas Deffieux et al. "Functional ultrasound neuroimaging: a review of the preclinical and clinical state of the art". en. In: *Curr. Opin. Neurobiol.* 50 (June 2018), pp. 128–135.

[26] Juan José Vaquero and Paul Kinahan. “Positron Emission Tomography: Current Challenges and Opportunities for Technological Advances in Clinical and Preclinical Imaging Systems”. en. In: *Annu. Rev. Biomed. Eng.* 17 (2015), pp. 385–414.

[27] Tim J von Oertzen. “PET and ictal SPECT can be helpful for localizing epileptic foci”. en. In: *Curr. Opin. Neurol.* 31.2 (Apr. 2018), pp. 184–191.

[28] Yoon Jae Kim et al. “A study on a robot arm driven by three-dimensional trajectories predicted from non-invasive neural signals”. en. In: *Biomed. Eng. Online* 14 (Aug. 2015), p. 81.

[29] Bijan Pesaran et al. “Investigating large-scale brain dynamics using field potential recordings: analysis and interpretation”. en. In: *Nat. Neurosci.* 21.7 (July 2018), pp. 903–919.

[30] Lai-Wo Stan Leung. *Field Potentials in the Central Nervous System: Recording, Analysis, and Modeling.*

[31] Changkyun Im and Jong-Mo Seo. “A review of electrodes for the electrical brain signal recording”. In: *Biomedical Engineering Letters* 6.3 (2016), pp. 104–112.

[32] Sylvain Baillet. “Magnetoencephalography for brain electrophysiology and imaging”. en. In: *Nat. Neurosci.* 20.3 (Feb. 2017), pp. 327–339.

[33] Christian Herff, Dean J Krusienski, and Pieter Kubben. “The Potential of Stereotactic-EEG for Brain-Computer Interfaces: Current Progress and Future Directions”. en. In: *Front. Neurosci.* 14 (Feb. 2020), p. 123.

[34] John P Donoghue. “Bridging the brain to the world: a perspective on neural interface systems”. en. In: *Neuron* 60.3 (Nov. 2008), pp. 511–521.

[35] Mehdi Jorfi et al. “Progress towards biocompatible intracortical microelectrodes for neural interfacing applications”. en. In: *J. Neural Eng.* 12.1 (Feb. 2015), p. 011001.

[36] Ritchie Chen, Andres Canales, and Polina Anikeeva. “Neural Recording and Modulation Technologies”. en. In: *Nat Rev Mater* 2.2 (Feb. 2017).

[37] Rich Pang, Benjamin J Lansdell, and Adrienne L Fairhall. “Dimensionality reduction in neuroscience”. en. In: *Curr. Biol.* 26.14 (July 2016), R656–60.

[38] Matthew P Ward et al. “Toward a comparison of microelectrodes for acute and chronic recordings”. en. In: *Brain Res.* 1282 (July 2009), pp. 183–200.

[39] Enming Song et al. “Materials for flexible bioelectronic systems as chronic neural interfaces”. en. In: *Nat. Mater.* 19.6 (June 2020), pp. 590–603.

[40] Kelsey A Potter et al. “Stab injury and device implantation within the brain results in inversely multiphasic neuroinflammatory and neurodegenerative responses”. en. In: *J. Neural Eng.* 9.4 (Aug. 2012), p. 046020.

[41] Jonathan Viventi et al. “Flexible, foldable, actively multiplexed, high-density electrode array for mapping brain activity in vivo”. en. In: *Nat. Neurosci.* 14.12 (Nov. 2011), pp. 1599–1605.

[42] R A Green et al. “Performance of conducting polymer electrodes for stimulating neuroprosthetics”. en. In: *J. Neural Eng.* 10.1 (Feb. 2013), p. 016009.

[43] William R Stauffer and Xinyan T Cui. “Polypyrrole doped with 2 peptide sequences from laminin”. en. In: *Biomaterials* 27.11 (Apr. 2006), pp. 2405–2413.

[44] Joseph Wang, Jinhua Dai, and Travis Yarlagadda. *Carbon NanotubeConducting-Polymer Composite Nanowires*. 2005.

[45] Laure V Kayser and Darren J Lipomi. “Stretchable Conductive Polymers and Composites Based on PEDOT and PEDOT:PSS”. en. In: *Adv. Mater.* 31.10 (Mar. 2019), e1806133.

[46] Dion Khodagholy et al. “In vivo recordings of brain activity using organic transistors”. en. In: *Nat. Commun.* 4 (2013), p. 1575.

[47] Zaid Aqrawe et al. “The influence of macropores on PEDOT/PSS microelectrode coatings for neuronal recording and stimulation”. In: *Sens. Actuators B Chem.* 281 (Feb. 2019), pp. 549–560.

[48] Quan Qing et al. “Nanowire transistor arrays for mapping neural circuits in acute brain slices”. en. In: *Proc. Natl. Acad. Sci. U. S. A.* 107.5 (Feb. 2010), pp. 1882–1887.

[49] Brian P Timko et al. “Electrical Recording from Hearts with Flexible Nanowire Device Arrays”. In: *Nano Lett.* 9.2 (Feb. 2009), pp. 914–918.

[50] Ning Li et al. *The promotion of neurite sprouting and outgrowth of mouse hippocampal cells in culture by graphene substrates*. 2011.

[51] Deshdeepak Sahni et al. “Biocompatibility of pristine graphene for neuronal interface”. en. In: *J. Neurosurg. Pediatr.* 11.5 (May 2013), pp. 575–583.

[52] Amel Bendali et al. *Purified Neurons can Survive on Peptide-Free Graphene Layers*. 2013.

[53] Gregg P Kotchey et al. *The Enzymatic Oxidation of Graphene Oxide*. 2011.

[54] Yingjie Li et al. *Surface Coating-Dependent Cytotoxicity and Degradation of Graphene Derivatives: Towards the Design of Non-Toxic, Degradable Nano-Graphene*. 2014.

[55] Rajendra Kurapati et al. *Dispersibility-Dependent Biodegradation of Graphene Oxide by Myeloperoxidase*. 2015.

[56] Sung Young Park et al. "Enhanced differentiation of human neural stem cells into neurons on graphene". en. In: *Adv. Mater.* 23.36 (Sept. 2011), H263–7.

[57] Dong-Wook Park et al. "Fabrication and utility of a transparent graphene neural electrode array for electrophysiology, in vivo imaging, and optogenetics". en. In: *Nat. Protoc.* 11.11 (Nov. 2016), pp. 2201–2222.

[58] Ta-Chung Liu et al. "Implantable Graphene-based Neural Electrode Interfaces for Electrophysiology and Neurochemistry in In Vivo Hyperacute Stroke Model". en. In: *ACS Appl. Mater. Interfaces* 8.1 (Jan. 2016), pp. 187–196.

[59] Duygu Kuzum et al. "Transparent and flexible low noise graphene electrodes for simultaneous electrophysiology and neuroimaging". en. In: *Nat. Commun.* 5 (Oct. 2014), p. 5259.

[60] Nicholas V Apollo et al. "Soft, Flexible Freestanding Neural Stimulation and Recording Electrodes Fabricated from Reduced Graphene Oxide". In: *Adv. Funct. Mater.* 25.23 (June 2015), pp. 3551–3559.

[61] Yichen Lu et al. "Flexible Neural Electrode Array Based-on Porous Graphene for Cortical Microstimulation and Sensing". en. In: *Sci. Rep.* 6 (Sept. 2016), p. 33526.

[62] Matthew J Nelson et al. "Review of signal distortion through metal microelectrode recording circuits and filters". en. In: *J. Neurosci. Methods* 169.1 (Mar. 2008), pp. 141–157.

[63] Eduard Masvidal-Codina et al. "High-resolution mapping of infraslow cortical brain activity enabled by graphene microtransistors". en. In: *Nat. Mater.* 18.3 (Mar. 2019), pp. 280–288.

[64] Nathan Schaefer et al. "Multiplexed neural sensor array of graphene solution-gated field-effect transistors". In: *2D Materials* 7 (Apr. 2020), p. 025046.

[65] William C Stacey et al. “Potential for unreliable interpretation of EEG recorded with microelectrodes”. en. In: *Epilepsia* 54.8 (Aug. 2013), pp. 1391–1401.

[66] Lucas H Hess et al. “Graphene transistor arrays for recording action potentials from electrogenic cells”. en. In: *Adv. Mater.* 23.43 (Nov. 2011), pp. 5045–9, 4968.

[67] Beom Joon Kim et al. “High-performance flexible graphene field effect transistors with ion gel gate dielectrics”. en. In: *Nano Lett.* 10.9 (Sept. 2010), pp. 3464–3466.

[68] L H Hess et al. “High-transconductance graphene solution-gated field effect transistors”. In: *Appl. Phys. Lett.* 99.3 (July 2011), p. 033503.

[69] Ramon Garcia-Cortadella et al. “Distortion-Free Sensing of Neural Activity Using Graphene Transistors”. en. In: *Small* 16.16 (Apr. 2020), e1906640.

[70] C Hébert, E Masvidal-Codina, et al. “Flexible graphene solution-gated field-effect transistors: efficient transducers for micro-electrocorticography”. In: *Adv. Funct. Mater.* (2018).

[71] A Guimerà-Brunet et al. “Neural interfaces based on flexible graphene transistors: A new tool for electrophysiology”. In: *2019 IEEE International Electron Devices Meeting (IEDM)*. Dec. 2019, pp. 18.3.1–18.3.4.

[72] Maria A Patestas and Leslie P Gartner. *A Textbook of Neuroanatomy*. en. John Wiley & Sons, May 2016.

[73] Henrik Alle, Arnd Roth, and Jörg R P Geiger. “Energy-efficient action potentials in hippocampal mossy fibers”. en. In: *Science* 325.5946 (Sept. 2009), pp. 1405–1408.

[74] Xi Duan, Sebastien Taurand, and Manuchehr Soleimani. “Artificial skin through super-sensing method and electrical impedance data from conductive fabric with aid of deep learning”. In: *Sci. Rep.* 9.1 (June 2019), p. 8831.

[75] György Buzsáki and Fernando Lopes da Silva. “High frequency oscillations in the intact brain”. en. In: *Prog. Neurobiol.* 98.3 (Sept. 2012), pp. 241–249.

[76] Oscar Herreras. “Local Field Potentials: Myths and Misunderstandings”. en. In: *Front. Neural Circuits* 10 (Dec. 2016), p. 101.

[77] György Buzsáki. “Theta oscillations in the hippocampus”. en. In: *Neuron* 33.3 (Jan. 2002), pp. 325–340.

[78] Eran Stark and Moshe Abeles. “Predicting movement from multiunit activity”. en. In: *J. Neurosci.* 27.31 (Aug. 2007), pp. 8387–8394.

[79] Stuart W Hughes et al. “Infraslow (<0.1 Hz) oscillations in thalamic relay nuclei basic mechanisms and significance to health and disease states”. en. In: *Prog. Brain Res.* 193 (2011), pp. 145–162.

[80] N A Aladjalova. “Infra-slow rhythmic oscillations of the steady potential of the cerebral cortex”. en. In: *Nature* 179.4567 (May 1957), pp. 957–959.

[81] J S Damoiseaux et al. “Consistent resting-state networks across healthy subjects”. en. In: *Proc. Natl. Acad. Sci. U. S. A.* 103.37 (Sept. 2006), pp. 13848–13853.

[82] M De Luca et al. “fMRI resting state networks define distinct modes of long-distance interactions in the human brain”. en. In: *Neuroimage* 29.4 (Feb. 2006), pp. 1359–1367.

[83] D Mantini et al. “Electrophysiological signatures of resting state networks in the human brain”. en. In: *Proc. Natl. Acad. Sci. U. S. A.* 104.32 (Aug. 2007), pp. 13170–13175.

[84] Jens P Dreier and Clemens Reiffurth. “The stroke-migraine depolarization continuum”. en. In: *Neuron* 86.4 (May 2015), pp. 902–922.

[85] Simo Monto et al. “Very Slow EEG Fluctuations Predict the Dynamics of Stimulus Detection and Oscillation Amplitudes in Humans”. en. In: *J. Neurosci.* 28.33 (Aug. 2008), pp. 8268–8272.

[86] S Vanhatalo et al. “Infraslow oscillations modulate excitability and interictal epileptic activity in the human cortex during sleep”. en. In: *Proc. Natl. Acad. Sci. U. S. A.* 101.14 (Apr. 2004), pp. 5053–5057.

[87] Jens P Dreier. “The role of spreading depression, spreading depolarization and spreading ischemia in neurological disease”. en. In: *Nat. Med.* 17.4 (Apr. 2011), pp. 439–447.

[88] Daniela Pietrobon and Michael A Moskowitz. “Chaos and commotion in the wake of cortical spreading depression and spreading depolarizations”. en. In: *Nat. Rev. Neurosci.* 15.6 (June 2014), pp. 379–393.

[89] Yilong Cui, Yosky Kataoka, and Yasuyoshi Watanabe. “Role of cortical spreading depression in the pathophysiology of migraine”. en. In: *Neurosci. Bull.* 30.5 (Oct. 2014), pp. 812–822.

[90] Martin Lauritzen et al. “Clinical relevance of cortical spreading depression in neurological disorders: migraine, malignant stroke, subarachnoid and intracranial hemorrhage, and traumatic brain injury”. en. In: *J. Cereb. Blood Flow Metab.* 31.1 (Jan. 2011), pp. 17–35.

[91] R P Kraig and C Nicholson. “Extracellular ionic variations during spreading depression”. en. In: *Neuroscience* 3.11 (1978), pp. 1045–1059.

[92] S Canals et al. “Longitudinal depolarization gradients along the somatodendritic axis of CA1 pyramidal cells: a novel feature of spreading depression”. en. In: *J. Neurophysiol.* 94.2 (Aug. 2005), pp. 943–951.

[93] Aristides A P Leao. “SPREADING DEPRESSION OF ACTIVITY IN THE CEREBRAL CORTEX”. In: *J. Neurophysiol.* 7.6 (Nov. 1944), pp. 359–390.

[94] Takahiro Takano et al. “Cortical spreading depression causes and coincides with tissue hypoxia”. en. In: *Nat. Neurosci.* 10.6 (June 2007), pp. 754–762.

[95] H Kager, W J Wadman, and G G Somjen. “Conditions for the triggering of spreading depression studied with computer simulations”. en. In: *J. Neurophysiol.* 88.5 (Nov. 2002), pp. 2700–2712.

[96] D F Rolfe and G C Brown. “Cellular energy utilization and molecular origin of standard metabolic rate in mammals”. en. In: *Physiol. Rev.* 77.3 (July 1997), pp. 731–758.

[97] G G Somjen. “Mechanisms of spreading depression and hypoxic spreading depression-like depolarization”. en. In: *Physiol. Rev.* 81.3 (July 2001), pp. 1065–1096.

[98] M Nedergaard and A J Hansen. “Spreading depression is not associated with neuronal injury in the normal brain”. en. In: *Brain Res.* 449.1-2 (May 1988), pp. 395–398.

[99] Fatemeh Bahari et al. “Spreading Depression and Seizure Unification Experimentally Observed in Epilepsy”. en. Oct. 2018.

[100] Viktor K Jirsa et al. “On the nature of seizure dynamics”. en. In: *Brain* 137.Pt 8 (Aug. 2014), pp. 2210–2230.

[101] Hippocrates and Francis Adams. *The Genuine Works of Hippocrates; Translated from the Greek by Francis Adams*. Bailliere, Tindall & Cox, 1939.

[102] Emmanouil Magiorkinis, Kalliopi Sidiropoulou, and Aristidis Diamantis. “Hallmarks in the history of epilepsy: epilepsy in antiquity”. en. In: *Epilepsy Behav.* 17.1 (Jan. 2010), pp. 103–108.

[103] William C Stacey and Brian Litt. “Technology insight: neuroengineering and epilepsy-designing devices for seizure control”. en. In: *Nat. Clin. Pract. Neurol.* 4.4 (Apr. 2008), pp. 190–201.

[104] Anthony Fauci et al. *Harrison’s Principles of Internal Medicine, 17th Edition*. en. Mcgraw-hill, Mar. 2008.

[105] Marvin M Goldenberg. “Overview of drugs used for epilepsy and seizures: etiology, diagnosis, and treatment”. en. In: *P T* 35.7 (July 2010), pp. 392–415.

[106] Ettore Beghi. “Treating epilepsy across its different stages”. en. In: *Ther. Adv. Neurol. Disord.* 3.2 (Mar. 2010), pp. 85–92.

[107] Carl E Stafstrom and Lionel Carmant. “Seizures and epilepsy: an overview for neuroscientists”. en. In: *Cold Spring Harb. Perspect. Med.* 5.6 (June 2015).

[108] G L Holmes and Y Ben-Ari. “The neurobiology and consequences of epilepsy in the developing brain”. en. In: *Pediatr. Res.* 49.3 (Mar. 2001), pp. 320–325.

[109] W T Blume et al. “Glossary of descriptive terminology for ictal semiology: report of the ILAE task force on classification and terminology”. en. In: *Epilepsia* 42.9 (Sept. 2001), pp. 1212–1218.

[110] “Guidelines for epidemiologic studies on epilepsy. Commission on Epidemiology and Prognosis, International League Against Epilepsy”. en. In: *Epilepsia* 34.4 (July 1993), pp. 592–596.

[111] Emily Oby and Damir Janigro. “The blood–brain barrier and epilepsy”. In: *Epilepsia* 47.11 (2006), pp. 1761–1774.

[112] E A van Vliet et al. “Blood–brain barrier leakage may lead to progression of temporal lobe epilepsy”. In: *Brain* 130.2 (Feb. 2007), pp. 521–534.

[113] Jan A Gorter, Erwin A van Vliet, and Eleonora Aronica. “Status epilepticus, blood–brain barrier disruption, inflammation, and epileptogenesis”. In: *Epilepsy Behav.* 49 (Aug. 2015), pp. 13–16.

[114] Nicola Marchi, Manoj Banjara, and Damir Janigro. “Blood–brain barrier, bulk flow, and interstitial clearance in epilepsy”. In: *J. Neurosci. Methods* 260 (Feb. 2016), pp. 118–124.

[115] Hkmcc Kandar et al. “Epilepsy and its management: A review”. In: *Journal of PharmaSciTech* 1.2 (2012), pp. 20–26.

[116] Linda Dalic and Mark J Cook. “Managing drug-resistant epilepsy: challenges and solutions”. en. In: *Neuropsychiatr. Dis. Treat.* 12 (Oct. 2016), pp. 2605–2616.

[117] G D Cascino. “Epilepsy: contemporary perspectives on evaluation and treatment”. In: *Mayo Clin. Proc.* (1994).

[118] J Engel Jr. “Surgery for seizures”. en. In: *N. Engl. J. Med.* 334.10 (Mar. 1996), pp. 647–652.

[119] S J Groiss et al. “Deep brain stimulation in Parkinson’s disease”. en. In: *Ther. Adv. Neurol. Disord.* 2.6 (Nov. 2009), pp. 20–28.

[120] John A Lawson and Ingrid E Scheffer. “Therapeutic use of medicinal cannabis in difficult to manage epilepsy”. en. In: *Br. J. Clin. Pharmacol.* 84.11 (Nov. 2018), pp. 2488–2490.

[121] Shivani Tiwari et al. “Biosensors for Epilepsy Management: State-of-Art and Future Aspects”. en. In: *Sensors* 19.7 (Mar. 2019).

[122] Jerome Engel Jr et al. “Epilepsy biomarkers”. en. In: *Epilepsia* 54 Suppl 4 (Aug. 2013), pp. 61–69.

[123] K J Reinikainen et al. “CT brain scan and EEG in the diagnosis of adult onset seizures”. en. In: *Epilepsy Res.* 1.3 (May 1987), pp. 178–184.

[124] Vassiliy Tsytsarev et al. “Photoacoustic and optical coherence tomography of epilepsy with high temporal and spatial resolution and dual optical contrasts”. en. In: *J. Neurosci. Methods* 216.2 (June 2013), pp. 142–145.

[125] Christian E Elger and Christian Hoppe. “Diagnostic challenges in epilepsy: seizure under-reporting and seizure detection”. en. In: *Lancet Neurol.* 17.3 (Mar. 2018), pp. 279–288.

[126] Martin Seeber et al. “Subcortical electrophysiological activity is detectable with high-density EEG source imaging”. en. In: *Nat. Commun.* 10.1 (Feb. 2019), p. 753.

[127] Edward H Bertram. “Electrophysiology in epilepsy surgery: Roles and limitations”. en. In: *Ann. Indian Acad. Neurol.* 17.Suppl 1 (Mar. 2014), S40–4.

[128] J Jacobs et al. “High-frequency oscillations (HFOs) in clinical epilepsy”. en. In: *Prog. Neurobiol.* 98.3 (Sept. 2012), pp. 302–315.

[129] Kevin J Staley, Andrew White, and F Edward Dudek. “Interictal spikes: harbingers or causes of epilepsy?” en. In: *Neurosci. Lett.* 497.3 (June 2011), pp. 247–250.

[130] G Buzsáki et al. “High-frequency network oscillation in the hippocampus”. en. In: *Science* 256.5059 (May 1992), pp. 1025–1027.

[131] A Bragin, C L Wilson, and J Engel Jr. “Chronic epileptogenesis requires development of a network of pathologically interconnected neuron clusters: a hypothesis”. en. In: *Epilepsia* 41 Suppl 6 (2000), S144–52.

[132] A Bragin et al. “Hippocampal and entorhinal cortex high-frequency oscillations (100–500 Hz) in human epileptic brain and in kainic acid–treated rats with chronic seizures”. en. In: *Epilepsia* 40.2 (Feb. 1999), pp. 127–137.

[133] Jose M Ibarz et al. “Emergent dynamics of fast ripples in the epileptic hippocampus”. en. In: *J. Neurosci.* 30.48 (Dec. 2010), pp. 16249–16261.

[134] Richard J Staba et al. “Single neuron burst firing in the human hippocampus during sleep”. en. In: *Hippocampus* 12.6 (2002), pp. 724–734.

[135] Elena Urrestarazu et al. “Interictal high-frequency oscillations (100-500 Hz) in the intracerebral EEG of epileptic patients”. en. In: *Brain* 130.Pt 9 (Sept. 2007), pp. 2354–2366.

[136] Julia Jacobs et al. “Interictal high-frequency oscillations (80-500 Hz) are an indicator of seizure onset areas independent of spikes in the human epileptic brain”. en. In: *Epilepsia* 49.11 (Nov. 2008), pp. 1893–1907.

[137] Shuang Wang et al. “Ripple classification helps to localize the seizure-onset zone in neocortical epilepsy”. en. In: *Epilepsia* 54.2 (Feb. 2013), pp. 370–376.

[138] A Ikeda et al. “Focal ictal direct current shifts in human epilepsy as studied by subdural and scalp recording”. en. In: *Brain* 122 (Pt 5) (May 1999), pp. 827–838.

[139] Somin Lee et al. “DC shifts, high frequency oscillations, ripples and fast ripples in relation to the seizure onset zone”. en. In: *Seizure* 77 (Apr. 2020), pp. 52–58.

[140] S Vanhatalo et al. “Very slow EEG responses lateralize temporal lobe seizures: an evaluation of non-invasive DC-EEG”. en. In: *Neurology* 60.7 (Apr. 2003), pp. 1098–1104.

[141] Shasha Wu et al. “Role of ictal baseline shifts and ictal high-frequency oscillations in stereo-electroencephalography analysis of mesial temporal lobe seizures”. en. In: *Epilepsia* 55.5 (May 2014), pp. 690–698.

[142] Daniel R Kramer et al. “Interplay between Cortical Spreading Depolarization and Seizures”. en. In: *Stereotact. Funct. Neurosurg.* 95.1 (Jan. 2017), pp. 1–5.

[143] Isamu Aiba and Jeffrey L Noebels. “Spreading depolarization in the brainstem mediates sudden cardiorespiratory arrest in mouse SUDEP models”. en. In: *Sci. Transl. Med.* 7.282 (Apr. 2015), 282ra46.

[144] Inge C M Loonen et al. “Brainstem spreading depolarization and cortical dynamics during fatal seizures in Cacna1a S218L mice”. en. In: *Brain* 142.2 (Feb. 2019), pp. 412–425.

[145] Nathan Schaefer et al. “Improved metal-graphene contacts for low-noise, high-density microtransistor arrays for neural sensing”. In: *Carbon N. Y.* 161 (May 2020), pp. 647–655.

[146] Nikolaos Mavredakis et al. “Understanding the bias dependence of low frequency noise in single layer graphene FETs”. en. In: *Nanoscale* 10.31 (2018), pp. 14947–14956.

[147] Nikolaos Mavredakis et al. *Bias dependent variability of low-frequency noise in single-layer graphene FETs*. 2020.

[148] Anastasios G Polyravas et al. “Impact of contact overlap on transconductance and noise in organic electrochemical transistors”. en. In: *Flex. Print. Electron.* 4.4 (Nov. 2019), p. 044003.

[149] K S Novoselov. *Electric Field Effect in Atomically Thin Carbon Films*. 2004.

[150] C Lee et al. *Measurement of the Elastic Properties and Intrinsic Strength of Monolayer Graphene*. 2008.

[151] Alexander A Balandin et al. “Superior thermal conductivity of single-layer graphene”. en. In: *Nano Lett.* 8.3 (Mar. 2008), pp. 902–907.

[152] R R Nair et al. “Fine structure constant defines visual transparency of graphene”. en. In: *Science* 320.5881 (June 2008), p. 1308.

[153] Mark Wilson. “Electrons in Atomically Thin Carbon Sheets Behave Like Massless Particles”. In: *Phys. Today* 59 (Jan. 2006), p. 21.

[154] A H Castro Neto et al. “The electronic properties of graphene”. In: *Rev. Mod. Phys.* 81.1 (2009), p. 109.

[155] P R Wallace. “The Band Theory of Graphite”. In: *Phys. Rev.* 71.9 (May 1947), pp. 622–634.

[156] R S Deacon et al. “Cyclotron resonance study of the electron and hole velocity in graphene monolayers”. In: *Phys. Rev. B Condens. Matter* 76.8 (Aug. 2007), p. 081406.

[157] Fengnian Xia et al. “Graphene field-effect transistors with high on/off current ratio and large transport band gap at room temperature”. en. In: *Nano Lett.* 10.2 (Feb. 2010), pp. 715–718.

[158] Kinam Kim et al. “A role for graphene in silicon-based semiconductor devices”. en. In: *Nature* 479.7373 (Nov. 2011), pp. 338–344.

[159] Jangyup Son et al. “Hydrogenated monolayer graphene with reversible and tunable wide band gap and its field-effect transistor”. en. In: *Nat. Commun.* 7 (Nov. 2016), p. 13261.

[160] K Nakada et al. “Edge state in graphene ribbons: Nanometer size effect and edge shape dependence”. en. In: *Phys. Rev. B Condens. Matter* 54.24 (Dec. 1996), pp. 17954–17961.

[161] Barbaros Özyilmaz et al. “Electronic transport in locally gated graphene nanoconstrictions”. In: *Appl. Phys. Lett.* 91.19 (Nov. 2007), p. 192107.

[162] Xiaolin Li et al. “Chemically derived, ultrasmooth graphene nanoribbon semiconductors”. en. In: *Science* 319.5867 (Feb. 2008), pp. 1229–1232.

[163] Marc Dvorak, William Oswald, and Zhigang Wu. “Bandgap opening by patterning graphene”. en. In: *Sci. Rep.* 3 (2013), p. 2289.

[164] D C Elias et al. *Dirac cones reshaped by interaction effects in suspended graphene*. 2011.

[165] Alexander S Mayorov et al. “Micrometer-scale ballistic transport in encapsulated graphene at room temperature”. en. In: *Nano Lett.* 11.6 (June 2011), pp. 2396–2399.

[166] Yanqing Wu et al. “State-of-the-art graphene high-frequency electronics”. en. In: *Nano Lett.* 12.6 (June 2012), pp. 3062–3067.

[167] F Giannazzo et al. *Challenges in graphene integration for high-frequency electronics*. 2016.

[168] A K Geim and K S Novoselov. “The rise of graphene”. In: *Nanoscience and Technology*. Co-Published with Macmillan Publishers Ltd, UK, Aug. 2009, pp. 11–19.

[169] Y-W Tan et al. “Measurement of scattering rate and minimum conductivity in graphene”. en. In: *Phys. Rev. Lett.* 99.24 (Dec. 2007), p. 246803.

[170] K S Novoselov et al. “Two-dimensional gas of massless Dirac fermions in graphene”. en. In: *Nature* 438.7065 (Nov. 2005), pp. 197–200.

[171] F Miao et al. “Phase-coherent transport in graphene quantum billiards”. en. In: *Science* 317.5844 (Sept. 2007), pp. 1530–1533.

[172] E H Hwang, S Adam, and S Das Sarma. “Carrier transport in two-dimensional graphene layers”. en. In: *Phys. Rev. Lett.* 98.18 (May 2007), p. 186806.

[173] Haiqun Chen et al. *Mechanically Strong, Electrically Conductive, and Biocompatible Graphene Paper*. 2008.

[174] Yong Liu et al. “Biocompatible graphene oxide-based glucose biosensors”. en. In: *Langmuir* 26.9 (May 2010), pp. 6158–6160.

[175] Shanying Han et al. “The application of graphene-based biomaterials in biomedicine”. en. In: *Am. J. Transl. Res.* 11.6 (June 2019), pp. 3246–3260.

[176] Enlai Gao et al. “Mechanical exfoliation of two-dimensional materials”. In: *J. Mech. Phys. Solids* 115 (June 2018), pp. 248–262.

[177] L Colombo, R M Wallace, and R S Ruoff. “Graphene Growth and Device Integration”. In: *Proc. IEEE* 101.7 (July 2013), pp. 1536–1556.

[178] Yuan Huang et al. “Reliable Exfoliation of Large-Area High-Quality Flakes of Graphene and Other Two-Dimensional Materials”. en. In: *ACS Nano* 9.11 (Nov. 2015), pp. 10612–10620.

[179] Cristina Gómez-Navarro et al. “Electronic transport properties of individual chemically reduced graphene oxide sheets”. en. In: *Nano Lett.* 7.11 (Nov. 2007), pp. 3499–3503.

[180] Goki Eda, Giovanni Fanchini, and Manish Chhowalla. “Large-area ultrathin films of reduced graphene oxide as a transparent and flexible electronic material”. en. In: *Nat. Nanotechnol.* 3.5 (May 2008), pp. 270–274.

[181] Yenny Hernandez et al. “High-yield production of graphene by liquid-phase exfoliation of graphite”. en. In: *Nat. Nanotechnol.* 3.9 (Sept. 2008), pp. 563–568.

[182] Peter Blake et al. “Graphene-based liquid crystal device”. en. In: *Nano Lett.* 8.6 (June 2008), pp. 1704–1708.

[183] Michael Segal. “Selling graphene by the ton”. en. In: *Nat. Nanotechnol.* 4.10 (Oct. 2009), pp. 612–614.

[184] Andrea C Ferrari et al. *Science and Technology Roadmap for Graphene, Related Two-dimensional Crystals, and Hybrid Systems*. en. Universitätsbibliothek der RWTH Aachen, 2015.

[185] Claire Berger et al. “Ultrathin Epitaxial Graphite: 2D Electron Gas Properties and a Route toward Graphene-based Nanoelectronics”. In: *J. Phys. Chem. B* 108.52 (Dec. 2004), pp. 19912–19916.

[186] Walt A De Heer et al. “Large area and structured epitaxial graphene produced by confinement controlled sublimation of silicon carbide”. In: *Proceedings of the National Academy of Sciences* 108.41 (2011), pp. 16900–16905.

[187] Claire Berger et al. “Electronic confinement and coherence in patterned epitaxial graphene”. en. In: *Science* 312.5777 (May 2006), pp. 1191–1196.

[188] M Sprinkle et al. “Scalable templated growth of graphene nanoribbons on SiC”. en. In: *Nat. Nanotechnol.* 5.10 (Oct. 2010), pp. 727–731.

[189] Jens Baringhaus et al. *Exceptional ballistic transport in epitaxial graphene nanoribbons*. 2014.

[190] Xuesong Li et al. “Large-area synthesis of high-quality and uniform graphene films on copper foils”. en. In: *Science* 324.5932 (June 2009), pp. 1312–1314.

[191] Keun Soo Kim et al. *Large-scale pattern growth of graphene films for stretchable transparent electrodes*. 2009.

[192] Johann Coraux et al. “Structural coherency of graphene on Ir(111)”. en. In: *Nano Lett.* 8.2 (Feb. 2008), pp. 565–570.

[193] Alfonso Reina et al. “Large area, few-layer graphene films on arbitrary substrates by chemical vapor deposition”. en. In: *Nano Lett.* 9.1 (Jan. 2009), pp. 30–35.

[194] Sukang Bae et al. “Roll-to-roll production of 30-inch graphene films for transparent electrodes”. en. In: *Nat. Nanotechnol.* 5.8 (Aug. 2010), pp. 574–578.

[195] Yufeng Hao et al. “The role of surface oxygen in the growth of large single-crystal graphene on copper”. en. In: *Science* 342.6159 (Nov. 2013), pp. 720–723.

[196] Luca Banszerus et al. “Ultrahigh-mobility graphene devices from chemical vapor deposition on reusable copper”. en. In: *Sci Adv* 1.6 (July 2015), e1500222.

[197] W Gannett et al. “Boron nitride substrates for high mobility chemical vapor deposited graphene”. In: *Appl. Phys. Lett.* 98.24 (June 2011), p. 242105.

[198] Hokwon Kim et al. “Activation energy paths for graphene nucleation and growth on Cu”. en. In: *ACS Nano* 6.4 (Apr. 2012), pp. 3614–3623.

[199] Andrea C Ferrari. “Raman spectroscopy of graphene and graphite: Disorder, electron–phonon coupling, doping and nonadiabatic effects”. In: *Solid State Commun.* 143.1 (July 2007), pp. 47–57.

[200] C V Raman and K S Krishnan. “A new type of secondary radiation”. In: *Nature* (1928).

[201] R Saito et al. “Raman spectroscopy of graphene and carbon nanotubes”. In: *Adv. Phys.* 60.3 (June 2011), pp. 413–550.

[202] D A Long. *Introductory Raman Spectroscopy. John R. Ferraro, Kazuo Nakamoto and Chris W. Brown. Academic Press, Amsterdam, Second Edition, 2003. xiii 434.* 2005.

[203] Andrea C Ferrari and Denis M Basko. “Raman spectroscopy as a versatile tool for studying the properties of graphene”. en. In: *Nat. Nanotechnol.* 8.4 (Apr. 2013), pp. 235–246.

[204] L M Malard et al. “Raman spectroscopy in graphene”. In: *Phys. Rep.* 473.5 (Apr. 2009), pp. 51–87.

[205] Michele Lazzeri et al. “Impact of the electron-electron correlation on phonon dispersion: Failure of LDA and GGA DFT functionals in graphene and graphite”. In: *Phys. Rev. B Condens. Matter* 78.8 (Aug. 2008), p. 081406.

[206] K Sato et al. “D-band Raman intensity of graphitic materials as a function of laser energy and crystallite size”. In: *Chem. Phys. Lett.* 427.1 (Aug. 2006), pp. 117–121.

[207] Axel Eckmann et al. “Probing the Nature of Defects in Graphene by Raman Spectroscopy”. In: *Nano Lett.* 12.8 (Aug. 2012), pp. 3925–3930.

[208] A C Ferrari et al. “Raman Spectrum of Graphene and Graphene Layers”. In: *Phys. Rev. Lett.* 97.18 (Oct. 2006), p. 187401.

[209] Allen J Bard, Larry R Faulkner, et al. “Fundamentals and applications”. In: *Electrochemical Methods* 2.482 (2001), pp. 580–632.

[210] M Gouy. *Sur la constitution de la charge électrique à la surface d'un électrolyte*. 1910.

[211] David Leonard Chapman. "LI. A contribution to the theory of electrocapillarity". In: *The London, Edinburgh, and Dublin philosophical magazine and journal of science* 25.148 (1913), pp. 475–481.

[212] J Kaspar. *Zur Theorie der elektrolytischen Doppelschicht und der potentialbestimmenden Ionenadsorption*. 1938.

[213] Serge Luryi. "Quantum capacitance devices". In: *Appl. Phys. Lett.* 52.6 (Feb. 1988), pp. 501–503.

[214] Tian Fang et al. "Carrier statistics and quantum capacitance of graphene sheets and ribbons". In: *Appl. Phys. Lett.* 91.9 (Aug. 2007), p. 092109.

[215] Jilin Xia et al. "Measurement of the quantum capacitance of graphene". en. In: *Nat. Nanotechnol.* 4.8 (Aug. 2009), pp. 505–509.

[216] Markus Dankerl et al. *Graphene Solution-Gated Field-Effect Transistor Array for Sensing Applications*. 2010.

[217] P Bergveld. "Development of an ion-sensitive solid-state device for neurophysiological measurements". en. In: *IEEE Trans. Biomed. Eng.* 17.1 (Jan. 1970), pp. 70–71.

[218] Simon M Sze and Kwok K Ng. *Physics of Semiconductor Devices*. en. John Wiley & Sons, Nov. 2006.

[219] Yu-Li Wang and Guang-Chao Zhao. "Electrochemical Sensing of Nitric Oxide on Electrochemically Reduced Graphene-Modified Electrode". en. In: *International Journal of Electrochemistry* 2011 (May 2011).

[220] G Giovannetti et al. *Doping Graphene with Metal Contacts*. 2008.

[221] Howard Reiss and Adam Heller. "The absolute potential of the standard hydrogen electrode: a new estimate". In: *J. Phys. Chem.* 89.20 (Sept. 1985), pp. 4207–4213.

[222] Seung Min Song et al. "Determination of work function of graphene under a metal electrode and its role in contact resistance". en. In: *Nano Lett.* 12.8 (Aug. 2012), pp. 3887–3892.

[223] Benno M Blaschke et al. *Mapping brain activity with flexible graphene microtransistors*. 2017.

[224] Marco Bobinger. “Controlled Modication of Graphene with Ozone”. MA thesis. TUM, 2014.

[225] Wei Li et al. “Ultraviolet/ozone treatment to reduce metal-graphene contact resistance”. In: *Appl. Phys. Lett.* 102.18 (May 2013), p. 183110.

[226] S Büttgenbach and M Feldmann. “Application of thick film resists in MEMS”. In: *ICMAT,(accepted)* (2005).

[227] Yanan Wang et al. “Resonance Raman spectroscopy of G-line and folded phonons in twisted bilayer graphene with large rotation angles”. In: *Appl. Phys. Lett.* 103.12 (Sept. 2013), p. 123101.

[228] Young Jun Kim et al. “Optical and Electrical Characteristics of Graphene Double Layer Formed by a Double Transfer of Graphene Single Layers”. en. In: *J. Nanosci. Nanotechnol.* 16.3 (Mar. 2016), pp. 2769–2772.

[229] A Gupta et al. “Raman scattering from high-frequency phonons in supported n-graphene layer films”. en. In: *Nano Lett.* 6.12 (Dec. 2006), pp. 2667–2673.

[230] A Righi et al. *Resonance Raman spectroscopy in twisted bilayer graphene.* 2013.

[231] Jae-Woong Jeong et al. “Soft materials in neuroengineering for hard problems in neuroscience”. en. In: *Neuron* 86.1 (Apr. 2015), pp. 175–186.

[232] Jonathan Rivnay et al. “Next-generation probes, particles, and proteins for neural interfacing”. en. In: *Sci Adv* 3.6 (June 2017), e1601649.

[233] Takashi D Yoshida Kozai and Daryl R Kipke. “Insertion shuttle with carboxyl terminated self-assembled monolayer coatings for implanting flexible polymer neural probes in the brain”. en. In: *J. Neurosci. Methods* 184.2 (Nov. 2009), pp. 199–205.

[234] Sarah Felix et al. “Removable silicon insertion stiffeners for neural probes using polyethylene glycol as a biodissolvable adhesive”. en. In: *Conf. Proc. IEEE Eng. Med. Biol. Soc.* 2012 (2012), pp. 871–874.

[235] Kyounghwan Na et al. “Novel diamond shuttle to deliver flexible neural probe with reduced tissue compression”. en. In: *Microsystems & Nanoengineering* 6.1 (June 2020), pp. 1–13.

[236] Hannah R Joo et al. “A microfabricated, 3D-sharpened silicon shuttle for insertion of flexible electrode arrays through dura mater into brain”. en. In: *J. Neural Eng.* 16.6 (Oct. 2019), p. 066021.

[237] S Takeuchi et al. *Parylene flexible neural probe with micro fluidic channel*.

[238] Stacie M Gutowski et al. "Protease-degradable PEG-maleimide coating with on-demand release of IL-1Ra to improve tissue response to neural electrodes". en. In: *Biomaterials* 44 (Mar. 2015), pp. 55–70.

[239] A Lecomte, V Castagnola, E Descamps, et al. "Silk and PEG as means to stiffen a parylene probe for insertion in the brain: toward a double time-scale tool for local drug delivery". In: *Journal of* (2015).

[240] Johan Agorelius et al. "An array of highly flexible electrodes with a tailored configuration locked by gelatin during implantation-initial evaluation in cortex cerebri of awake rats". en. In: *Front. Neurosci.* 9 (Sept. 2015), p. 331.

[241] Gustav Lind et al. *Gelatine-embedded electrodes—a novel biocompatible vehicle allowing implantation of highly flexible microelectrodes*. 2010.

[242] Meng-Chen Lo et al. "Coating flexible probes with an ultra fast degrading polymer to aid in tissue insertion". en. In: *Biomed. Microdevices* 17.2 (Apr. 2015), p. 34.

[243] Dan Lewitus et al. *Ultrafast resorbing polymers for use as carriers for cortical neural probes*. 2011.

[244] P J Gilgunn et al. *An ultra-compliant, scalable neural probe with molded biodissolvable delivery vehicle*. 2012.

[245] Christina Hassler, Tim Boretius, and Thomas Stieglitz. *Polymers for neural implants*. 2011.

[246] Zhuolin Xiang et al. *Ultra-thin flexible polyimide neural probe embedded in a dissolvable maltose-coated microneedle*. 2014.

[247] Lee W Tien et al. "Silk as a multifunctional biomaterial substrate for reduced glial scarring around brain-penetrating electrodes". In: *Adv. Funct. Mater.* 23.25 (2013), pp. 3185–3193.

[248] Fan Wu, Maesoon Im, and Euisik Yoon. *A flexible fish-bone-shaped neural probe strengthened by biodegradable silk coating for enhanced biocompatibility*. 2011.

[249] Heung Jae Chun et al. *Novel Biomaterials for Regenerative Medicine*. en. Springer, Oct. 2018.

[250] Rossana Boni. *Neural Tissue Engineering: An Investigation on Silk Fibroin/PEG/PVA Electrospun Nanofibres for Regenerating Brain Tissue : this Thesis is Submitted for the Degree of Master of Science, Centre for Bioengineering and Nanomedicine, University of Otago, Dunedin, New Zealand*. en. University of Otago, 2019.

[251] Yu-Qing Zhang. *Preparation of Silk Fibroin Nanoparticles and Enzyme-Entrapped Silk Fibroin Nanoparticles*. 2018.

[252] David Kaplan and Structure Workshop on Silks: Biology, Properties Genetics (1993 : Charlottesville Va.) *Silk Polymers: Materials Science and Biotechnology*. en. American Chemical Society, 1994.

[253] Charu Vepari and David L Kaplan. "Silk as a Biomaterial". en. In: *Prog. Polym. Sci.* 32.8-9 (2007), pp. 991–1007.

[254] Yang Cao and Bochu Wang. "Biodegradation of silk biomaterials". en. In: *Int. J. Mol. Sci.* 10.4 (Mar. 2009), pp. 1514–1524.

[255] Andrea S Gobin, Victoria E Froude, and Anshu B Mathur. "Structural and mechanical characteristics of silk fibroin and chitosan blend scaffolds for tissue regeneration". en. In: *J. Biomed. Mater. Res. A* 74.3 (Sept. 2005), pp. 465–473.

[256] Fiorenzo G Omenetto and David L Kaplan. "A new route for silk". In: *Nat. Photonics* 2.11 (Nov. 2008), pp. 641–643.

[257] Brian D Lawrence et al. "Bioactive silk protein biomaterial systems for optical devices". en. In: *Biomacromolecules* 9.4 (Apr. 2008), pp. 1214–1220.

[258] Xianyan Wang et al. "Nanolayer biomaterial coatings of silk fibroin for controlled release". en. In: *J. Control. Release* 121.3 (Aug. 2007), pp. 190–199.

[259] Dae-Hyeong Kim et al. "Dissolvable films of silk fibroin for ultrathin conformal bio-integrated electronics". In: *Nat. Mater.* 9.6 (June 2010), pp. 511–517.

[260] Xiao Hu et al. "Biomaterials derived from silk–tropoelastin protein systems". In: *Biomaterials* 31.32 (Nov. 2010), pp. 8121–8131.

[261] Ung-Jin Kim et al. "Three-dimensional aqueous-derived biomaterial scaffolds from silk fibroin". en. In: *Biomaterials* 26.15 (May 2005), pp. 2775–2785.

[262] Qiang Lu et al. "Green process to prepare silk fibroin/gelatin biomaterial scaffolds". en. In: *Macromol. Biosci.* 10.3 (Mar. 2010), pp. 289–298.

[263] Xiaohui Zhang, Michaela R Reagan, and David L Kaplan. "Electrospun silk biomaterial scaffolds for regenerative medicine". en. In: *Adv. Drug Deliv. Rev.* 61.12 (Oct. 2009), pp. 988–1006.

[264] Lim Jeong et al. "Time-resolved structural investigation of regenerated silk fibroin nanofibers treated with solvent vapor". en. In: *Int. J. Biol. Macromol.* 38.2 (Mar. 2006), pp. 140–144.

[265] Xiaoqin Wang et al. "Silk coatings on PLGA and alginate microspheres for protein delivery". en. In: *Biomaterials* 28.28 (Oct. 2007), pp. 4161–4169.

[266] Andreas S Lammel et al. "Controlling silk fibroin particle features for drug delivery". en. In: *Biomaterials* 31.16 (June 2010), pp. 4583–4591.

[267] Xiaoqin Wang et al. "Silk nanospheres and microspheres from silk/pva blend films for drug delivery". en. In: *Biomaterials* 31.6 (Feb. 2010), pp. 1025–1035.

[268] Xiaoqin Wang et al. "Sonication-induced gelation of silk fibroin for cell encapsulation". en. In: *Biomaterials* 29.8 (Mar. 2008), pp. 1054–1064.

[269] Tuna Yucel et al. "Non-equilibrium silk fibroin adhesives". en. In: *J. Struct. Biol.* 170.2 (May 2010), pp. 406–412.

[270] Gary G Leisk et al. "Electrogelation for protein adhesives". en. In: *Adv. Mater.* 22.6 (Feb. 2010), pp. 711–715.

[271] Osnat Hakimi et al. "Spider and mulberry silkworm silks as compatible biomaterials". In: *Composites Part B* 38.3 (Apr. 2007), pp. 324–337.

[272] Chenhua Zhao and Tetsuo Asakura. *Structure of Silk studied with NMR.* 2001.

[273] Gregory H Altman et al. "Silk-based biomaterials". en. In: *Biomaterials* 24.3 (Feb. 2003), pp. 401–416.

[274] P Poza et al. "Fractographic analysis of silkworm and spider silk". In: *Eng. Fract. Mech.* 69.9 (June 2002), pp. 1035–1048.

[275] L D Miller et al. "Investigation of the nanofibrillar morphology in silk fibers by small angle X-ray scattering and atomic force microscopy". en. In: *Int. J. Biol. Macromol.* 24.2-3 (Mar. 1999), pp. 159–165.

[276] S Putthanarat et al. "Investigation of the nanofibrils of silk fibers". In: *Polymer* 41.21 (Oct. 2000), pp. 7735–7747.

[277] Yu-Qing Zhang. "Applications of natural silk protein sericin in biomaterials". en. In: *Biotechnol. Adv.* 20.2 (May 2002), pp. 91–100.

[278] Sunita Nayak and Subhas C Kundu. *Silk Protein Sericin: Promising Biopolymer for Biological and Biomedical Applications*. 2016.

[279] A J Hyde and C Wippler. "Molecular weight of silk fibroin". In: *J. Polym. Sci. A* 58.166 (Apr. 1962), pp. 1083–1088.

[280] Yu Qi et al. "A Review of Structure Construction of Silk Fibroin Biomaterials from Single Structures to Multi-Level Structures". en. In: *Int. J. Mol. Sci.* 18.3 (Mar. 2017).

[281] Danielle N Rockwood et al. "Materials fabrication from Bombyx mori silk fibroin". en. In: *Nat. Protoc.* 6.10 (Sept. 2011), pp. 1612–1631.

[282] Kevin McGrath and David Kaplan, eds. *Protein-Based Materials*. Birkhäuser Boston, 1997.

[283] David Whitford. *Proteins: Structure and Function*. en. John Wiley & Sons, Apr. 2013.

[284] Carl Ivar Branden and John Tooze. *Introduction to Protein Structure*. en. Garland Science, Mar. 2012.

[285] L Nelson David, M Cox Michael, and L Nelson David. *Lehninger principles of biochemistry*. WH Freeman, 2005.

[286] Q X Ruan et al. "An investigation into the effect of potassium ions on the folding of silk fibroin studied by generalized two-dimensional NMR–NMR correlation and Raman spectroscopy". In: *FEBS J.* (2008).

[287] Xiao Hu et al. "Regulation of silk material structure by temperature-controlled water vapor annealing". en. In: *Biomacromolecules* 12.5 (May 2011), pp. 1686–1696.

[288] Jun Magoshi et al. "Crystallization of silk fibroin from solution". In: *Thermochim. Acta* 352-353 (July 2000), pp. 165–169.

[289] H-J Jin et al. *Water-Stable Silk Films with Reduced β-Sheet Content*. 2005.

[290] Gustavo R Plaza et al. *Thermo-hygro-mechanical behavior of spider dragline silk: Glassy and rubbery states*. 2006.

[291] Chengjie Fu, David Porter, and Zhengzhong Shao. "Moisture effects onAntheraea pernyiSilk's mechanical property". en. In: *Macromolecules* 42.20 (Oct. 2009), pp. 7877–7880.

[292] Yuan Cheng et al. "On the strength of β-sheet crystallites of Bombyx mori silk fibroin". en. In: *J. R. Soc. Interface* 11.96 (July 2014), p. 20140305.

[293] John M Gosline, Mark W Denny, and M Edwin DeMont. “Spider silk as rubber”. In: *Nature* 309.5968 (June 1984), pp. 551–552.

[294] Ahuva Weltman, James Yoo, and Ellis Meng. “Flexible, Penetrating Brain Probes Enabled by Advances in Polymer Microfabrication”. en. In: *Micromachines (Basel)* 7.10 (Oct. 2016).

[295] Jiawei Liu et al. *Healing of skin wounds using a new cocoon scaffold loaded with platelet-rich or platelet-poor plasma*. 2017.

[296] Xiao Hu, David Kaplan, and Peggy Cebe. *Determining Beta-Sheet Crystallinity in Fibrous Proteins by Thermal Analysis and Infrared Spectroscopy*. 2006.

[297] Duy Toan Pham, Nuttawut Saelim, and Waree Tiyaboonchai. “Crosslinked fibroin nanoparticles using EDC or PEI for drug delivery: physicochemical properties, crystallinity and structure”. In: *J. Mater. Sci.* 53.20 (2018), pp. 14087–14103.

[298] David J Belton et al. *A robust spectroscopic method for the determination of protein conformational composition – Application to the annealing of silk*. 2018.

[299] M A Koperska et al. “Degradation markers of fibroin in silk through infrared spectroscopy”. In: *Polym. Degrad. Stab.* 105 (July 2014), pp. 185–196.

[300] Joydip Kundu et al. “Silk fibroin nanoparticles for cellular uptake and control release”. en. In: *Int. J. Pharm.* 388.1-2 (Mar. 2010), pp. 242–250.

[301] Amy M Hopkins et al. “Silk Hydrogels as Soft Substrates for Neural Tissue Engineering”. In: *Adv. Funct. Mater.* 23.41 (Nov. 2013), pp. 5140–5149.

[302] Sergio Franco. *Design with Operational Amplifiers and Analog Integrated Circuits*. en. WCB/McGraw-Hill, 1998.

[303] Matthew A Carlton and Jay L Devore. “Introduction to Signal Processing”. In: *Probability with Applications in Engineering, Science, and Technology*. Ed. by Matthew A Carlton and Jay L Devore. Cham: Springer International Publishing, 2017, pp. 563–596.

[304] Alexander A Balandin. “Low-frequency 1/f noise in graphene devices”. en. In: *Nat. Nanotechnol.* 8.8 (Aug. 2013), pp. 549–555.

[305] Thomas Ihn. *Semiconductor Nanostructures: Quantum States and Electronic Transport*. en. Oxford University Press, 2010.

[306] Paritosh Karnatak et al. “1 / f noise in van der Waals materials and hybrids”. In: *Advances in Physics: X* 2.2 (Mar. 2017), pp. 428–449.

[307] J Bernamont. “Fluctuations de potentiel aux bornes d’un conducteur metallique de faible volume parcouru par un courant”. In: *Annales de Physique*. Vol. 11. 1937, pp. 71–140.

[308] R F Voss. “1/f (Flicker) Noise: A Brief Review”. In: *33rd Annual Symposium on Frequency Control*. May 1979, pp. 40–46.

[309] L K J Vandamme and R G M Penning de Vries. “Correlation between most 1/f noise and CCD transfer inefficiency”. In: *Solid State Electron.* 28.10 (Oct. 1985), pp. 1049–1056.

[310] W Shockley and W T Read. “Statistics of the Recombinations of Holes and Electrons”. In: *Phys. Rev.* 87.5 (Sept. 1952), pp. 835–842.

[311] C T Sah. “Theory of low-frequency generation noise in junction-gate field-effect transistors”. In: *Proc. IEEE* 52.7 (July 1964), pp. 795–814.

[312] Guanxiong Liu et al. “Origin of 1/f noise in graphene multilayers: Surface vs. volume”. In: *Appl. Phys. Lett.* 102.9 (Mar. 2013), p. 093111.

[313] S V Melkonyan et al. “Phonon mechanism of mobility equilibrium fluctuation and properties of 1/f-noise”. In: *Physica B Condens. Matter* 382.1 (June 2006), pp. 65–70.

[314] M A Stolyarov et al. “Low-noise near-ballistic BN-graphene-BN heterostructure field-effect transistors for energy efficient electronic applications”. In: *2015 Fourth Berkeley Symposium on Energy Efficient Electronic Systems (E3S)*. Oct. 2015, pp. 1–2.

[315] Morteza Kayyalha and Yong P Chen. “Observation of reduced 1/f noise in graphene field effect transistors on boron nitride substrates”. In: *Appl. Phys. Lett.* 107.11 (Sept. 2015), p. 113101.

[316] Yu-Ming Lin and Phaedon Avouris. “Strong Suppression of Electrical Noise in Bilayer Graphene Nanodevices”. In: *Nano Lett.* 8.8 (Aug. 2008), pp. 2119–2125.

[317] Iddo Heller et al. “Charge Noise in Graphene Transistors”. In: *Nano Lett.* 10.5 (May 2010), pp. 1563–1567.

[318] S Rumyantsev et al. *Low-frequency noise in graphene field-effect transistors*. 2011.

[319] Filippo Giubileo and Antonio Di Bartolomeo. “The role of contact resistance in graphene field-effect devices”. In: *Prog. Surf. Sci.* 92.3 (Aug. 2017), pp. 143–175.

[320] Adrien Allain et al. “Electrical contacts to two-dimensional semiconductors”. en. In: *Nat. Mater.* 14.12 (Dec. 2015), pp. 1195–1205.

[321] Xiangyu Yan et al. “Edge-Contact Formed by Oxygen Plasma and Rapid Thermal Annealing to Improve Metal-Graphene Contact Resistance”. en. In: *ECS J. Solid State Sci. Technol.* 7.2 (Feb. 2018), p. M11.

[322] Eiichiro Watanabe et al. “Low contact resistance metals for graphene based devices”. In: *Diam. Relat. Mater.* 24 (Apr. 2012), pp. 171–174.

[323] Wei Sun Leong, Chang Tai Nai, and John T L Thong. “What Does Annealing Do to Metal–Graphene Contacts?” In: *Nano Lett.* 14.7 (July 2014), pp. 3840–3847.

[324] A Gahoi et al. “Systematic comparison of metal contacts on CVD graphene”. In: *2015 45th European Solid State Device Research Conference (ESSDERC)*. Sept. 2015, pp. 184–187.

[325] Wei Li et al. “Highly reproducible and reliable metal/graphene contact by ultraviolet-ozone treatment”. In: *J. Appl. Phys.* 115.11 (Mar. 2014), p. 114304.

[326] Max Seifert et al. “Role of grain boundaries in tailoring electronic properties of polycrystalline graphene by chemical functionalization”. en. In: *2D Mater.* 2.2 (May 2015), p. 024008.

[327] Teresa Cusati et al. “Electrical properties of graphene-metal contacts”. In: *Sci. Rep.* 7.1 (July 2017), p. 5109.

[328] Zengguang Cheng et al. “Suspended Graphene Sensors with Improved Signal and Reduced Noise”. In: *Nano Lett.* 10.5 (May 2010), pp. 1864–1868.

[329] H Pandey et al. “All CVD Boron Nitride Encapsulated Graphene FETs With CMOS Compatible Metal Edge Contacts”. In: *IEEE Trans. Electron Devices* 65.10 (Oct. 2018), pp. 4129–4134.

[330] Stefania Castelletto et al. “Hexagonal boron nitride: a review of the emerging material platform for single-photon sources and the spin-photon interface”. en. In: *Beilstein J. Nanotechnol.* 11 (May 2020), pp. 740–769.

[331] Malay Jana and Raj N Singh. “Progress in CVD synthesis of layered hexagonal boron nitride with tunable properties and their applications”. In: *Int. Mater. Rev.* 63.3 (Apr. 2018), pp. 162–203.

[332] Nicholas Petrone et al. *Flexible Graphene Field-Effect Transistors Encapsulated in Hexagonal Boron Nitride*. 2015.

[333] Paritosh Karnatak et al. "Current crowding mediated large contact noise in graphene field-effect transistors". en. In: *Nat. Commun.* 7 (Dec. 2016), p. 13703.

[334] Mengchuan Tian et al. "Tunable 1/f Noise in CVD Bernal-Stacked Bilayer Graphene Transistors". en. In: *ACS Appl. Mater. Interfaces* 12.15 (Apr. 2020), pp. 17686–17690.

[335] Manohar Kumar et al. "Ultra low 1/f noise in suspended bilayer graphene". In: *Appl. Phys. Lett.* 106.26 (June 2015), p. 263505.

[336] Myrsini Lafkioti et al. "Graphene on a hydrophobic substrate: doping reduction and hysteresis suppression under ambient conditions". en. In: *Nano Lett.* 10.4 (Apr. 2010), pp. 1149–1153.

[337] Wi Hyoung Lee et al. *Control of Graphene Field-Effect Transistors by Interfacial Hydrophobic Self-Assembled Monolayers*. 2011.

[338] Sk Fahad Chowdhury et al. *Improvement of graphene field-effect transistors by hexamethyldisilazane surface treatment*. 2014.

[339] Dae Yool Jung et al. "Interface engineering for high performance graphene electronic devices". In: *Nano Convergence* 2.1 (2015), pp. 1–17.

[340] Sharanya Arcot Desai et al. "Improving impedance of implantable microwire multi-electrode arrays by ultrasonic electroplating of durable platinum black". In: *Front. Neuroeng.* 3 (2010), p. 5.

[341] C de Haro et al. *Electrochemical platinum coatings for improving performance of implantable microelectrode arrays*. 2002.

[342] C Boehler, T Stieglitz, and M Asplund. "Nanostructured platinum grass enables superior impedance reduction for neural microelectrodes". en. In: *Biomaterials* 67 (Oct. 2015), pp. 346–353.

[343] Krishnan Padmanabhan and Nathaniel N Urban. "Disrupting information coding via block of 4-AP-sensitive potassium channels". en. In: *J. Neurophysiol.* 112.5 (Sept. 2014), pp. 1054–1066.

[344] Y Fueta and M Avoli. "Effects of antiepileptic drugs on 4-aminopyridine-induced epileptiform activity in young and adult rat hippocampus". en. In: *Epilepsy Res.* 12.3 (Sept. 1992), pp. 207–215.

[345] Andrey Zakharov et al. *Segregation of seizures and spreading depolarization across cortical layers*. 2019.

[346] Jed A Hartings et al. "Direct current electrocorticography for clinical neuromonitoring of spreading depolarizations". en. In: *J. Cereb. Blood Flow Metab.* 37.5 (May 2017), pp. 1857–1870.

[347] Andrea M Harriott et al. "Spreading depression as a preclinical model of migraine". en. In: *J. Headache Pain* 20.1 (May 2019), p. 45.

[348] Maeike Zijlmans et al. *High-frequency oscillations as a new biomarker in epilepsy*. 2012.

[349] Daniel K Wójcik. *Current Source Density (CSD) Analysis*. 2015.

[350] Chella Kamarajan et al. "The use of current source density as electrophysiological correlates in neuropsychiatric disorders: A review of human studies". en. In: *Int. J. Psychophysiol.* 97.3 (Sept. 2015), pp. 310–322.

[351] A M L Coenen and E L J M Van Luijtelaar. "Genetic animal models for absence epilepsy: a review of the WAG/Rij strain of rats". en. In: *Behav. Genet.* 33.6 (Nov. 2003), pp. 635–655.

[352] A M Coenen and E L Van Luijtelaar. "The WAG/Rij rat model for absence epilepsy: age and sex factors". en. In: *Epilepsy Res.* 1.5 (Sept. 1987), pp. 297–301.

[353] Jonas Terlau et al. "Spike-wave discharges in absence epilepsy: segregation of electrographic components reveals distinct pathways of seizure activity". en. In: *J. Physiol.* 598.12 (June 2020), pp. 2397–2414.

[354] Dong-Wook Park et al. "Graphene-based carbon-layered electrode array technology for neural imaging and optogenetic applications". en. In: *Nat. Commun.* 5 (Oct. 2014), p. 5258.

[355] Weijian Yang and Rafael Yuste. "In vivo imaging of neural activity". en. In: *Nat. Methods* 14.4 (Apr. 2017), pp. 349–359.

[356] Jens P Dreier et al. "Recording, analysis, and interpretation of spreading depolarizations in neurointensive care: Review and recommendations of the COSBID research group". en. In: *J. Cereb. Blood Flow Metab.* 37.5 (May 2017), pp. 1595–1625.

[357] Andrew P Carlson et al. "Cortical spreading depression occurs during elective neurosurgical procedures". en. In: *J. Neurosurg.* 126.1 (Jan. 2017), pp. 266–273.

[358] Emilio Russo et al. “Upholding WAG/Rij rats as a model of absence epileptogenesis: Hidden mechanisms and a new theory on seizure development”. en. In: *Neurosci. Biobehav. Rev.* 71 (Dec. 2016), pp. 388–408.

A

Appendix A

A.1 Fabrication parameters

In this part of the Appendix a more detailed description of the microfabrication of gSGFETs is given; parameters for the different steps are displayed with Tables for spcific photoresist used.

A.1.1 Processing protocol for rigid graphene SGFETs

Substrate Cleaning

- The SiO_2 wafer were cleaned in acetone and isopropyl alcohol (IPA) in an ultrasonic bath for 5 minutes each.
- wafer were then cleaned for 5 minutes in an oxygen plasma (200 W, 1.4 mbar).

First metal layer

- **Resist depoition and structuring**: Photoresist (AZ 5214E) was spin coated on the wafer followed by a softbake. Next, the mask was aligned and the resist was UV exposed. In case of the AZ 5214E the reversal bake and flood exposed were performed afterwards. In a last step the resist was developed. The detailed parameters for both resists are given in Table A.1.
- **Metal evaporation**: Metals (10nm titanium as an adhesion layer and 100nm gold) were evaporated by e-beam evaporation at a pressure below $1 \cdot 10^{-7}$ mbar)

- **Lift-off** was performed in acetone. If necessary, samples were placed in an ultrasonic bath. After cleaning in acetone and two times in IPA, wafers were dry-blown with nitrogen.

Photoresist	AZ 5214E
Spin coating	30 s @4500rpm
Pre-exposure bake (hotplate)	1min at 90ºC
Exposure (with mask)	4 sec (54 mJ at i-line)
Post-exposure bake	2min at 120 ºC
Flood exposure (without mask)	30 sec
Development	45 sec in AZ 726MIF + rinse 50sec in water cascade

Table A.1: Photoresist AZ 5214 (negative) process parameters for lift-off

Graphene transfer and structuring

- **Graphene transfer**: After the fishing the graphene/PMMA-A4 stack, the wafer is placed on an hotplate at 40 ºC for several hours. Then a temperature ramp is performed in a UHV chamber ($1 \cdot 10^{-7}$mbar) up to 180 ºC. After 5min the temperature is brought back to RT and the PMMA removed in heated acetone (1h) and then in IPA.
- **Graphene etching**: After transfer and PMMA resist removal, HiPR-6512 photoresist was spin coated and structured by means of photolithograpy (see Table A.2). The graphene was etched by oxygen RIE (1 min, 150W)
- **Resist removal and cleaning**: Resist was removed by two baths in acetone followed by two baths in IPA, 5 minutes each.

Photoresist	HiPR-6512
Spin coating	50s @4000rpm
Pre-exposure bake (hotplate)	2min at 80ºC
Exposure (with mask)	14 sec (54 mJ at i-line)
Post-exposure bake	2min at 80 ºC
Development	1min 40sec in Dev OPD 4262 + 1min water

Table A.2: HiPR 6512 Photoresist process parameters (thickness 1-1.2 μm)

Second Metal layer

The photolitography with inverted AZ 5214 photoresist and lift-off processes are identical to the one used for the first metal layer. The metal evaporated by ebeam for the second layer are 10nm Ni/ 100nm Au. It is however crucial to use no ultra sound and instead agitate the acetone to the wafer using a glass pipette.

Passivation layer:

- **Resist deposition and structuring**: After rinsing the samples with acetone and IPA, the wafer are dehydrated on an hotplate for 10 min at 80ºC. Then, SU8 resist was spin coated, pre-baked, exposed and developed following the process described in Table A.3.
- **Hard-bake** is done to melt all cracks and make the passivation conform to the underlying structures. Samples were cured for 1 h 30min at 120 ºC in nitrogen atmosphere, to avoid graphene oxidation.

Steps	Passivation (SU8-2005)
Clean substrate	Oxygen-plasma 1min 300W
Dehydration	5min @ 110ºC
Spin coat	3000rpm, 30s
Relaxation time	10 min
Soft-bake (SB)	3min @65ºC ↗ (5ºC/min) 8 min @ 95ºC ↘ RT
Exposure	10 s (No mask - flood exposure)
Relaxation time	Lay flat 10 min
Post-exposure bake (PEB)	2min @ 65ºC ↗ (5ºC/min) 3min @ 95ºC ↘ RT
Development	50sec in Dev mrv600 + 50sec in IPA
Hard-bake (HB)	↗ (2ºC/min) 120ºC 1h 30min @ 120ºC ↘ RT

Table A.3: Process parameters for passivation with SU8

A.1.2 Processing protocol for flexible graphene SGFETs

The process flow for flexible graphene SGFETs (polyimide neural probes), are very similar as the steps for rigid gSGFETs. Therefore, only steps that differe from the above mentioned step will be detailed. Substrate preparation:

- **Substrate cleaning**: SiO_2 wafers were cleaned in acetone and IPA in an ultrasonic bath. After dry-blowing with nitrogen the samples were cleaned in an oxygen plasma (200W, 5min).
- **Formation of PI substrate**: Samples were placed on a hotplate for 10min at 150 ºC to remove water from the surface. Samples were moved from the hotplate directly to the spin-coater and cooled using a nitrogen gun. A big drop

of Polyimide[1] was deposited in the middle of the wafer. After 60 s waiting time, the polyimide was spin coated, first at 4000 rpm for 30 s (dispensing), then at 6000 rpm for 60 s (thinning), followed by 2 s at 9000 rpm (edge bead removal). Samples were then pre-baked at 120 ºC for 3 min. Afterwards samples were cured under nitrogen atmosphere. Temperature was ramped from 120 ºC to 200 ºC at a rate of less than 4 ºC/min. After holding for half an hour at 200 ºC temperature was increased with the same rate as before to 350 ºC and kept there for 1 hour. After cool down the hotplate at RT, the wafer was removed from the nitrogen atmosphere.

The next steps to produce flexible epicortical neural probe are identical to the process flow for rigid gSGFETs.

PI structuring, etching and peeling

- **Protective structure photoresist**: to cut the PI with the shape of the neural probes, is performed by spin coating a thick protective photoresist (positive AZ 9260). The process parameter to structure the photoresist are shown in Table A.4.
- **PI etching**: the wafer is then placed in the Ar/O_2-RIE (50sccm Ar/ 60 sccm O_2; source: 1200W, chuck 40W) for $\sim 20 - 25$min until the PI is completely etched.
- **Photoresist removal**: The remaining photoresist is then removed in acetone (10min) and two times rinsed in ISA (20min each).
- **Peeling**: the flexible devices on the wafer are then wet with water drops, and carefully peeled-off from the rigid SiO_2 substrate.

[1]Polyimide 2611 HD Microsystems

Photoresist	AZ 9260 (thickness 16 um)
Spin coating	30s @820rpm
Pre-exposure bake (hotplate)	7 min 30sec @110ºC
Bad edge removal	along the wafer perimeter
Multi-exposure (structure mask)	(36sec + 40sec waiting time) x3
Development	7min in developer AZ400K mixed with water (1:3) + rinse 2min in water

Table A.4: Process parameters for cutting the PI substrate; sacrificial AZ 9260 photoresist

A.1.3 Processing protocol for gDNP - formation of via-holes

To shrink the width of the gDNP shank, a two layer PI with metal tracks connected via -holes has been implemented as described in chapter 3 (section 3.2). The formation of via-holes to interconnect the metal tracks (Figure 3.9) is described in more details as follows:

- **Second PI deposition**: Wafer were placed on a hotplate for 10min at 150 ºC to remove water from the surface. Samples were moved from the hotplate directly to the spin-coater and cooled using a nitrogen gun. PI was then deposited and spin coated first at 700 rpm for 50 s (dispensing), then at 5000 rpm for 70 s (thinning), followed by 2 s at 9000 rpm (edge bead removal) to reach a thickness of $\approx 3\mu$m.
  Samples were then pre-baked at 120 ºC for 3 min. Afterwards samples were cured under nitrogen atmosphere. Temperature was ramped from 120 ºC to 200 ºC at a rate of less than 4 ºC/min. After holding for half an hour at 200 ºC temperature was increased with the same rate as before to 350 ºC and kept there for 1 hour.

- **Aluminum mask**: Photoresist (AZ 5214E) was spin coated on the 2nd PI layer, and stuctured using a clear field mask by means of photolithography; photoresist AZ 5214E reversal was spin coated and structured following recipe of Table A.1. Then, 200 nm aluminum were e-beam evaporated. A lift off step in a ultra-sound bath of acetone (5min 3.5 kHz) followed; the wafer was then rinsed in IPA and dryied with nitrogen. Thus, an Al mask is formed on top of the 2nd PI layer with open circle in the region that need to be etched in the next step.

- **RIE**: the wafer is then placed in the Ar/O_2-RIE (50sccm Ar/ 60 sccm O_2; source: 1200W, chuck 40W) for $\sim 10-15$min until the PI is completely etched.
- **Aluminum etching**: aluminum is chemically removed using a NI555 stripper (Microchemicals GmbH) at 60 ºC for 1 hour, followed by a rinse in isopropyl alcohol for 30s, ethanol for another 30s and finally blew them dry with nitrogen.
- **Second metal evaporation**: To interconnect the PI-encapsulated metal layer with the upper metal tracks, photoresist (AZ 5214E) was spin coated on the wafer and defined by photolithography (Table A.1) . Then Ti/Au (20/200 nm) was deposited by e-beam and a lift-off step in ultra-sound acetone bath was done to define the second metal tracks, now interconnected to the first metal layer underneath the PI layer (see Figure 3.9 in the main text).

A.2 Physiscal characterisation of graphene

Raman Spectroscopy.
Raman measurements were performed with a Witec spectrometer in backscattering configuration, using a 600 gr/nm grating which provided a spectral resolution of 3 cm_{-1}/pixel. A solid state laser with 488 nm excitation wavelength was focused on the sample with a 50x objective leading to a spatial resolution below 0.8 μm. The laser power was kept below 1.5 mW to avoid sample heating. Average spectras and histograms (Figure 3.2, Figure 3.13a-c) were obtained from the statistical analysis of Raman mappings over an area of 30 μm x 30 μm in the center of the sample.
The integrated peak intensity ratio A_{2D}/A_G, A_D/A_G and the G-peak position ω_G are calculated by fitting each peak with a Lorentzian after previously substracting the background.
Atomic force Microscope.
AFM measurements were performed using an Asylum MFP-3D Atomic Force microscope equipped with electronic for conductive AFM, tip station, electrochemical cell and vacuum chuck for 4 inch wafers.
AFM scan images over a areas of 1 μm x 1 μm and 5 μm x 5 μm were recorded in standard air-tapping mode with Budget sensors Tap150Al-G tips (5 N/m). A scan rate of 0.8 Hz was used (Figure 3.13d, Figure 4.5c)

A.3 Noise in gSGFET - Supplementary information

The approximate dependence of the total resistance on the length of the graphene channel expressed in equation 4.16 (section 4.3) is derived in the following steps. The normalised current noise can be written as:

$$\frac{S_I}{I_{DS}^2} = \frac{S_{R_T}}{R_T^2} = \frac{S_{R_T} I_{DS}^2}{V_{DS}^2} \tag{A.1}$$

The relation between the total resistance noise power S_{R_T} and normalised current noise I_{RMS}/I_{DS}^2 is:

$$\frac{I_{RMS}}{I_{DS}^2} = \sqrt{\frac{S_{R_T}}{V_{DS}^2}} \propto \sqrt{S_{R_C} + S_{R_{Ch}}} \tag{A.2}$$

Using the same mechanism of noise generation of surface noise as in silicon MOSFETs, leads to the observed $S_{R_C}/R_C^2 \propto 1/(A_C \cdot n_C^2)$. Here, we propose the same physical explanation for the contact noise in graphene FETs[309, 310, 311]:

$$\frac{S_{R_C}}{R_C^2} = \frac{\kappa_B T N_T}{\alpha A_C n_C^2} \Rightarrow S_{R_C} = \frac{\kappa_B T N_T}{\alpha n_C^2} \cdot \frac{R_C^2}{A_C} \propto \frac{L_T^2}{W^2 \cdot W \cdot L_T} \tag{A.3}$$

With the tunnelling constant, A_C being the graphene area underneath the metal contacts, n_C the charge density in the lattice at contact site, W the width of the graphene/contact and L_T as the transfer length (defined as the length where the current injections decreases by a factor of 1/e). For the channel noise:

$$\frac{S_{R_{Ch}}}{R_{Ch}^2} = \frac{\kappa_B T N_T}{\alpha A_{Ch} n_{Ch}^2} \Rightarrow S_{R_{Ch}} = \frac{\kappa_B T N_T}{\alpha n_{Ch}^2} \cdot \frac{R_{Ch}^2}{A_{Ch}} \propto \frac{L^2}{W^2 \cdot W \cdot L} \tag{A.4}$$

With $A_{Ch} = L \cdot W$ being the active area of the graphene gSGFET and n_{Ch} the charge density in the channel. Combining eq. (A.3) and eq. (A.4) into eq. (A.2) gives the desired dependence on L:

$$\frac{I_{RMS}}{I_{DS}^2} \propto \sqrt{\frac{k_{R_C} L_T}{W^3} + \frac{k_{R_{Ch}} L_{Ch}}{W^3}} \tag{A.5}$$

where k_{R_C} and $k_{R_{Ch}}$ include all the constants which are independent of the channel dimensions for S_{R_C} and $S_{R_{Ch}}$ respectively.

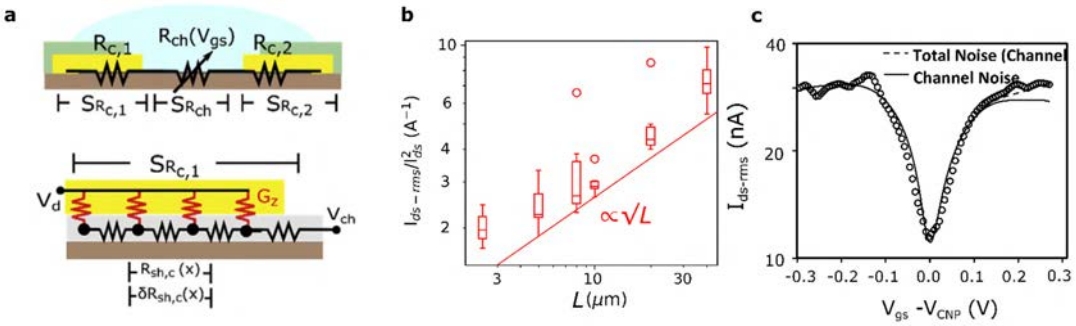

Figure A.1: a. Top: schematic of a gSGFET showing the contact resistance ($R_C = R_{C,1} + R_{C,2}$), channel resistance (R_{Ch}) and the noise contributions from the contacts ($S_{R_C} = S_{R_{C,1}} + S_{R_{C,2}}$) and the channel ($S_{R_{Ch}}$). Bottom: Schematic of the equivalent circuit of the transmission-line contact at the graphene-metal interface. The distributed elements representing the sheet resistance of graphene along the contact ($S_{R_{Sh,C}}(x)$) are defined together with the local fluctuations in the sheet resistance (δR_{Sh}). The drain voltage (V_D) and the potential at the channel/contact interface (V_{Ch}) are also defined.
b. The normalized integrated noise I_{RMS}/I_{DS}^2 for gSGFETs with contacts treated with UVO for 40 min is shown for different channel lengths. The red straight line indicates the $\propto \sqrt{L}$ trend corresponding to channel dominated noise.
c. The V_{GS} bias dependence of I_{RMS} is shown for gSGFETs with a 5 μm long channel and contacts treated for 40 min with UVO. Adapted from [145]

Dominance of channel noise in gSGFETs with high R_{sh}.

Contact resistance increases, after reaching a minimum, in case of excessively long UVO treatment times (section 4.3, Figure 4.6c). This increase can be attributed to the creation of defects on the graphene sheet which is under the metal contacts, which means an increase in R_{sh}. Yet, this increase in R_{sh} is expected to further reduce the contact noise, as described by the transmission line model [145]. Figure A.1b shows the dependence of the normalized integrated noise on the channel length for gSGFETs with contacts treated with UVO for 40 min, which led to an increased contact resistance (see section 4.3). The relationship with L corresponds to a channel noise dominated regime. These results can be further supported by the bias dependence of the integrated noise in Figure A.1c, which can be explained by the noise contribution from the channel resistance rather than the contacts. The fact that contact noise does not increase with the density of defects located in the graphene sheet section at the contacts, implies that this noise origins in trapping-detrapping events. However, the improvement of contact noise with the density of defects in the graphene sheet must have a threshold, which is likely to be the rise of mobility noise for large density of defects.

A.4 Supplementary information - Silk-fibroin bioresorbable shuttle

A.4.1 Mould fabrication

To stiffen the flexible gDNP, we applied a casting technique using a polydimethylsiloxane (PDMS) mould with the same shape of the neural probes, as previously reported[239]. To obtain the molds, PDMS (mixture 1:10) was cast on a 4-inch silicon wafer with 200 μm or 100 μm thick SU-8 photoresist patterns, respectively.
The SU8[2] master mould was fabricated using photolithography steps resumed in Figure A.2. To start, a first thin SU8-layer[3] is spun on the Si/SiO_2 wafer to form a seed layer (thickness $\sim$2.5 μm) for the thicker and patterned SU8-structre[4] (step 1. in Figure A.2).

[2]MicroChem-SU8-2000, Permanent Epoxy Negative Photoresist
[3]MicroChem, SU8-2005
[4]MicroChem, SU8-2050

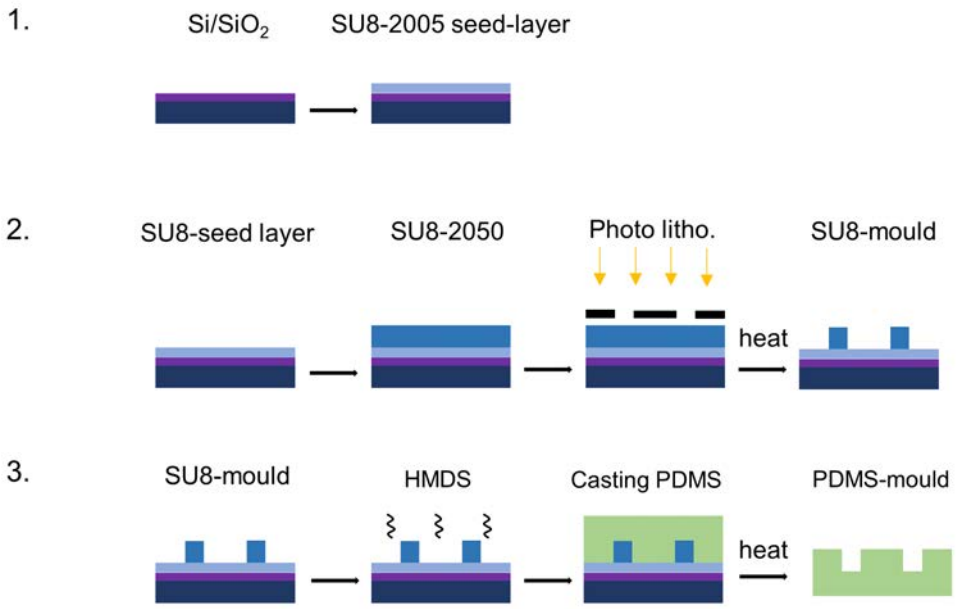

Figure A.2: Process flow for the fabrication of the PDMS mould. **Step 1.** the placement of a thin SU8 seed layer, in order to reduce thermal expansion stress between the patterned SU8 and the Si/SiO_2 substrate. **Step 2.** A thicker SU8 is spun and patterned by means of photolithography using a mask. After the development, the illuminated SU8 is permanently hardened by a hard-bake step. **Step 3.** The patterned SU8 master mould is functionalised with HMDS. Then the HMDS is cast on the SU8 master mould and cured by heat. After 5-6h curing at 70 ^{o}C, the PDMS mould can be easily detached from the inverted SU8-master mould.

Then SU8-2050 is spun on the seed-layer and pattern via photolithography, using a high resolution film photomask mask[5] with the shapes of the gDNP (see Figure A.3). Depending on the spin parameters, we were able to reach a thickness of the SU8 of 200 μm or 100 μm (see Table A.5), which we used to control the thickness of the SF shuttle. The SU8-master mould was fabricated with the pattern inverted to the PDMS mould, since the PDMS is cast and cured on it (step 2. in Figure A.2).

[5]Provider: JD Photo Data

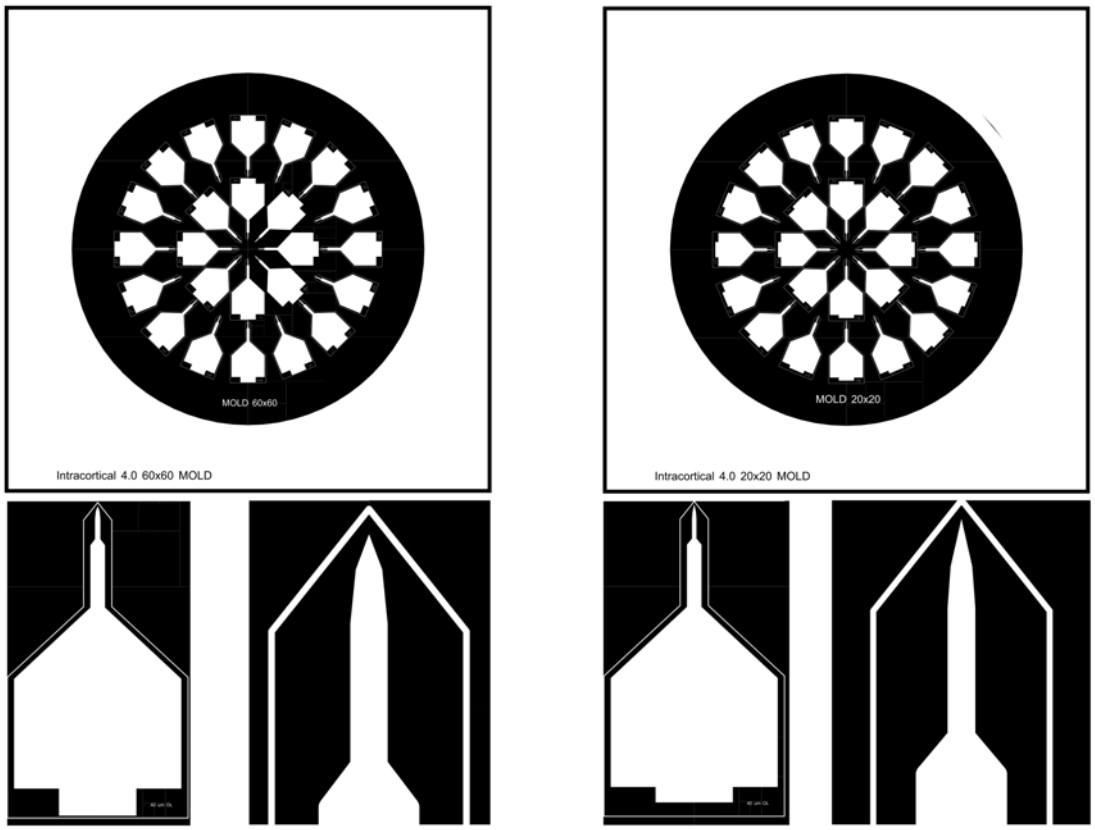

Figure A.3: Photolithography mask to fabricate the SU8-master mould. The two mask are for the GDNP with 60x60 μm^2 graphene active area gDNP (right), and for the smaller 20x20 μm^2 (left) respectively.The mould are placed radially to maximize the available space on the wafer.

Once the SU8 master mould has been fabricated, we cast on it PDMS and cured it on a hotplate at 70ºC for 5-6 h (step 3. Figure A.2). It is to be noted that, before casting the PDMS, it is crucial to treat the SU8-master mould with Hexamethyldisilazane (HMDS), in order to be able to peel the PDMS form the SU8-master mold. Therefore a special set-up is used (HMDS is very volatile and has acute inhalation toxicity (category 4) [6]), which heats up the sample at 100 ºC and floods it twice for 40 s with HMDS vapors. To achieve best results, the PDMS needs to be cast on the SU8 mould, immediately after the HMDS-functionalisation. Finally the PDMS mould can be carefully peeled from the SU8 master mould (step 3. in Figure A.2). The details of the fabrication steps are presented in Table A.5.

[6]SAFETY DATA SHEET of 1,1,1,3,3,3-Hexamethyldisilazane - Fisher Scientific

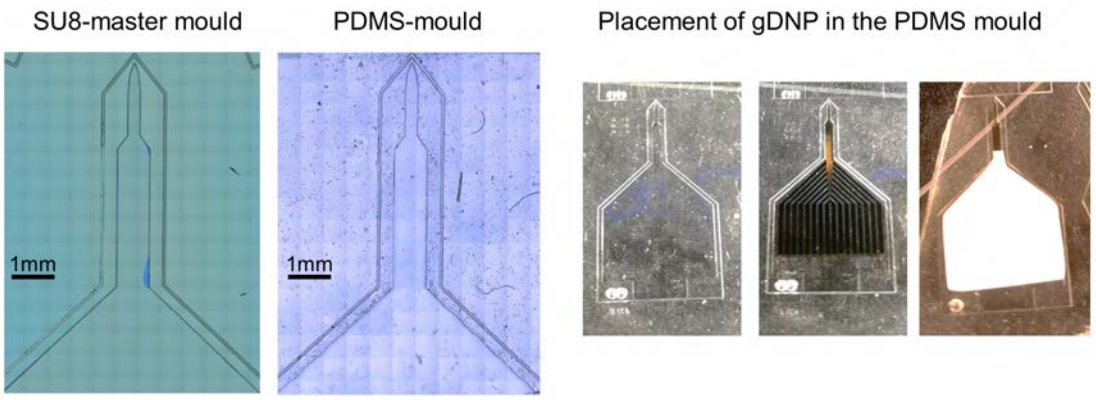

Figure A.4: Photographs of the finalised SU8-master and PDMS mould.The probe is then placed in the PDMS mould (right pictures), subsequently a plastic spacer is sticked to the bottom part to interface with the ZIF connector.

Steps	SU8-2005, seed layer (2.5 um)	SU8-2050 (200um)	SU8-2050 (100um)
Clean substrate	Oxygen-plasma 1min 300W	Oxygen-plasma 1min 300W	Oxygen-plasma 1min 300W
Dehydration	5min @ 110ºC	5min @110ºC	5min @ 110ºC
Spin coat	3000rpm, 30s	700 rpm, 30s	1500 rpm, 30s
Relaxation time	10 min	1 h	30 min
Soft-bake (SB)	3min @65ºC ↗ (5ºC/min) 8 min @ 95ºC ↘ RT	5 min @ 65ºC ↗ (2ºC/min) 3h @ 95ºC ↘ RT	5min @65ºC ↗ (2ºC/min) 90min @95ºC ↘ RT
Exposure	10 s (No mask - flood exposure)	60 s (mould mask)	30 s (mould mask)
Relaxation time	Lay flat 10 min	Lay flat 10 min	Lay flat 10min
Post-exposure bake (PEB)	2min @ 65ºC ↗ (5ºC/min) 3min @ 95ºC ↘ RT	5min @ 65ºC ↗ (2ºC/min) 15min @ 95ºC ↘ RT	3min @ 65ºC ↗ (2ºC/min) 12min @ 95ºC ↘ RT
Development	-	13 min in mrDev-600 2min in IPA	7min in mrDev-600 2min in IPA
Hard-bake (HB)	↗ (2ºC/min) 120ºC 1h 30min @ 120ºC ↘ RT	↗ (2ºC/min) 120ºC 1h 30min @ 120ºC ↘ RT	↗ (2ºC/min) 120ºC 1h 30min @ 120ºC ↘ RT

Table A.5: Fabrication steps for the master mould used for the stiffening technique with silk-fibroin.

A.4.2 Materials and methods

Materials Silk fibroin solution (from domesticated Bombyx mori silkworm) (50 mg/ml) was bought from Sigma, thawed slowly at 4 ºC, then aliquot into smaller volumes and stored at freeze under -80ºC. Precise amounts are thawed at 4 ºC just before their use. The Artificial cerebrospinal fluid (ACSF) used in this project contained (in mM): 125 NaCl (Sigma, S5886), 2.5 KCl (Sigma, P5405), 2 $CaCl_2$

· H_2O (Sigma, C3881), 1.3 $MgCl_2$· $6H_2O$ (Sigma, M0250), 1.3 NaH_2PO_4 (Sigma, 71505), 25 $NaHCO_3$ (Sigma, 792519), 10 glucose (Sigma, G6152). All the chemicals are used as received unless otherwise mentioned. Milli-Q water (Merck Millipore, UK) or Endotoxin free water was used for all the experiments.

FTIR Fourier transform infrared spectroscopy (FTIR) of the polymer hydrogel coating was measured using a Tensor 27 spectrometer (Bruker, UK), equipped with a 3000 Series High Stability Temperature Controller with RS232 Control (Specac, UK) and a MKII Golden Gate Single Reflection ATR system (Specac, UK). The bottom plate of the Golden Gate ATR system was cleaned using water and ethanol and then preheated at 60 ^{o}C, to allow the complete evaporation of the solvents. After that, the dried (37^{o}C/ overnight) polymer film was placed on the holder and the transmittance spectra were recorded by obtaining 32 scans in the 4000–700 cm^{-1} range, with a resolution of 4 cm^{-1}.

Contact Angle

The contact angle images were recorded and analysed by Theta Optical Tensiometer (Biolin Scientific, Sweden) running OneAttension software (version 2.3) based on the Young-Laplace equation. The measurements were done by using 0.35 μL droplets of water in air. Samples were prepared by drop casting polymer hydrogel solution on a glass substrate. Samples were left to dry overnight at 37 ^{o}C in a drying cabinet. To prepare the sample for FTIR, XRD and contact angle measurements, the silk fibroin solution was drop casted on a clean glass slide and placed on a hot plate at 50^{o}C for 15 min and later at 80°C for 1.5 hr. Finally, it was stored in the 37^{o}C overnight.

Moisture content The moisture content of the different recipe of polymer hydrogel coating was calculated by drying the coated polyimide dummy electrode in an oven at 40 °C for 24 h. The weight of the samples at two different time points, such as before (W_b) and after (W_a) the drying process, was measured using an electronic weighing balance with an accuracy of 0.0001 g. The actual moisture content (MC [%]) was determined by using the equation below:

$$MC = \frac{W_b - W_a}{W_b} \cdot 100 \tag{A.6}$$

AFM topografic analysis Atomic force microscopic (AFM) images were obtained in tapping mode, using a Multimode 8 atomic force microscope (Bruker,

UK) in air. OTESPA tips (Bruker, UK) of 10 nm curvature radius was mounted on a tapping mode silicon cantilever, with a typical resonant frequency of 300 kHz and a spring constant of 42 Nm^{-1} to acquire the images. The obtained images were further processed on Nanoscope Analysis software (version 1.4, Bruker, UK).
To prepare the sample for AFM imaging, silk fibroin was drop cast on a clean mica substrate and placed in the oven at 37°C overnight.

Assessment of mechanical properties of the stiffened gDNPs

Standard compression tests against a hard silicon (Si) substrate were performed to assess the mechanical properties of our SF-coated probes. Buckling experiments were carried out in a UMIS nanoindenter from Fischer-Cripps Laboratories. A custom clamp was fabricated to fix the probes at the end of the indenter shaft that, in turn, was connected to the actuator and the load cell. Buckling tests were carried out at a loading rate of 8.8 mN/s. Once the indenter detected noticeable buckling, the test was automatically stopped. The maximum load that the indenter can apply is 500 mN. Applied force vs displacement was measured until the probe started buckling and eventually broke down. We additionally measured the Young's modulus of the SF cured at 80 ºC by means of nano-indentation tests. SF was drop casted on a 2x2cm^2 Si chip and cured.
The indentation measurements were performed using a NHT2 Nanoindentation Tester from Anton-Paar, equipped with a Berkovich pyramidal-shaped diamond tip. A maximum applied load of 5 mN was applied with a loading segment of 30 s followed by a load holding segment of 10 s and an unloading segment of 30 s. The hardness and reduced Young's modulus are reported as an average value of at least twenty indentations, performed on top of each sample (in the central region). Young's modulus values in the range of 10 GPa where measured for 80 ºC cured SF

A.5 *In vivo* experiments in anesthetized adult male Wistar rats

A.5.1 Ethical approval and animal handling

All experimental procedures[7] were conducted in accordance with the European Union guidelines on protection of vertebrates used for experimentation (Directive 2010/63/EU of the European Parliament and of the Council of 22 September 2010) and all experiments were approved by the ethics committee of the Hospital Clinic de Barcelona. Rats were kept under standard conditions (room temperature (23 ± 1)°C, 12:12 h light–dark cycle, lights on at 08:00), with food (A04, Harlan) and water available *ad libitum*.

A.5.2 Acute preparation surgeries

Eleven adult male Wistar rats (225–375 g) were used in this study. Animals were deeply anaesthetized with isoflurane (4% induction, 1–3% maintenance) and all pressure and incision points were infiltrated with local anaesthetic lidocaine. Once under the surgical plane of anaesthesia, animals were transferred to a stereotaxic frame with body temperature constantly monitored and maintained at 37°C by means of a thermal blanket. A craniotomy and durotomy were performed on the left or right hemisphere in order to record with epicortical or intracortical arrays, respectively. Additionally, a craniotomy and durotomy were performed over the prefrontal cortex to topically administer 5 mM KCl to induce CSD. The large craniotomy was centred at 43 mm anterio-posterior (AP) and 42.5 mm medio-lateral (ML) and was 6 mm AP by 4.5 mm ML in size, while the smaller craniotomy, located at 50 mm AP and 42 ML, was 2.5 mm AP by 1.25 mm ML. A Ag/AgCl electrode pellet was inserted in the temporal muscle and used as reference, both for recordings and for the measurement of the transistor transfer curve. All recording probes, either gSGFETs or microelectrodes, were placed directly on the cortical surface and kept in place by adherence to the tissue (see Figure A.6).

[7] In vivo experiments were performed at the *Institut d'Investigacions Biomèdiques August Pi i Sunyer (IDIBAPS)* Barcelona, Spain, in collaboration with Dr. Maria V. Sanchez-Vives and Dr. Miguel Dasilva who performed all surgeries

A.5.3 Custom electronics for recordings with gSGFET

A custom electronic instrumentation was used (see Figure A.5), which provides current-to-voltage conversions and bias control for each channel. The instrumentation splits the recorded signals into two bands with different gains: LPF (< 0.16 Hz, 10^4 gain) and BPF (0.16 Hz $< f <$ 160 kHz, 10^6 gain).

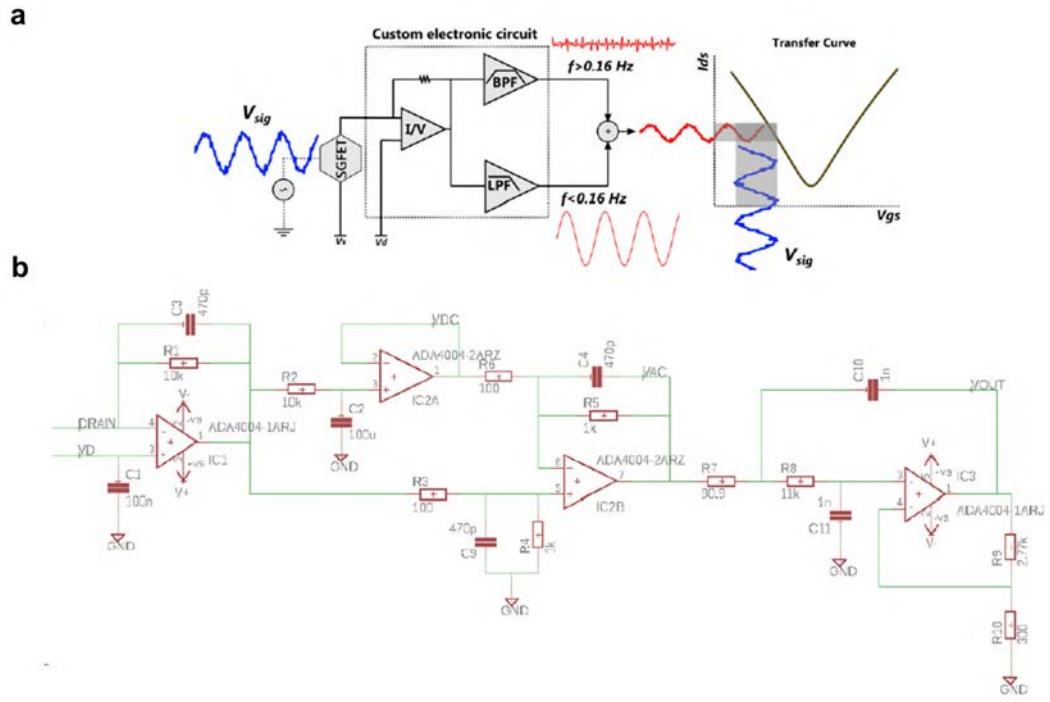

Figure A.5: a, gSGFET recording setup and signal post processing methodology. The custom electronic circuit is used to perform the *in vivo* characterization and record the transistor currents in the low-pass-filtered (LPF) band and the band-pass-filtered (BPF) band. From the combination of both signals and taken into account the current-to-voltage conversion, the wide-band signal (V_{sig}) is obtained. **b**, Schematic of the custom electronic instrumentation which controls the polarization of the gSGFETS (V_{gs}, **Vds**) and amplifies differently the two previously mentioned bands: LPF ($\approx 0 - 0.16$ Hz, gain=10^4) and BPF (0.16 Hz-10 kHz, gain=10^6). From [63]

In the experiments where only the gSGFET array was measured, the LPF signals and bias control were managed by a data acquisition system[8], while the BPF signals were directly acquired by a commercial electrophysiological recording system consisting of a programmable gain amplifier (Multichannel Systems) and digitizer interface[9]. The LPF and BPF bands were sampled at 1 Hz and 5 kHz respectively. Before the beginning of the recordings, the transfer curve of the gSGFET was

[8]National Instruments USB-6353
[9]CED 1401 and Spike2 software, Cambridge Electronic Design

measured *in situ* to determine the optimum bias point, generally around -0.1 V of the CNP.

A.5.4 Reference electrode

The voltages applied at drain (D) and source (S) terminals used to operate graphene transistors are referred to the reference electrode (G). The reference electrode is generally grounded in anaesthetized subjects to ensure stable recordings, since the subject is grounded at many points. However, the requirement of the reference electrode to be grounded is not necessary; a proper operation of the graphene transistor is achieved when the reference electrode is properly placed in a non-active location and does not have drifts and oscillations that interfere with the recording. To be noted, the gSGFETs are less sensitive than microelectrode technology to the baseline drift associated with the reference electrode. In commonly used microelectrode d.c.-coupled recordings, the baseline drift can lead to saturation of the amplifiers, while the operation principle of graphene transistors does not lead to saturation. The drift of the reference electrode shifts however the biasing point, which could lead to non-optimal performance of gSGFETs. This can be easily solved by changing the transistor bias to the new optimal V_{gs}, which can be obtained by calibrating *in vivo* the gSGFETs (measuring the transfer curve).

A.5.5 Combined recordings with microelectrodes and glass micropipette

For gSGFET comparison experiments with microelectrodes and the glass micropipettes with Ag/AgCl wire ($\approx$ 0.15 M) a total of four subjects were used: two subjects were measured with gSGFETs, microelectrodes and a micropipette, one with gSGFETs and microelectrodes (data from Figure 5.3a) and another one with gSGFETs and a micropipette (data from Figure 5.3b). A custom Simulink model was used to simultaneously measure graphene transistors through an adapted g.HIamp biosignal amplifier (g.tec medical engineering) while microelectrodes and the solution-filled glass micropipette were recorded using an g.USBamp (g.tec medical engineering). The same reference electrode was used by both amplifiers, and signals were sampled at 4.8 kHz.

A.6 *In vivo* experiments in pre-clinical rodent model of epilepsy

A.6.1 Electronics for in vivo recordings with gDNPs

The experimental setup used to perform the in vivo recordings provides Vs and Vd bias control and current-to-voltage conversion for up to 16 channels (g.RAPHENE, g.tec medical engineering GmbH, Austria). The instrumentation splits the recorded signals into two bands with different gains: low-pass filtered (LPF, < 0.16 Hz, 10^4 gain) and band-pass filtered (BPF, 0.16 Hz $< f <$ 160 kHz, 10^6 gain). Two custom Simulink models were used: i) to perform the transfer curve of the microtransistors once inserted and at the end of the experiment; ii) to set the Vs and Vd bias and acquire the recorded signals. Signals were sampled at 9.6 kHz and at 19kHz depending on the type of experiment.

A.6.2 Ethical approval and animal handling for acute and chronic experiments

Animal experiments were conducted in accordance with the United Kingdom Animal (Scientific Procedures) Act 1986, and approved by the Home Office (license PPL70-13691). C57BL/ mice were bred (2-4 month old males), while WAG rats were imported (Charles river, used 6-9 months of age). Animals were housed on 12 h/12 h dark/light cycle, and food and water were given *ad libitum*. Prior to headbar sugery, animals were group housed, but after this, animals were individually housed.

A.6.3 Acute preparation surgeries for headbar attachment and craniotomy

For both surgeries, aseptic techniques were used with mice anaesthetized using isoflurane (988-3245, Henry Schein, U.S.A.) and placed in a stereotaxic frame (David Kopf Instruments Ltd., U.S.A.). Viscotears applied (Bausch + Lomb, U.S.A.) and pain relief, which consisted of sub-cutaneous Bupenorphine (0.5 mg / Kg; Ceva, France) and Metacam (15 mg /Kg; Boehringer Ingelheim, Germany), were injected. Saline was administered just before recovery or every 45 mins depending on the length of surgery. To apply the headbars for the Neurotar system the skin on the top of the head was cut to expose the skull. The skull was cleaned and dried, which

enabled drilling (RA1 008, Henry Schein, U.S.A.) of a small hole in the left hand visual cortex for a metal support screw (00-96X3-32, Plastics One, U.S.A.). Using vetbond (1469SB, 3M, U.S.A.), the headplate (Model 9, Neurotar, Finland) was firmly attached and strengthened using dental cement before Kwik-cast (KWIK-CAST, W.P.I., U.K.) covered the exposed skull. Mice were checked daily to ensure recovery. After at least 5-days of recovery, habituation was performed by placing the mouse in the Neurotar frame for increasing periods of time (15-60 mins) over several days. On the day of recording, a craniotomy was performed. Under Isoflurane anaesthesia, with administration of pain medication and intra-muscular Dexamethasone (1 mg / Kg; intra-muscular; 7247104; MSD Animal Health, U.S.A.), two areas were exposed. A large (2x2mm) craniotomy over somatosensory and visual cortex on the right-hand side and a small drill hole over the motor cortex on the left hand side. Cold Cortex buffered saline was continually applied to the craniotomies. After completion, exposed dura was covered with Cortex buffered saline, sterilised slygard ($\sim 200\mu$m thickness), and a kwik-cast layer. After $\sim$ 2-hours post-recovery, the animal was moved to the Neurotar frame and the craniotomies were exposed by removal of the kwickcast and sylguard. The gDNP was carefully connected to a PCB and lowered using a micromanipulator to just above the dura over the visual cortex. The dura was gently pierced using either micro-dissection scissors or a 26-gauge needle, and the gDNP lowered $\sim$ 2 mm into the brain. A reference wire ($Ag/AgCl_2$) was placed in the ipsilateral motor cortex and g.tec hardware (see Electronics for in vivo recordings with gDNPs) used to perform a DC characterisation curve to determine the optimal Vgs and initiate the recordings. Chemoconvulsant was injected into the brain using a Nanofil injection system (W.P.I., U.K.). At the end of the experiment, sodium pentobarbital was administered intra-peritoneally.

A.6.4 Recording with solution-filled glass micropipette

Borosilicate capillary tubes (OD: 1.50mm, ID: 0.86mm, Warner Instruments) were pulled using a horizontal puller (Sutter instruments P-97, resistance of 3-5 MOhm) and filled with artificial Cerebral Spinal Fluid (NaCl: 119mM, KCl: 2.5mM, $CaCl_2$: 2.5mM, $MgSO_4$: 1.3mM, NaH_2PO_4: 1.25mM, $NaHCO_3$: 25mM, Glucose: 10mM) and attached to an Axon instruments CV-7B head stage. A micro-manipulator (MM3301, WPI) was used to position the pipette above the cortical surface before insertion approximately 400μm into the cortex. The head-stage was provided with the same reference as the gDNP, a chlorinated silver wire touching the ipsilateral motor cortex. The headstage was connected to a Multiclamp 700B amplifier (Axon

Instruments) operating in current clamp mode. Analogue-Digital Conversion and TTL pulse delivery for temporal synchronisation was achieved using the Micro1401 MkII (CED, Cambridge, U.K.). Data was acquired using WINEDR sampling at 20 kHz with a 4 kHz Bessel filter.

A.6.5 Chronic preparation surgery and recording

First, the gDNP was fibroin coated, as already described previously, to aid insertion. The rat was anaesthetised to a surgical depth using Isoflurane. After placement in a stereotaxic frame, Viscotears were applied and pain medication, which consisted of Bupenorphine (0.15 mg / Kg; sub-cutaneous; Ceva, France) and Metacam (4.5 mg /Kg; sub-cutaneous; Boehringer Ingelheim, Germany). The skull was cleaned and dried. Small burr holes ($\sim$ 1 mm) were drilled at four positions: 1) Somatosensory cortex for gDNP (since the perioral somatosensory cortex is the focal area for SWDs[358]) ; 2) contralateral cerebellum for a reference Ag/AgCl wire held in place by a nylon screw; 3) Motor cortex, ipsilateral, for a support screw ; and 4) Visual cortex, ipsilateral, for a support screw. The metal screws were inserted and provided structural support for the dental cement. Next, the gDNP and the reference wire were inserted, and a DC characterisation curve confirmed that the transistors were performing optimally. Dental cement, mixed with vetbond, was applied around the PCB for support. Animals were weighed daily and their physiology was monitored to ensure a full recovery. For recording, animals were anaesthesia-free and moving, with the PCB-interface on the head connected to an Omnetics cable (A79635, Omnetics, U.S.A.) that interfaced with the g.tec recording hardware as described above. After $\sim$ 5-minutes for settling, a DC characterisation curve was recorded to allow accurate calibration of the gSGFETs. A script calculated the optimal V_{GS} based on the transfer curves. Recordings were performed for $\sim 10 - 60$ minutes twice a week for 10 weeks. After recording, the Omnetics wire was disconnected and a protective cap was applied.

A.6.6 In-vivo data analysis

All electrophysiological data were analysed using Python 3.7 packages (Matplotlib, Numpy, Neo and Elephant) and the custom library PhyREC (https://github.com/aguimera/PhyREC). The conversion of the recorded current signals (LPF and BPF) to a voltage signal was performed by summation of the two signals and interpolation in the in vivo/chronic measured transfer curve of the

corresponding gSGFET. The transfer curves were always measured at the beginning and end of every recording to ensure that no significant variations were present, and to detect any malfunctioning transistor. Moreover, all electrophysiological recordings presented in this thesis have been calibrated with the nearest-recorded transfer curve, to ensure high fidelity in the voltage-converted signals.
The SNR shown in Figure 5.7b was evaluated by the ratio of the RMS mean value over 25 seconds of baseline recording (spontaneous activity) and post-mortem (no activity). The signal is BP filtered in three different bands corresponding to the LFP activity (1-70 Hz), high frequency (80-200 Hz) and very high frequency activity (200-4000 Hz). RMS values were calculated with a sliding window of 500 ms for the 1-70 Hz band and with a sliding window of 10 ms for the other two bands. For each BP filtered signal the mean RMS ratio was calculated and averaged for all 14 channels in the gDNP. SNR for the different bands is evaluated from a total of 4 in-vivo experiments with 4 different gDNPs (Figure 5.7b). SNR is expressed in dB ($20 \ln |RMS(S_{ignal})/RMS(N_{oise})|$).

The silencing of neuronal activity shown in Figure 5.12b, was extracted using the AC-coupled recording (HP >0.5 Hz). Then the RMS values of the pre-ictal phase (calculated with a sliding window of 1 s) are averaged over 50 s time. Similar analysis was performed for the time during the SD (15 s, see Figure A.12). The ratio of the two averaged RMS values corresponds to the neuronal activity variation [%] (before and during the SD).
The amplitude of the hippocampal SD and hyperpolarization wave in Figure 5.12b, is evaluated using the recording low-passed filtered in the infra-slow regime (<0.5 Hz) and re-sampled at 3 Hz (instead of 9.6 kHz used in the original recording). The zero of the voltage was set using the mean value of the signal 50 s before the pre-ictal phase (see Figure A.12), the minimum and maximum values for each channel were extracted (corresponding to the SD and the hyperpolarisation amplitude, respectively).
Current source density analysis applied to the low-frequency part of the recording (shown in Figure 5.14 and Figure 5.15), was calculated with the python open source Elephant library (Elephant electrophysiology analysis toolkit) using the class "Current Source Density analysis (CSD)" and the method 1D – StandardCSD was chosen for the linear gDNP array. A homogeneous conductivity of the neural tissue of $\sigma = 0.3$ S/m across the different layers of the mouse brain was used for the calculations.

The ISA concurrency with the SWDs shown in the histogram in Figure 5.24 was evaluated by performing the Hilbert transform to extract the phase of the ISA (0.01-0.1 Hz) and the RMS between 5-9 Hz (typical bandwidth for the SWD). Figure 5.23 and Figure A.14 show in more detail the dependency of ISA phase and SWD amplitude along the vertical profile.

DC-shift preceding seizures

The analysis used to extract the values presented in Figure 5.16 is described in the following:

Intracortical probes with 14 channels, 60x60 μm^2 and 100 μm^2 apart were inserted in the visual cortex of awake rodents. 4-aminopiridine was injected targeting layers 3-4 to evoke epileptiform activity. Concurrent DC-shifts and seizures were observed. 20 minute recordings starting from one minute before the first seizure following 4-aminopyridine injection were selected. Seizures with concurrent high-amplitude depolarizations such as CSDs were excluded from analysis. Resulting dataset consists of two experiments with 4/4 and 3/5 seizures analyzed respectively. 20 min recordings were filtered in two bands: DC-coupled (lowpass filter: <0.1 Hz) and seizure band (bandpass second order filter: 4-12 Hz). Signals were downsampled to 96 Hz. The RMS value of the seizure band was calculated with a 0.5 s sliding window, above and below the thresholds of given value, optimized for each recording, and validated by visual inspection. This allowed calculating the start and end of each seizure as well as its duration. Epochs at around -20 s before seizure start, and at the end of seizure plus 10 s, were extracted for analysing the DC-shifts. Drift was then corrected using a linear detrend (scipy.detrend) and zero voltage set to the mean of the first 10s of the epoch. The minimum amplitude of the epoch was then used as the amplitude of the DC-shift. To determine the onset, a threshold at -0.2 mV was used.

A.6.7 In-vivo experiments - Supplementary Figures

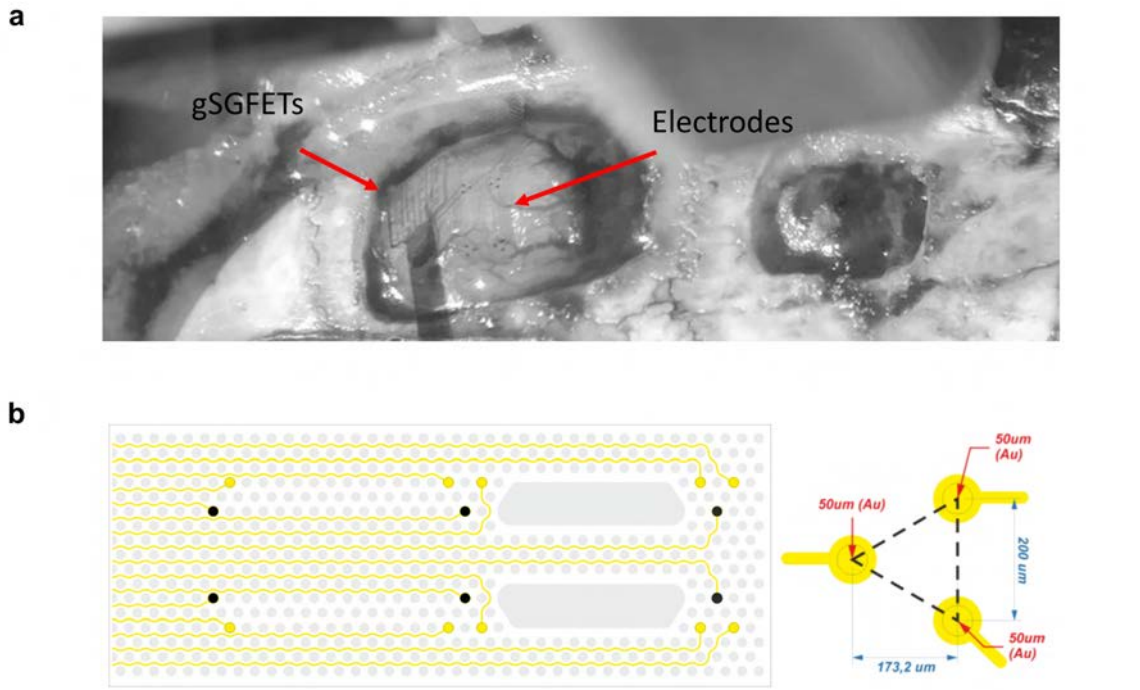

Figure A.6: a. Photographs of the craniotomies and epicortical probes (transistors and electrodes) positioning for the results shown in Figure 5.3. **b**. Layout of the microelectrode array used for the comparison of ultraslow frequency recordings with a gSGFET array (left), and dimensions and separation of the electrodes in each triode (right). The central electrodes that were deposited with platinum black are depicted in grey. Adapted from [63]

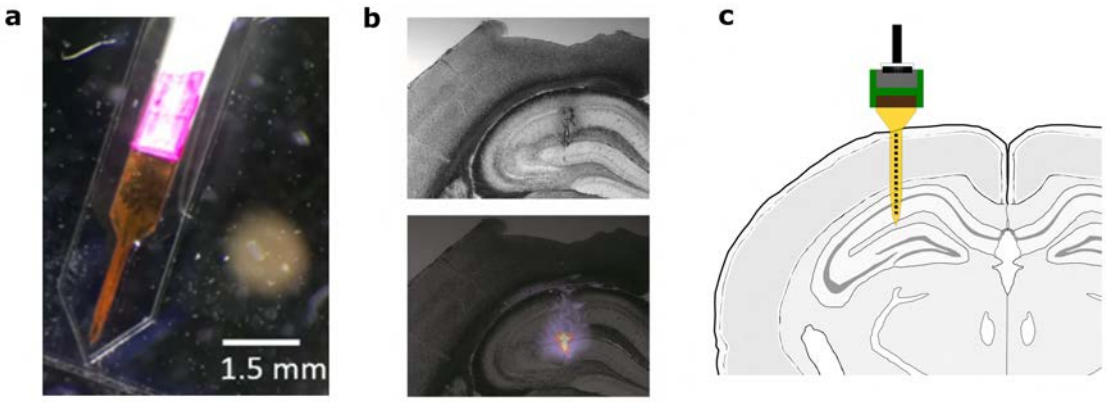

Figure A.7: a. Photograph of the gDNP placed in the PDMS mold before back-coating with silk-fibroin. The back side of the tip (the side without graphene) is coated with Dil stain (Invitrogen^{TM}; Vybrant^{TM} CM-DiI Cell-Labeling Solution) before the SF is applied. **b**. Histology image of a coronal cross section of the mouse brain after the recording. Dil stain marks the position of the tip of the probe in the hippocampus. **c**. Cartoon of the coronal section of the mouse brain, indicating the position of the probe accordingly to the histology image.

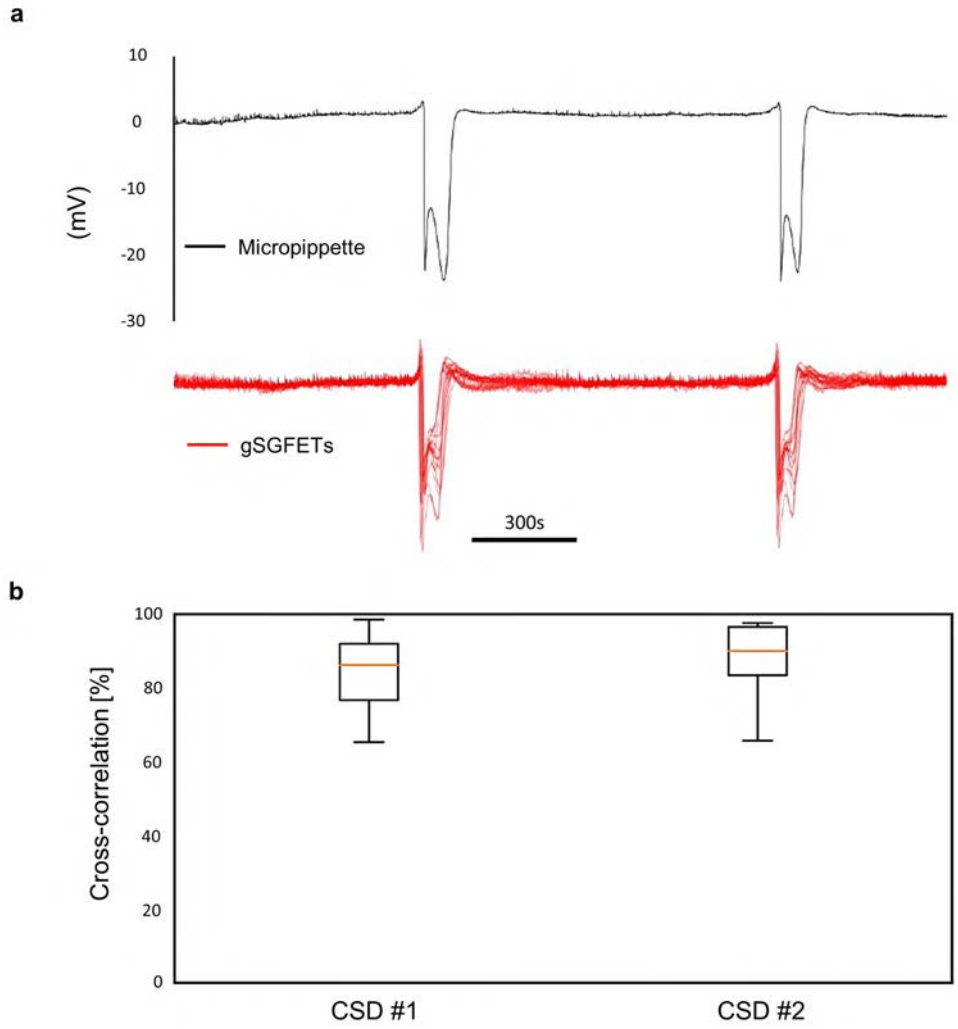

Figure A.8: **a**. In vivo recordings of a 16 channel epicortical array (red lines) and micropipette (black line) for comparison. **b**. Boxplots of the maximum cross-correlation (center line, median; box limits, upper and lower quartiles) of the 16 gSGFETs recordings and the micropipette recording for the two CSDs in **a**, showing the high similarity of gSGFETs and micropipette CSD recordings. Cross-correlations were calculated using *matplotlib.pyplot.xcorr* function, matplotlib version 2.1.0, for 400 s long signals sampled at 5 Hz and centred at the corresponding CSD. Adapted from [63]

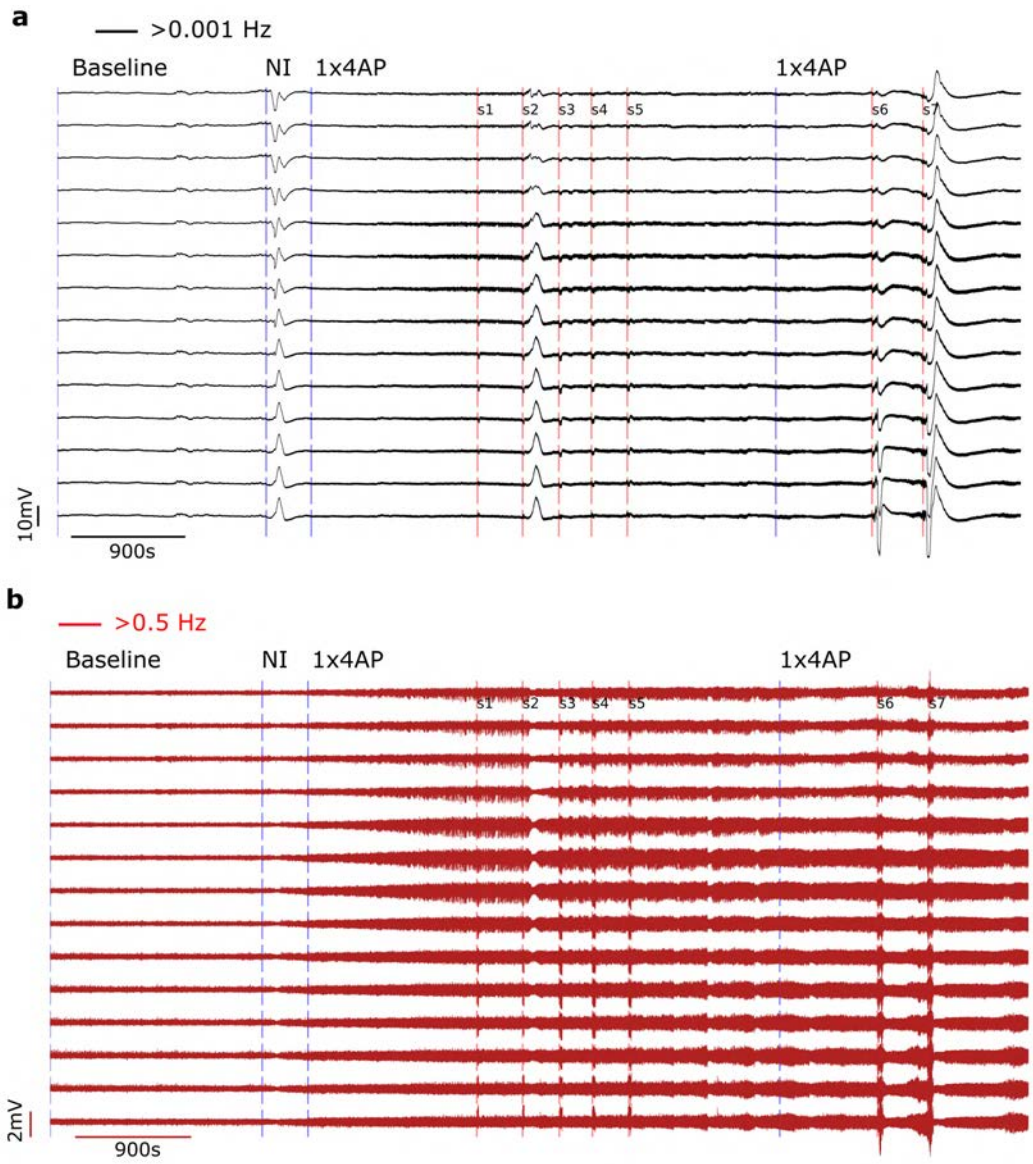

Figure A.9: **a**. 2 hours of in depth full-bandwidth recording filtered (>0.001 Hz). **b**. Same recording filtered above 0.5 Hz, showing the loss of low frequency information for conventional electrodes. Red vertical lines correspond to the seizure events (s1-s7), blue line describe the action during the in-vivo experiment, such as needle insertion (NI) and the injection of 4AP to induce epileptiform activity.

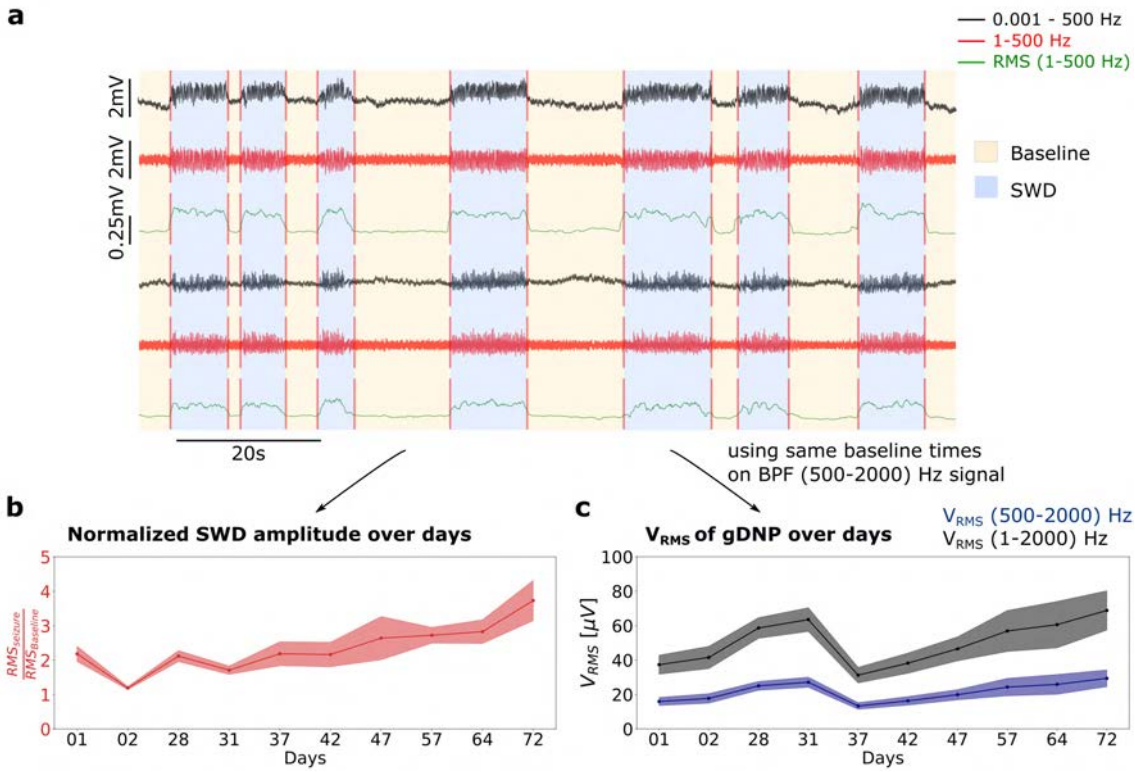

Figure A.10: a. The automatic detection of the SWDs is performed calculating the RMS (green) of the HP filtered signal $1-500$ Hz (red) (sliding window 0.01 s). The mean value of the RMS along the whole recording is used as threshold level: everything above is considered SWD, everything below is baseline. **b**. normalised SWD amplitude over the implanted time. The ratio of the averaged RMS value during the SWDs and RMS value in the baseline is averaged for all channel on the gDNP. **c**. For the VRMS evaluation of the gDNP, we use the same detection strategy to filter out the SWDs event and average the RMS only in the baseline for the HP $500-2000$ Hz. Then using the 1/f type of noise of graphene transistors[304] (see equation (A.7)), we extrapolate the VRMS of the gDNP in the range $1-2000$ Hz using equation (A.8).

$$V^2_{RMS} = \int_{f_1}^{f_2} S_V \mathrm{d}f = \int_{f_1}^{f_2} \frac{1}{f} \mathrm{d}f = \ln|\frac{f_2}{f_1}| \tag{A.7}$$

$$V^2_{RMS,BW_2} = V^2_{RMS,BW_1} \times \frac{\ln|\frac{f_f,BW_2}{f_i,BW_2}|}{\ln|\frac{f_f,BW_1}{f_i,BW_1}|} \tag{A.8}$$

Where S_v is the noise power ($1/f$ type of noise), f_f, BW_2 , f_i, BW_2 are the final and initial frequencies of the bandwidth BW_2 and f_f, BW_1 , f_i, BW_1 the initial and final frequencies of BW_1. In our case $BW_2 = [1-2000]$ Hz and $BW_1 = [500-2000]$ Hz.

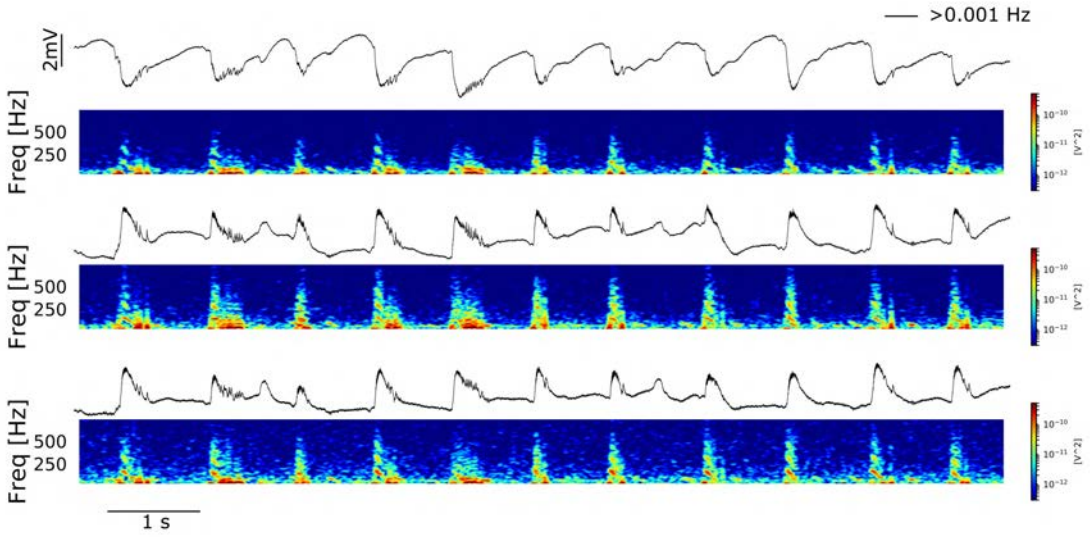

Figure A.11: Spectrograms (range 10-750 Hz) of the interictal activity with associated HFOs and sharp ripple waves in three different depths (shown in Figure 5.8). The spectrogram revels layer-specific high frequency tones of the HFOs. Top channel: superficial cortex; middle channel: lower layer of neocortex; bottom channel: CA1 region in hippocampus.

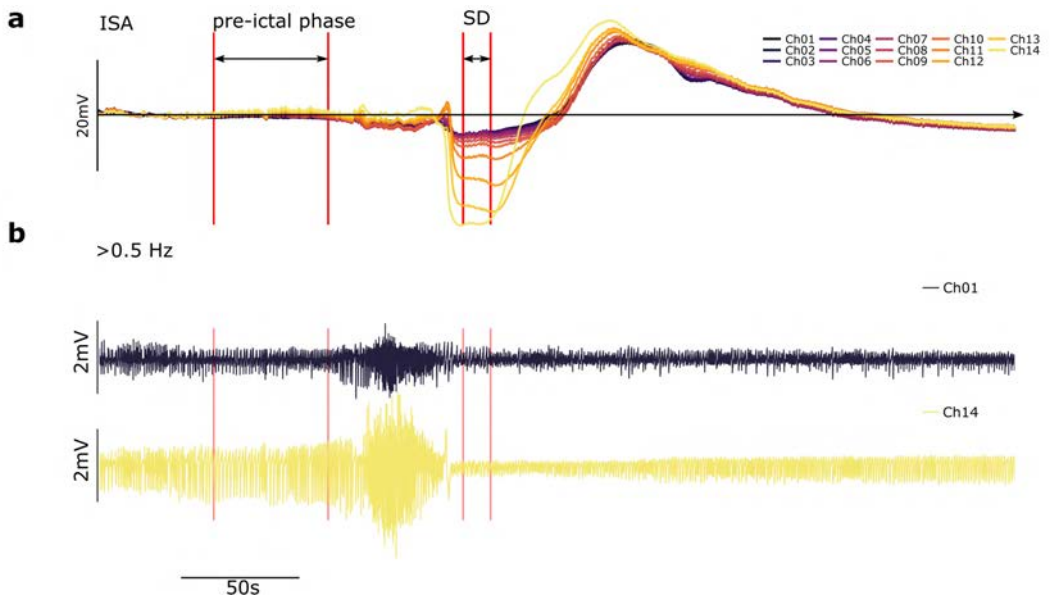

Figure A.12: **a**. shows the ISA activity (0.5 Hz) of the recording shown in Figure 5.12. All the channels are overlapped with colour gradient corresponding to their depth. **b**. HP filtered (0.5 Hz) recording for Ch01 and Ch14. The neural activity variation in Figure 5.12 displays the neural silencing scenario that is happening after the hippocampal SD. The neural activity variation is evaluated in terms of ratio of the mean values of the RMS (sliding window of 1s) of the HP filtered (0.5 Hz) signal during the SD and during the pre-ictal phase respectively. For the calculation of the amplitude of the SD and hyperpolarisation the minimum and maximum values shown in panel (**a**) are averaged in a short time window (2s). The amplitudes are calculated in reference to the zero set by averaging the first 50s of the pre-ictal phase.

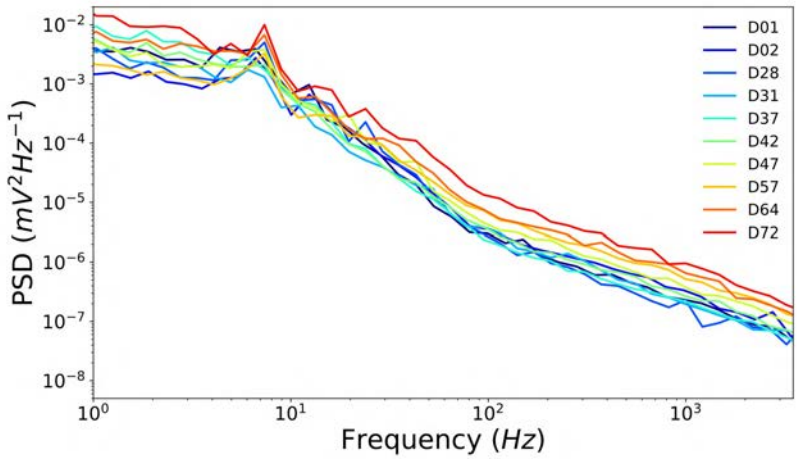

Figure A.13: Averaged power spectral density (PSD) of all working channels on the gDNP over implantation time. The averaged PSD values are calculated over 500s of neural recordings. The peak around 8 Hz represents the frequency of the spontaneous SWDs.

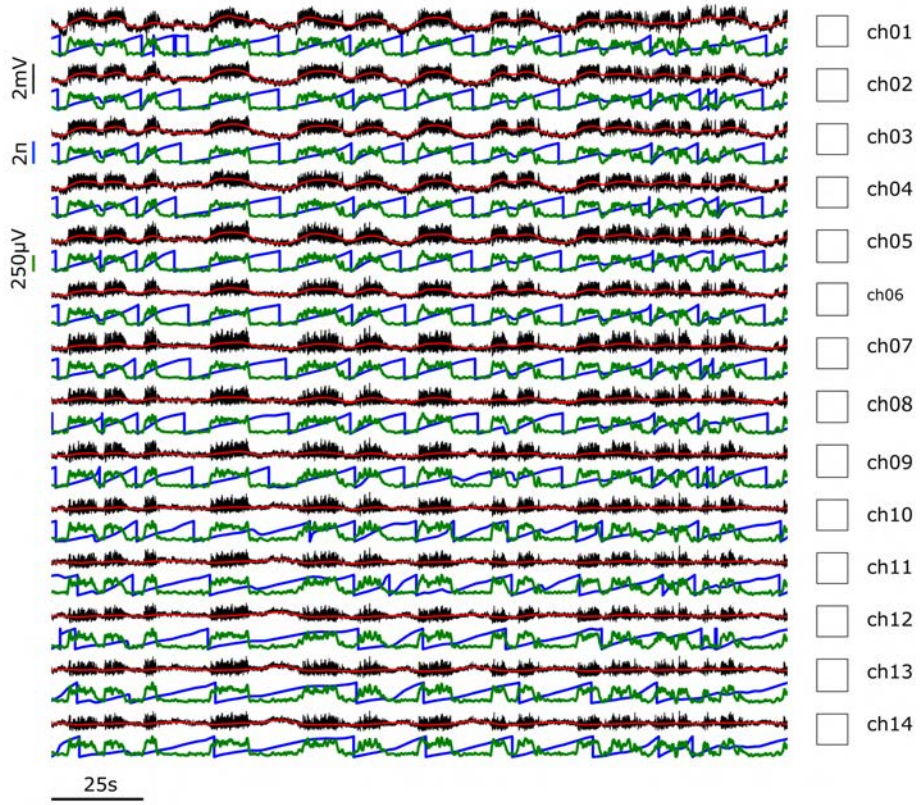

Figure A.14: Vertical recording profile across the cortical laminae (somatosensory cortex) of the WAG-Rij rat illustrating the layer-specific DC-shift during the absence seizure (SWD). Root-mean square (RMS, green) calculated between 5-9 Hz and ISA phase ($0.01 - 0.1$ Hz blue).

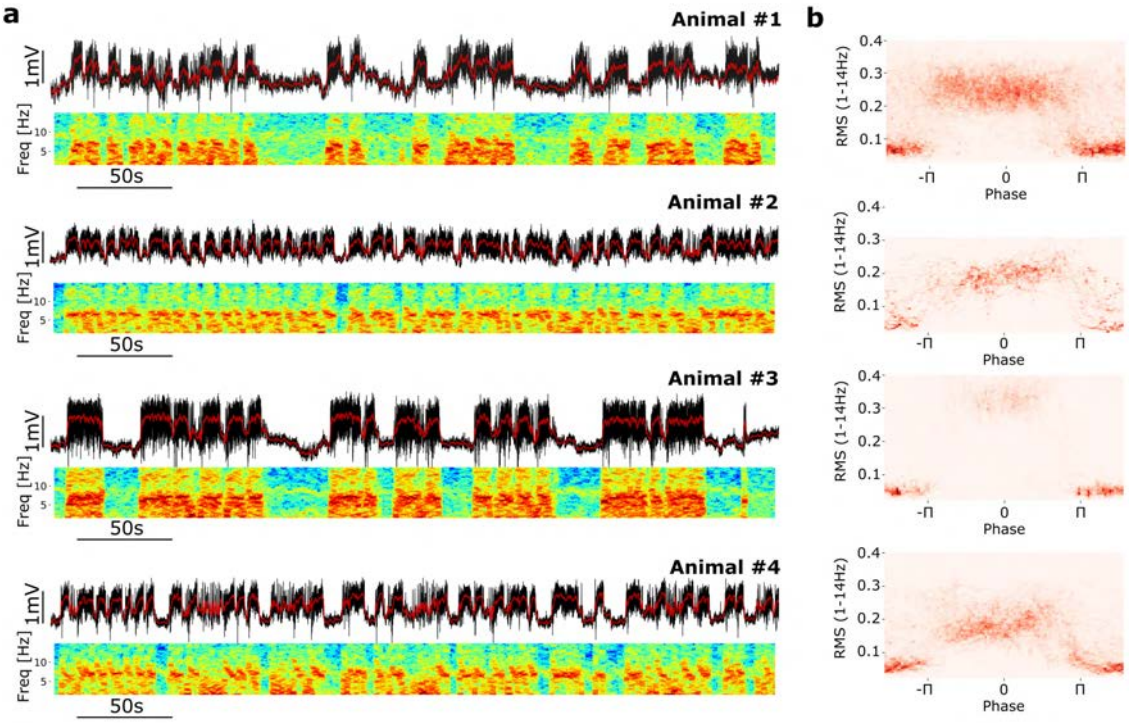

Figure A.15: a. Long recording (380s) showing the relationship between ISA and SWDs observed in all four implanted WAG-Rij rats. The full bandwidth (black) and HP <0.5 Hz (red) are overlapped. Spectrograms of the activity (1-14 Hz) to visualize the recruitment of SWDs. **b**. Density distribution for each WAG-Rij rat evaluated over a long recording (1600s). y-axes correspond to the RMS (1-14 Hz) associated with SWD while in the x-axis the phase of the ISA (0.005-0.05 Hz) computed by Hilbert transformation (red represents higher density).

A.7 Immunohistochemistry and Biocompatibility Assessment

A.7.1 Device manufacture and sterilization

Two types of flexible gDNP where fabricated for the immunohistochemical study: one with graphene and one without graphene, following the fabrication steps described above (see Section 3.1). In the devices gDNP without graphene the graphene, instead of being defined by RIE, was etched away. By doing so, we make sure that all the fabrication steps are equal for both, gDNP with and gDNP without graphene. For comparison to rigid devices currently available on the market, iridium Neuronexus electrodes (A1x32-Poly2-5mm-50s-177) with a thickness of 15μm and length 5mm were implanted. Devices were sterilised individually with ethylene oxide, using an Anprolene AN-74i sterilizer, performed according to manufacturer's instructions.

A.7.2 Surgical implantation of devices

Adult male Sprague-Dawley rats (230-280g) were used for this study (Charles River, England). All animals were kept in individually ventilated cages (Techniplast, GR1800) in groups of 3-4, housed at a constant ambient temperature of 21 ± 2°C and humidity of 40–50%, on a 12-h light, 12-h dark cycle. All rats were given free access to diet and water. Experimental procedures were conducted in compliance with the Animal welfare act 1998, with approval of the Home Office and local animal welfare ethical review body (AWERB). Animals were anaesthetized with Isoflurane (2-3%) throughout surgery, and depth of anaesthesia was monitored with the toe pinch reflex test. Animals were fixed to a stereotaxic frame (Kopf, model 900LS), and body temperature was maintained with a thermal blanket. A small craniotomy ($\sim$ 3mm) was made with a micro drill (WPI, OmniDrill35) above the somatosensory cortex, the dura was excised and one of three depth probe devices were implanted; i) graphene device, ii) no graphene device, or iii) Neuronexus device, at coordinates relative to bregma; anteroposterior (AP): 0mm, dorsoventral (DV): $\pm$3.5mm, and mediolateral: $-$1.5mm. The craniotomy site was sealed with Kwik Sil (WPI), secured with dental cement, the skin was sutured closed, and anaesthetic was withdrawn, with saline (20ml/kg) and buprenorphine (0.03mg/kg in saline) given subcutaneously to replace lost fluids and reduce post-operative pain.

A.7.3 Tissue collection and processing

Animals were culled at 2, 6 or 12 weeks' post-implantation dependent on the analysis to be performed. Tissue was taken either for immunohistochemical analysis of cells related to inflammatory processes, or for cytokine analysis of inflammatory markers.

Histology. At the end of the experimental period (2, 6 or 12 weeks) rats were anaesthetized with Isoflurane and culled via cardiac perfusion with heparinised (10U/ml, Sigma-Aldrich) phosphate buffered saline (PBS), followed by 4% Paraformaldehyde (PFA, Sigma-Aldrich) in PBS. Brains were then post-fixed in 4% PFA in PBS for 24 hours, transferred to 0.01% Sodium Azide PBS (Sigma S-8032) thereafter, and stored at 4°C. Axial plane brain sections were cut at 50μm thickness with a vibrotome (Leica, VT1200). Sections at an approximate depth probe site depth of 0.8mm were selected for staining. Sections were stained free-floating for two markers; i) ionized calcium binding adaptor molecule 1 (Iba1) to quantify microglial population, or ii) Glial fibrillary acidic protein (GFAP) staining to assess astrocyte presence. Tissue sections were stained with rabbit anti-Iba1 (1:1000, Wako), and chicken anti-GFAP (1:2000, Abcam ab4674) overnight at 4°C. Sections were incubated with the secondary antibodies; anti-rabbit Alexa Fluor (AF) 560, and anti-chicken AF647 (all 1:500, Thermofisher) for 2 hours at room temperature. Sections were mounted onto slides and coverslips were mounted with Prolong Gold antifade mounting media (Thermofisher). Slides were imaged with a Leica SP8 confocal microscope with a 10x objective lens. Laser power and digital gain was kept consistent across imaging sessions. A single optical section of the tissue surrounding the probe sight was taken within the middle portion of the section as to avoid edge effects. Microglial cells were individually classified into one of four morphologies; Grade 0 (resting/ramified), Grade 1 (de-ramifying/re-ramifying), Grade 2 (activated/amoeboid) or Grade 3 (clustered activated). Activation was determined as a percentage of total microglial cells which were either Grade 3 or 4.

Enzyme-Linked ImmunoSorbent Assay (ELISA) Protocol. For ELISA, animals were culled by rising concentration of CO_2. Brain tissue was extracted, snap frozen in liquid nitrogen, and stored at -80°C until further use. Brain tissue was lysed by addition of NP-40 lysis buffer (150 mM NaCl, 50 mM Tric-Cl, 1% Nonidet P40 substitute, Fluka, pH adjusted to 7.4) containing protease and phosphatase inhibitor (Halt^{TM} Protease and Phosphatase Inhibitor Cocktail, ThermoFisher Scientific) followed by mechanical disruption of the tissue (TissueLyser LT, Qiagen). Samples

were centrifuged at 5000RPM for 10 minutes, and the supernatant stored at 4°C until further use. A bead-based multiplex ELISA kit was run, which included markers interleukin-1a (IL-1a), interleukin-1beta (IL-1b), interleukin-17 alpha (IL-17a), and interleukin-33 (IL-33) (Cat. No. 740401, Biolegend). The standard instructions for the kit were used, with protein loaded at a fixed volume of 15μL. After incubation, beads were run on the BD FACSVerse flow cytometer, and the data analysed using LEGENDplexTM Data Analysis software.

Immunohistochemical data analysis. Raw TIF files were loaded into a custom Python3.7 script (github.com/kebarr/biocompatibility_study). We averaged the data obtained from each section in an animal prior to plotting, so each data point corresponds to a single animal. The values for each section were obtained as described below.

1. **GFAP evaluation** The fluorescence intensity of the normalised GFAP images was assessed as a function of distance from the probe site. First, the probe site was localised in each image, based on the bright fluorescence around its edges (Figure A.17 and Figure A.19a). The region identified as the probe site was used as a base mask for quantifying the fluorescence intensity, and the intensity in the masked area was summed, so that it could be later subtracted when calculating the intensity in bands around the probe site. To quantify the intensity within a distance of one pixel from the edge of the probe site, the binary dilation operation was applied to the probe site mask. Then, the intensity within the dilated mask was summed, and the intensity inside the region of the base mask was subtracted, leaving the total intensity within the ring around the probe site. This process was then repeated, always subtracting the total intensity from the previous masked area as we iterated outwards up to 200 pixels from the probe site. To visualise this data, all the curves obtained for each condition were smoothed using a Savitzky-Golay filter, then averaged by the lineplot function in the Python seaborn (version 0.9.0) package, giving one final curve.

2. **Iba1 evaluation**. IBA1 fluorescence images were used to quantify the microglial activation. First, the cells were segmented based on pixel values exceeding a simple, manually set, threshold. The segmented cells were then labelled using the 'measure.label' function from scikit-image (v 0.16.2), and their region properties were quantified using the 'measure.regionprops' function. One of these properties is called the 'extent,' which compares the area of the

bounding box of the labelled object to the area of the object itself. Spindly objects, such as microglia that are not activated, will have a large bounding box for a relatively small object area, leading to a small extent. Rounder objects without long protrusions, such as activated microglia, will occupy a large amount of their bounding box, leading to a larger extent. Hence, this metric can be used to classify whether microglia are activated or not. As example of how this classification strategy works, please see Figure A.19. Manual cross-checking of a number of cell counts was performed to validate the automated classification.

Statistical analysis. For histological staining, all data sets are n=3, with the exception of 2-week graphene, which is n=4, and 12 weeks Neuronexus probes which are n=2, due to an inability to locate the probe location in histological sections for one animal implanted. For ELISA testing, gDNP with and without graphene hemisphere data sets are n=3 or 4 at all timepoints, while contralateral hemispheres were combined, giving n=7.

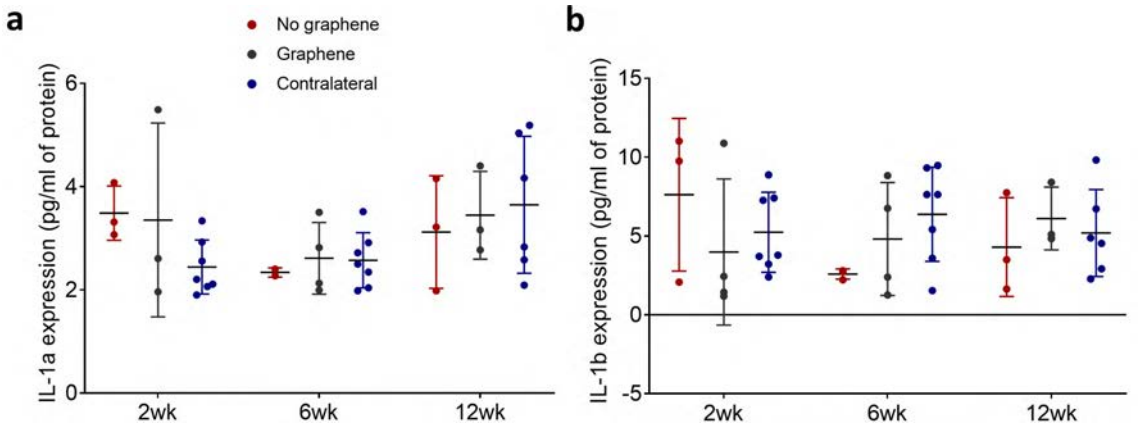

Figure A.16: ELISA data for pro-inflammatory markers such as (**a**) interleukin-1a (IL-1a) and (**b**) interleukin-1beta (IL-1b), showed no evidence of increased neuro-inflammation for either gDNP with and without graphene at any timepoint, even when compared to the contralateral hemisphere, where there was no device implanted.

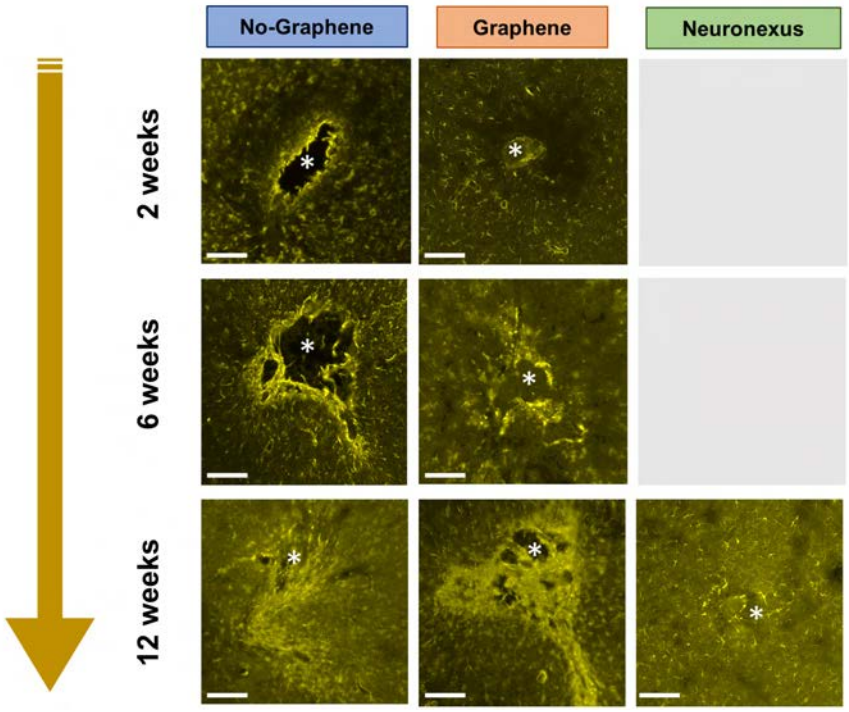

Figure A.17: GFAP fluorescence intensity images in the area surrounding probe implantation site (withe star, 0.8mm depth) for "no-graphene" gDNPs, "graphene" gDNPs and rigid Neuronexus probes at 2, 6 and 12 weeks post implantation.

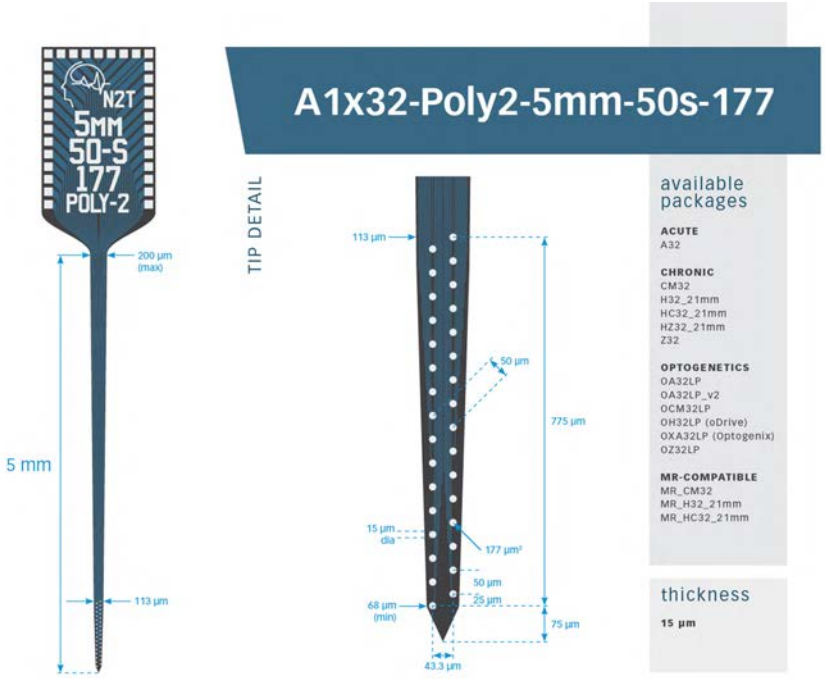

Figure A.18: Neuronexus silicon probe (16 Channels, model name: A1x16-Poly2-5mm-50s-177) inserted in the rat brain as a comparison benchmark for the biocompatibility assessment of the SF-coated gDNP displayed in this thesis. Source: Neuronexus productdescription.

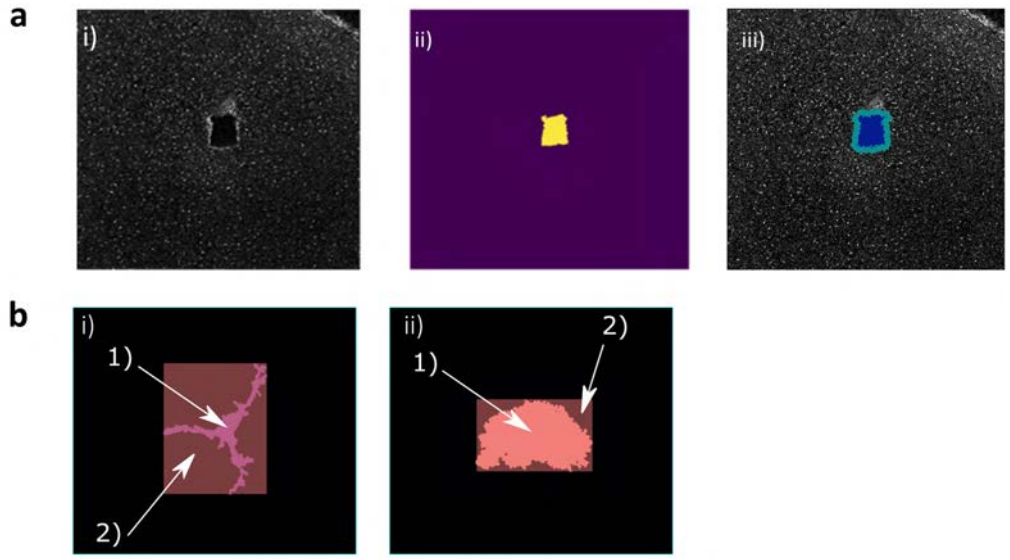

Figure A.19: Schematic diagram indicating the strategy used for the quantitative analysis of histologic images. **a**. General strategy used for analysis of each type of fluorescence image: i) Original image; ii) Probe site located; iii) Having located the probe site, a binary dilation operation is applied to increase the size of the mask induced by the probe site by one pixel in every direction. The area and intensity in the outer band are calculated, then the process is repeated. This figure is for explanatory purposes only, and is not to scale. **b**. Quantifying the microglia activation, based on the ratio of the area of bounding box (2) to the area of cell (1): i) Unactivated cells are small, with long dendrites, so have a large bounding box. ii) Activated cells are rounder, with no dendrites, so the cell body occupies most of the bounding box.